

Optimising Bioremediation End-Points for the Safe and Effective Long-Term Stewardship of UK Radwaste Impacted Land

*A thesis submitted to the University of Manchester for the degree of Doctor of
Philosophy in the Faculty of Science and Engineering*

2020

Gianni F. Vettese

School of Natural Sciences

Academic Supervisors: Jonathan Lloyd, Kath Morris and Sam Shaw

Table of Contents

List of Figures	7
Abbreviations	17
Abstract.....	18
Declaration.....	19
Copyright statement	20
Acknowledgements.....	21
About the Author	22
Chapter 1: Project Relevance, Research Rationale and Aims and Thesis Structure	23
1.0 Project Relevance.....	23
1.1 Research Rationale and Aims.....	23
1.2 Thesis Structure	24
Chapter 2: Literature Review	26
2.0 Nuclear Energy	26
2.1 The Nuclear Fuel Cycle, Nuclear Legacy, Radioactive Waste Management plans and Desirable End-Points	27
2.11 Nuclear Fission and Energy Production	27
2.12 The Nuclear Fuel Cycle	28
2.13 The Disposal of Nuclear Waste	29
2.2 Radioactively Contaminated Land and the Sellafield Site	32
2.21 Radioactively Contaminated Sites	32
2.22 The Sellafield Site	33
2.23 A Brief History of the Sellafield Site	33
2.24 The (Hydro-)Geology of the Sellafield site	34
2.25 Radioactive Contamination and Groundwater Monitoring at the Sellafield Site	35
2.26 Radionuclide Mobility – Speciation, Oxidation State, pH and Hydrolysis.....	36
2.27 Remediation Strategies.....	38
2.28 The Nuclear Provision & Suitable End-points	39
2.3 Microorganisms and Bioremediation	41
2.31 Microorganisms & Microbial Diversity.....	41
2.32 Bioremediation	42
2.4 Iron Biogeochemistry	44
2.41 The Chemistry of Fe	44
2.42 Microbial Respiration of Fe(III)	44

2.43	Dissimilatory Iron-Reducing Bacteria: Geobacter and Shewanella	46
2.44	Iron Nano-Particles	49
2.5	Uranium: Nuclear and Biogeochemistry	50
2.51	Nuclear U Chemistry	50
2.52	U Biogeochemistry	51
2.53	The Elusive U(V)	53
2.54	U mobility at the Sellafield site	54
2.55	Microbial Respiration of U	54
2.56	The Longevity of U(IV) end-points	56
2.57	U Interactions with Fe	57
2.58	U Phosphates	58
2.59	U reduction during Sulphate reducing conditions	59
2.510	U interactions with slow release donors – MRC	60
2.6	Strontium Nuclear and Biogeochemistry	60
2.61	Nuclear Sr Chemistry	60
2.62	Bioremediation of Sr	60
2.63	Sr Mobility at the Sellafield Site	61
2.64	Sr-nZVI Interactions	62
2.65	Sr Phosphates	62
Chapter 3:	Research Methods	63
3.1	Microbiological methods	63
3.11	Pure Culture Experiments:	63
	Geobacter	63
	Shewanella	64
3.12	Batch Bioreduction Microcosm Experiments	64
3.13	Batch Reoxidation Remobilisation Microcosms	66
3.14	Sediment Columns	66
3.2	Aqueous Geochemical Analyses	68
3.21	pH and Eh Measurements	68
3.22	Ion Chromatography	68
3.23	Inductively-Coupled Plasma Atomic Emission Spectroscopy and Mass Spectrometry	68
3.24	UV VIS Spectrophotometry	69
3.25	Luminescence Spectroscopy	73
3.26	Raman Spectroscopy	74

3.27 PHREEQC Computational Analysis	76
3.3 Solid Phase Analyses	77
3.31 Powder X-ray Diffraction (P-XRD)	77
3.32 Loss On Ignition (LOI)	78
3.33 X-ray Fluorescence (XRF).....	78
3.34 X-ray Absorption Spectroscopy (XAS)	80
3.35 High Energy Resolution Fluorescence Detected (HERFD) XANES	84
3.36 Environmental Scanning Electron Microscopy and Energy Dispersive X-ray Spectroscopy .	85
3.37 Microbial Analysis – 16S rRNA Gene Sequencing	85
3.4 Preparation of Uranyl dichloride Stock Solutions.....	Error! Bookmark not defined.
Chapter 4: Multiple Lines of Evidence Identify U(V) as a Key Intermediate during U(VI) Reduction by <i>Shewanella oneidensis</i> MR1.....	87
Chapter 5: Comparison of Radionuclide End-Points; the Long-Term Stabilities of U and Sr Co-Treated Sediments after Oxygen and Nitrate Perturbations	117
5.1 Abstract.....	118
5.2 Introduction	119
5.3 Materials and methods.....	121
5.31 Sediment Characterisation.....	121
5.32 Batch Microcosm Experiments	121
5.33 Oxidative Remobilisation of U and Sr	122
5.34 Solid-phase Analysis.....	122
5.35 Proprietary substrates	122
5.4 Results and Discussion	123
5.41 Batch Microcosm Experiments	123
5.42 Microbial Analysis After Batch Incubation.....	126
5.43 Speciation of Solid Phase U and Sr: XAS	128
5.44 Oxidative Remobilisation of U and Sr	131
5.45 Microbial Analysis of the Remobilised Samples	133
U Speciation in the Remobilised Nanoscale Zero Valent Iron Samples	133
5.5 Conclusions	133
5.6 Acknowledgements.....	134
5.7 Supporting Information	134
SI 1: Sediment and Synthetic Groundwater Composition	134
SI 2: Experiment Design and Visible Changes	135

SI 3: pH and Eh changes	135
SI 4: Ion Chromatography	137
SI 5: Total Aqueous Fe.....	149
SI 6: Microbial Community Characterisation	150
SI 7: Additional X-ray Absorption Spectroscopy Data and Analysis.....	154
SI 8: Powder X-Ray Diffraction	161
SI 8: Control Precipitation Experiment.....	161
Chapter 6: Quantifying the Stability of Remediation End-Points for Uranium and Strontium Contaminated Land: Potential Impact of Ground- and Seawater Ingress.....	162
6.1 Abstract.....	163
6.2 Introduction	164
6.3 Materials and Methods.....	166
6.31 Sediment Characterisation and Batch Treatment Phase	166
6.32 Column Design and Operation.....	166
6.33 Column Sacrifice.....	167
6.4 Results and Discussion	167
6.41 U(VI) and Sr Batch Incubation Experiments.....	167
6.42 Column Effluent Geochemistry	168
6.43 Solid Phase Geochemistry.....	171
6.5 Conclusions	174
6.6 Acknowledgements.....	174
6.7 Supporting Information	174
S1: Experimental Setup	174
S2: Column effluents.....	177
S3: Column End-points.....	181
Chapter 7: Thesis Conclusions and Future Work	187
Chapter 8: List of References	190
Chapter 9: (Appendix 1) Travel Bursaries, Awards and Conference Presentations	223
9.1 Travel Bursaries.....	223
9.2 Awards	223
9.3 Conference Presentations.....	223
9.31 Oral Presentations	223
9.32 Poster Presentations.....	223

Chapter 10: (Appendix 2) Using Urea as an Electron Donor/ pH Conditioner for Sr Contaminated Lands	224
Abstract.....	224
Introduction	224
Methods.....	226
Sediment characterisation	226
Microcosm experimental	226
Geochemical analyses.....	226
Results and discussion	227
Change in pH and consumption of urea	227
Sr Solution Chemistry	228
Conclusions and Further work:	229

List of Figures

Figure 1: Nuclear energy generation by country (TWh). Taken from the International Atomic Energy Agency (IAEA) Power Reactor Information System (PRIS) Database (IAEA, 2020).	27
Figure 2: Generating energy from nuclear fission, a cartoon image of a Pressurized Water Reactor. Image taken from (United States Nuclear Regularoty Comission, 2017).	28
Figure 3: The open and closed (inc. orange arrows) nuclear fuel cycles	29
Figure 4: A map of the NDA's 17 nuclear decommissioning sites, with Sellafield and the nearby Low Level Waste Repository circled in red. Adapted from (NDA, 2004).	30
Figure 5: a) Total radioactivity at 2019 (TBq); and b) Lifetime Total proportion of Waste Volume by Type (%).	31
Figure 6: Examples of multi-barrier systems for Intermediate Level Waste (left hand side), and for High Level Waste (right hand side). Image taken from (The Department of Energy and Climate Change, 2014).	32
Figure 7: An aerial view of the Sellafield site. Taken from (NDA, 2019b)	33
Figure 8: A conceptual model of the Sellafield Site, describing the regional hydrogeology. Taken from (Sellafield Ltd., 2015)	35
Figure 9: An overview of the Sellafield site (blue) and the Separation Area (red). A)The groundwater monitoring wells network; B) Average total alpha concentrations (results below the CEAR target Limit of Detection (LOD) of 0.03 Bq l^{-1} are displayed on the figure as <LOD); and C) Average ^{90}Sr concentrations (results below the CEAR target LOD of 0.12 Bq l^{-1} are displayed on the figure as <LOD); copied from (Sellafield Ltd., 2017).	36
Figure 10: Changing oxidation state with Eh for selected radionuclides at pH(7). Where does U(V) lie? Adapted from (Lloyd, 2003).	37
Figure 11: A proposed end point for a successfully decommissioned nuclear site. SEPA recommend that operators should establish and maintain a waste management plan until the site reaches its' target reference state as demonstrated above. Taken from [(Scottish Environment Protection Agency, 2016)].	39
Figure 12: (Left) The Rocky Flats site in June 1995 prior to the final clean-up operation; and (right) the Rocky Flats National Wildlife Refuge. Images taken from (U.S. Department of Energy, 2019).	40
Figure 13: The mechanisms used by microbes to immobilise U in contaminated groundwater. Image taken from (Newsome et al., 2014a).	43
Figure 14: Conceptual illustration of the process of uranium bioremediation. (a) Native bacteria present in contaminated sediments can couple the oxidation of organic carbon compounds with the reduction of $\text{U(VI)}_{(\text{aq})}$. (b) Reduced U(IV) can be re-oxidised when C addition stops, or upon the arrival of oxidants; in this case O_2 , NO_3 , and Fe(III) . Low permeability coatings, such as FeS , can suppress re-oxidation and maintain stability of immobilized U(IV) . Taken from (Williams et al., 2013).	44

Figure 15: the iron cycle, showing chemical and microbial redox transformations. Oxidative processes are in blue and reductive processes are in red.....	44
Figure 16: A phylogenetic tree based on the 16S rRNA gene sequences of microorganisms reported to be capable of conserving energy for growth from Fe(III) reduction. Taken from reference [(Lovley et al., 2004)].	45
Figure 17: examples of microbial Fe reduction mediated by: a) direct contact, b) electron shuttle and c) use of a chelating agent. Oxidative processes are in blue and reductive processes are in red.....	46
Figure 18: Demonstrating microbial growth by coupling the oxidation of acetate with the reduction of Fe(III). Oxidative processes are in blue and reductive processes are in red.....	46
Figure 19: Simplified schematic diagram of a typical <i>Geobacter</i> cell showing proposed models for electron transfer pathways during reduction of solid phase metal Fe or Mn phases. Yellow arrows represent proposed electron transfer paths, identified c-type cytochromes are in red. OM - outer membrane, PS - peptidoglycan periplasm, IM - inner membrane. Taken from (Shi et al., 2007).	47
Figure 20: Simplified schematic diagram of a typical <i>S. oneidensis</i> MR-1 cell showing proposed models for direct (contact) electron transfer pathways during reduction of solid phase metal Fe or Mn phases at the cell surface. Yellow arrows represent proposed electron transfer paths, identified c-type cytochromes are in red. OM - outer membrane, PS - peptidoglycan periplasm, IM - inner membrane. Taken from reference (Shi et al., 2007).	48
Figure 21: (from left to right) riboflavin, riboflavin mononucleotide and anthraquinone-2,6-disulphonate in oxidised forms. Riboflavin is excreted by <i>S. oneidensis</i> MR1, AQDS can be used as a synthetic analogue.....	49
Figure 22: microbially mediated reduction of Fe(III) by means of catalytic redox transformations of an extracellular riboflavin molecule. As done by <i>Shewanella oneidensis</i> MR-1. Oxidative processes are in blue and reductive processes are in red.....	49
Figure 23: Cartoon schematic (Left) and TEM (Right) of Carbo-Iron® (bar 100 nm). Taken from (Mackenzie et al., 2016).....	50
Figure 24: Induced fission of ^{235}U . A neutron is absorbed by the ^{235}U nucleus, it momentarily forms an excited, and unstable ^{236}U nucleus. In turn, this ^{236}U nucleus splits into lighter fission products ^{141}Ba and ^{92}Kr , releasing some more neutrons, energy and gamma rays (not shown).	51
Figure 25: Speciation diagram of U(VI)O_2^{2+} as a function of pH in natural waters. Taken from (Choppin, 2006)	52
Figure 26: Redox couples for U(VI) species compared to environmentally relevant redox couples within sediments at circumneutral pH. Taken from (Ginder-Vogel and Fendorf, 2007).....	52
Figure 27: Examples of isolated and characterised $[\text{UO}_2]^+$ compounds. Image modified from [(Arnold et al., 2009; Berthet et al., 2003; Natrajan et al., 2006)].	54
Figure 28: 16S rRNA based phylogenetic tree of U(VI)-reducing prokaryotes. Taken from (Williams et al., 2013).	55
Figure 29: U adsorption, precipitation and incorporation in Fe rich systems. Taken from (Roberts et al., 2017).	58

Figure 30: Sr sorption by inner-sphere and outer-sphere complexation.	61
Figure 31: Resting cells of <i>G. sulfurreducens</i> in NaHCO ₃ buffer solution	63
Figure 32: Resting cells of <i>S. oneidensis</i> MR-1 in NaHCO ₃ buffer solution.	64
Figure 33: Culturing <i>S. oneidensis</i> MR-1 on Fe(III) rich agar plate.	64
Figure 34: Examples of remobilisation experiments; A) aerobic perturbations in conical flasks and; B) nitrate amended serum bottles.	66
Figure 35: A) schematic depicting the column setup; B) a photo of a column. Influent flowed from the bottom to the top of the column.	67
Figure 36: the chemical structure of Ferrozine.	70
Figure 37: BromoPADAP assay: the standards (blue crosses) are 0, 2.5, 5, 10, 15 and 25 ppm UO ₂ ²⁺ . The analyte concentration (red cross) was calculated by inserting the absorbance value into the line of best fit equation.	71
Figure 38: Chemical structure of 2-(5-bromo-2-pyridylazo)-5-diethylaminophenol for spectrophotometric determination of Uranium(VI) in solution.	71
Figure 39: Comparison of the Urea standards ran in DIW (blue) and AGW (red).	72
Figure 40: Schiff base hydrochloride formation, the product is responsible for the yellow coloured solution measured.	72
Figure 41: Describing molecular fluorescence. (blue) a molecule is electronically excited from a ground state to an excited state; often by absorption of energy in the form of light. (yellow) Non-radiative decay processes lower the molecules energy to the vibrational ground state of the current state. (red) In order to jump from the excited state back to the ground state the molecule loses radiative energy in the form of a photon. If the two electronic states have the same degeneracy it is fluorescence, if they do not it is phosphorescence.	73
Figure 42: The steady state emission profile of UO ₂ ²⁺ (3 mM) in HCO ₃ (30 mM) and lactate (10 mM) in the absence (red line) and presence (black line) of <i>Shewanella oneidensis</i> MR1 (λ_{ex} = 420 nm).	74
Figure 43: Jablonski energy diagram for Raman scattering.	75
Figure 44: the 3 fundamental vibration modes of the free uranyl ion. Note v2a and v2b signify the two possible planes of vibration making the bending vibration doubly degenerate.	76
Figure 45: (a) UO ₂ (CO ₃) ₃ ⁴⁻ , and (b) UO ₂ (CO ₃) ₂ ²⁻ , displaying how the partially bounded system in (b) has unbound sites ready to react.	76
Figure 46: Bragg diffraction, showing two beams of incident X-rays with identical wavelength (λ) and phase being scattered by a crystalline solid with inter-planar distance (d). The lower beam travels a further 2dsin θ than the top, constructive interference occurs when dsin θ is a multiple of the wavelength of the radiation.	78
Figure 47: The photoelectric effect, describing the ejection of a core electron from the absorbing atom.	79
Figure 48: Simplified schematic of the Itrax core scanner. Taken from (Bishop, 2017).	80

Figure 49: Simplified schematic of a synchrotron.....	80
Figure 50: Simplified diagram of the experimental hutch, beamline B.18 at the Diamond Light Source. Image adapted from (Dent et al., 2009).	81
Figure 51: A typical absorption cross section, plotting absorption (μE) vs. energy at the U L_{III} -edge of bio- UO_2 ($E^0 = 17,169$ eV). Pre-edge, XANES, absorption edge and EXAFS regions are labelled in red, green, blue and purple respectively.	82
Figure 52: Comparison of Uranium L_3 -edge XANES spectra of uraninite (red) and uranyl triscarbonate (grey) (Brookshaw et al., 2015). Point a indicates the presence of a U-O_{ax} bond, points B and C indicate the presence of longer U(VI)-O_{eq} and U(IV)-O bonds.	83
Figure 53: Uranium M_4 -edge HERFD-XANES spectra for uraninite (blue), U_3O_8 (red) and schoepite (grey), with arrows indicating the increase in peak position with increasing oxidation state.	84
Figure 54: The Polymerase Chain Reaction (PCR). Taken from (CK-12.org, 2016).	86
Figure 55: the bright yellow UO_2Cl_2 , HCl solution in the preparation of UO_2Cl_2 stock. Error! Bookmark not defined.	
Figure 56: Aqueous U (left) and Sr (middle) concentrations in ppm, and bioavailable Fe(II) as a percentage of total bioavailable Fe (right). With data for the incubation period (black lines, also marked by the grey area) and remobilisation data for each species after aeration (red lines) or when amended with nitrate (blue lines). Measurements were performed in triplicate with error bars representing 1 standard deviation (σ). Incubation phases are highlighted in grey and remobilisation phases are left blank.	125
Figure 57: Aqueous U (left) and Sr (middle) concentrations in ppm, and Fe(II) as a percentage of total bioavailable Fe (right). With data for the incubation period (black lines, also marked by the grey area) and remobilisation data for each species after aeration (red lines) or when amended with nitrate (blue lines). Measurements were performed in triplicate with error bars representing 1 standard deviation (σ). Incubation phases are highlighted in grey and remobilisation phases are left blank.	126
Figure 58: U L_3 -edge EXAFS data and fits (red) for bio-reduced species in k^3 (left) and the respective Fourier transforms (right) with calculated contributions from U(IV) (%).	129
Figure 59: Sr K-edge EXAFS spectra and fits, k^3 weighted data (left) and the Fourier transforms (right).	131
Figure 60: Photographs of: (top) the 1.5 L microcosms at the start of the experiments (day 0) and; the remobilisation experiments following aerobically agitated (middle) and nitrate amended (bottom) systems. At the start of the remobilisation studies (day 300). Note the colour change (darkening) in the electron amended (2) and sulphate rich system (3) between days 0 and 300.	135
Figure 61: Changes in pH across all experiments. Incubation phases are highlighted in grey and remobilisation phases are left blank.	136
Figure 62: Eh values across all experiments. Incubation phases are highlighted in grey and remobilisation phases are left blank. Error bars represent 1 standard deviation based on triplicate measurements.	137

- Figure 63: Acetate (left axis) and Lactate (right axis) concentrations in the electron donor system [1]. With data for the incubation phase (black lines) and remobilisation data for each species after aeration (red lines) or when amended with nitrate (blue lines). Measurements were performed in triplicate with error bars representing 1 standard deviation (σ). Incubation phases are highlighted in grey and remobilisation phases are left blank..... 137
- Figure 64: Nitrate concentrations in the no treatment system [1]. With data for the incubation phase (black lines) and remobilisation data for each species after aeration (red lines) or when amended with nitrate (blue lines). Measurements were performed in triplicate with error bars representing 1 standard deviation (σ). Incubation phases are highlighted in grey and remobilisation phases are left blank..... 138
- Figure 65: Sulphate concentrations in the no treatment system [1]. With data for the incubation phase (black lines) and remobilisation data for each species after aeration (red lines) or when amended with nitrate (blue lines). Measurements were performed in triplicate with error bars representing 1 standard deviation (σ). Incubation phases are highlighted in grey and remobilisation phases are left blank..... 138
- Figure 66: Acetate (left axis) and Lactate (right axis) concentrations in the electron donor system [2]. With data for the incubation phase (black lines) and remobilisation data for each species after aeration (red lines) or when amended with nitrate (blue lines). Measurements were performed in triplicate with error bars representing 1 standard deviation (σ). Incubation phases are highlighted in grey and remobilisation phases are left blank..... 139
- Figure 67: Nitrate concentrations in the electron donor system [2]. With data for the incubation phase (black lines) and remobilisation data for each species after aeration (red lines) or when amended with nitrate (blue lines). Measurements were performed in triplicate with error bars representing 1 standard deviation (σ). Incubation phases are highlighted in grey and remobilisation phases are left blank..... 139
- Figure 68: Sulphate concentrations in the electron donor system [2]. With data for the incubation phase (black lines) and remobilisation data for each species after aeration (red lines) or when amended with nitrate (blue lines). Measurements were performed in triplicate with error bars representing 1 standard deviation (σ). Incubation phases are highlighted in grey and remobilisation phases are left blank..... 140
- Figure 69: Acetate (left axis) and Lactate (right axis) concentrations in the excess sulphate system [3]. With data for the incubation phase (black lines) and remobilisation data for each species after aeration (red lines) or when amended with nitrate (blue lines). Measurements were performed in triplicate with error bars representing 1 standard deviation (σ). Incubation phases are highlighted in grey and remobilisation phases are left blank..... 140
- Figure 70: Nitrate concentrations in the excess sulphate system [3]. With data for the incubation phase (black lines) and remobilisation data for each species after aeration (red lines) or when amended with nitrate (blue lines). Measurements were performed in triplicate with error bars representing 1 standard deviation (σ). Incubation phases are highlighted in grey and remobilisation phases are left blank..... 141
- Figure 71: Sulphate (left axis) and thiosulphate (right axis) concentrations in the excess sulphate system [3]. With data for the incubation phase (black lines) and remobilisation data for each species

after aeration (red lines) or when amended with nitrate (blue lines). Measurements were performed in triplicate with error bars representing 1 standard deviation (σ). Incubation phases are highlighted in grey and remobilisation phases are left blank..... 141

Figure 72: Nitrate concentrations in the MRC system [4]. With data for the incubation phase (black lines) and remobilisation data for each species after aeration (red lines) or when amended with nitrate (blue lines). Measurements were performed in triplicate with error bars representing 1 standard deviation (σ). Incubation phases are highlighted in grey and remobilisation phases are left blank.. 142

Figure 73: Sulphate concentrations in the MRC system [4]. With data for the incubation phase (black lines) and remobilisation data for each species after aeration (red lines) or when amended with nitrate (blue lines). Measurements were performed in triplicate with error bars representing 1 standard deviation (σ). Incubation phases are highlighted in grey and remobilisation phases are left blank.. 142

Figure 74: Glycerol Phosphate (left axis) and phosphate (right axis) concentrations in glycerol phosphate system [5]. With data for the incubation phase (black lines) and remobilisation data for each species after aeration (red lines) or when amended with nitrate (blue lines). Measurements were performed in triplicate with error bars representing 1 standard deviation (σ). Incubation phases are highlighted in grey and remobilisation phases are left blank..... 143

Figure 75: Acetate concentrations in glycerol phosphate system [5]. With data for the incubation phase (black lines) and remobilisation data for each species after aeration (red lines) or when amended with nitrate (blue lines). Measurements were performed in triplicate with error bars representing 1 standard deviation (σ). Incubation phases are highlighted in grey and remobilisation phases are left blank..... 143

Figure 76: Nitrate concentrations in glycerol phosphate system [5]. With data for the incubation phase (black lines) and remobilisation data for each species after aeration (red lines) or when amended with nitrate (blue lines). Measurements were performed in triplicate with error bars representing 1 standard deviation (σ). Incubation phases are highlighted in grey and remobilisation phases are left blank..... 144

Figure 77: Sulphate concentrations in glycerol phosphate system [5]. With data for the incubation phase (black lines) and remobilisation data for each species after aeration (red lines) or when amended with nitrate (blue lines). Measurements were performed in triplicate with error bars representing 1 standard deviation (σ). Incubation phases are highlighted in grey and remobilisation phases are left blank..... 144

Figure 78: Propionate (left y-axis) and acetate (right y-axis) concentrations in NanoFeR 25s system [6]. With data for the incubation phase (black lines) and remobilisation data for each species after aeration (red lines) or when amended with nitrate (blue lines). Measurements were performed in triplicate with error bars representing 1 standard deviation (σ). Incubation phases are highlighted in grey and remobilisation phases are left blank..... 145

Figure 79: Nitrate concentrations in NanoFeR 25s system [6]. With data for the incubation phase (black lines) and remobilisation data for each species after aeration (red lines) or when amended with nitrate (blue lines). Measurements were performed in triplicate with error bars representing 1 standard deviation (σ). Incubation phases are highlighted in grey and remobilisation phases are left blank.. 146

Figure 80: Sulphate concentrations in NanoFeR 25s system [6]. With data for the incubation phase (black lines) and remobilisation data for each species after aeration (red lines) or when amended with nitrate (blue lines). Measurements were performed in triplicate with error bars representing 1 standard deviation (σ). Incubation phases are highlighted in grey and remobilisation phases are left blank.....	146
Figure 81: Acetate (left y-axis) and lactate (right y-axis) concentrations in Carbo-Iron system [7]. With data for the incubation phase (black lines) and remobilisation data for each species after aeration (red lines) or when amended with nitrate (blue lines). Measurements were performed in triplicate with error bars representing 1 standard deviation (σ). Incubation phases are highlighted in grey and remobilisation phases are left blank.....	147
Figure 82: Nitrate (left y-axis) and nitrite (right y-axis) concentrations in Carbo-Iron system [7]. With data for the incubation phase (black lines) and remobilisation data for each species after aeration (red lines) or when amended with nitrate (blue lines). Measurements were performed in triplicate with error bars representing 1 standard deviation (σ). Incubation phases are highlighted in grey and remobilisation phases are left blank.....	147
Figure 83: Sulphate concentrations in Carbo-Iron system [7]. With data for the incubation phase (black lines) and remobilisation data for each species after aeration (red lines) or when amended with nitrate (blue lines). Measurements were performed in triplicate with error bars representing 1 standard deviation (σ). lioreduction phases are highlighted in grey and remobilisation phases are left blank.	148
Figure 84: Total aqueous Fe as determined by ICP-MS spectroscopy, x-axes show total aqueous Fe concentrations (mM) and y-axes show time (days) Error bars represent 1 standard deviation based on triplicate measurements. incubation phases are highlighted in grey and remobilisation phases are left blank.....	149
Figure 85: 16S rRNA microbial community by phylogenetic class in the control experiment (left), and the natural attenuation system [1] after: 1 day (second from the left), 300 days (middle), 400 days – aerobic remobilisation (second from the right) and 400 days – nitrate remobilisation (right). With OTUs in square brackets.....	151
Figure 86: 16S rRNA microbial community by phylogenetic class in the control experiment (left), and the electron donor system [2] after: 1 day (second from the left), 300 days (middle), 400 days – aerobic remobilisation (second from the right) and 400 days – nitrate remobilisation (right). With OTUs in square brackets.....	152
Figure 87: 16S rRNA microbial community by phylogenetic class in the control experiment (left), and the excess nitrate system [3] after: 1 day (second from the left), 300 days (middle), 400 days – aerobic remobilisation (second from the right) and 400 days – nitrate remobilisation (right). With OTUs in square brackets.....	152
Figure 88: 16S rRNA microbial community by phylogenetic class in the control experiment (left), and the MRC system [4] after: 1 day (second from the left), 300 days (middle), 400 days – aerobic remobilisation (second from the right) and 400 days – nitrate remobilisation (right). With OTUs in square brackets.....	153

Figure 89: 16S rRNA microbial community by phylogenetic class in the control experiment (left), and the glycerol phosphate system [5] after: 1 day (second from the left), 300 days (middle), 400 days – aerobic remobilisation (second from the right) and 400 days – nitrate remobilisation (right). With OTUs in square brackets.....	153
Figure 90: 16S rRNA microbial community by phylogenetic class in the control experiment (left), and the NanoFeR 25s system [6] after: 1 day (second from the left), 300 days (middle), 400 days – aerobic remobilisation (second from the right) and 400 days – nitrate remobilisation (right). With OTUs in square brackets.....	154
Figure 91: 16S rRNA microbial community by phylogenetic class in the control experiment (left), and the Carbo-Iron system [7] after: 1 day (second from the left), 300 days (middle), 400 days – aerobic remobilisation (second from the right) and 400 days – nitrate remobilisation (right). With OTUs in square brackets.....	154
Figure 92: U L ₃ -edge XANES spectra collected at 77 K. Standards: Uranyl(VI) triscarbonate from (Brookshaw et al., 2015), U(VI) phosphate from (Newsome et al., 2015c) U(IV) phosphate from (Newsome et al., 2015a), synthetic U(IV)O ₂ standard from (Neill et al., 2018).....	155
Figure 93: EXAFS fits for bio-reduced MRC. Comparing EXAFS data (grey) with fits using just two O shells (red), two O shells + P (blue), and two O shells + S (green). The fit using an S shell is included in Table 12.	158
Figure 94: The Fourier transform of the U L ₃ -edge EXAFS showing the shell by shell fitting method of the Carbo-iron nanoparticles following reaction with U.	160
Figure 95: Selected geochemical data in the aqueous precipitation experiments. Left) Aqueous U (red) and Sr (grey) concentrations; and right) pH (grey) and Eh (red).	161
Figure 96: A) U removal, B) Sr removal, and C) Fe(II) as a % of total bioavailable Fe in the incubation phase. System 1: Electron Donor (grey squares), System 2: Glycerol phosphate (red circles), System 3: Carbo-Iron (blue triangles), and System 4: NanoFeR 25s (green inverted triangles). Data adapted from and previously discussed in (Vettese <i>et al.</i> , 2020, Thesis Chapter 5).	168
Figure 97: U concentrations in effluents with artificial groundwater treatments (left, blue) and artificial seawater treatments (right, red), with systems in the order from top to bottom: electron donor, glycerol phosphate, Carbo-Iron and NanoFeR 25s.....	170
Figure 98: Sr concentrations in effluents with artificial groundwater treatments (left, blue) and artificial seawater treatments (right, red), with systems in the order from top to bottom: electron donor, glycerol phosphate, Carbo-Iron and NanoFeR 25s.....	170
Figure 99: XRF counts against normalised depth, with water flow drawn in blue. The top (0) of each plot represents the outflow section and the bottom (1) of each plot represents the inflow section of the columns, plotted for U (red), Sr (green), and either Fe (brown) or P (purple). Data from the columns subject to artificial groundwater ingress are on the top and to seawater are on the bottom.	173
Figure S100: A) schematic depicting the column setup; B) a photo of a column. Influent flowed in to the bottom of the columns and effluent was sampled from the top.....	175
Figure S101: All 8 columns. Influent flowed in to the bottom of the columns and effluent was sampled from the top.....	175

Figure S102 A-C: Photos of the column experiments at day 80, showing: A) the groundwater experiments amended with glycerol phosphate (left) and NanoFeR 25s (right); seawater experiments amended with glycerol phosphate (B) and NanoFeR 25s (C).	176
Figure S103: Representative, Br ⁻ tracer breakthrough curve from a 3 cm long sediment column at a flow rate of 4.8 mL/min. Influent Br ⁻ concentrations (10 mg/L) were reached in the effluent groundwater after 12 min. 'Breakthrough' was therefore determines to be at 50 % of the influent concentration 5 mgL ⁻¹ or 9.1 mins.	177
Figure S104: Variation in pH for the 4 columns with aerobic groundwater (left, full lines) and for the 4 columns with aerobic seawater (right, dashed lines). System 1: Electron Donor (grey squares), System 2: Glycerol phosphate (red circles), System 3: Carbo-Iron (blue triangles), and System 4: NanoFeR 25s (green inverted triangles).	178
Figure S105: Variation in effluent Eh for the 4 columns with aerobic groundwater (left, full lines) and for the 4 columns with aerobic seawater (right, dashed lines). System 1: Electron Donor (grey squares), System 2: Glycerol phosphate (red circles), System 3 Carbo-Iron (blue triangles), and System 4: NanoFeR 25s (green inverted triangles).	178
Figure 106: Chloride (A), Sulphate (B) and Nitrate (C) concentrations in column effluents with: Electron donor (grey), Glycerol phosphate (red), Carbo-Iron (blue) and NanoFeR 25s (green). Results from columns 1-4 AGW have full lines (left) and columns 5-8 ASW have dashed lines (right).....	180
Figure 107: Ferrozine analysis on the effluent columns with aerobic groundwater (left, full lines) and for the 4 columns with aerobic seawater (right, dashed lines). System 1: Electron Donor (grey squares), System 2: Glycerol phosphate (red circles), System 3 Carbo-Iron (blue triangles), and System 4: NanoFeR 25s (green inverted triangles).	181
Figure 108: Bio-available Fe(II) as a percentage of total bioavailable Fe taken on the solid phase end-points. Columns in blue were ran with artificial groundwater and columns in red were ran with artificial seawater. The numbers at the bottom of each box represents the bio-available Fe(II) concentration (mM). Error bars represent 1 standard deviation taken from triplicate measurements.	182
Figure S109: 8 core halves prepared for XRF scanning using the Itrax Core Scanner.	184
Figure 110: Sulphur counts vs normalised depth for the 4 columns with aerobic groundwater (left) and for the 4 columns with aerobic seawater (right,). System 1: Electron Donor (grey), System 2: Glycerol phosphate (red), System 3 Carbo-Iron (blue), and System 4: NanoFeR 25s (green). Influent flowed in to the bottom of the columns and effluent was sampled from the top.	184
Figure 111: Pearson correlation coefficients plots of the XRF data for U, Sr, Mn, Fe and Si where a value of +1 (blue) represents a full positive correlation, 0 (no colour) represents no correlation and -1 (red) represents a full negative correlation. Data plotted for the electron donor and glycerol phosphate systems with groundwater on top (red) and seawater on bottom (blue).....	185
Figure 112: Pearson correlation coefficients plots of the XRF data for U, Sr, Mn, Fe and Si where a value of +1 (blue) represents a full positive correlation, 0 (no colour) represents no correlation and -1 (red) represents a full negative correlation. Data plotted for the Carbo-Iron and NanoFeR 25s systems with groundwater on top (red) and seawater on bottom (blue).....	186
Figure 113: Urea consumption over 224 days. With the experiment in blue, and a no sediment, solution only control in orange. Error bars represent 1 standard deviation over triplicate measurements. ...	227

Figure 114: pH changes over 224 days. With the experiment in blue, a no urea added control in red and a no sediment, solution only (including urea) control in orange.....	228
Figure 115: Sr removal in filtered experiments.	228
Figure 116: Changes in bio-available Fe(II) as determined via the Ferrozine assay.	229

Abbreviations

AGW - Artificial Ground Water

ASW - Artificial Sea Water

AQDS - Anthraquinone-2,6-disulphonate, a synthetic analogue to humics

DoE - Department of Energy

EXAFS – Extended X-ray Absorption Fine Structure

EARP – Enhanced Actinide Removal Plant

GDF - Geological Disposal Facility

IC – Ion Chromatography

ICP-MS – Inductively Coupled Plasma - Mass Spectrometry

LCF – Linear Combination Fitting

LLW/ILW/HLW - Low, Intermediate and High Level Waste, respectively

nZVI – Nano Zero-Valent Iron

PPB – Parts per Billion

PPM – Parts Per Million

PUREX - Plutonium URanium EXtraction

PWR – Pressurised Water Reactor

SEPA - the Scottish Environmental Protection Agency

SEM-EDX – Scanning Electron Microscopy (with) Energy Dispersive X-ray Analysis

SRB – Sulphate-Reducing Bacteria

VLLW – Very low level wastes

XAS – X-ray absorption spectroscopy

(HERFD) XANES – (High Energy Resolution Fluorescence Detected) X-ray absorption near-edge spectroscopy

XRF – X-Ray Fluorescence

XRD – X-Ray Diffraction

Abstract

The development of nuclear energy for both civil and military demands has created a significant legacy of waste and contamination at nuclear facilities worldwide. Understanding the biogeochemical behaviour of radionuclides under environmentally relevant conditions is required to protect the wider environment with respect to contaminated lands and the long-term storage of wastes. This PhD is centralised on the contaminated land scenario and focusses largely on bioremediation and chemical treatment. Bioremediation utilises the microbial interactions to clean a contaminated site; it presents a relatively cheap, selective and *in-situ* approach that can be used on a large scale. It is a promising alternative to traditional “Dig-and-Dump” or engineered barrier systems which are available but are often expensive, highly invasive and non-selective. Two elements present in radioactive contaminated lands are U and Sr and they are the focus of this project. Under oxidising conditions U is present in its mobile form as U(VI), however by influencing the redox chemistry insoluble U(IV) minerals can precipitate. This reduction can be influenced by microbial metabolisms when stimulated via the addition of an organic electron donor. Conversely, environmental Sr is almost always present as non-redox active Sr(II), the environmental mobility of Sr is thus principally governed by sorption to minerals, where it behaves similarly to other divalent cations such as Mg(II) or Ca(II). Interestingly, both U and Sr can also be incorporated into phosphate biominerals.

This thesis focuses on 2 core subjects. The first investigates the mechanism(s) for bioreduction of aqueous U(VI) in model Fe(III)-reducing bacteria *Shewanella oneidensis* MR1. Whilst the bioreduction of U(VI) to U(IV) is well studied, the mechanism(s) underpinning this transformation are not yet fully understood; previous work has suggested that the bioreduction of U(VI) by model Fe(III)-reducing bacteria proceeds via a pentavalent U(V) intermediate. This work utilises a multi-technique approach which, for the first time, identifies U(V) as an intermediate under environmentally relevant conditions. It boasts the first publication to use state-of-the-art U M_{4} -edge High Resolution X-ray Absorption Near-Edge Structure (HR-XANES) in a microbial system. Furthermore, not only did this work successfully identify a U(V) intermediate, which appears to be more stable than previously thought, but it also discovered long-term stabilisation of U(V) in the post reduction solids. This discovery has led to further research within the Manchester Geomicrobiology Group. The second subject discussed in this thesis compares the long-term effectiveness of various bioremediation and chemical strategies which co-target U and Sr. Here, batch microcosm experiments were set up using a range of treatments which were monitored during incubation and then the remobilisation of the contaminants was studied upon exposure to air or nitrate. Whilst many different treatments have been studied over long timescales, varying experimental conditions means that the results are not directly comparable. The work carried out here provides clear and concise comparisons between seven different bioremediation or chemical systems in the co-treatment of U and Sr. At key time points radionuclide speciation was characterised using X-ray absorption spectroscopy (XAS) and the microbial communities were analysed using 16S rRNA gene analysis. This work identified that systems treated with glycerol phosphate or nanoscale zero-valent iron (nZVI) treatments worked best. Finally, the best 3 treatments were used in flow-through sediment columns to assess U and Sr migration after the intrusion of ground- and seawater; they were compared to a standard electron donor control experiment. This work further demonstrated enhanced stability of solid phase U and Sr contaminants treated using nZVI or glycerolphosphate. It also found that seawater increased the contaminant migration by up to tenfold.

Declaration

I, the author of this thesis declare that no portion of the work referred to in this thesis has been submitted in support of an application for another degree or qualification of this or any other university or institute of learning.

Copyright statement

i. The author of this thesis (including any appendices and/or schedules to this thesis) owns certain copyright or related rights in it (the “Copyright”) and s/he has given The University of Manchester certain rights to use such Copyright, including for administrative purposes.

ii. Copies of this thesis, either in full or in extracts and whether in hard or electronic copy, may be made only in accordance with the Copyright, Designs and Patents Act 1988 (as amended) and regulations issued under it or, where appropriate, in accordance with licensing agreements which the University has from time to time. This page must form part of any such copies made.

iii. The ownership of certain Copyright, patents, designs, trademarks and other intellectual property (the “Intellectual Property”) and any reproductions of copyright works in the thesis, for example graphs and tables (“Reproductions”), which may be described in this thesis, may not be owned by the author and may be owned by third parties. Such Intellectual Property and Reproductions cannot and must not be made available for use without the prior written permission of the owner(s) of the relevant Intellectual Property and/or Reproductions.

iv. Further information on the conditions under which disclosure, publication and commercialisation of this thesis, the Copyright and any Intellectual Property and/or Reproductions described in it may take place is available in the University IP Policy (see <http://documents.manchester.ac.uk/DocuInfo.aspx?DocID=487>), in any relevant Thesis restriction declarations deposited in the University Library, The University Library’s regulations (see <http://www.manchester.ac.uk/library/aboutus/regulations>) and in The University’s policy on Presentation of Theses.

Acknowledgements

Before I start my individual thank you's, I'd like to mention what a fantastic job opportunity this has been. Not only have I worked in a fantastic city, I've made some great friends for life, I've travelled (Japan, Swiss-Italy, France, Germany & Scotland, not to mention the holidays) and experienced some amazing cultures and all whilst working on cutting-edge science. It's been an amazing 4 years and I will not be able to express my full gratitude in 1 page... But here goes...

First of all I would like to express my gratitude and thanks to my academic supervisors Kath, Jon and Sam. Thank you for providing me with the opportunity to study as your student, in your amazing research group which has provided me with so many fantastic memories and opportunities. Your patience, guidance and friendship have not only made this thesis possible but have really helped me grow into the man I want to be. I'd also like to thank my funders at the National Nuclear Laboratory and the Nuclear Decommissioning Authority for funding my PhD. I'd like to express my gratitude to the technical staff present at UoM who have also made this possible, thanks to Al, Paul, John, Chris, Heath, Cath and Karen who have all helped me so much over the years and have always had time for a conversation. The housekeeping department have always put a smile on my face, particularly Mike and Tony. Throughout this journey, I have spent sooo much time synchrotrons and I have loved it (maybe not every minute of it) so to the chaps at Diamond Light Source: Steve, Fred and Gianantonio; at KIT: Jurij, Bianca and Tonya and Kristina at ESRF, none of this would have been possible without you all and I look forward to continuing to work with you.

To Manchester Geomicrobiology! What an amazing group! Here's to 'the youngsters': Matt, Chris Foster & Egan-Morriss, Franky, Dean and Callum. Matt, thanks so much for your help during your masters, we are the batch microcosm dream team! I hope you enjoyed my rambling teachings and I'm so glad you stayed! Egan-Morriss, at least I won 2 games of squash, I don't think I will ever win a full match. And here's to my day 1 crew that have been with me the whole time, you have travelled the world with me and ridden the emotional rollercoaster that is a PhD. Adrian, Hannah, Kurt, Ellen, Lynn, Alana, Will, Connaugh, Faraaz, Luke & Tom love you all and couldn't have done it without you! We have been through a lot together, I can't thank you enough and I look forward to working together and keeping in touch. Luke and Tom especially have been like super nerdy science brothers through this. Lynn, thanks for all the abuse, it makes me smile. And to Manu, I love you being in Manchester, what a special 6 months (+ Japan) and what an amazing bromance. Cheers for all the beers, whiskeys, coffees, and drunken sing alongs.

Next I must thank Luca and the Vettese's in Blackpool, I've had so many amazing times with you all. Thank you for taking me in and making me feel at home in the North. To my family: Mum, Dad and Mateo. You are so amazing, without what you have made me I could not have done any of this. Thanks for the amazing holidays, and the ridonkulous lock-down write up period (what a blast!). More importantly, thanks for never judging, but always loving and always listening. To Emma thank you for being my partner through this, for laughing at my jokes, making me laugh, making me organised and for taking me to Rudys at least once a week. To Harry and Jack, you two have been my rocks, source of laughter and plenty of beers through the PhD, undergraduate and I'm sure through life. I'll miss having you guys so close when I move away.

About the Author

The author graduated from the University of Manchester in 2016 with an integrated MChem before joining the Geomicrobiology group in the School of Earth and Environmental science at the University of Manchester to start a PhD. The author is a collaborator on 2 publications as a result of his masters work (Goodwin et al., 2020, 2016).

Chapter 1: Project Relevance, Research Rationale and Aims and Thesis Structure

1.0 Project Relevance

Currently, nuclear power supplies approximately 10 % of the world's electricity demands (IAEA, 2020). Over the last 75 years nuclear operations have resulted in a legacy of radioactive contaminated land at nuclear sites across the globe. In the UK nuclear energy is planned to provide part of the country's energy demands as part of a mix of supply methods whilst reducing carbon emissions (UK Government, 2019). The global nuclear legacy is a large, expensive and topic of high public interest, in the UK alone the estimated cost and time frame for clean-up is estimated as £99-232 billion over 120 years (NDA, 2019a). The Sellafield site is the largest in the UK, it has an estimated 13 million m³ of potentially radioactive contaminated land. Here, as well as at many other polluted sites, contaminant mobility is monitored periodically using a system of boreholes (NDA, 2019b) and many management strategies prefer monitored natural attenuation rather than traditional *ex-situ* disposal techniques. However, when this is not sufficient targeted remediation approaches techniques may offer a less invasive strategy as a method of controlling radionuclide transport in contaminated lands.

1.1 Research Rationale and Aims

This thesis explores of the effects of targeted *in-situ* bioremediation and chemical treatments on key radioactive contaminants, U and Sr, under conditions relevant to nuclear contaminated sites with a larger focus on the Sellafield site. U was chosen as it is the dominant radionuclide by mass in radioactive wastes and moreover, it is common as a radioactive contaminant across the entire nuclear cycle. Although Sr mobility at the Sellafield site is mostly contained to the Separation Area it is much more mobile than other contaminants (e.g. U) at the Sellafield site, and so Sr was also considered a priority. Furthermore, by studying both U and Sr chapters 5 and 6 can target one redox-active and one redox-inactive radionuclide. First, this work aims to understand the mechanism(s) of U bioreduction in a pure culture experiment using model Fe(III)-reducing bacteria *Shewanella oneidensis* MR1. Confirming a mechanistic understanding of U speciation during its enzymatic reduction is key to comprehending environmental U behaviour and microbial interactions. The second objective is to investigate the long-term effectiveness of several bioremediation and chemical treatments which co-targeted U and Sr. Establishing a comprehensive dataset to compare different leading bioremediation and chemical treatments is important to help underpin the safety cases for the geodisposal of radwaste inventories and in contaminated land scenarios.

This led to the development of the following thesis objectives:

1. To understand if the reduction mechanism of U(VI) by model Fe(III)-reducing bacteria proceeds via a pentavalent U(V) intermediate.
2. If it does, then to identify the lifetime, speciation and reaction pathway of the U(V) intermediate.
3. To characterise the biological, geological and chemical changes of co-treated U and Sr using a range of biogeochemical and chemical treatments in systems relevant to contaminated land.
4. To examine their potential as targeted remediation strategies for both U and Sr in various remobilisation studies after ingress of air, nitrate, groundwater and seawater.

In order to answer these research questions the author set up pure culture, batch microcosm and flow through column experiments. Here, experiments were carried out under environmentally relevant conditions using synthetic groundwater and sediments representative of the Sellafield site and using synthetic seawater representative of the Irish Sea. Throughout this project, the author employed a multi-technique approach which combined many novel experimental techniques. The changing biogeochemistry was monitored using a range of analytical techniques including ion chromatography, inductively coupled plasma mass spectrometry, luminescence spectroscopy, X-ray absorption spectroscopy, X-ray diffraction and 16S rRNA gene sequencing.

1.2 Thesis Structure

This thesis has been submitted in publication format and comprises 3 research chapters produced for publication. There are also 2 appendices (Chapters 10 & 11) detailing other research which was not written into publication format. All research chapters include a statement of the contributions made by the author and the other collaborators. At the time of submission Chapter 4: Paper 1 had been published, it is therefore included in the thesis in its published journal format. Chapters 5 and 6, Papers 2 and 3 respectively, have been written as ready for publication.

- Chapter 2 (Literature Review) provides a detailed and up-to-date examination of the wider scientific knowledge relevant to this Thesis.
- Chapter 3 (Research Methods) describes the experimental and analytical techniques used during the project.
- Chapter 4 (Paper 1) is entitled: “Multiple Lines of Evidence Identify U(V) as a Key Intermediate during U(VI) Reduction by *Shewanella oneidensis* MR1”. It details an experimental investigation into the mechanism of uranyl(VI) reduction by resting cells of *Shewanella oneidensis* MR1. This chapter is presented as a lead-author manuscript and is published in Environmental Science and Technology (2020).

Contributors: *Gianni F Vettese* – principal author, completed all of the experimental work and analysis; *K. Morris, L. Natrajan, S. Shaw, T. Vitova, J. Galanzew, D. Jones and J. Lloyd* – co-authors provided conceptual guidance and extensive manuscript review.

- Chapter 5 (Paper 2) is entitled: “Chapter 5: Comparison of Radionuclide End-Points; the Long-Term Stabilities of U and Sr Co-Treated Sediments after Oxygen and Nitrate Perturbations”. It monitors the biogeochemical changes through 7 batch microcosm experiments which are co-treating U and Sr over a 300 day period. It then assess the effects of the ingress of air or nitrate. This chapter is presented as a lead-author manuscript and is written with intent to publish into Earth and Space Chemistry.

Contributors: *Gianni F Vettese* – principal author, completed all of the experimental work and analysis; *K. Morris, L. Townsend, S. Shaw and J. Lloyd* – co-authors provided, conceptual guidance and extensive manuscript review; *M. White-Pettigrew* – co-author, helped carry out the experimental work; *C. Boothman* – carried out microbial analysis and interpretation of the 16s RNA data.

- Chapter 6 (Paper 3) is entitled: “Uranium and Strontium Remobilisation in Previously Bioreduced Sediment by Ground- and Seawater Ingress”. It investigates the stabilities of 4 U and Sr co-treated end-points following remobilisation studies in flow-through columns with aerobic ground- or seawater as the influent. This chapter is presented as a lead-author manuscript and is written with intent to publish into Chemical Geology.

Contributors: *Gianni F Vettese* – principal author, completed all of the experimental work and analysis; *K. Morris, S. Shaw and J. Lloyd* – co-authors provided conceptual guidance and extensive manuscript review; *C. Boothman* – carried out microbial analysis and interpretation of the 16S rRNA data.

- Chapter 7 (Thesis Conclusions and Future Work) provides a summary of the key findings in this research and suggests the authors views on future work that could carry on from these findings.
- A full list of references used throughout this study is provided in chapter 8.
- Chapter 9 (Appendix 1) details conference presentations made by the author.
- Finally, chapter 10 describes any additional pieces of work carried out by the author over the course of the PhD that are relevant to the work but did not form part of a publication.

Chapter 2: Literature Review

This chapter provides the necessary context for the work presented in this thesis. It provides a summary of key information on in the area of nuclear energy, discussing the nuclear fuel cycle, the nuclear legacy, radioactive waste management, desirable end-points, and nuclear sites across the globe with specific details on the Sellafield site and its contaminants. Through this, it illustrates the context, science and necessity for the work presented in this thesis by providing a short summary of the nuclear legacy, its disposal plans and the relevant biogeochemistry surrounding the topic. Later, it summarises the key scientific principles surrounding the work presented in this thesis. It provides an in-depth summary of microbes and their use in bioremediation, iron biogeochemistry, and the environmental nuclear chemistry and biogeochemistry of U and Sr.

2.0 Nuclear Energy

Concerns of climate change have initiated a search for sustainable energy sources that have low carbon emissions; the UK has set the challenging task of reducing greenhouse gas emissions to net zero by 2050 (UK Government, 2019). Whilst renewables can provide low carbon energy, they have lower energy outputs than carbon-based fuels and the power that they generate is not always constant because they can be affected by weather. Nuclear energy, however, could supply a substantial fraction of energy contributing to the nation's needs. Although the safety and management of nuclear wastes can be of public concern, nuclear power promises a reliable, secure and low CO₂ emitting method of energy production which outcompetes the energy outputs of renewables and carbon based fuels with minimal negative impacts on global warming (IPCC, 2014). The UK Department of Energy and Climate Change wants nuclear power to represent an "important part of a balanced mix of generating technologies", as demonstrated by the construction of new nuclear power stations such as Hinkley point C with French and Chinese investors (The Department of Energy and Climate Change, 2016).

Today, almost 450 nuclear power reactors provide electricity to over 50 countries supplying approximately 10 % of the world's energy (IAEA, 2020). From country to country the proportion of electricity generated varies widely, for example, whilst France obtains approximately 75 % of its energy from nuclear power plants, nuclear energy only provides 3-5 % of Argentina and Brazil's energy demands (WNA -World Nuclear Association, 2019) (Figure 1). In the UK, nuclear energy currently represents 15-20 % of energy production; this is based on 15 operational nuclear reactors at 7 UK power plants (Stolworthy, n.d.; *UK Energy Statistics, Q1 2018 Trends in the use of renewable energy*, 2018). There are a further 30 UK-based power reactors which are permanently shut down and in a various stages of decommissioning.

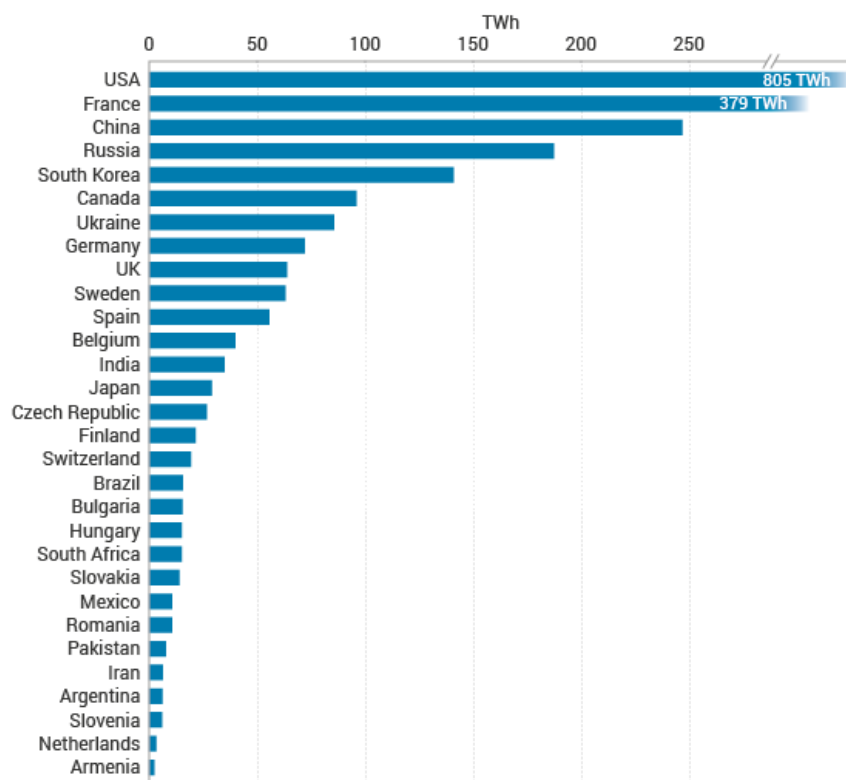
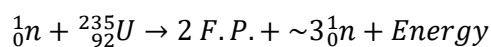


Figure 1: Nuclear energy generation by country (TWh). Taken from the International Atomic Energy Agency (IAEA) Power Reactor Information System (PRIS) Database (IAEA, 2020).

2.1 The Nuclear Fuel Cycle, Nuclear Legacy, Radioactive Waste Management plans and Desirable End-Points

2.1.1 Nuclear Fission and Energy Production

Nuclear fission occurs when a fissile nucleus becomes unstable by absorbing a slow neutron (a slow neutron typically has kinetic energy > 1 eV). The absorber splits into smaller atoms, known as fission products, releasing energy and some more neutrons at the same time. The released neutrons can strike other nearby fissile atoms, and if there is sufficient concentration of them it will start a chain reaction. Equation 1 uses ^{235}U as an example.



Equation 1: Fission of ^{235}U . The potential energy release from one metric ton of typical enriched U can release over 10^9 kWh of energy, the equivalent to 1.6×10^5 equivalent units of coal (Harvard College Review, 2015).

The neutrons produced during fission are referred to as ‘fast’, meaning they have an energy in the MeV range but as the probability of fission is greater with slow neutrons, a moderator is used to lower the energy of the fast neutrons. In a Pressurised Water Reactor (PWR: Figure 2 below), the excess energy heats the core water (the primary cooling circuit) which is held under pressure to prevent it from boiling. This is then transferred to water outside the core (the secondary cooling circuit) via a heat exchanger, here the water is allowed to boil into steam, which then drives a turbine and generates electricity. In a Pressurised Water Reactor (PWR) the water is boiled in a separate cooling circuit to the water that in the reactor vessel to minimise radioactive contamination. After the steam drives the turbine, the condenser uses a third stream of water to cool the steam back to water so that

it may be recycled. Reactor designs vary depending on the materials used for the coolant, moderator and fuel type (Table 1).

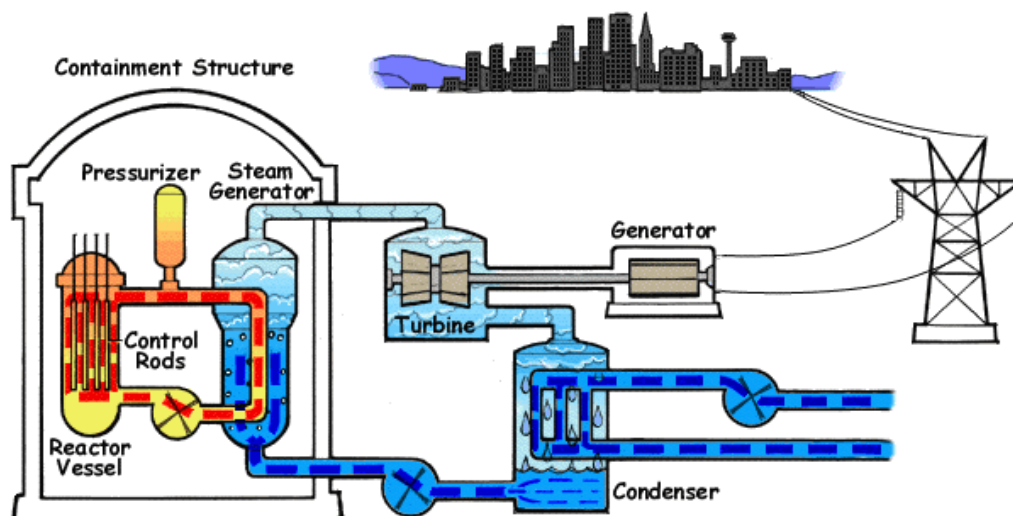


Figure 2: Generating energy from nuclear fission, a cartoon image of a Pressurized Water Reactor. Image taken from (United States Nuclear Regularoty Comission, 2017).

Table 1: Example nuclear reactors describing their coolant, moderator and fuel (Jensen and Nonbol, 1998; Stacey, 2007)

Reactor Type	Coolant	Moderator	Fuel
Gas-cooled reactors (MAGNOX ^a , AGR ^b)	CO ₂	Graphite	Natural or enriched uranium
Boiling Water Reactors (BWR)	Light Water	Light Water	Enriched Uranium
Pressurised Water Reactors (PWR)	Light Water	Light Water	Enriched Uranium
Pressurised Heavy Water Reactors (PHWR/CANDU)	Heavy Water	Heavy Water	Natural Uranium
Light Water Graphite Reactors	Light Water	Graphite	Enriched Uranium

^a Magnesium-aluminium oxide alloy (MAGNOX), ^b Advanced Gas-cooled Reactor (AGR)

2.12 The Nuclear Fuel Cycle

The nuclear fuel cycle refers to the entire process of generating electricity from nuclear fission (Figure 3 summarises). First U is mined; as natural U has the isotopic ratios ²³⁸U (99.2762 %), ²³⁵U (0.7182 %) and ²³⁴U (0.0056 %), then the U is enriched in ²³⁵U before fuel fabrication. Fuel fabrication varies for different reactor designs, where some older designs can run on ~0.7 % ²³⁵U (MAGNOX/CANDU), more modern reactors tend to generate electricity using ~3 % fissile U. ²³⁵U can be enriched by 2 possible methods, both of which work on the small difference in mass of the relative isotopes; these are energy intensive gas diffusion or by centrifugation. The enriched U is then manufactured into suitable fuel units, typically in the form of rods of UO₂ pellets.

The 'back-end' of the nuclear fuel cycle concerns the treatment of the spent fuel, disposal of wastes and decommissioning of nuclear sites. Once obsolete, spent fuel (e.g. for Light Water Reactors [LWR] spent fuel is composed of: 93 % depleted U, 5 % fission products, 1% Pu (Feiveson et al., 2011)) is

removed from the reactor and is placed in cooling ponds for several years; this allows ‘hotter’ radionuclides with shorter half-lives ($\tau_{1/2} < 10$ y) to decay. From here, the cycle can be closed or open, with the choice of system adopted depending on many complex economic and political standpoints. In an open cycle, the spent fuel is considered waste and is sent directly to storage; but in a closed cycle after cooling, the spent fuel’s cladding is removed and its contents are dissolved in nitric acid. In the UK, the PUREX (Plutonium URanium EXtraction) process is then used to separate U, Pu, minor actinides and fission products in solution (Openshaw et al., 1989). The depleted U can be remanufactured into fuel or used as depleted U in weapon manufacturing. The Pu can be used for weapons or recycled and mixed with U for the manufacture of MOX (Mixed OXide) fuel; although, no UK power plants are licensed to burn MOX fuel nor do they have any commitment to reprocess spent fuel. The mixed fission products and minor actinides (Np, Am, Cm) are calcined into highly active borosilicate glass for storage/disposal. As an example, the USA, Finland and Sweden operate closed cycles, whereas the UK and France reprocess fuel so that it may be reused at a later date. In the UK, spent fuel reprocessing has generated significant amounts of radioactive waste and accounts for ~ 73 % (by volume) of the UK radioactive waste inventory (NDA, 2019b). Furthermore the residual nitric acid liquor produced from the PUREX process produces a highly active liquor waste containing fission products; the leaks of such effluents to the subsurface is responsible for a large fraction of the radioactively contaminated lands at reprocessing sites (Dirkes et al., 2009; Fredrickson et al., 2004; Novikov et al., 2006; Sellafield Ltd., 2015).

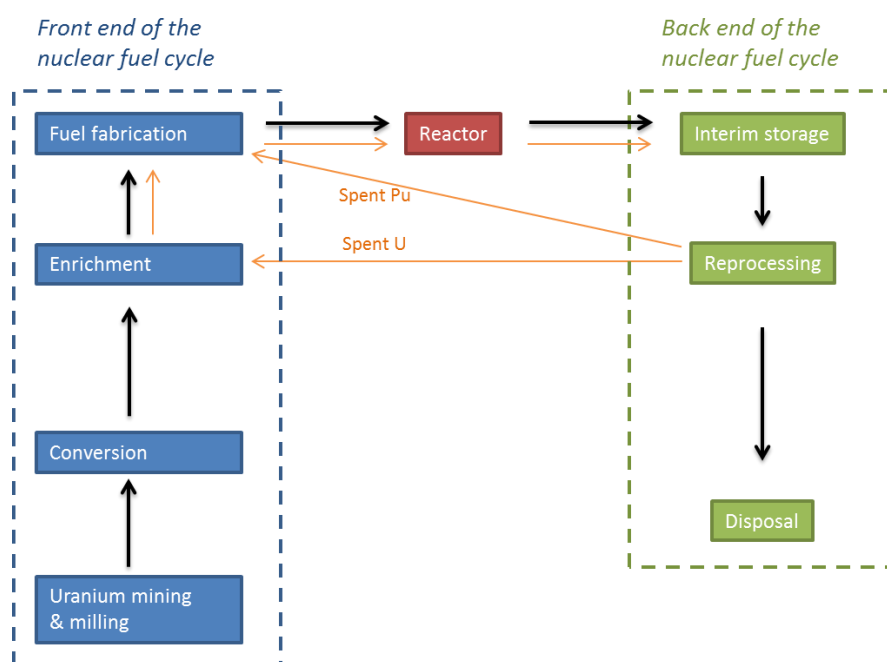


Figure 3: The open and closed (inc. orange arrows) nuclear fuel cycles

2.13 The Disposal of Nuclear Waste

Since its discovery in the mid 20th century, the use of nuclear energy for civilian and military purposes has led to a considerable legacy of radioactive waste which must be managed. Although a worldwide challenge (Anderson et al., 2003; Cruickshank, 2012; Lovley et al., 1991; Newsome et al., 2014a), this PhD focusses on issues surrounding UK contaminated lands. The 2019 UK Radioactive Waste Inventory reported $\sim 165,000$ m³ of radioactive waste, attributing to 216,000 tonnes due to mining, mill tailings, extraction streams, decommissioning wastes and reprocessing effluents from the nuclear fuel cycle,

almost 75% of this is stored at the Sellafield site, Cumbria (NDA, 2019b)(Figure 4). Furthermore the 2019 Radioactive Waste Inventory forecasted a lifetime total of 4,470,000 m³ of packaged radioactive waste (Nuclear Decommissioning Authority: NDA and NDA, 2019). The radioactive waste amassed in the UK is currently in interim storage until its final stewardship has been decided. As the radionuclides present in radioactive waste cannot be destroyed, methods which can limit or control their mobility must be exploited thus reducing potential contact with the local biosphere.



Figure 4: A map of the NDA's 17 nuclear decommissioning sites, with Sellafield and the nearby Low Level Waste Repository circled in red. Adapted from (NDA, 2004).

Nuclear waste is separated into very low, low, intermediate and high level wastes (VLLW, LLW, ILW and HLW respectively) (NDA, 2017). VLLW is only lightly contaminated; it usually comes from hospitals and universities and can be disposed of in appropriately permitted landfill sites. LLW (and VLLW) comprises 90.6 % of radioactive waste by volume and is defined as anything with levels of radioactivity lower than 4 gigabecquerel (GBq) per tonne of alpha activity or 12 GBq per tonne of beta/gamma activity (Figure 5, Table 2). In the UK, LLW undergoes shallow geological burial at the Drigg LLW repository, Cumbria, although it is the largest fraction by volume, by radioactivity, it only accounts for ~1% of the radioactive waste (Figure 5, Table 2). ILW (which has a greater activity than LLW, but does not generate heat) and HLW (which has a greater activity than LLW and does generate heat) are held in interim storage until a long-term solution is found (Valentin, 2007). HLW comprises less than 1% of radioactive wastes by volume but incorporates the vast majority of radiation (NDA, 2019b) (Figure 5, Table 2). It is predominantly composed of the vitrified by-products of fission, and the reprocessing of spent fuels and contains both short- and long-lived radionuclides which produce large quantities of heat and must be contained in cooled environments. Short term storage will allow significant attenuation of radiation and heat until long term storage is achieved (Crossland, 2012; International Atomic Energy Agency, 2005; NDA, 2019b; Wilson, 1996).

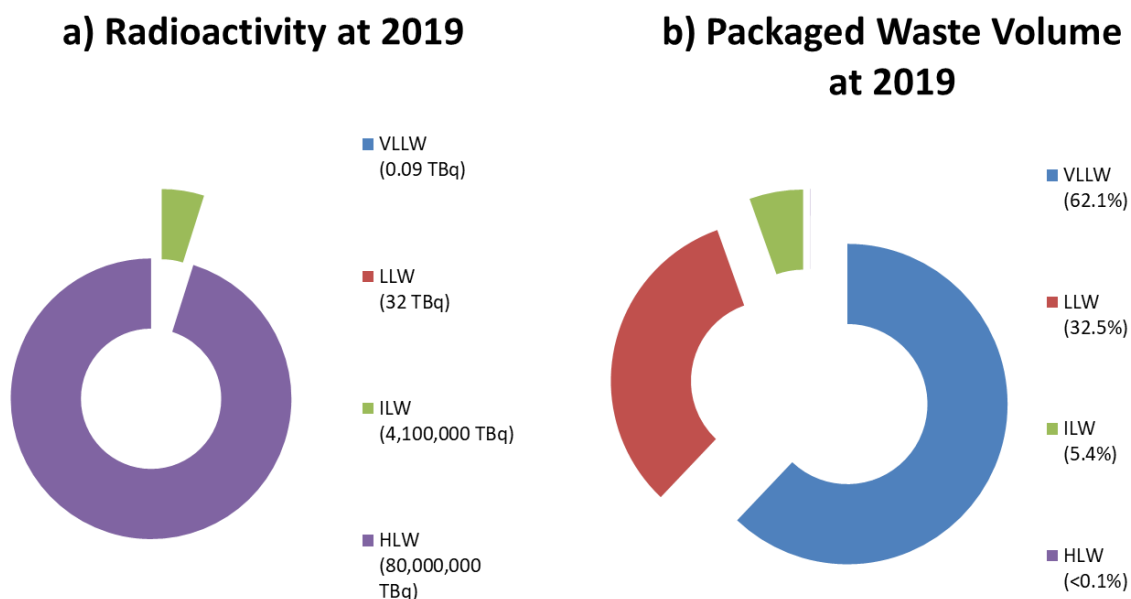


Figure 5: a) Total radioactivity at 2019 (TBq); and b) Lifetime Total proportion of Waste Volume by Type (%).

Table 2: The UK inventory of nuclear materials consistent with the NDA (NDA, 2019b).

Type	Radioactivity at 2019 (TBq)	Radioactivity at 2019 (%)	Packaged Volume at 2019 (m ³)	Packaged Volume at 2019 (%)
VLLW	0.09	1.1×10^{-7}	1.0×10^3	0.8
LLW	32	2.8×10^{-5}	2.7×10^4	20.7
ILW	4.1×10^6	4.9	1.0×10^5	76.9
HLW	80.0×10^6	95.1	2.2×10^3	1.6
Total	84.1×10^6	100	1.3×10^5	100

In 2008 UK government decided that higher activity wastes (HLW and ILW) should be disposed of in an underground geological repository (DEFRA, 2008). The Geological Disposal Facility (GDF) is intended to safely and securely contain radioactive wastes (Morris et al., 2011; The Department of Energy and Climate Change, 2014) and at a depth of 200-1000 metres. Geological disposal buries higher activity radioactive waste deep underground far away from the bio-sphere (by comparison: the London underground at its deepest is 65 m). A GDF will employ an 'engineered multi-barrier' concept (Figure 6) where the outside environment is protected from the waste by a series of barriers complimented by the host rock in order to minimise contaminant release and mobility over long timescales. Choosing a suitable host rock requires considerable investigation and characterisation as it is important to minimise the possibility of rock fracturing and groundwater flow to the facility. Whilst France and Switzerland are studying sites with weaker sedimentary rocks such as clays (ASN, 2017; NAGRA, 2018), Sweden and Finland are currently designing facilities in hard igneous rocks such as granite (Kärnbränslehantering, 2019). Waste will be placed inside a grout filled steel drum that is held within an underground storage unit which is backfilled with concrete, ensuring that no harmful amounts of radioactive waste will ever come into contact with the surface. Whilst the design concept for a GDF is well understood the UK has not yet confirmed a site for its own GDF however, any sites containing rock formations that may be exploited by future generations for natural resources have been excluded (DEFRA, 2008).

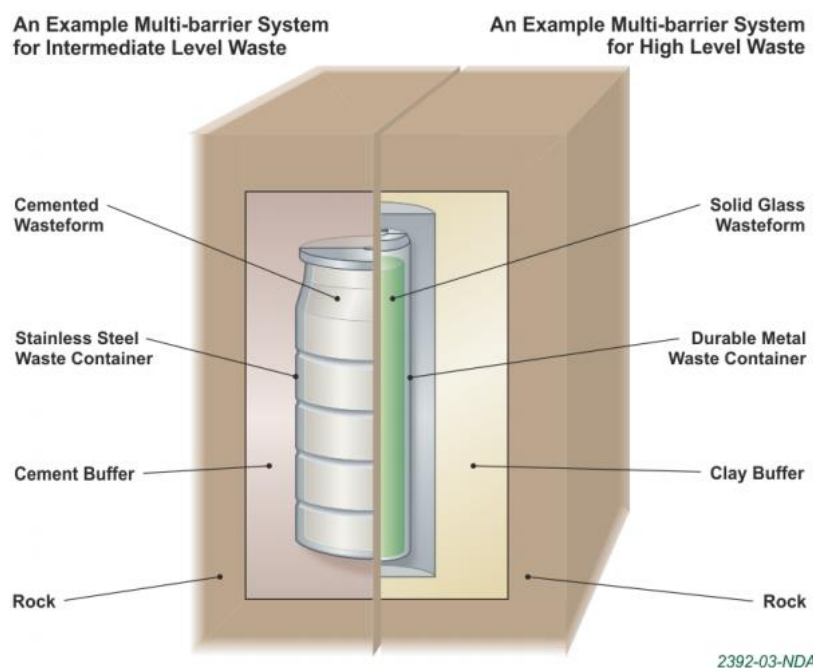


Figure 6: Examples of multi-barrier systems for Intermediate Level Waste (left hand side), and for High Level Waste (right hand side). Image taken from (The Department of Energy and Climate Change, 2014).

2.2 Radioactively Contaminated Land and the Sellafield Site

2.2.1 Radioactively Contaminated Sites

Historically, authorised releases of radioactivity to the environment have occurred through the testing of nuclear weapons and through the authorised discharge of radioactive effluents to the oceans. Furthermore, nuclear accidents such as the Windscale fire (1957), Three Mile Island (1979), Chernobyl (1987) and Fukushima (2011) have resulted in the accidental release of radioactivity. The groundwater and sediments at several nuclear licenced research facilities have also been contaminated with radionuclides due to leaks to the subsurface. Owing to their long history of nuclear research and the nuclear arms race during the Cold-War, the USA, Russia and the UK have some of the most heavily contaminated nuclear sites including Hanford (USA), Oak Ridge (USA), Mayak (Russia) and Sellafield (UK) (Istok et al., 2004; Sellafield Ltd., 2015). Although the Sellafield site contains almost 70,000 m³ of intermediate and high level wastes, with values predicted to increase to up to 180,000 m³ before the year 2100 (NDA, 2013), compared to equivalent global nuclear sites its area is significantly smaller despite having a comparable radionuclide inventory (Table 3). Any releases from this large inventory are monitored using groundwater monitoring wells at the Sellafield site.

Table 3: Comparison of the site area (km²) and the respective radioactive waste inventories categorised by HLW, LLW and ILW from nuclear sites across the globe. Data sourced from (Mckinley et al., 2001; NDA, 2016; Sellafield Ltd., 2015; Standing et al., 2002; Watson et al., 2004; Zachara et al., 2007)

Site	Sellafield (UK)	Oak Ridge (USA)	Hanford (USA)	Mayak (Russia)
Site Area (km ²)	6	220	1,500	200
Radioactive Waste Inventory (m ³)	HLW	-	950,000	56,800
	ILW	-	-	232,000
	LLW	6,310	73,000	429,000,000

2.22 *The Sellafield Site*

As the chemistry, geology and microbiology studied in this thesis are representative of the Sellafield site this section briefly describes its history, geology and details its subsurface radioactive contaminants. Although it is only 1 of 17 of the NDA's nuclear decommissioning sites, Sellafield contains nearly 75% of the total radioactivity in the UK (NDA, 2016, 2013) (Figure 4). The Sellafield site is the largest nuclear site in Europe, and is likely the most complex (Sellafield Ltd, 2018) (Figure 7). As reprocessing at the Thermal Oxide Reprocessing Plant (Thorp) and the Magnox reprocessing plants nears completion, work at Sellafield is becoming more focused on the remediation, decommissioning and clean-up of its legacy.



Figure 7: An aerial view of the Sellafield site. Taken from (NDA, 2019b)

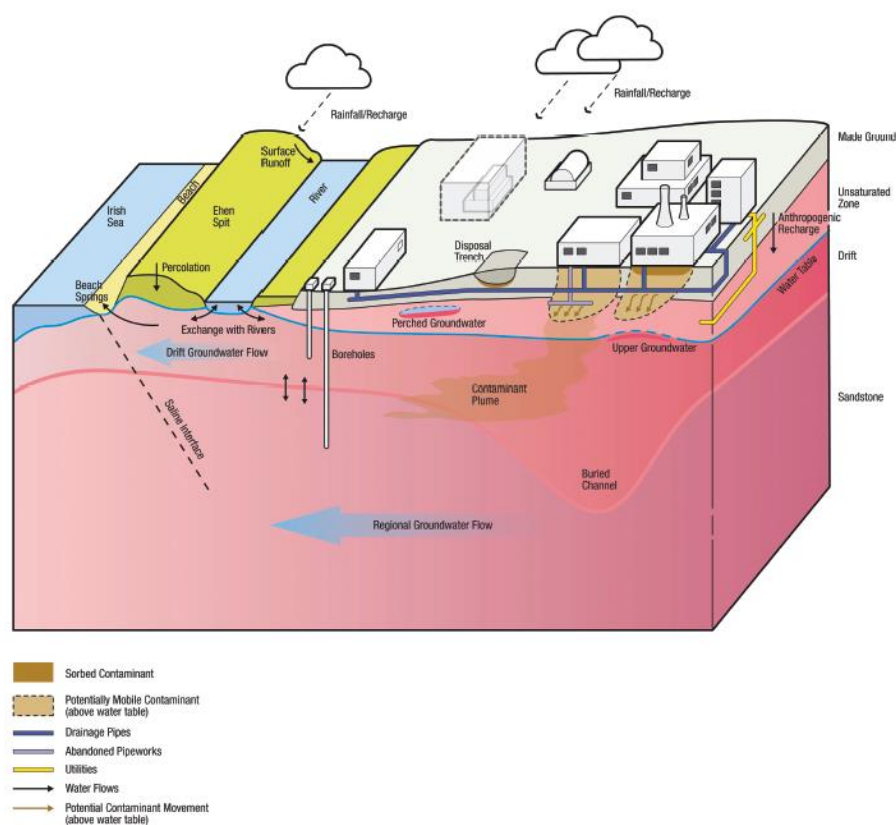
2.23 *A Brief History of the Sellafield Site*

Located in Cumbria, the Sellafield site has been operational since the 1940s, where it was used as a Royal Ordnance Factory supporting the Second World War and the national defence. After the war had finished, it was converted into a Pu production plant for the nations atomic weapons programme. In the 1950s Calder Hall, the world's first commercial nuclear power station, and the Windscale Advanced Gas-Cooled Reactor (AGR), tasked with producing weapons grade Pu, were built on the Sellafield site. As a result, work on the Sellafield site involved the reprocessing of spent nuclear fuel to recover U and Pu. In 1957, after a serious fire in the Windscale Piles broke out (and was safely put out), the Piles were shut down and the ongoing decommissioning of these structures began in 2001. With the exception of one prototype reactor built in the 1960s, the following expansion of the facilities at the Sellafield site have been concerned with either the reprocessing of spent nuclear fuel or the temporary storage and management of nuclear waste. Sellafield has 2 reprocessing plants: Magnox and Thorp, a vitrification plant which concentrates fission products into solid glass blocks which can

be stored as high level wastes, and 2 plants tasked with reducing radioactive contaminant concentrations in liquid low levels waste effluents, the Enhanced Actinide Removal Plant (EARP) and the solvent treatment plant. The Separation Area (highlighted in Figure 9) incorporates an area of approximately 31 hectares and sits on the original site purposed for Pu production, accordingly most of the contamination sources are located beneath the Separation Area (Cruickshank, 2012). Currently, Sellafield is the only nuclear licenced site in England that can safely manage low, intermediate and high level radioactive waste.

2.24 The (Hydro-)Geology of the Sellafield site

The Sellafield geology consists of deposits of sandstone, sand gravel, silts and clay. Generally, the regional groundwater flows from the Cumbrian fells at higher elevations towards the Sea at lower elevations in a southwest direction, with a typical travel time of 10-20 years from the northern boundary to the coast (Figure 8). At increasing depths the sandstone beds become increasingly weathered, this leads to localised shallower zones which have faster groundwater flows (Cruickshank, 2012). Groundwater flow is also affected by numerous of fissures, fractured fault zones and mudstone/clay bands. Furthermore, there is a local groundwater mound beneath the Separation Area which is believed to be a result of leaching processes (Cruickshank, 2012). This means that the mobile radioactive contaminants leaving the separation area can be discharged either southwest to the Irish Sea or southeast to the River Calder. As the Sellafield site has been used industrially since the 1940s it has extensive surface layers of built ground, consisting of tarmac, concrete bricks and wood. Considering all the varying materials, each with varying size, depth and hydraulic properties, that comprise the Sellafield site, they make its hydrogeology highly complex.



"Surface contamination moves slowly downward carried by infiltrating surface water until it enters the aquifer"

Figure 8: A conceptual model of the Sellafield Site, describing the regional hydrogeology. Taken from (Sellafield Ltd., 2015)

2.25 Radioactive Contamination and Groundwater Monitoring at the Sellafield Site

Over the past 80 years there has been a series of both authorised and accidental releases of radioactivity to the subsurface at Sellafield (Cruickshank, 2012). As a result of this, the Compilation of Environment Agency Requirements (CEAR) have set requirements that Sellafield provides an annual groundwater monitoring report since 1993 (Sellafield Ltd., 2015). Here, the concentrations of contaminants leaving the site should be lower than the values depicted by the World Health Organisation (WHO). The document *'Guidelines for Drinking-water Quality'* takes the effects of chemical and radioactive toxicity into account to establish the upper concentration limits of pollutants in "safe" drinking water (World Health Organisation, 2006). Thus, the groundwater composition and hydrogeology are assessed using a network of groundwater monitoring wells, these highlight the critical components of the site infrastructure including the source, nature and migration pathways of contaminants in temporal, spatial, qualitative and quantitative detail. They ensure that the transport of radionuclides is controlled and their locations at the Sellafield site are shown in Figure 9A below (Sellafield Ltd., 2015). Figure 9 also encircles the Separation Area, this was the focal point of historical activities and contains the majority of the radioactive waste and legacy operational buildings. Within the Separation Area are the Highly Active Liquor Tanks and the Solid Waste Storage Facility which between them are estimated to account for > 99% (by activity) of the total radionuclides released to the subsurface (Sellafield Ltd., 2015). Isotopes of U, in particular ^{234}U and ^{238}U are the dominant alpha emitters in Sellafield groundwaters, as such they dominate the total activity measured. Other

significant alpha-emitters such as ^{239}Pu , ^{240}Pu , ^{237}Np and ^{241}Am have been detected, although their concentrations are below the WHO guidelines in any given well. The distribution of all alpha emitters demonstrate that the mobility of alpha emitting radionuclides such as U is relatively restricted past the Separation Area (Figure 9B), this is likely governed by sorption processes (Sellafield Ltd., 2017, 2015). Alpha activity concentrations have been highest in 5 wells located in the northwest corner of the Separation Area (Figure 9B) since 1986. These values have been steadily decreasing every year suggesting the distribution and sorption of alpha emitting radionuclides (Sellafield Ltd., 2017, 2015; Stamper et al., 2014). In the case of ^{90}Sr , its concentrations are mainly localised within the Separation Area although there is evidence for ^{90}Sr migration downstream of the Separation Area (Figure 9C).

Radioactive waste streams usually arise from site operations such as storage, reprocessing and decommissioning. Liquors containing high levels of radioactivity are routed directly to storage where they are vitrified and remain on site. Liquid effluents of intermediate activity are sent to interim decay storage before treatment in EARP prior to discharge. Liquors of lower activity are routed directly to EARP or other plants for treatment to ensure minimal radioactivity before discharge. As a result, discharges of radioactivity to the sea have declined significantly since the 1970s (Sellafield Ltd., 2017).

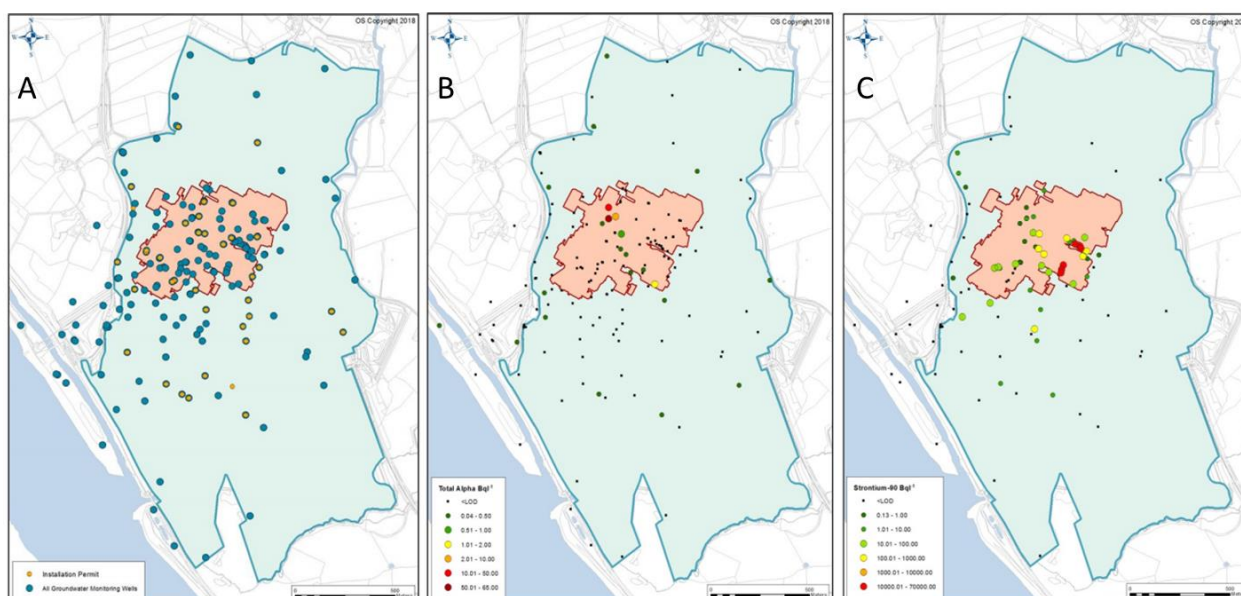


Figure 9: An overview of the Sellafield site (blue) and the Separation Area (red). A) The groundwater monitoring wells network; B) Average total alpha concentrations (results below the CEAR target Limit of Detection (LOD) of 0.03 Bq l⁻¹ are displayed on the figure as <LOD); and C) Average ^{90}Sr concentrations (results below the CEAR target LOD of 0.12 Bq l⁻¹ are displayed on the figure as <LOD); copied from (Sellafield Ltd., 2017).

2.26 Radionuclide Mobility – Speciation, Oxidation State, pH and Hydrolysis

A wide range of physicochemical, chemical and biological interactions, pH, Eh and sediment geology, affect the mobility of each contaminant differently. For example, the oxidation state of metals affects their chemical reactivity and thus behaviour. Many key radioactive contaminants are redox sensitive and their mobility can be dictated by changing their oxidation state. In the case of U, Tc and Np the oxidised forms are soluble and the reduced are relatively insoluble (under standard conditions), however, some contaminants behave in more complex ways (e.g. Pu) or are not susceptible to redox changes and must be treated via other solutions (Figure 10).

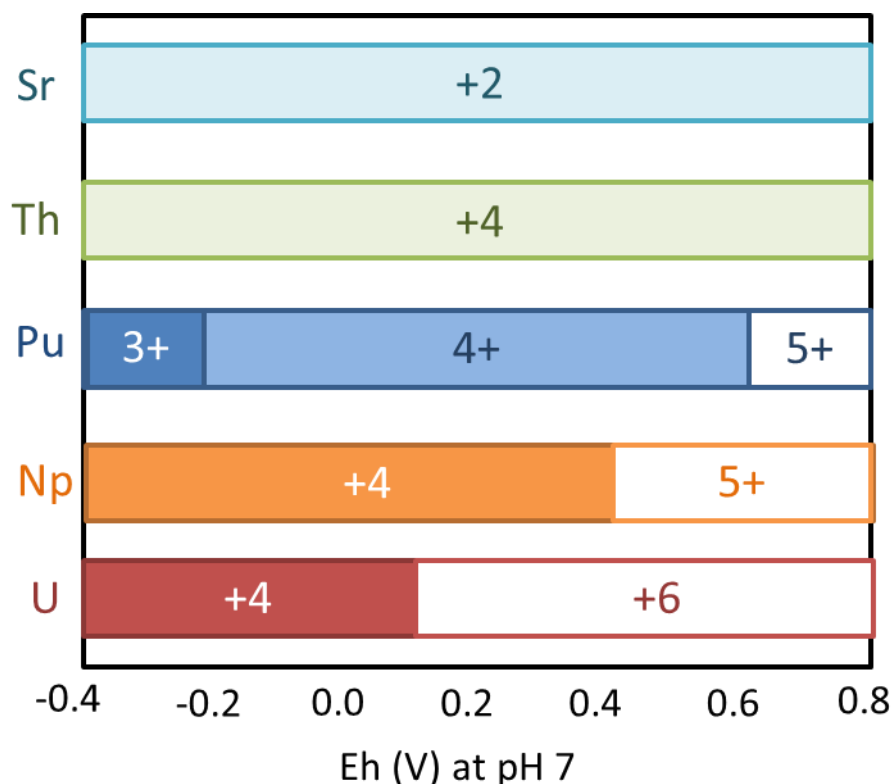


Figure 10: Changing oxidation state with Eh for selected radionuclides at pH(7). Adapted from (Lloyd, 2003).

The pH of groundwater is governed by its composition and the local geology, and strongly influences the sorption of radionuclides such as U and Sr (Fuller et al., 2016; Waite et al., 1994). Under acidic conditions mineral surfaces tend to be positively charged and radionuclides tend to exist in cationic forms and protons compete for binding sites, lowering the net attractions between the negatively charged surfaces and the cationic radionuclides (Davis et al., 2006). As pH increases the mineral surfaces become more negatively charged, whilst the radionuclides remain cationic, increasing the forces of attraction which may lead to precipitation. At Sellafield, groundwater pH ranges from 4.8 to 8.5, although the majority of the readings are circumneutral (Sellafield Ltd., 2017). Groundwater ingress into cementitious barriers, which are designed into GDF multi-barrier systems, will create high pH conditions lasting extended periods of time (DEFRA, 2008; NAGRA, 2018; The Department of Energy and Climate Change, 2014; Van Veelen et al., 2014). These conditions will minimise radionuclide migration via the formation of insoluble hydrolysis products and increased cation sorption to negatively charged mineral surfaces (Braney et al., 1993; Schwyn et al., 2012; Smith et al., 2018, 2015).

Radionuclides can also sorb strongly to the surface of organics, iron (oxy)hydr-oxides and clays; these processes are, however, strongly hindered at low pH and in the presence of complexing ligands (especially carbonate) or competing cations (Brookshaw et al., 2015; Ching-kuo and Langmuir, 1985; Gu et al., 2005; Newsome et al., 2014a; Winstanley et al., 2019). Many non-radioactive contaminants also affect the mobility of contaminant species and are monitored accordingly (Sellafield Ltd., 2017). Co-contaminants such as nitrate and ammonia are found at elevated concentrations on the site because of their extensive use in the nuclear fuel cycle, and microbial metabolisms involving nitrate and ammonia will have significant effects on the subsurface biogeochemistry (Fujita et al., 2010; Law et al., 2010a; Thorpe et al., 2012b, 2012a).

2.27 Remediation Strategies

A useful conceptual model for minimising pollution risks is the source-pathway-receptor process. In the case of nuclear sites the source is likely to be leaks or spills. The pathway is probably achieved via mobilisation in the groundwater and uptake of the contaminant species through plant roots, or drinking of contaminated water. The receptors include vegetation, aquatic and terrestrial life and eventually reaching the human population. The application of the model in many remediation strategies for contaminated environments removes or disrupts the source or pathway to eradicate the risk to any receptor, this demonstrates that without all three components there is no associated risk. A variety of groundwater remediation techniques are available and a summary of common techniques are described in Table 4 (below).

Table 4: A summary of common remediation methods for contaminated environments. Adapted from (Cleary, 2018).

Method	Description	Strengths	Weaknesses
Dig-and-dump	Excavate contaminated land and dispose in a landfill	<ul style="list-style-type: none"> - Quick and easy - Well established 	<ul style="list-style-type: none"> - Expensive. - Only moves contamination to next site. - Logistics and costs with radioactive materials are further emphasised.
Pump-and-treat	Groundwater is pumped above ground-level then treated and replaced with clean water	<ul style="list-style-type: none"> - Generates less waste than Dig-and-Dump - Well established 	<ul style="list-style-type: none"> - Expensive - Large volumes to treat - May change groundwater biogeochemistry - Often requires long timescales
Bioremediation	Includes <i>in-situ</i> stimulation of the native microbial community via injection of simple organic electron donors, thus promoting the precipitation of soluble contaminant species	<ul style="list-style-type: none"> - Environmentally friendly - Economical - Minimises risk associated for site staff 	<ul style="list-style-type: none"> - Clogging of injection wells possible. - Remobilisation / re-oxidation risk
Targeted Remediation	<i>In-situ</i> injection of nanoparticles or targeted electron donors which demonstrate enhanced contaminant removal compared to standard bioremediation	<ul style="list-style-type: none"> - Highly effective - Promotes long-term stability - Minimises risk associated for site staff 	<ul style="list-style-type: none"> - More expensive than simple organic electron donors - Issues with regulations
Monitored natural attenuation	The controlled release of contaminants retarded by natural processes such as sorption, precipitation or radioactive decay.	<ul style="list-style-type: none"> - Cheaper - Easy - Minimises risk associated for site staff 	<ul style="list-style-type: none"> - Requires continuous monitoring - Medias responses to the 'Do nothing' approach

2.28 The Nuclear Provision & Suitable End-points

The Nuclear Provision, is the leading estimate of the cost and duration to clean up 17 of the UK's earlier nuclear sites, it gives the leading estimates of the timescale and cost to clean up Britain's nuclear legacy, with current estimates of £117-225 billion over the next 120 years (NDA, 2019a). The Environmental Agency and the Office for Nuclear Regulation are responsible for the regulation and decommissioning of radioactive waste contaminated sites. 'Guidance on Requirements for Release of Nuclear Sites from Radioactive Substances Regulation', published by the Scottish Environment Protection Agency (SEPA), discusses requirements for operators of nuclear sites to follow in order to ensure compliance of radiological regulations so that the site may ultimately achieve unrestricted use as an end-point (Scottish Environment Protection Agency, 2016)(Figure 11).

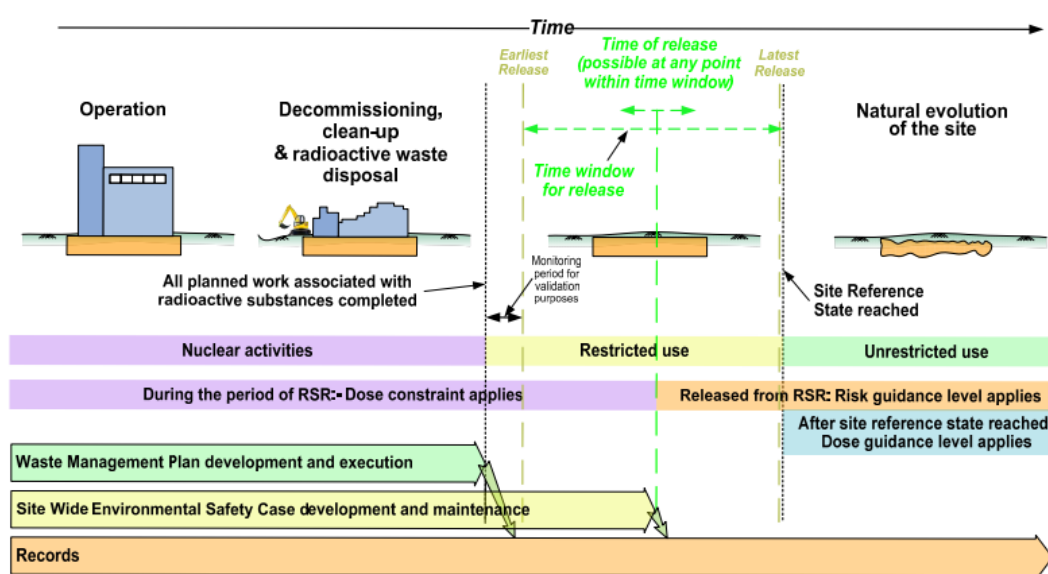


Figure 11: A proposed end point for a successfully decommissioned nuclear site. SEPA recommend that operators should establish and maintain a waste management plan until the site reaches its' target reference state as demonstrated above. Taken from [(Scottish Environment Protection Agency, 2016)].

Here, the Rocky Flats Plant, Colorado USA serves as a suitable example of a decommissioned site. Beginning in 1952, the facility primarily fabricated mainly Pu for military purposes for nearly 40 years; during this period, manufacturing activities, accidents and waste management processes lead to significant contamination on site. The remediation of the site involved the decommissioning of roughly 800 structures, 1.3 million cubic meters of waste and more than 16 million gallons of contaminated water before it achieved regulatory approved closure in 2006. Soil removal techniques were employed to remediate contaminated areas down to 1 meter below the surface and replacing it with fresh soil; and soils contaminated at deeper than 1 meter were left in place (Clark et al., 2006). Today, on the site of the former facility, only one part is still owned and managed by the US DoE and is off-limits to the public, whilst the remainder of the site serves as a national wildlife refuge (Figure 12). This refuge is deemed as suitable for unrestricted use by the public and undergoes an environmental review every 5 years by the US DoE, EPA and the Colorado Department of Public Health and Environment. Here, the most recent review states that the "remedy at the site is protective of human health and the environment" (Surovchak, 2017).



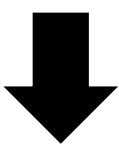
Figure 12: (Left) The Rocky Flats site in June 1995 prior to the final clean-up operation; and (right) the Rocky Flats National Wildlife Refuge. Images taken from (U.S. Department of Energy, 2019).

2.3 Microorganisms and Bioremediation

2.3.1 Microorganisms & Microbial Diversity

The word 'microorganism' describes a very large and diverse group of very small but hardy lifeforms that are microscopic in size and often exist as single-cells or amongst a colony of cells. Collectively, they inhabit almost all areas of the planet and can be found thriving in even the most hostile and extreme environments (Hafenbradl et al., 1997; Makarova et al., 2001; Murray et al., 2012). Microbial activity plays a key role in global elemental cycles; it affects Eh, pH, and can cause the weathering and formation of minerals. The study of microbiology aims to understand the microbial world and harness its potential for our benefit. Mankind has engineered ecosystems which promote microbial activity: we can use their metabolisms to remediate wastewaters (Liu et al., 2004), extract metal from ores and recover them from wastewaters (Hutchins et al., 1986; Lundgren and Silver, 1980), clean-up environmental pollutants (Cl:Aire, 2004; Omoregie et al., 2013), and even to treat early-stage bladder cancers (Lamm et al., 1992). Microbial activity in systems can cause undesired changes too; activities in oil and gas transmission lines and deposits can often lead to substantial financial losses (Zhu et al., 2003), groundwater contamination with pathogens can be a direct cause of severe illnesses, and in some cases microbial activities can lead to contamination of drinking waters with trace toxic metals such as As (Ahmed et al. et al., 2006; Ashbolt, 2004). Like humans, microbes also gain energy through respiration. Under aerobic conditions some microbes couple the reduction of oxygen with the oxidation of simple organic compounds. Compared to other environmentally relevant electron acceptors, the complete reduction of oxygen to water generates the greatest net energy and thus is the preferable respiratory mechanism for "aerobic" organisms. In the absence of oxygen, a range of microbes can use other electron acceptors to generate energy in the subsurface where oxygen levels are depleted; the preference for one terminal electron acceptor over another is determined by its relative concentrations and energy yield as summarised in Table 5 (Ahmann et al., 1994; Lovley et al., 1991; Lovley and Phillips, 1988; Myers and Nealson, 1988). The extent of redox reactions can often be limited by other factors such as the availability of primary electron donors (typically simple organic molecules) and water (Madigan et al., 2015). Therefore, the addition of aqueous electron donors to the subsurface can stimulate microbial metabolisms, and when this is done as a method of treating contaminated environments this process is known as bioremediation.

Table 5: Describing the diminishing energy potential for the reduction of terminal electron acceptors with depth. Values given for pH 7 (Lloyd, 2003).

Reaction	ΔE_h^0 (mV)	Depth (Increasing from top to bottom)
$O_2 + 4H^+ + 4e^- \rightarrow 2 H_2O$	+820	
$2NO_3^- + 12H^+ + 10e^- \rightarrow N_2 + 6 H_2O$	+740	
$FeOOH + HCO_3^- + 2H^+ + e^- \rightarrow FeCO_3 + 2 H_2O$	-50	
$SO_4^{2-} + 9H^+ + 8e^- \rightarrow HS^- + 4H_2O$	-220	
$CO_2 + 8H^+ + 8e^- \rightarrow CH_4 + 2H_2O$	-240	

2.32 Bioremediation

Bioremediation utilises the actions of microbes present in the subsurface to alter the biogeochemistry present via several mechanisms illustrated in Figure 13 (below). These include: *i*) bioreduction, the enzymatic reduction of species to gain energy for a metabolism; *ii*) biomineralisation, the process by which living organisms precipitate minerals with microbially generated ligands often localised at the cell surface or within the cell membrane; *iii*) biosorption, the physiochemical sorption which concentrates species onto functional groups present in its cellular structure; and *iv*) bioaccumulation, the gradual accumulation of a substance in an organism.

As aforementioned, the mobility of many species are sensitive to changes in oxidation state; for example, the reduction of solid phase Fe(III) and Mn(V) oxides yields soluble, and therefore mobile Fe(II) and Mn(II) species respectively (Canfield and Thamdrup, 2009). Alternatively, reduction can lead to the formation of less soluble phases; this is seen, for example, in the transformation from soluble U(VI) to relatively insoluble U(IV) (Lovley et al., 1991; Williams et al., 2013). Injections of electron donor into a contaminated geosphere stimulates growth of the indigenous microbial community, developing anoxic conditions in the subsurface where bioreduction can occur (Figure 14). Through bioreduction, we can make use of these microbially-mediated redox changes, offering a more attractive proposition than traditional strategies such as pump-and-treat or dig-and-dump, which are generally highly invasive and expensive. Bioreduction is also generally more attractive than other biological solutions such as biosorption or bioaccumulation as the reduced form is generally more stable (Cuney, 2010; Mohapatra et al., 2010; Newsome et al., 2014a). The success of bioremediation has been demonstrated widely under experimental conditions for a host of environmental contaminants including radionuclides (Begg et al., 2011; Fuller et al., 2015; Law et al., 2011, 2010b; Masters-Waage et al., 2017; Thorpe et al., 2017, 2012b; Wilkins et al., 2007), other toxic metals (Aksu and Kutsal, 1991; Bhattacharya and Venkobachar, 1984; Foster et al., 2014; Tiwari et al., 1995), toxic compounds from i.e. oil spills, dyes or pesticides (Atlas and Hazen, 2011; Dar et al., 2019; Khan et al., 2019; Wang et al., 2009). furthermore it has been proven in field-scale studies for both U and Sr in the USA (Anderson et al., 2003; Istok et al., 2004; Senko et al., 2002; Williams et al., 2013, 2011; Yabusaki et al., 2007).

Bioremediation is much less invasive than classic remediation techniques; take for example a case which targeted aqueous ^{90}Sr at the Hanford site. Here, a pump-and-treat system was designed to reduce ^{90}Sr leaching into the adjacent Colombia River. The method employed required that the contaminated groundwater was pumped into the treatment system where ^{90}Sr is removed prior to re-injection back into the aquifer upgradient of the pumping site. In 2003 alone, this required the removal of > 114 million litres of water in order to remove 7.4 GBq of ^{90}Sr (Dirkes et al., 2009).

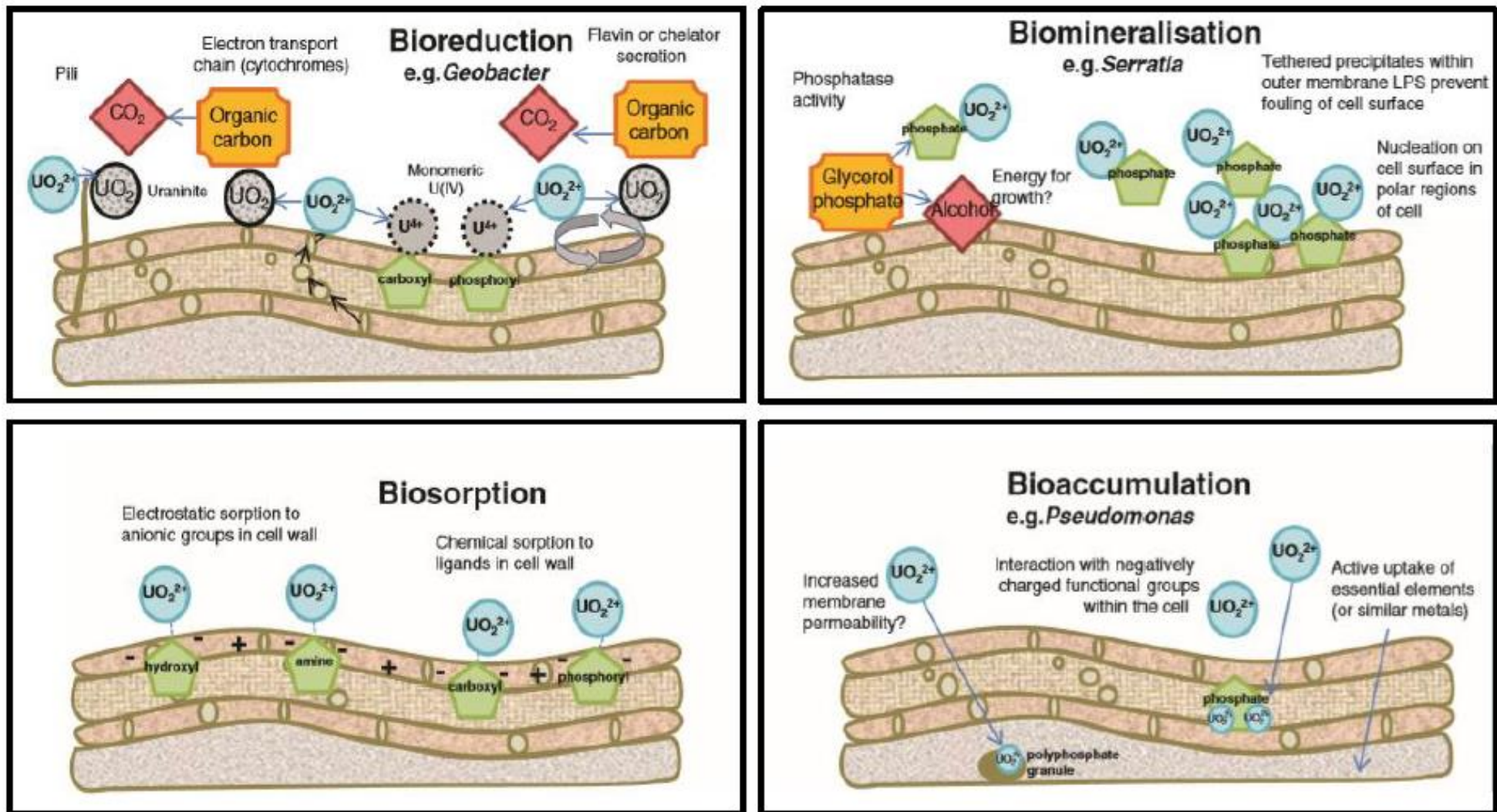


Figure 13: The mechanisms used by microbes to immobilise U in contaminated groundwater. Image taken from (Newsome et al., 2014a).

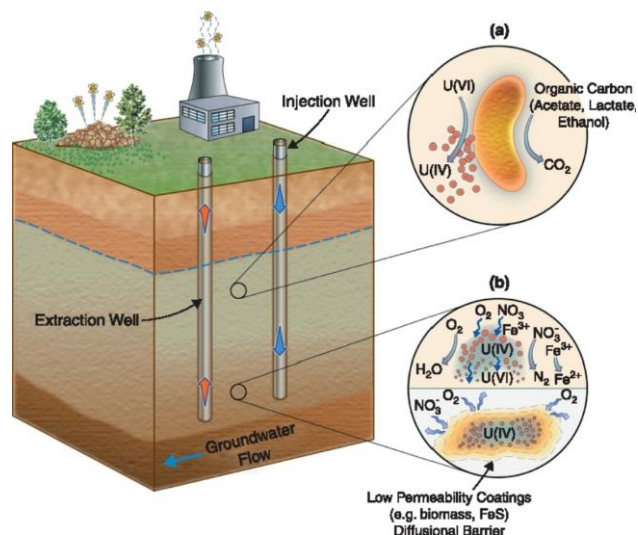


Figure 14: Conceptual illustration of the process of uranium bioremediation. (a) Native bacteria present in contaminated sediments can couple the oxidation of organic carbon compounds with the reduction of U(VI)_(aq). (b) Reduced U(IV) can be re-oxidised when C addition stops, or upon the arrival of oxidants; in this case O₂, NO₃⁻, and Fe(III). Low permeability coatings, such as FeS, can suppress re-oxidation and maintain stability of immobilized U(IV). Taken from (Williams et al., 2013).

2.4 Iron Biogeochemistry

2.4.1 The Chemistry of Fe

Fe is highly abundant in the earth's crust as a stable, redox active metal (Housecroft, Catherine E.; Sharpe, 2012). The iron cycle (Figure 15) considers ferric (Fe[III]) and ferrous (Fe[II]) iron in the Earth's surface, and metallic iron (Fe⁰) which is naturally present in Earth's core but is also synthesised anthropogenically at the surface via smelting processes (Madigan et al., 2015). Ferrous iron is stable under anaerobic or acidic conditions, it is generally more soluble than ferric [Fe(III)] iron, which is predominantly found as oxy-hydroxide minerals. One electron transfers between Fe(II) and Fe(III) in the subsurface occur as either biotic or abiotic redox reactions.

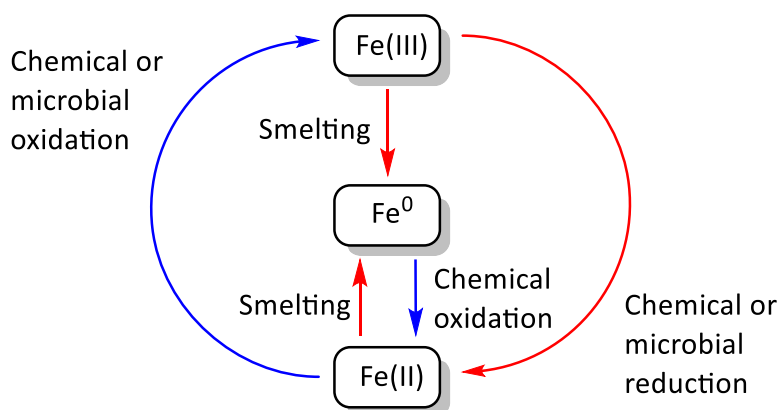


Figure 15: the iron cycle, showing chemical and microbial redox transformations. Oxidative processes are in blue and reductive processes are in red.

2.4.2 Microbial Respiration of Fe(III)

The ability of microorganisms to reduce Fe(III), as well as Mn(IV), has been known since the early 20th century (Harder, 1919). However, the coupling of Fe(III) and Mn(IV) reduction to the oxidation of organic carbon or H₂ was only recently described in the *Gram-negative* bacteria *Geobacter*

metallireducens and *Shewanella oneidensis* MR-1 (Lovley and Phillips, 1988; Myers and Nealson, 1988). As Fe(III) is a ubiquitous terminal electron acceptor (TEA), and there is an enormous range of organisms which couple Fe(III)-reduction to the oxidation of a wide host of electron donors (Figure 16) (Lovley et al., 2004). Moreover, as Fe(III) phases and electron donors exist in a multitude of forms, different phylogenetic groups have developed varying mechanisms to catalyse these processes. The anaerobic reduction of Fe(III) by *Bacteria* (known as Dissimilatory Iron Reducing Bacteria [DIRB]) and *Archaea* has an influential role in the geochemistry and bioremediation of contaminated subsurfaces between nitrate and sulphate reducing zones (Li et al., 2015).

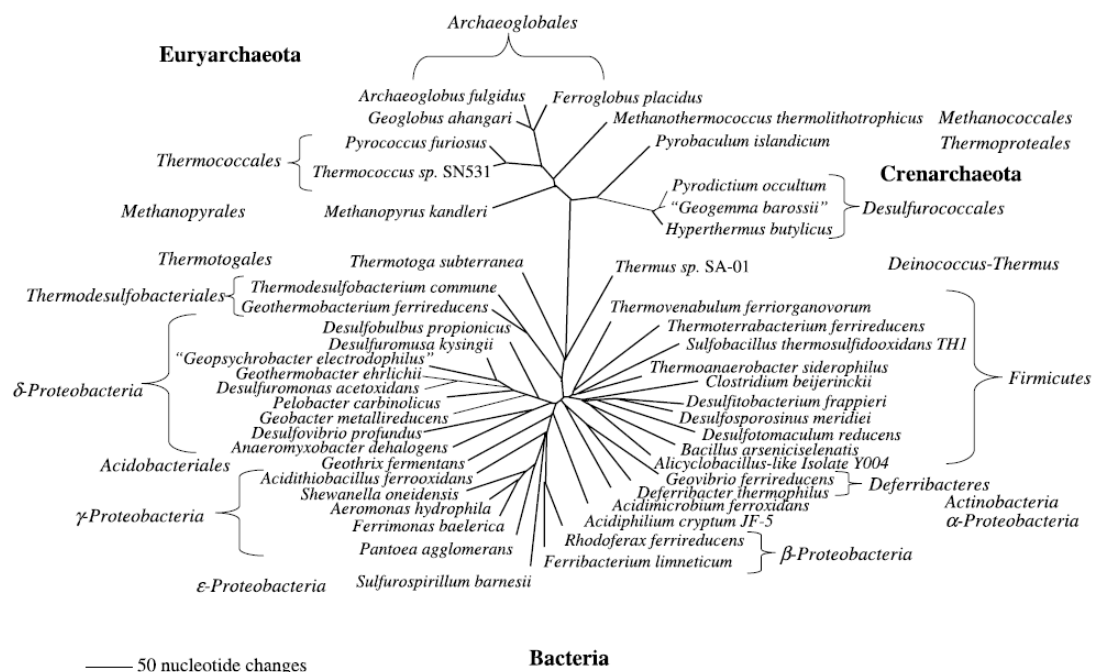


Figure 16: A phylogenetic tree based on the 16S rRNA gene sequences of microorganisms reported to be capable of conserving energy for growth from Fe(III) reduction. Taken from reference (Lovley et al., 2004).

Mechanisms for Fe(III)-reduction may involve direct contact or proceed via indirect pathways. Direct methods require the Fe(III)-respiring bacterium to make physical contact with the substrate in order to transfer electrons. Indirect methods may use extracellular electron shuttles, or chelating agents. Electron shuttles are extracellular, redox active compounds that cycle between reduced and oxidised states; they may be naturally occurring humics, quinones or the synthetic humic analogue: anthraquinone-2,6-disulphonate (AQDS) (Lovley et al., 1996). Finally, chelating agents are ligand systems secreted by the bacteria, which help solubilise and thus increase the bioavailability of insoluble metals.

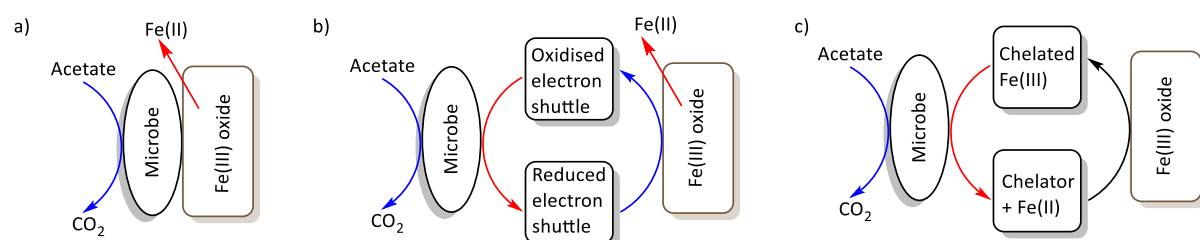


Figure 17: examples of microbial Fe reduction mediated by: a) direct contact, b) electron shuttle and c) use of a chelating agent. Oxidative processes are in blue and reductive processes are in red.

By coupling the oxidation of organics with the reduction of electron acceptors DIRB can control the long-term fate of metals (such as Fe, Figure 18), radionuclides and chemical pollutants in contaminated lands. For example in 1991, it was found that DIRB could transfer electrons to soluble hexavalent U as a method of obtaining energy for growth, forming insoluble U(IV) phases and offering a method of biological remediation to U contaminated environments (Lovley et al., 1991).

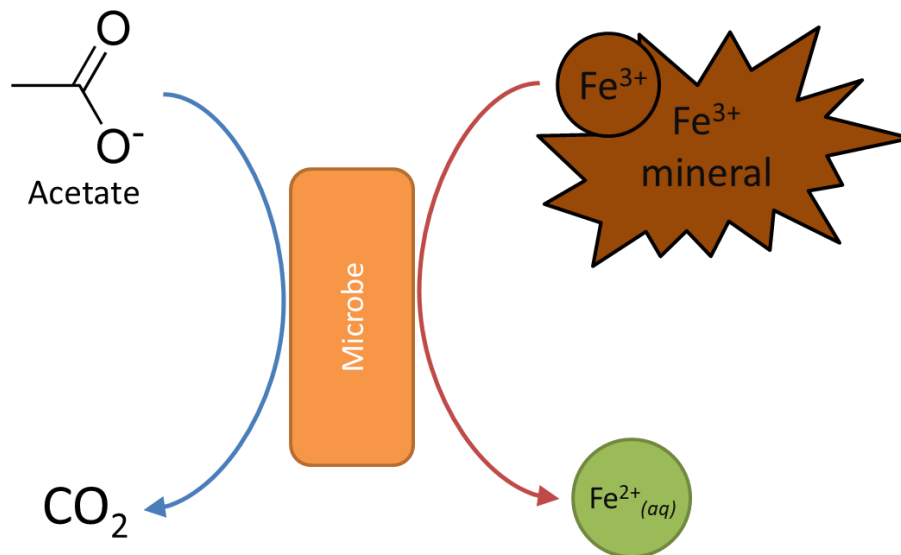
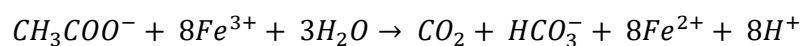


Figure 18: Demonstrating microbial growth by coupling the oxidation of acetate with the reduction of Fe(III). Oxidative processes are in blue and reductive processes are in red.

2.43 Dissimilatory Iron-Reducing Bacteria: *Geobacter* and *Shewanella*

Members of the *Geobacter* genus are model organisms for the study of enzymatic Fe(III)-reduction, they have a full genomic sequence available, are abundant in natural subsurface environments, and are often the predominant Fe(III)-reducing species in areas where metal-reduction is an active process (“JCVI: Home,” n.d.; Lovley et al., 2004; Röling, 2014). *Geobacter* species are *Gram-negative* obligate anaerobes that can couple the complete oxidation of electron donors, such as acetate, with the reduction of Fe(III) and Mn(IV), according to Equation 2 (Lovley et al., 2011, 1987; Lovley and Phillips, 1988; Myers and Nealson, 1988).



Equation 2: Stoichiometric equation demonstrating the metabolic reduction of Fe(III) coupled with the oxidation of acetate. $\Delta G^\circ = -814$ kJ (pH 7). (Lovley and Phillips, 1988).

Geobacter species must make contact with a substrate in order to reduce it. To do this, they produce flagella, which allow them to move towards Fe substrates via chemotaxis, and conductive pili which act as conducting nanowires that transfer electrons to the Fe(III) acceptors (Childers et al., 2002). An array of *c*-type cytochromes transfer electrons from the cell membrane to the extracellular pili and from the ends of the pili to the insoluble substrate (Reguera et al., 2005; Shi et al., 2007) (Figure 19 below). Many *Geobacter* isolates can use hydrocarbons, H₂, an electrode, or other small organic compounds as electron donors (Butler et al., 2007; Harwood and Gibson, 1997; Lovley, 2006).

Alternative electron acceptors include but are not limited to: S(0) (Lovley and Phillips, 1994), Co(III) (Caccavo et al., 1994), Cr(VI) (D. R. Lovley et al., 1993), U(VI) (Lovley et al., 1991), V(V) (Ortiz-Bernad et al., 2004), Ag(I) (Law et al., 2008), Hg(II) (D. R. Lovley et al., 1993), Tc(VII) (Lloyd and Macaskie, 1996), Np(V) (Renshaw et al., 2005), Pu(IV) (Boukhalfa et al., 2007), humics and AQDS (Lovley et al., 1998).

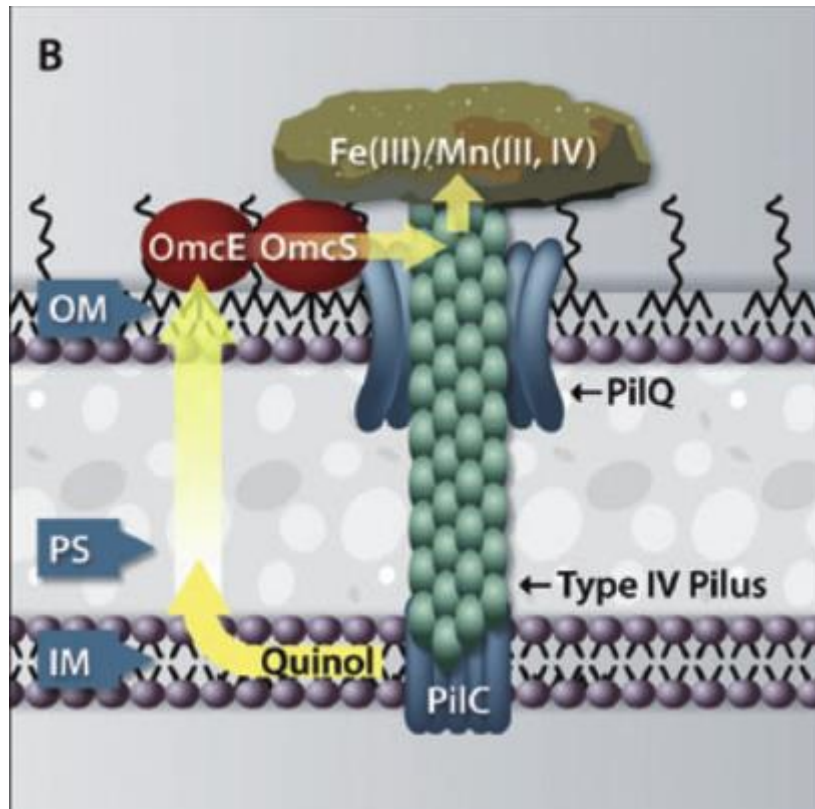


Figure 19: Simplified schematic diagram of a typical *Geobacter* cell showing proposed models for electron transfer pathways during reduction of solid phase metal Fe or Mn phases. Yellow arrows represent proposed electron transfer paths, identified c-type cytochromes are in red. OM - outer membrane, PS - peptidoglycan periplasm, IM - inner membrane. Taken from (Shi et al., 2007).

Given the use of *S. oneidensis* MR1 in chapter 4, the cell structure is given in more detail than *G. sulfurreducens*. The *Shewanella* genus is a hallmark species for respiratory versatility; they can respire Fe(III) and Mn(IV) (Lovley and Phillips, 1988; Myers and Nealson, 1988), nitrate (Myers and Myers, 1997), Cr(VI) (Myers et al., 2000), U(VI) (Lovley et al., 1991), Pu(IV) (Boukhalfa et al., 2007), Np(V), Tc(VII) (Fredrickson et al., 2008; Lloyd and Macaskie, 1996; Newsome et al., 2014a) and unlike *Geobacter*, they can respire oxygen. *Shewanella* spp. are also motile due to a single flagellum and several representatives have a full genomic sequence available (Heidelberg et al., 2002; Satomi, 2014). Electrons are transferred from the cytoplasmic membrane, through the periplasm, out of the outer membrane of the cell and onto the extracellular electron acceptors via a series of multiheme c-type cytochromes (Clarke et al., 2011; Coursolle et al., 2010; L. Shi et al., 2009; Shi et al., 2012). The dominant system in the transmembrane transfer of electrons is the protein complex MtrABC, and consists of MtrA (on the interior of the outer membrane) connected to MtrC (on the outer membrane) via MtrB (an outer membrane porin) (Figure 20). For every MtrC protein, two OmcA (Outer-membrane cytochrome A) proteins also aid in extracellular electron transfers (Marshall et al., 2006; Shi et al., 2007). A secondary set of Mtr proteins, MtrDEF, behave as less effective homologues to MtrABC (Clarke et al., 2011; Edwards et al., 2015, 2014). Cells lacking the genes for these proteins show

substantially hindered respiratory capabilities (Coursolle et al., 2010; Myers and Myers, 1997; Schwalb et al., 2003). Furthermore, *S. oneidensis* MR1 nanowires, as extensions of the cell periplasm and outer membrane localised to MtrC and OmcA cytochromes, also aid in electron transfer from to extracellular electron acceptors (Pirbadian et al., 2014).

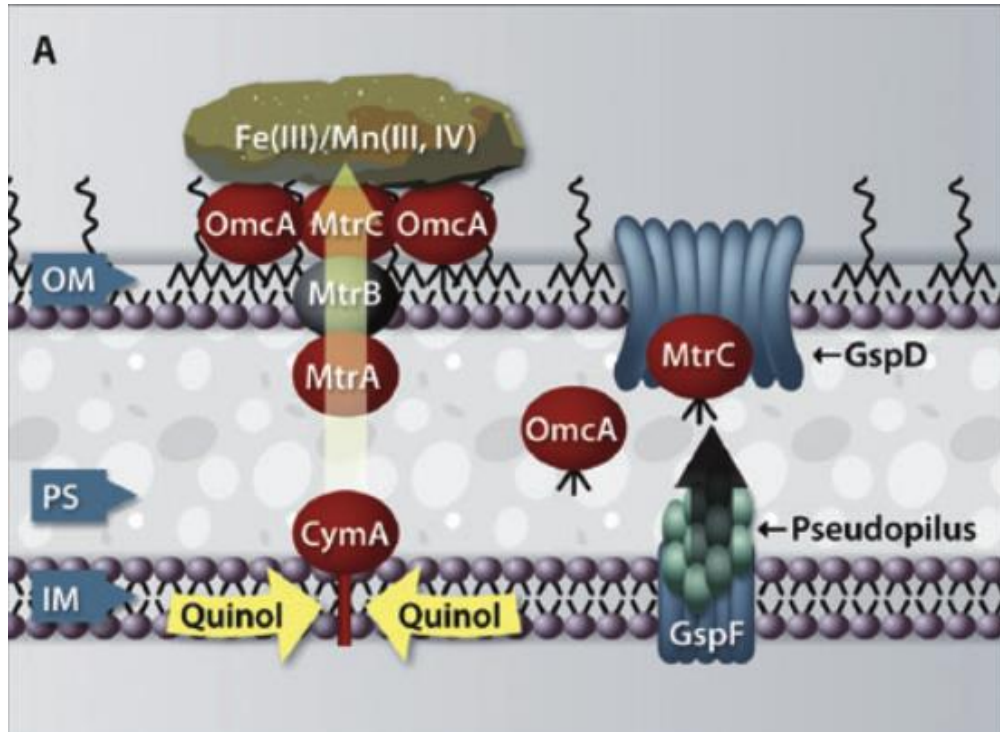


Figure 20: Simplified schematic diagram of a typical *S. oneidensis* MR-1 cell showing proposed models for direct (contact) electron transfer pathways during reduction of solid phase metal Fe or Mn phases at the cell surface. Yellow arrows represent proposed electron transfer paths, identified c-type cytochromes are in red. OM - outer membrane, PS - peptidoglycan periplasm, IM - inner membrane. Taken from reference (Shi et al., 2007).

In addition to electron transfer mechanisms involving direct contact, *S. oneidensis* MR1 can indirectly interact with substrates by secreting extracellular flavins (Figure 21 & 22 below) and siderophores, which act as electron shuttles and chelating agents respectively (Kotloski and Gralnick, 2013; Ledyard and Butler, 1997; Suzuki et al., 2010; Von Canstein et al., 2008). Naturally occurring humics and the synthetic humic analogue AQDS present in sediments may also act as electron shuttles (Nevin and Lovley, 2002; Von Canstein et al., 2008); electron shuttling can account for up to 75% of extracellular electron transfer processes in *Shewanella* species (Kotloski and Gralnick, 2013).

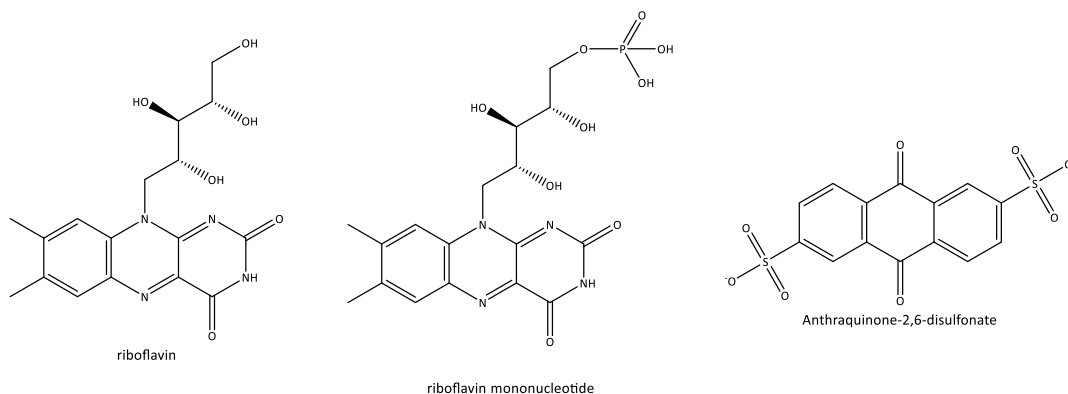


Figure 21: (from left to right) riboflavin, riboflavin mononucleotide and anthraquinone-2,6-disulphonate in oxidised forms. Riboflavin is excreted by *S. oneidensis* MR1, AQDS can be used as a synthetic analogue.

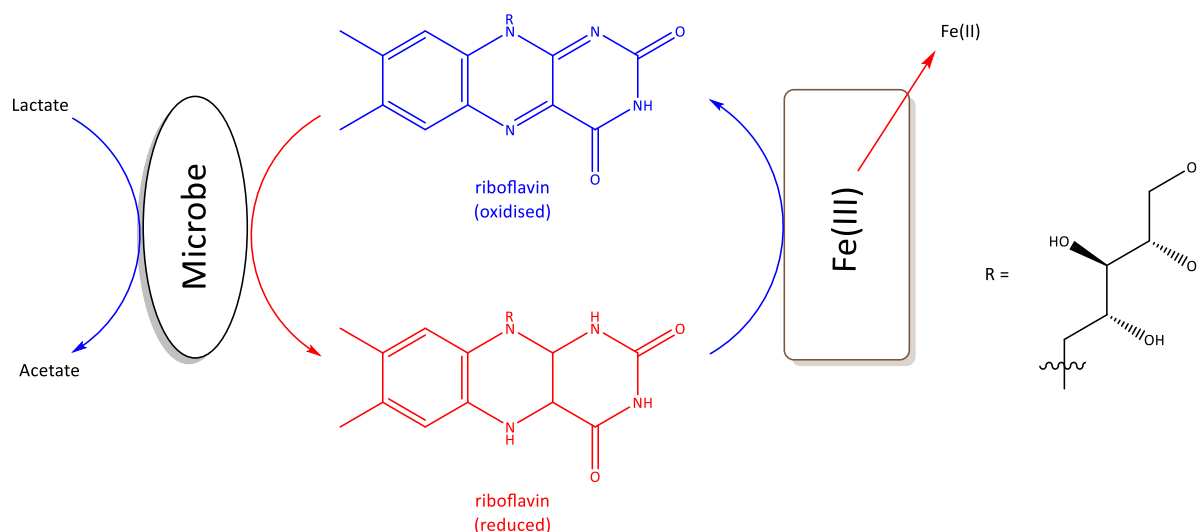
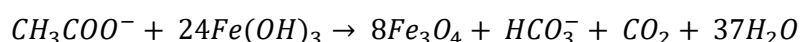


Figure 22: microbially mediated reduction of Fe(III) by means of catalytic redox transformations of an extracellular riboflavin molecule. As done by *Shewanella oneidensis* MR-1. Oxidative processes are in blue and reductive processes are in red.

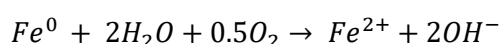
2.44 Iron Nano-Particles

Fe nano-particle injections can be used as an *in-situ* targeted remediation strategy for contaminated sites; they serve as mobile and permeable reactive barriers which require minimal invasive action. Here, Fe(II)-containing minerals such as magnetite [Fe_3O_4 or $\{(Fe^{3+})^{Td}(Fe^{2+}Fe^{3+})^{Oh}O_4^{2-}\}$] and nano-zero-valent iron (nZVI) particles are of particular significance (Crane et al., 2011; Dickinson and Scott, 2010). Due to their size, nano-particles are easily injected into the subsurface, they have a high surface to volume ratio, as well as an elevated surface energy, density of reactive sites and mobility compared to larger species resulting in enhanced remediation capabilities (James T. Nurmi et al., 2004). Although magnetite can be synthesized chemically, Fe(III)-reducing bacteria such as *G. sulfurreducens* can reduce various forms of ferric iron to nano-scale bio-magnetite (Byrne et al., 2011; Cutting et al., 2010; Lovley et al., 1987). Equation 3 describes bio-magnetite formation.

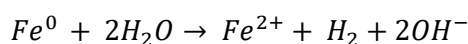


Equation 3: Bio-magnetite formation via enzymatically catalysed reduction of $Fe(OH)_3$ coupled with acetate oxidation. $\Delta G_0' = -712$ kJ/reaction (Lovley and Phillips, 1988).

nZVI is a strong reducing agent that has received a lot of attention over the past two decades, it has been used to treat a broad range of environmental pollutants in both laboratory and field-scale experiments (Li et al., 2006; Zhang and Elliott, 2006). The aerobic and anaerobic corrosion reactions for ZVI are explained in Equation 4 and Equation 5 respectively. In either case the reaction increases pH and produces Fe(II)-bearing minerals such as magnetite (Bosch et al., 2010; Dickinson and Scott, 2010; Kumar et al., 2014a; Liu et al., 2014; Torrey et al., 2015). The anaerobic corrosion of ZVI also produces H_2 which can act as an electron donor to promote further microbial activity (Lovley et al., 2004, 1989; Muyzer and Stams, 2008; Nedwell and Banat, 1981).



Equation 4: Aerobic corrosion of Fe^0 ; $\Delta E_0 = +1.67$ V (Dickinson and Scott, 2010).



Equation 5: Anaerobic corrosion of Fe⁰; ΔE₀ = - 0.39 V (Dickinson and Scott, 2010).

nZVI's affinity for mineral surfaces and agglomeration effects causes limited mobility in sediments; ultimately, this leads to unsatisfactory transport within the subsurface and clogging around injection wells. To overcome this nZVI particles have been optimised by tailoring the structures of the particles or by coating them with additives (Joshi et al., 2018; Mackenzie et al., 2015; Micić et al., 2017; Velimirovic et al., 2016). The NanoRem project (NanoRem.eu, 2014) studied a series of Fe nanoparticles that developed safe, economic and practical nanotechnologies for the *in-situ* remediation of contaminated groundwaters; some of these included: NANOFeR 25s, Carbo-iron (Figure 23), biomagnetite and nano-goethite (Bosch et al., 2010; Byrne et al., 2015; Mackenzie et al., 2012; "Nanoremediation Nanotechnology for Contaminated Land Remediation," n.d.; Newsome et al., 2019, 2016; Tiraferri et al., 2017). NANOFeR 25s and Carbo-iron were used in (chapters 5 and 6). NANOFeR 25S is an aqueous dispersion of nZVI particles suspended in a biodegradable surfactant ("NANOFeR 25S | NANOIRON," n.d.) and Carbo-Iron is a composite of 10-25 wt% nZVI particles fixed within activated carbon colloids (d50 particle size 0.8 μm) (Bleyl et al., 2012). Although Carbo-iron demonstrates enhanced mobility and stability in suspension compared to standard nZVI, Carbo-Iron can still be further improved via the addition of surfactant stabilisers, such as carboxymethylcellulose. Carbo-Iron was successful in laboratory tests and in field use as a treatment for a tetrachloroethene (PCE) contaminated site in Lower Saxony, Germany (Mackenzie et al., 2016) and both NanoFeR 25S and Carbo-Iron were successfully used as a treatment for Tc(VII) contamination in batch microcosm experiments (Newsome et al., 2019).

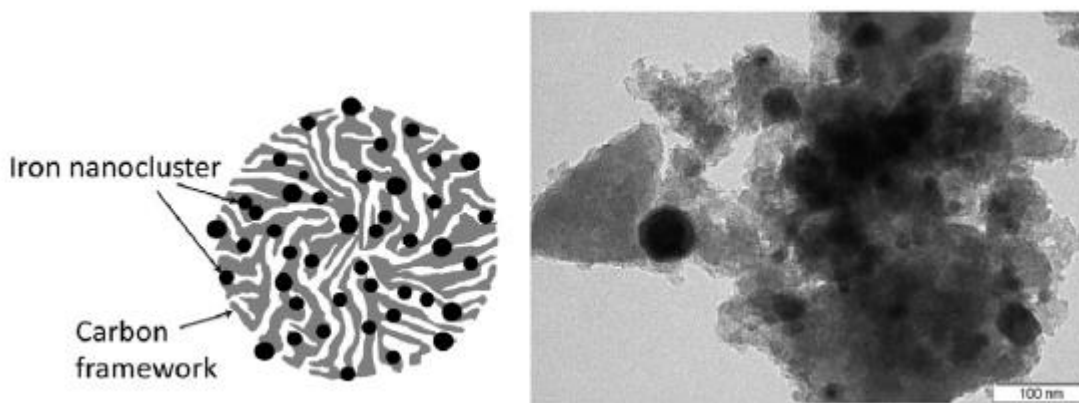


Figure 23: Cartoon schematic (Left) and TEM (Right) of Carbo-Iron® (bar 100 nm). Taken from (Mackenzie et al., 2016).

2.5 Uranium: Nuclear and Biogeochemistry

2.5.1 Nuclear U Chemistry

U is a naturally occurring, radioactive actinide element with atomic number 92. It has 6 valence electrons and has been isolated in the metallic (0), +2, +3, +4, +5 and +6 oxidation states (MacDonald et al., 2013). Despite its discovery in 1789 (by W.H. Klaproth), it wasn't until the discovery of radioactivity in 1896 (H. Becquerel) and of nuclear fission in 1938 (O. Hahn and F. Strassman), that U occupied a central role in modern day science. There are three naturally occurring U isotopes: ²³⁸U (99.2762 %), ²³⁵U (0.7182 %) and ²³⁴U (0.0056 %). Whilst ²³⁸U is fertile (not fissionable, but can be converted into a fissile material via neutron absorption), ²³⁵U is fissile (capable of sustaining a nuclear

fission chain reaction, Figure 24); they both have long half-lives (4.46 billion and 704 billion years respectively) (“Institute for Energy and Environmental Research,” n.d.), and ultimately gain stability at the end of their decay chain as Pb. U occurs naturally in the subsurface at ppm concentrations and is present at elevated concentrations in U bearing minerals such as uraninite. Here, it is extracted from its ore and used industrially in the civilian sector as fuel for nuclear power stations, and in the military sector in nuclear weapons production and as a high density penetrator munition. All three uses can lead to U subsurface contamination.

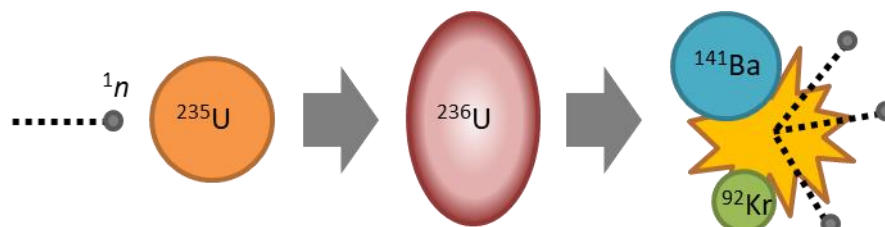


Figure 24: Induced fission of ^{235}U . A neutron is absorbed by the ^{235}U nucleus, it momentarily forms an excited, and unstable ^{236}U nucleus. In turn, this ^{236}U nucleus splits into lighter fission products ^{141}Ba and ^{92}Kr , releasing some more neutrons, energy and gamma rays (not shown).

2.52 U Biogeochemistry

U is the most significant radionuclide by mass in radioactive wastes and is therefore significant in many radioactive contaminated land scenarios. U is not only radioactive, but it also has ecological concerns related to its chemotoxicity as a heavy metal. Under normal environmental conditions U predominantly exists in two oxidation states, either as soluble U(VI) or as sparingly soluble U(IV). Hexavalent U, as the ubiquitous uranyl ion $[\text{U}(\text{VI})\text{O}_2]^{2+}$, dominates under oxidising conditions. The uranyl(VI) structure is well studied using both theoretical and experimental approaches. Its collinear, axial U-O bonds have a formal bond order of three, resulting in short, chemically robust bonds; other ligands bind around the equatorial plane and are often weakly coordinated relative to the dioxygenyl bonds. Accordingly, most uranyl chemistry takes place around the equatorial ring. Free uranyl(VI) dominates under acidic conditions ($\text{pH} < 5$), as pH increases the free uranyl ion is highly stabilised in the presence of carbonate ligands as UO_2CO_3 , $\text{UO}_2[\text{CO}_3]_2^{2-}$ and $\text{UO}_2[\text{CO}_3]_3^{4-}$ (Grenthe et al., 1992). Uranyl carbonates have an increased solubility and thus mobility in solution (Runde, 2000), and account for $\geq 90\%$ of dissolved U in ocean waters (Choppin, 1989) (Figure 25). In the absence of carbonate, uranyl hydroxide species dominate higher pH systems (Choppin, 2006). The migration rates of aqueous uranyl ions in aquifers are significantly retarded as the uranyl ion adsorbs strongly to Fe- and Mn-(hydr)oxides, organic molecules, silicates and some clays (Borovec, 1981; Brookshaw et al., 2015; Ching-kuo and Langmuir, 1985; Gu et al., 2005; Langmuir, 1978; Newsome et al., 2014a; Winstanley et al., 2019). At elevated pH , the formation of U(VI) colloids at significantly increases mobility (Bots et al., 2014).

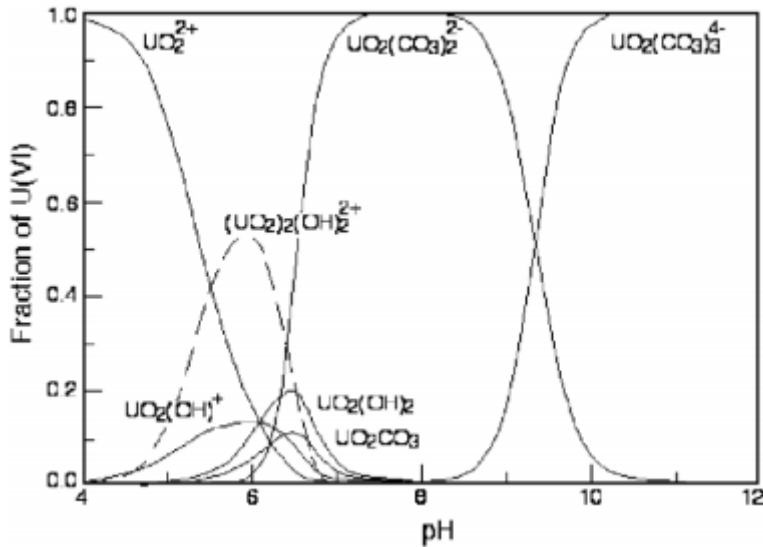


Figure 25: Speciation diagram of $U(VI)O_2^{2+}$ as a function of pH in natural waters. Taken from (Choppin, 2006)

Under reducing conditions U chemistry is dominated by relatively insoluble U(IV) minerals typically uraninite (Derek R. Lovley and Phillips, 1992) or monomeric UO_2 (Bernier-Latmani et al., 2010). Under ambient conditions the uranyl(VI)/U(IV) redox couple is similar to the Fe(III)/Fe(II) redox couple and thus the enzymatic reduction of uranyl(VI) and Fe(III) often occur concomitantly (Figure 26)(Newsome et al., 2015b, 2014a, 2014b). Indeed, at sites with elevated U concentrations in naturally reducing zones, the US Department of Energy (DoE) have found relatively insoluble U(IV) dominating U speciation (Campbell et al., 2012). Under silicate rich and alkaline conditions, such as those present in nuclear fuel storage and disposal, U(IV)-silicate colloids can form (Neill et al., 2019, 2018). They represent a possible pathway for U migration, despite being in the less soluble, U(IV) oxidation state.

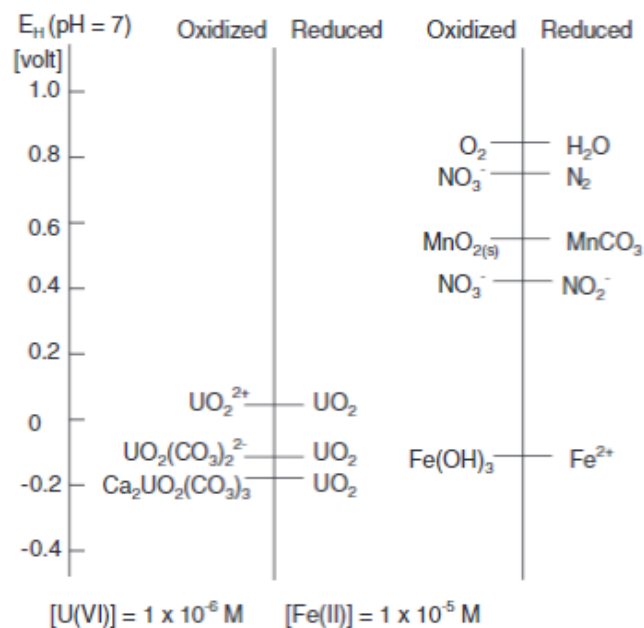
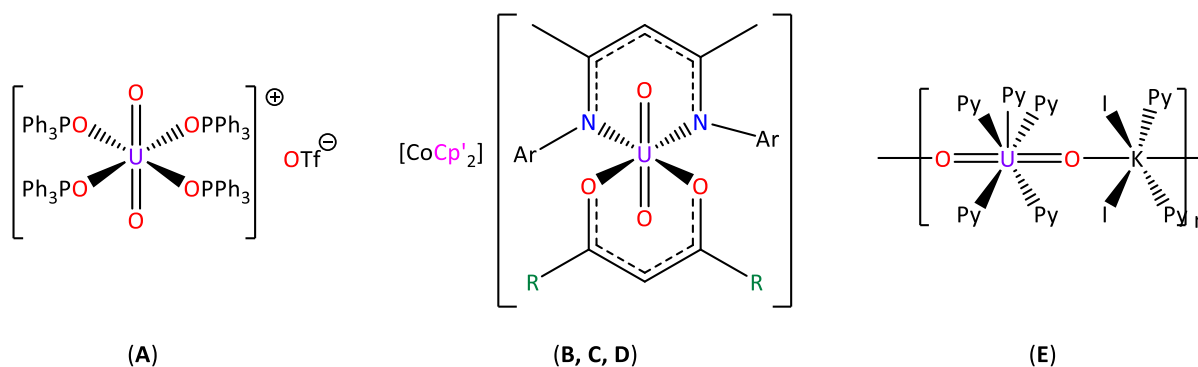


Figure 26: Redox couples for U(VI) species compared to environmentally relevant redox couples within sediments at circumneutral pH. Taken from (Ginder-Vogel and Fendorf, 2007).

2.53 The Elusive U(V)

Although U(VI) and U(IV) are the most environmentally relevant oxidation states of U, pentavalent U, U(V), may also be present in much lower abundances. Naturally occurring U(V) is uncommon but exists in the mixed valence mineral wyartite and in the mixed valence U-oxides: U_3O_8 and U_4O_9 , in all cases U(V) is incorporated in a non-uranyl type coordination (Burns and Finch, 1999; Conradson et al., 2004; Kvashnina et al., 2013). U(V), as uranate-like species have been identified in the presence of Fe-bearing phases, typically by incorporation of U(V) into the mineral lattice in a uranate type coordination (Collins and Rosso, 2017; Ilton and Bagus, 2011; Kerisit et al., 2016; Pidchenko et al., 2017; Roberts et al., 2017; Sun et al., 2018; Tsarev et al., 2017, 2016a). Here, the presence of U(V) is indicative of a single electron transfer mechanism to U(VI) in Fe rich environmentally relevant systems, which has led to stabilisation of U(V) in the resultant Fe(II)-bearing mineral phases for up to 142 days (Pidchenko et al., 2017; Roberts et al., 2017). U(V) compounds in a uranate-like orientation are found in more symmetric coordination environments as cubic or octahedral species where coordination numbers are generally 6. Uranate(V) U-O bond lengths are reported as 2.11-2.16 Å for the MUO_3 series, where M is a group 1 alkali metal ions (Li^+ , Na^+ , K^+ and Rb^+) (Kemmler, 1965; Soldatov et al., 2007), however upon incorporation into Fe minerals these bond lengths extend to 2.17-2.19 Å (Pidchenko et al., 2017; Roberts et al., 2017).

Unlike other actinyl(V) species such as $[Np(V)O_2]^+$ and $[Pu(V)O_2]^+$, which are expected to be environmentally significant (Choppin and Wong, 1998; Renshaw et al., 2005; Runde, 2000), the uranyl(V) cation is relatively unstable under environmentally relevant conditions due to disproportionation reactions which form more stable uranyl(VI) and U(IV) (Arnold et al., 2009; Ekstrom, 1974). Recent publications, however, have demonstrated an ever-broadening field of stability for uranyl(V) in environmental settings. Indeed, in aqueous media, uranyl(V) is reported as a transient species stabilised for up to 2 weeks afforded by complexation with e.g. CO_3^{2-} species (Cohen, 1970; Docrat et al., 1999; Madic et al., 1983; Wester and Sullivan, 1980), and moreover, it was recently stabilised in water for a period of months (Faizova et al., 2018). Compared to uranyl(VI) species, uranyl(V) species demonstrate elongated and weaker U=O bonds: 1.9 Å in uranyl(V) vs. 1.8 Å in uranyl(VI) (Docrat et al., 1999; Ikeda et al., 2007). This is attributable to increased electron density at the U(V) centre which firstly weakens the electrostatic forces of attraction between the positively charged U centre and the negatively charged O^{2-} ligands, and secondly adds an electron to the previously unpopulated, anti-bonding, lowest unoccupied molecular orbital. Strictly anaerobic synthetic chemistry has isolated and characterised several uranyl(V) compounds; these are often stabilised through careful ligand choices (Figure 27)(Berthet et al., 2003; Natrajan et al., 2006). The disproportionation mechanism by which uranyl(V) finds stability is proposed to proceed via a uranyl(V)-uranyl(V) dimer, encounter complex (Collins and Rosso, 2017; Ekstrom, 1974).



(A) Tf = F₃CSOOO⁻; (B) R = Me, Cp' = C₅Me₅; (C) R = Ph, Cp' = C₅Me₅; (D) R = CF₃, Cp' = C₅H₅; (E) Py = C₅H₅N

Figure 27: Examples of isolated and characterised [UO₂]⁺ compounds. Image modified from [(Arnold et al., 2009; Berthet et al., 2003; Natrajan et al., 2006)].

2.54 U mobility at the Sellafield site

Well monitoring at the Sellafield site shows that the mobility of U is mostly contained within the Separation area (Figure 9). Here, alpha activity is localised to 5 wells in the north-west corner of the Separation area, where total alpha activity has been slowly declining year on year, this demonstrates that U transport is largely governed by sorption processes (Sellafield Ltd., 2015; Stamper et al., 2014).

2.55 Microbial Respiration of U

In the environment, microbial activity plays an important role in governing U speciation and mobility. Indeed, reduction of mobile U(VI) to immobile U(IV) phases can be achieved via microbial metabolism and it has been proposed as a remediation technique for U contaminated waters (Gorby and Lovley, 1992; Lovley et al., 1991). After bioreduction, U speciation is often stated to be uraninite, UO₂ (Gorby and Lovley, 1992; Derek R. Lovley and Phillips, 1992; Suzuki et al., 2002), although, recently a range of other, non-uraninite U(IV) end-points have been identified (Alessi et al., 2012; Bernier-Latmani et al., 2010; Bhattacharyya et al., 2017; Istok et al., 2016; Newsome et al., 2015a). Whilst the abiotic reduction of U(VI) to U(IV) can also occur in the presence of Fe(II)-containing phases (Brookshaw et al., 2015; Ilton et al., 2004; Latta et al., 2012a), it is generally accepted that the dominant reduction mechanism for U(VI) under normal environmental conditions proceeds via microbial metabolism (Bargar et al., 2013; Williams et al., 2013). *Geobacter sp.* and *Shewanella sp.* were the first microbes proven capable of enzymatically reducing U(VI) to precipitate U(IV) biominerals (Lovley et al., 1991). This was soon followed by a series of other species in the 1990's: *Desulfotomaculum sp.* (Tebo and Obratzsova, 1998), *Desulfovibrio sp.* (D R Lovley and Phillips, 1992), and *Clostridium sp.* (Francis et al., 1994). Since then, a plethora of U(VI) reducing prokaryotes have been documented as shown in Figure 28 (Williams et al., 2013).

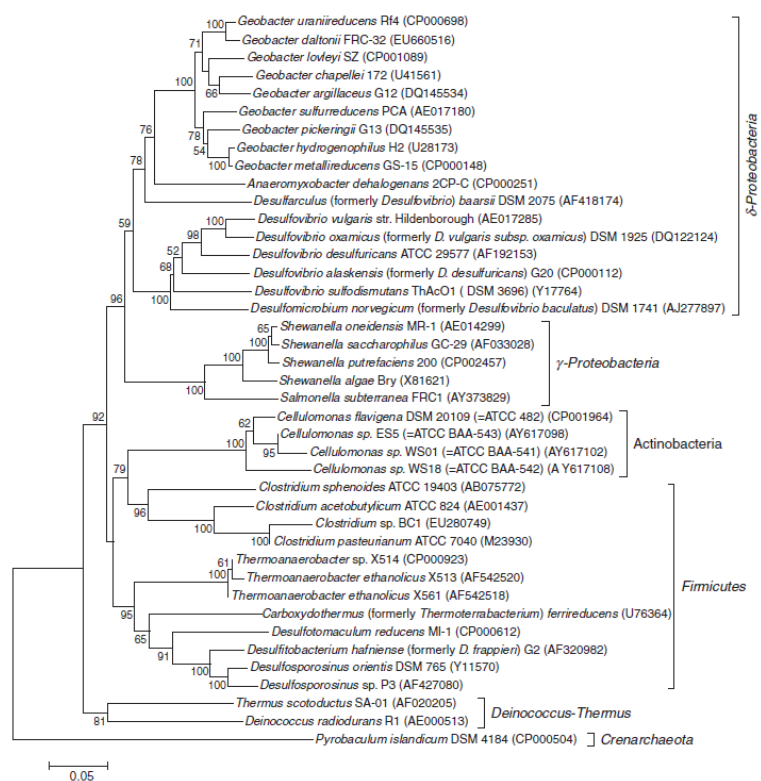


Figure 28: 16S rRNA based phylogenetic tree of U(VI)-reducing prokaryotes. Taken from (Williams et al., 2013).

The mechanisms of U(VI) reduction varies between organisms, and some species may have multiple electron pathways. Both *Geobacter* and *Shewanella* species can transfer electrons from the cell surface to U(VI) via c-type cytochromes (Lloyd, 2003) and whilst the electron transport mechanism(s) for extracellular electron transfer by *Geobacter* and *Shewanella* to Fe(III) are well described (see section 2.43 Dissimilatory Iron-Reducing Bacteria: *Geobacter* and *Shewanella*), the validity of these same mechanism(s) for the reduction of radionuclides are studied less comprehensively. In *Geobacteraceae*, U(VI) bioreduction requires physical contact through the extension of extracellular pili, although some U also precipitates within the periplasm (Figure 19) (Cologgi et al., 2011; Reguera, 2012; Shelobolina et al., 2007). In contrast, *Shewanella* can not only reduce U(VI) via direct contact, but it can also use extracellular electron shuttles to indirectly reduce U(VI) (Figure 17) (Suzuki et al., 2010). In *S. oneidensis* MR1 the Mtr pathway is essential for the reduction of U(VI) (Marshall et al., 2006). Existing studies have used mutants that are lacking in outer membrane multiheme cytochromes MtrC and OmcA, found a decreased ability to reduce U(VI) (Cherkouk et al., 2016; Marshall et al., 2006); in contrast, the ability of these mutants to reduce Tc(VII) remained largely unaffected (Marshall et al., 2008).

The enzymatic reduction mechanism of U(VI) is a topic of high debate, in some cases it is proposed to be mediated by a single electron transfer forming an intermediary U(V) state which disproportionates to more stable U(IV) and U(VI) (Equation 6) (Jones et al., 2015; Renshaw et al., 2005). Although U(V) intermediates have been demonstrated in *G. sulfurreducens* using fluorescence spectroscopy, XAS and Density Functional Theory (DFT) (Jones et al., 2015; Renshaw et al., 2005; Sundararajan et al., 2008), and in a multispecies biofilm using the combined use of fluorescence spectroscopy and confocal laser scanning microscopy (Grossmann et al., 2009), the inherent instability of the uranyl(V) ion means that comprehensive evidence of the intermediate had not been presented, and had not been well

documented outside the *Geobacter* genus; thus chapter 4 discusses uranyl(VI) reduction by model Fe(III)-reducing bacterium *S. oneidensis* MR1 and demonstrates, unequivocally the existence of a U(V) intermediate (Vettese et al., 2020).

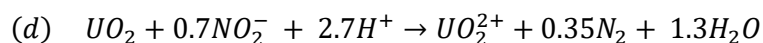
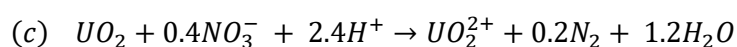
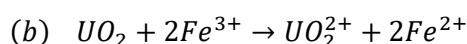
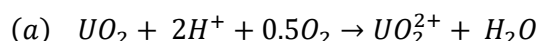


Equation 6: The disproportionation of uranyl(V).

The bioreduction of U(VI) to sparingly soluble U(IV) as a means of remediating U contaminated groundwater has been studied extensively in laboratory experiments, and has been extended to field scale test sites in the USA (Anderson et al., 2003; Istok et al., 2016, 2004; Vrionis et al., 2005; Williams et al., 2011; Wu et al., 2006). Of particular significance are the field-scale tests conducted at the Rifle site, Colorado. Here, the capacity for aqueous U removal from contaminated groundwater by indigenous Fe(III)-reducing bacteria was assessed over a 3 month period (Anderson et al., 2003). The experiment consisted of 20 injection wells (acetate 1 or 3 mM) up-stream of 15 monitoring wells; in as little as 9 days U(VI) and Fe(III) levels decreased concurrently and in some cases U(VI) levels dropped below the EPA prescribed levels of 0.18 μ M within 50 days. The *Geobacteraceae* family played a key role, representing up to 40 % of the microbial community during key periods. Areas of maximum U(VI) and Fe(III) reduction correlated with maxima in the *Geobacteraceae* 16S rRNA gene sequences across multiple separate areas, possibly due to non-homogeneous distribution of acetate within the aquifer (Vrionis et al., 2005). However once Fe(III) concentrations became depleted, sulphate reducers, as the next electron acceptor dominated and, U removal rates dropped. After the bioreduction experiment was complete, the ingress of oxygen into the sediments led to the re-oxidation of the bioreduced U and this led to several conclusions. Whilst the first confirmed the role of metal-reducing microorganisms in a real-system setting, the second highlighted that sustained bioremediation could not be achieved due to reoxidation processes (Senko et al., 2002). Ultimately, this meant that bioreduction as a method of remediation for U contaminated sediments needed further work before it could be used on an industry wide scale.

2.56 The Longevity of U(IV) end-points

In the presence of oxidising agents bioreduced U(IV) phases are highly susceptible to oxidative remobilisation (Equations 7a-d). Common oxidants include dissolved oxygen (Abdelouas et al., 1999; Bi et al., 2013; Komlos et al., 2008b; Law et al., 2011; Moon et al., 2007; Newsome et al., 2015b; Senko et al., 2002), nitrate, and denitrification intermediates (Beller, 2005; Finneran et al., 2002; Istok et al., 2016, 2004; Law et al., 2011; Moon et al., 2009; Newsome et al., 2015b; Senko et al., 2002), Fe-oxides (Ginder-Vogel et al., 2010, 2006; Nevin and Lovley, 2000; Sani et al., 2005, 2004; Spycher et al., 2011), Mn-oxides (Liu et al., 2002; Wang et al., 2014; Zachara et al., 2002) and oxidised humic matter (Newsome et al., 2015a).



Equations 7a-d: Chemical oxidation of U(IV) by: (a) O₂, (b) Fe(III), (c) nitrate, and (d) nitrite.

Often these oxidants can be found as co-contaminants at nuclear facilities where the environmental biogeochemistry is complex and dynamic. Take, for example nitrate, which is often present in high concentrations due to the use of nitric acid in plant operations (Fields et al., 2005; Law et al., 2010a). Here, high levels of nitrate can severely hinder the biostimulation potential of an environment via a combination of several mechanisms. As nitrate has a relatively high reduction potential, it often out-competes other contaminant species as an electron donor under anaerobic conditions (Abdelouas et al., 1998; Li and Krumholz, 2008), this may retard or even completely inhibit indirect reductions by chemically oxidising the relevant middle species (*i.e.* by oxidising Fe(II) to Fe(III) thus inhibiting Tc(VII) reduction) (Law et al., 2010a). Nitrate has been shown to not only lower U removal rates during bioreduction (Senko et al., 2002), but furthermore, decrease microbial diversity and activities at low pH (≤ 5) conditions (Fields et al., 2005; Nevin et al., 2003; Petrie et al., 2003a). Whilst the mechanisms of nitrate-mediated U(IV) oxidation occur biotically (Newsome et al., 2015b), the denitrification intermediates oxidise U(IV) via abiotic pathways (Senko et al., 2002). Dissimilatory nitrate reduction and denitrification reactions produce OH^- and CO_3^- which create a highly oxidising environment that can chemically re-oxidise U(IV) to U(VI), reversing the desired effects of U immobilisation (Law et al., 2010a; Senko et al., 2002; Thorpe et al., 2012a).

The rate and extent of U(IV) re-oxidation is highly variable; this is largely due to the wide diversity of possible environmental conditions and oxidant concentrations. For example, bioreduced sediments spiked with nitrate have resulted in 3-97 % U remobilisation, suggesting large deviations in the data (Law et al., 2011; Moon et al., 2007). Although by comparison, multiple examples studying the aerobic agitation of reduced sediments in open conical flasks have reported complete U oxidation within 60 days (Law et al., 2011; Newsome et al., 2015b, 2015c). Furthermore, flowing column experiments using environmentally relevant dissolved oxygen concentrations (20 % O_2 / 0.27 mM) similarly, found almost complete U re-oxidation within 54 days (Moon et al., 2007). Interestingly, a study by Newsome *et al.* found that varying U concentration and period of ageing showed little differences in U(IV) recalcitrance; but in fact, it was the effect of maintained electron donor that significantly hindered oxidative U(IV) re-oxidation (Newsome et al., 2015b). Given this, if we want to successfully treat U contaminated sites using bioremediation, we must find suitable electron donors which can immobilise contaminants over long timescales in a safe, efficient and effective manner.

2.57 U Interactions with Fe

As mentioned previously, aqueous U(VI) sorbs to the surface of many Fe-(hydr)oxide surfaces (Moyes et al., 2000; Waite et al., 1994; Winstanley et al., 2019), but more stable U(IV) end points can be achieved via U incorporation into or sorption onto Fe-oxides. After sorption to the surface, U(VI) can be reduced enzymatically (Law et al., 2011) or abiotically (Ilton et al., 2004; Latta et al., 2012a) to form chemically incorporated species (Crane et al., 2011; Latta et al., 2012b; Marshall et al., 2015; O'Loughlin et al., 2003; Pidchenko et al., 2017; Roberts et al., 2017; Van Veelen et al., 2014). Moreover, when U(VI) is present during the formation of environmentally relevant Fe(II/III) (oxyhydr)oxides (such as magnetite, goethite, hematite, vivianite), it is both reduced and stabilised via incorporation mechanisms (Law et al., 2011; Marshall et al., 2014). Here, a plethora of recent work has shown that the U is present in a pentavalent oxidation state, often in a uranate-like structure (Figure 29) (Marshall et al., 2015; Pidchenko et al., 2017; Roberts et al., 2017; Tsarev et al., 2017, 2016b).

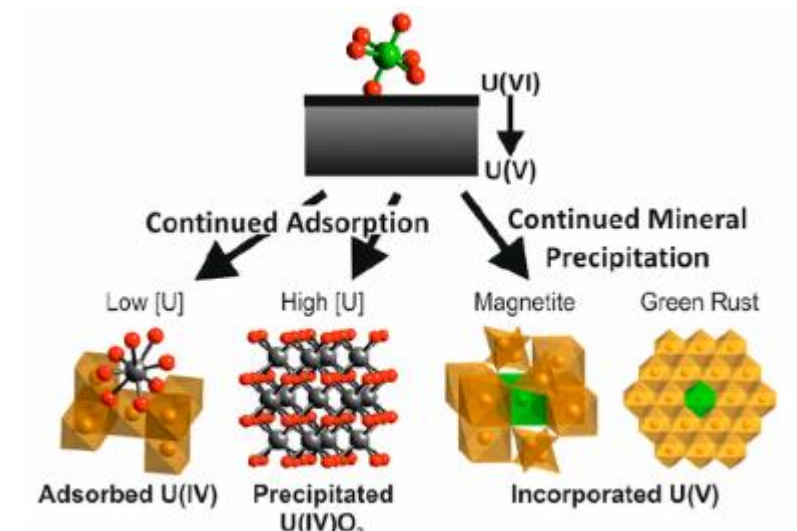


Figure 29: U adsorption, precipitation and incorporation in Fe rich systems. Taken from (Roberts et al., 2017).

Another Fe-based method for radionuclide immobilisation uses nZVI; here it can serve as an *in-situ* amendment or as a permeable reactive barrier. The short term reduction properties of U by nZVI are particularly well studied in the lab, field and in computational models (Farrell et al., 1999; Morrison et al., 2001; Simon et al., 2003; Wang and Salvage, 2005), they suggested a rate of removal within a matter of hours depending on reaction conditions (Crane et al., 2011; Tsarev et al., 2017, 2016a). However, the longevity of simple nZVI treatments yielded poor results as the partial re-release of U was reported after just one week of treatment with nZVI (Crane et al., 2011).

Two of the enhanced ZVI treatments designed as a part of the NanoRem project (NanoFeR 25s and Carbo-Iron) were used in this study (chapters 5 and 6) to assess their compatibility for the co-treatment of U and Sr contaminated sediments. Whilst there are no direct studies using Carbo-Iron or NANOFeR 25s to treat U; nZVI supported on activated carbon frameworks has previously been suggested for the remediation of metal contaminants (Ponder et al., 2001). Moreover, U(VI) can adsorb to activated carbon (Abbasi and Streat, 1994; Caccin et al., 2013; Han et al., 2018; Kütahyalı and Eral, 2004; Qadeer et al., 1992; Qadeer and Hanif, 1994; Saleem et al., 1992), biochars (Ashry et al., 2016; Dong et al., 2017; Jang et al., 2018; Jin et al., 2018; Kumar et al., 2011), and graphene oxides via non-redox processes under appropriate conditions (Sun et al., 2015).

2.58 U Phosphates

Another alternative U remediation strategy involves the precipitation of uranium-phosphate minerals such as ningyoite [$U_2(PO_4)_3 \cdot 12H_2O$] and autinite [$Ca(UO_2)_2(PO_4)_2 \cdot 10-12H_2O$]. U-phosphates can be found in the natural environment when U and phosphate are both present at elevated concentrations (Bernier-Latmani et al., 2010; Buck et al., 1996; Jerden and Sinha, 2003; Murakami et al., 1997; Pinto et al., 2012). U phosphates are exceedingly insoluble, thermodynamically stable and relatively insensitive to oxidative remobilisation (Dzik et al., 2017; Finch and Murakami, 1999; Jensen et al., 2002; Latta et al., 2016; Macaskie et al., 1992; Macaskie and Dean, 1985a, 1985b, 1984; Michel et al., 1986) and as a result they have been suggested as a matrix for storage of radioactive wastes (Brandel et al., 2001; Fuller et al., 2002).

The chemical stimulation of U-phosphate precipitation via the addition of simple phosphates occurs rapidly and causes the clogging of injection wells (Wellman et al., 2006). This problem can be

overcome through the *in-situ* addition of slow-release phosphates which allow sufficient time for the phosphate ions to spread to a wider environment before precipitation occurs (Macaskie et al., 1992; Paterson-Beedle et al., 2010; Wellman et al., 2009). Accordingly, the long-term bio-mineralisation of radionuclides using organo-phosphates proposes a particularly promising future. In this case, indigenous bacteria slowly break down the organophosphate bond, releasing a carbon based electron donor, which can be used as an energy source for the local bacteria; moreover, the released orthophosphate can precipitate U-phosphates via microbial metabolism (as U(IV) or U(VI)) (Giammar et al., 2014; Newsome et al., 2015a, 2015c; Pan et al., 2016; Z. Shi et al., 2009; Wang et al., 2017; Wen et al., 2018). This enzymatic process was first demonstrated using *Citrobacter* sp.; whereby, the *Citrobacter* cells overproduced a phosphatase enzyme which liberated HPO_4^{2-} from glycerol-2-phosphate and lead to the bioaccumulation of cell bound MHPO_4 (M = U, Sr, Cd, Pb, Cu). In column studies, this system could deposit up to 900% of its cellular dry weight as accumulated U in the form of HUO_2PO_4 (Macaskie et al., 1992; Macaskie and Dean, 1985a, 1985b, 1984; Michel et al., 1986), and the results could be further enhanced by addition of NH_4Ac into the solution (Yong and Macaskie, 1995). Numerous other microbial species can precipitate U when supplied with an organophosphate compound; it has been executed successfully in laboratory experiments (Beazley et al., 2011, 2007; Green et al., 2013; Macaskie et al., 1992; Newsome et al., 2015a; Shelobolina et al., 2009; Thomas and Macaskie, 1996; Yung and Jiao, 2014) and biogenic U-phosphates have been identified in US DoE sites at Fernald, Ohio and Hanford, Washington (Buck et al., 1996; Catalano et al., 2006; Singer et al., 2009; Stubbs et al., 2009). Here, Martinez *et al.* successfully identified microbial communities capable of hydrolysis of organophosphates (specifically glycerol-2, and -3-phosphates) in sediments from the U.S. DoE Oak Ridge Field Research Centre. Demonstrating the possibility of using organophosphates as a method for *in-situ* bioremediation of contaminated sediments (Martinez et al., 2014).

Interestingly, U(VI) reduction coupled to phosphate biomineralisation can also produce U(IV) phosphates, these have elevated thermochemical stability and are thus are less soluble and less prone remobilisation than their hexavalent counterparts (Boyanov et al., 2011; Cleary et al., 2019; Khijniak et al., 2005; Michel et al., 1986; Muto, 1965; Newsome et al., 2015c, 2015a; Rui et al., 2013). Although a possible limitation to the longevity of radionuclide-phosphates is that under phosphate-limited conditions bacteria may potentially “mine” uranyl phosphates, harvesting the phosphate and liberating U back into solution (Katsenovich et al., 2012; Rui et al., 2013; Smeaton et al., 2008).

2.59 U Reduction During Sulphate-Reducing Conditions

Sulphate-reducing bacteria (SRB) can enzymatically reduce soluble uranyl(VI) to relatively insoluble U(IV) (Derek R. Lovley et al., 1993) and furthermore, aqueous sulphide, generated by SRBs can abiotically reduce uranyl(VI) to immobile U(IV) (Hyun et al., 2014; Jensen, 1958). Iron-sulphide minerals (*i.e.* mackinawite $[\text{FeS}]$) can buffer the re-oxidation and remobilisation rates of U by scavenging oxidants and acting as a reducing agent (Abdelouas et al., 1999; Bi et al., 2013; Carpenter et al., 2015; Istok et al., 2016; Moon et al., 2009). Despite this a field-scale study demonstrated that excess sulphate consumed primary electron donors, as a result this created less effective U removal rates. Furthermore, the high levels of reduced U(IV), Fe(II) and sulphide led to the clogging of injection wells, which suggests that sulphate-reducing conditions may in fact compromise maintained U immobilisation strategies (Williams et al., 2011). There is conflicting evidence from various studies which suggest that inducing sulphate reducing conditions can affect the bioreduction rates, extents and longevity of bioreduced U in either positive or negative ways (Converse et al., 2013; Komlos et

al., 2008a; J. Luo et al., 2007; Moon et al., 2009; Spear et al., 2000; Williams et al., 2011). To help clarify this, some of the work carried out in chapter 5 assesses the effects of inducing sulphate reducing conditions for U and Sr bioremediation.

2.510 U Interactions with Slow Release Electron Donors

Where many studies using simple electron donors such as acetate, lactate or ethanol have found the need for repeated application of fluid, slow release electron donors remain in the subsurface for longer whilst they slowly degrade over extended periods of time; they thus sustain reducing conditions and minimise the need for repeat amendments (Adamson et al., 2003; Faybishenko et al., 2008; Tang et al., 2013; Watson et al., 2013; Zhang et al., 2015). MRC (as discussed in Chapter 5) is such a compound, it is a cysteine-based organosulphur ester compound with a carbon backbone (glycerol and sorbitol) embedded in a polylactate matrix (Regenesis, 2015). The active component (sorbitol hexacysteinate) acts as a direct reducing agent and its hydrolysis provides lactic acid which can act as an electron donor to stimulate the indigenous microbial community. This slow-release property can last an estimated 12-18 months after injection. MRC has been proven in both the lab and in field-scale case studies for Cr contaminated aquifers (Regenesis, 2016a, 2016b), and more recently as a long-term immobilization treatment for Tc (Newsome et al., 2017). To the best of our knowledge MRC has not yet been used to treat U or Sr contaminated sediments and hence it has been used in Chapter 5.

2.6 Strontium Nuclear and Biogeochemistry

2.61 Nuclear Sr Chemistry

The element strontium (Sr) is a alkaline earth metal, and like all alkaline earth metals Sr occurs in minerals as the Sr^{2+} ion, rather than as a free metal. First discovered in 1790 in Strontian, Scotland, it was not isolated until 1808. Sr is reasonably abundant, representing ~0.04 % of the Earth's crust as a mixture of 4 stable isotopes ^{84}Sr , ^{86}Sr , ^{87}Sr and ^{88}Sr with near abundances 0.56%, 9.86 %, 7.00 % and 82.58 %; although these numbers vary as ^{87}Sr is the stable daughter of naturally occurring, ^{87}Rb decay (RSC, 2018). 16 other radioactive isotopes of Sr can be synthesised, of these, ^{89}Sr ($t_{1/2}$ 50.5) and ^{90}Sr ($t_{1/2}$ 28.8 y) are of most relevance as they are the by-products of nuclear fission reactions. ^{89}Sr is used medically in the palliation of bone pain for cancer patients (Bauman et al., 2005; Brundage et al., 1998) and to treat osteoporosis (a condition that weakens bones). ^{90}Sr , also known as radiostrontium, is regarded as the most hazardous isotope; it is a high yielding (6 %) fission product with a half-life of 28.8 y, that decays by beta emission to ^{90}Y ($t_{1/2}$ 64.2 h). Due to the chemical similarity of Sr^{2+} and Ca^{2+} ions, some Sr is found naturally, for example, as a trace contaminant in bones (which are mostly composed of the Ca-phosphate mineral, hydroxyapatite [$\text{Ca}_5(\text{PO}_4)_3(\text{OH})$]), although it has no physiological function at the concentrations present (Wasserman, 1998). In a similar fashion, the ingestion of ^{90}Sr is particularly harmful to animals, its bone-seeking properties lead to its' substitution for Ca in bones, this then causes irradiation of bone marrow; increasing the chances of contracting bone cancer or leukaemia (Pors Nielsen, 2004). Because ^{90}Sr , from nuclear incidents poses a considerable health risk, the bioremediation of ^{90}Sr contaminated systems are of considerable interest.

2.62 Bioremediation of Sr

Under normal environmental conditions ^{90}Sr is present as the aqueous Sr^{2+} cation which is highly insensitive to redox changes, its mobility is thus largely governed by sorption to negatively-charged mineral surfaces and its geochemical behaviour is similar to that of Ca^{2+} . At low ionic strengths and

near-neutral conditions Sr^{2+} sorbs to mineral surfaces which have a large cation exchange capacity and surface area, mainly aluminosilicates, Fe-oxides and clays (Balek et al., 1996; Carroll et al., 2008; Chorover et al., 2008; Dyer et al., 2000; Higgo, 1987; Karasyova et al., 1999; O 'day et al., 2000; Patterson and Spoel, 1981; Saunders and Toran, 1995; Torstenfelt et al., 1982). Here, it often forms outer-sphere complexes to minerals in competition with other cations (Figure 30) (Axe et al., 1998; Dyer et al., 2000, 1999; Dyer and Umar, 1999; Fuller et al., 2016; O 'day et al., 2000; Thorpe et al., 2014, 2012b; Wallace et al., 2012). Sr sorption to clays is optimal at circumneutral pH, when the pH drops below the point of zero charge limited sorption is expected due to repulsion of the Sr^{2+} cation and its hydrated sphere to the net positively charged clay surface. Furthermore, ionic strength also affects Sr^{2+} sorption due to cation competition (Wallace et al., 2012). Sr bound via outer sphere sorption is susceptible to desorption, and thus remobilisation (Handley-Sidhu et al., 2014, 2011; Wallace et al., 2012). More recalcitrant Sr^{2+} phases can be formed in several ways. First of all, under highly alkaline conditions ($\text{pH} > 12.5$), Sr^{2+} (as SrOH^+) forms inner-sphere complexes on mineral surfaces where it does not desorb even at high ionic strengths (Fuller et al., 2016). Alternatively, Sr^{2+} can isomorphically substitute for Ca^{2+} or incorporate into forming Ca-carbonate or Ca-phosphate minerals such as calcite (Fujita et al., 2004) or (hydroxyl-)apatite (Cleary et al., 2019; Handley-Sidhu et al., 2011; Macaskie and Dean, 1985b) respectively. Simple electron donors (such as acetate, lactate or glycerol) have a limited effect on Sr removal from solution (Brookshaw et al., 2016; Cleary et al., 2019; Thorpe et al., 2012b).

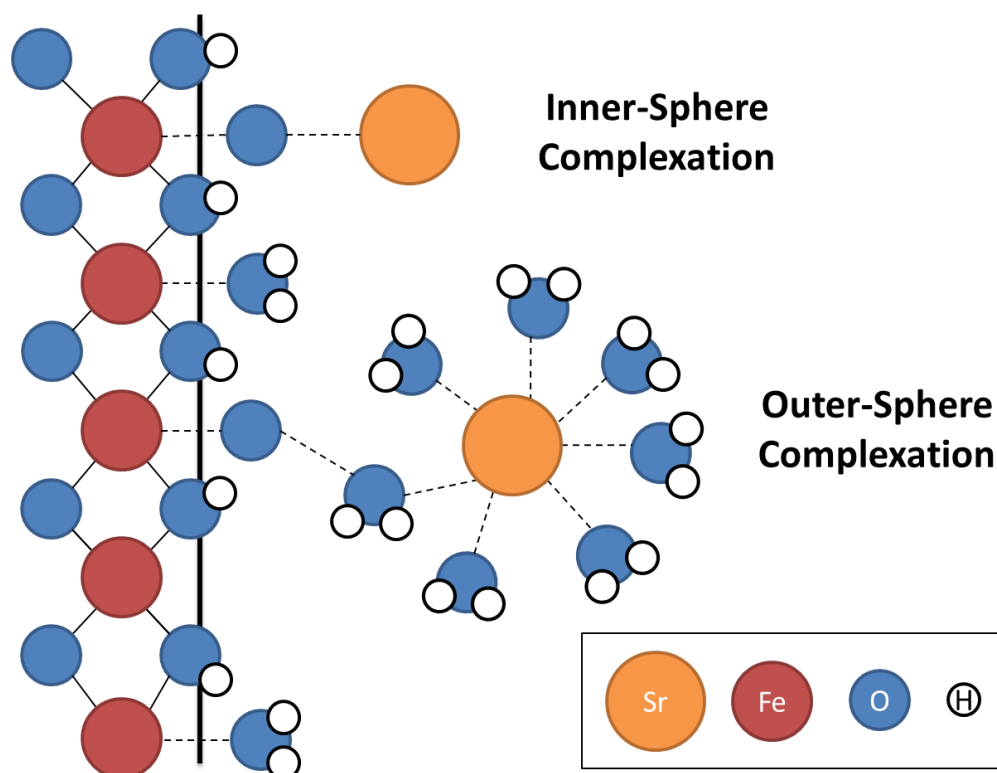


Figure 30: Sr sorption by inner-sphere and outer-sphere complexation.

2.63 Sr Mobility at the Sellafield Site

Sr^{2+} transport through the Sellafield site is mostly contained within the Separation area (Figure 9) and the predominant source of Sr^{2+} arises from tanks containing corroded MAGNOX fuel cladding

("Sellafield Integrated Waste Strategy," 2009). Here, the leachate is present with a high pH in the range of 9-11.5 and high ionic strengths, and as a result Sr mobility is expected to be dictated by outer-sphere complexation with surface minerals (Wallace et al., 2012). In a similar fashion, ⁹⁰Sr at the Hanford site is also reported as sorbed to sediments (Dirkes et al., 2009).

2.64 Sr-nZVI Interactions

As mentioned previously, two enhanced ZVI treatments NanoFeR 25s and Carbo-Iron, were used in this thesis (chapters 5 and 6) to assess their compatibility for the co-treatment of U and Sr contaminated sediments. Whilst there are no direct studies using Carbo-Iron or NANOFeR 25s to treat Sr; nZVI supported on activated carbon frameworks has previously been suggested for the remediation of metal contaminants (Ponder et al., 2001), as Sr can adsorb to activated carbon (Caccin et al., 2013; Chegrouche et al., 2009; Kaçan and Kütahyalı, 2012) and biochars (Jang et al., 2018). One study also demonstrated up to 77 % Sr removal from solution using pure Fe⁰ particles; although, upon exposure to oxygen almost half of the Sr was remobilised suggesting that nZVI acted as an inefficient method of Sr remediation over long periods of time (Efecan et al., 2009).

2.65 Sr Phosphates

Like U phosphate minerals, Sr phosphate minerals are also highly stable. As mentioned previously, the isomorphic substitution of Sr²⁺ for Ca²⁺ in Ca-phosphate minerals such as hydroxyapatite [Ca₅(PO₄)₃OH] occurs naturally and can achieve loadings of up to 11 wt% Sr (Belousova et al., 2002; Verbeeck et al., 1977). The recalcitrance of Sr phosphates has already been proven in both laboratory and field-scale studies (Moore et al., 2004; Szecsody et al., 2009; Vermeul et al., 2014). Here, the results showed increased Sr uptake, and elevated recalcitrance in desorption experiments compared to untreated soils; further investigation found that this was due to slow (over 15 months) substitution of Sr into the apatite structure (Szecsody et al., 2009; Vermeul et al., 2014). Microbial communities capable of hydrolysing organophosphate bonds have also been isolated in sediments extracted from the U.S. DoE Oak Ridge Field Research Centre, and some ningyoite ores are suggested to be of biogenic origin, highlighting the prolonged stability of Sr-phosphates and its viability for use as an *in-situ* remediation method (Doinikova, 2007; Martinez et al., 2014).

Chapter 3: Research Methods

This chapter describes routine experimental and analytical techniques used throughout the PhD. This thesis used a range of pure culture, batch microcosm and column experiments to investigate the fate of U and Sr. Sample preparation, data analysis and many of the analytical techniques were performed by the author. In cases where they were performed by or in conjunction with technical laboratory staff members appropriate acknowledgements are made. All chemical reagents used were of analytical grade and solutions were made using deionised water (18 Ω). All glassware was washed with a 5% Decon solution overnight, and then nitric acid (5%) overnight and rinsed three times with deionised water before and after use.

3.1 Microbiological methods

The following section describes experimental set-ups which were used to prepare microbiological samples.

3.1.1 Pure Culture Experiments:

Cultures of wild type *Geobacter sulfurreducens* and *Shewanella oneidensis* MR-1 were grown during the PhD, *S. oneidensis* MR-1 was used in Chapter 5: Paper 1. Both species have been well described in previous chapters (Chapters 2.1 and 2.2).

Geobacter

Cultures of *G. sulfurreducens* were grown in modified freshwater growth medium NBAF for 48 hours prior to addition to experiments. The composition of the modified freshwater medium, NBAF, is described below (in grams per litre of de-ionised water) and was adapted from Lovely (1988) (Lovley and Phillips, 1988).

Fumaric acid (4.64 g, 40 mM), calcium chloride dehydrate (0.04 g, 0.27 mM), magnesium sulphate heptahydrate (0.1 g, 0.41 mM), sodium bicarbonate anhydrous (1.8 g, 21.43 mM), sodium carbonate monohydrate (0.5 g, 4.72 mM), sodium acetate (2.04 g, 24.87 mM), 100 X NB Mix (10 mL), NB Mineral Elixer (10 mL), vitamin Mix (DL) (15 mL), sodium selenite (1 mL, [1 mM]_{initial}, [1 μ M]_{final}) was added to 0.8 L de-ionised water containing a stirrer bar. The medium was topped up to 1 L and mixed until all components were fully dissolved. The resulting solution was degassed using 80:20 N₂:CO₂ mix and the pH adjusted to 7 using NaOH (10 M). The final solution was stored under sterile, anaerobic conditions. The 100 X NB Mix, NB Mineral Elixer and vitamin Mix (DL) contain trace quantities of vitamins and minerals required by bacteria for growth.



Figure 31: Resting cells of *G. sulfurreducens* in NaHCO₃ buffer solution

Shewanella

Cultures of *S. oneidensis* MR-1 were streaked onto an agar plate from a laboratory culture frozen at -80 °C. Cells were maintained on an agar plate and were sub-cultured every three weeks or less. For resting cell experiments, cells were grown in sterile Tryptic Soy Broth (TSB) overnight. The following day cells were grown in *Shewanella* minimal media for 24 hr. Late log phase cells were harvested *via* centrifugation (5000 *g*, 20 mins) and washed 3 times in relevant anaerobic 30 mM NaHCO₃ buffer.

Shewanella minimal medium is composed of 50 mL of SMM stock solutions 1-4, 40 mL of SMM stock solutions 6 and 7 and 1 mL of SMM stock solution 5 topped up to a litre using de-ionised water.

SMM stock 1 is composed of (Per litre of de-ionised water): ammonium sulphate (23.79 g, 180 mM), dibasic potassium phosphate (19.85 g, 114 mM), monobasic potassium phosphate (8.98 g, 66 mM) and sodium bicarbonate (3.36 g, 40 mM). Per litre of de-ionised water, SMM stock 2 is composed of: magnesium sulphate heptahydrate (4.93 g, 20 mM). Per litre of de-ionised water, SMM stock 3 is composed of: calcium chloride dehydrate (1.44 g, 10 mM). Per litre of de-ionised water, SMM stock 4 is composed of: disodium edetate (0.45 g, 1.34 mM), boric acid (0.07 g, 1.12 mM), sodium chloride 11.70 mg, 200 μM), iron(II) sulphate heptahydrate (30 mg, 108 μM), cobalt(II) chloride (23.80 mg, 100 μM), nickel(II) chloride hexahydrate (23.80 mg, 100 μM), sodium molybdate dehydrate (16.10 mg, 78 μM), sodium selenite (4.30 mg, 30 μM), manganese(II) carbonate (5.8 mg, 26 μM), zinc(II) chloride (1.00 mg, 20 μM) and copper(II) sulphate pentahydrate (1.00 mg, 4 μM). Per litre of de-ionised water, SMM stock 5 is composed of: L-arginine hydrochloride (20 mL), L-glutamate (20 mL) and L-serine (20 mL). Per litre of de-ionised water, SMM stock 6 is composed of: DL-lactate (337 mL, 2M). Per litre of de-ionised water, SMM stock 7 is composed of: fumarate (58.06 g, 400 mM) and sodium bicarbonate (3.36 g, 40 mM).

3.12 Batch Bioreduction Microcosm Experiments

Batch sediment microcosm experiments were used in chapters 4, 5 and 6 to explore the effect of various remediation techniques on the aqueous geochemistry and fate of U and Sr. Batch experiments were carried out in either 100 or 2000 mL glass serum bottles sealed with self-healing butyl rubber stoppers; they were sampled with a needle and syringe using anaerobic aseptic technique, injecting Ar into the microcosms to replace the volume removed when sampling. Whilst triplicate microcosms allow an estimation of experimental error (reported as one standard deviation as error), sterile controls help identify biotic processes and no treatments controls simulate background effects, or the 'natural attenuation' conditions.

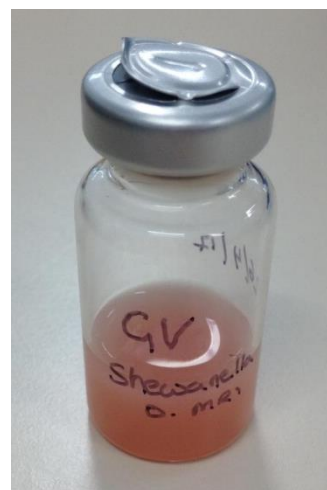


Figure 32: Resting cells of *S. oneidensis* MR-1 in NaHCO₃ buffer solution.



Figure 33: Culturing *S. oneidensis* MR-1 on Fe(III) rich agar plate.

Batch microcosms are a useful tool for experiments that mimic environmental conditions. They are not, however, completely representative of a subsurface aquifer system: i) a solid:solution ratio of 1:10 is non-representative; ii) batch microcosms are closed systems, they therefore are not subject to the degassing of waters under pressure and there is no groundwater flow; and iii) they do not account for heterogeneity in the subsurface.

Batch microcosms were set up with a 10:1 ratio of aqueous to solid phase defined by mass. In 100 mL experiments, 10 (± 0.05) g of characterised sediment was added to 100 mL of artificial groundwater (AGW), representative of the Sellafield region (Wilkins et al., 2007), its composition is listed in Table 6. For 1.5 L microcosms the same ratio was applied (150 g of sediment to 1.5 L AGW). After addition of the salts the AGW was degassed by flushing with a N₂:CO₂ (80:20) mixture for 1 hr/L and the pH was adjusted to 7 (± 0.1), before sterilising in an autoclave (120 °C, 20 min). Sample sediments representative of the UK Sellafield reprocessing site were collected from the Calder Valley, Cumbria, in December 2017, as previously done (Law et al., 2010a; Newsome et al., 2014b; Thorpe et al., 2012a). These have been reported previously to have similar (bio)geochemical and mineralogical properties to those present on the nearby the Sellafield site. Samples were transferred directly to Manchester in sealed sterile containers and stored at 7 °C prior to use. Sediment was typically used within 6 months, larger objects such as gravel and plant roots were hand picked out of sediments before weighing. Sediment mineralogy and composition were characterised using PXRD and XRF spectroscopies respectively. The recipe for AGW is representative of Sellafield groundwater and is described below in Table 6 (Wilkins et al., 2007). The ionic strength (*I*) of solutions was calculated according to Equation 8, below.

$$I = \frac{1}{2} \sum_i^n c_i z_i^2$$

Equation 8: Ionic strength (*I*). Where *c_i* is the concentration (M) of the *i*th species and *z_i* is the charge on the *i*th species.

Compound	M _R	Concentration	
	g/mol	g/L	mM
KCl	74.55	0.0066	0.089
MgSO ₄ .7H ₂ O	246.47	0.0976	0.39
MgCl ₂ .6H ₂ O	203.30	0.081	0.39
CaCO ₃	100	0.1672	1.67
NaNO ₃	84.99	0.0275	0.32
NaCl	58.44	0.0094	0.16
NaHCO ₃	84.01	0.2424	2.88
Ionic Strength	0.017 M		

Table 6: Artificial groundwater composition (Wilkins et al., 2007).

Sediments were added to pre-weighed serum bottles before sealing, with self-healing butyl rubber stoppers. In experiments with added electron donor, amendments were first filter sterilised (22 μm) before adding to the microcosms. Microcosms were incubated in the dark at room temperature; in cases of aerobic experiments they were swirled manually periodically. During sampling microcosms were first shaken, then the rubber tops were sterilised using ethanol and were then sampled anaerobically using a needle and syringe flushed with Ar. After extraction 100 μL of the slurry was used to measure the 0.5 N HCl extractable Fe(II) and Fe_{total} values (described below), the remaining solution was centrifuged (16,200 g, 5 mins) to separate the solid and supernatant phase. ICPMS and

IC analyses were typically performed on the supernatant and the remainder was used to monitor the pH and Eh.

3.13 Batch Reoxidation Remobilisation Microcosms

Batch remobilisation studies were carried out in Chapter 6. They examined the stability of U and Sr solid phase “end-points” in the sediment microcosms after anaerobic incubation for 300 days, some microcosm “end-points” were subject to remobilisation by exposure to either air or 10 mM nitrate (Figure 34). Here, 5 (\pm 0.1) g of end-point sediment in 20 mL of supernatant was transferred from the respective microcosm bottles into either: i) 100 mL conical flasks with foam bungs and Al foil lids, resulting in a 1:4 ratio of slurry to air; or ii) 100 mL sealed serum bottles spiked with nitrate forming a final concentration of 10 mM nitrate; where they were sampled and monitored periodically over 100 days.

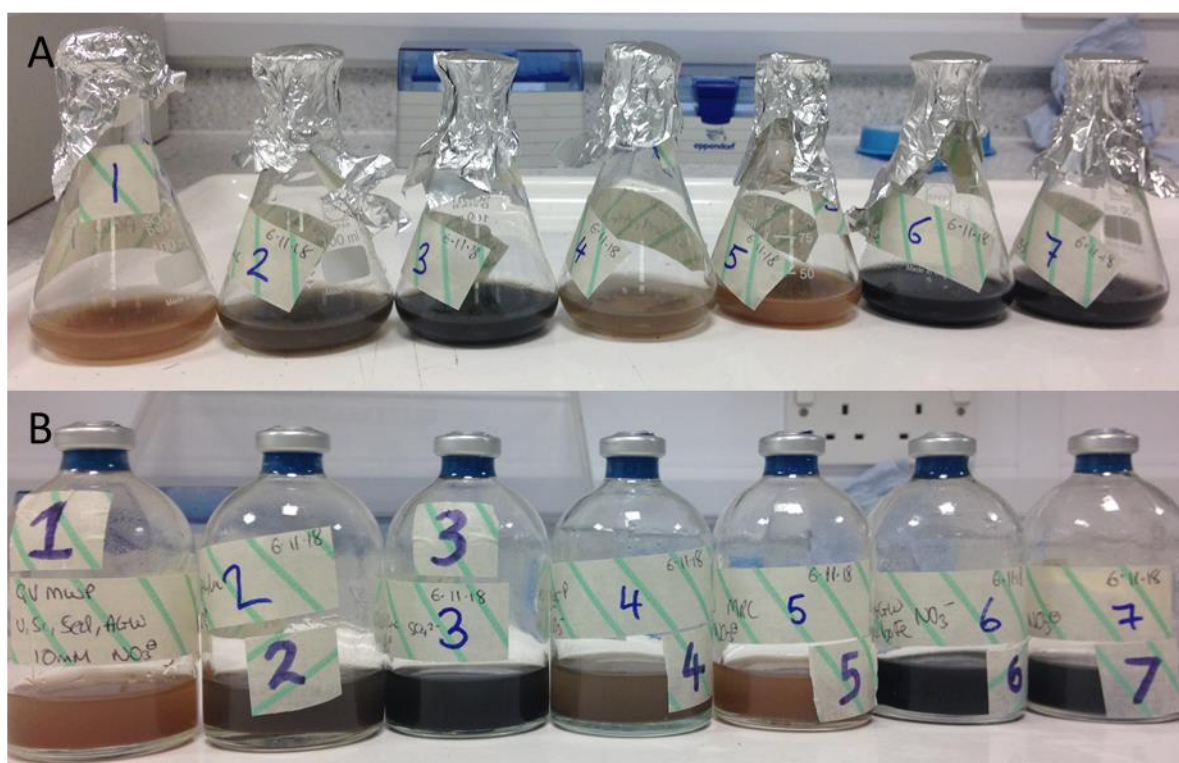


Figure 34: Examples of remobilisation experiments; A) aerobic perturbations in conical flasks and; B) nitrate amended serum bottles.

3.14 Sediment Columns

Although batch microcosm experiments can provide useful information on removal mechanisms and effectiveness, they provide limited applicability to actual subsurface transport due to (i) the low solid: solution ratio, and (ii) lack of influent of starting materials with the possible build-up of end products due to being a closed system. To better represent a contaminated subsurface column experiments were conducted in Chapter 7 using pre-treated sediments generated in batch experiments. Their objective was to assess the long-term stabilities of a range of U and Sr co-treated sediments after aging for 1 year. These end points were from a range of bioremediation and chemical based treatments.

The column experimental design was adapted and developed from past work done in the University of Manchester Geomicrobiology laboratories (Figure 35)(Thorpe et al., 2017, 2016). Columns were set up by packing roughly 3 cm of bioreduced sediments into Perspex columns, a peristaltic pump pushed aerobic artificial groundwater or artificial seawater through the columns and flow rate of 1.2 mL/ hour, representative of groundwater flow in the Sellafield subsurface (Thorpe et al., 2017). The column was an 11.6 cm tall Perspex tube with an inner diameter of 2.8 cm, with a Perspex lid at the top and bottom, sealed with a nitrile O-ring held tight with screws and bolts. To prevent leaks all joints on the column were glued with glue. The bottom end of the column was packed with a 1 cm layer of glass wool to disperse water flow paths and provide uniform water transport up the column. This was followed by a 3 cm layer of (1 M HCl washed) quartz sand. Then 3 cm of bioreduced sediments were added and the remaining 1 cm was packed with glass wool to prevent blockages in the effluent.

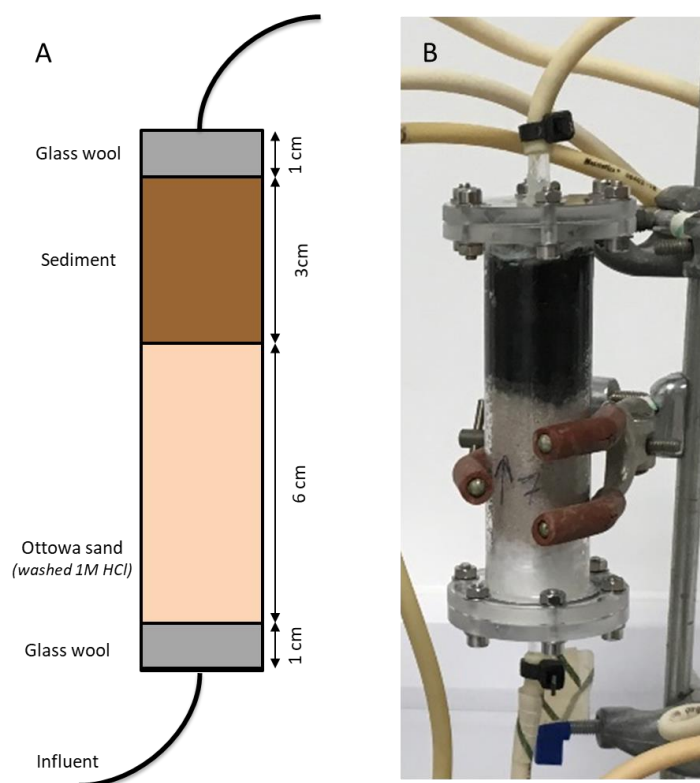


Figure 35: A) schematic depicting the column setup; B) a photo of a column. Influent flowed from the bottom to the top of the column.

Influents, as artificial groundwater (Table 6, above) or artificial seawater (Table 7, below) went in from bottom to top in order to prevent the build-up of preferential flow paths and to support degassing (Lewis and Sjöström, 2010). SrCl_2 was omitted from the artificial seawater recipe to prevent it from interfering with the immobilised Sr phases which were being assessed. The columns and water reserves were kept in the dark using cardboard boxes covered in Al foil to prevent the growth of photosynthetic algae.

Compound	M_R	Concentration	
	g/mol	g/L	mM
NaCl	58.44	23.9968	41.05
KCl	74.55	0.8772	11.70
$\text{MgCl}_2 \cdot 6\text{H}_2\text{O}$	203.30	11.4427	56.28

CaCl ₂ . 2H ₂ O	219.08	1.5699	7.29
SrCl ₂	158.53	0.0243	0.15
Na ₂ SO ₄	142.04	4.3635	30.72
NaHCO ₃	84.01	0.1707	2.03
Ionic Strength	0.67 M		

Table 7: Adapted artificial seawater composition (Todd and Yuan, 1992). SrCl₂ has a strikethrough it as it was omitted from the recipe to allow for monitoring of the Sr retained. Ionic strength was calculated using Equation 8.

Sampling was carried out periodically by collecting the effluent from the tubing. The pH and Eh were monitored and the samples were also analysed for soluble U, Sr and Fe by ICPMS. Following completion of the column experiments, they were sliced vertically in half using a dremmel and the geochemical changes through the column profile were assessed. One half of each column was kept under anaerobic conditions; here, each half was separated into thirds and each third was used to prepare an EXAFS sample and assess the bio-available Fe(II) using the Ferrozine method (Stokey, 1970). The other half was taken for 1-dimensional XRF analysis using an Itrax core scanner. After the XRF scanning, the column was again chopped into thirds, where 0.5 g of sediment was digested in aqua-regia and the samples were analysed for U, Sr, Fe, Mn, P and Ca using Inductively Coupled Plasma – Mass Spectrometry (ICPMS).

3.2 Aqueous Geochemical Analyses

The aqueous geochemistry of samples were measured using the following techniques:

3.21 pH and Eh Measurements

Aqueous phase pH and Eh measurements were made using a Jenway 3520 pH Meter. pH calibrations were made daily using Fluka buffer solutions at pH 4, 7 and 10. Eh calibrations were made daily using a Mettler Toledo 220 eV buffer solution. The respective probe was washed with DI water and dried before each individual measurement was taken.

3.22 Ion Chromatography

Concentrations of Br⁻, PO₄⁻, NO₃⁻, NO₂⁻, SO₄²⁻, glycerol phosphate and volatile fatty acids were assessed using ion chromatography (Bassil et al., 2015; Cleary et al., 2019; Kuippers et al., 2019; Newsome et al., 2019, 2015c). In ion chromatography an aqueous mixture of compounds are passed through a polar column. Here, different ions travel at different rates; more polar molecules with higher affinities for the stationary phase are slower to elute from the column. Effluents chemical compositions are determined by their retention time compared to known standards, and their concentrations are determined through integration of the area under the chromatogram produced.

Samples were frozen (-80 °C) at the time of sampling and prior to IC analysis samples were defrosted, re-suspended and then re-centrifuged (16,200 g, 5 mins). The supernatant was diluted such that the analyte concentrations did not exceed 100 ppm. Monitoring of aqueous phosphate and nitrate was performed using a Dionex ICS 5000 with an AS18 2 mm ion exchange column at 0.25 mL/min and monitoring of sulphate, nitrite, glycerol phosphate and volatile fatty acids was performed using a Dionex ICS 5000 with an AS11HC 0.4 mm high-capacity ion exchange column at 0.015 mL/min.

3.23 Inductively-Coupled Plasma Atomic Emission Spectroscopy and Mass Spectrometry

Inductively-Coupled Plasma Atomic Emission Spectrometry (ICPAES) and Inductively Coupled Plasma Mass Spectrometry (ICPMS) were used to determine total concentrations of aqueous Ca, Mn, Fe, Sr

and U. In both techniques aqueous samples are injected into a nebuliser and finer particles are then ionised by an Ar plasma, the concentrations of elements/ions are determined differently in ICPAES and MS. ICPAES thermally excites the ionised sample releasing outer shell electrons, and the following relaxation of these electrons releases a photon of characteristic wavelength, which is diagnostic for each element. In ICPMS, after passing through a series of skimming cones the ionised atoms enter a vacuum chamber where each atom is separated in a quadrupole on a basis of m/z (mass/charge) ratio; the concentration of each ion is determined by the counts. Although ICPMS is more sensitive than ICPAES it can suffer from isobaric interference as two ions of the same m/z ratio are indistinguishable.

Prior to analysis supernatant (16,000 g, 5 mins) samples were diluted to appropriate concentrations in 2 % HNO_3 . ICPAES was used to determine Ca, Fe, Sr and U concentrations below 100 ppm. ICPMS was used to determine Fe, Sr and U concentrations below 100 ppb. Where necessary, dilutions were made to achieve such limits. As ICPMS can achieve lower detection limits, it is often used in preference to ICPAES. Samples were analysed using an Agilent 7500CX (ICPMS) or a Perkin-Elmer Optima 5300 DV (ICPAES). Sample analysis was performed by Mr P Lythgoe at the University of Manchester.

3.24 UV VIS Spectrophotometry

Spectrophotometric methods were routinely used to assess the concentrations of 0.5 N HCl extractable Fe(II) and 0.5 N HCl extractable Fe_{total} by the Ferrozine assay, $\text{U(VI)}_{(\text{aq})}$ by the Bromo-PADAP assay and urea using an assay adapted from literature (Knorst et al., 1997). This section describes the basic principles of absorption spectroscopy and its first and arguably simplest use: UV Vis spectroscopy.

In UV Vis spectroscopy a monochromatic light is passed through a sample of a known path length and the absorbance is measured. The absorbance of energy results in a transition from a lower (atomic/ molecular) energy level to a higher (atomic/ molecular) energy level thus producing absorption spectra. Conversely, emission spectra are the result of a transition from a higher energy level to a lower energy, which ejects a photon. The Beer-Lambert Law (Equation 9, below) demonstrates the direct relationship between the absorbance (A) and concentration (c) of an absorbing species given the same path length (l) and molar absorption coefficient (ϵ). Colorimetric assays such as ferrozine (Stookey, 1970), Bromo-PADAP (Johnson and Florence, 1971) and the urea assay (Knorst et al., 1997) use chelating compounds to bind to the free ions in solution, which generate a coloured compound that absorbs light at low concentrations. These absorbance values can be converted into concentrations by calibrating with standards of a known concentration, although the absolute concentrations determined are not precise they are reproducible and fit for use when other measurements are not available. Measurements were made by the author using a Jenway 6850 UV/Vis spectrophotometer.

$$A = \epsilon c l = \log_{10} \frac{I_0}{I}$$

Equation 9: The Beer-Lambert law. Where A is absorbance, ϵ is the molar extinction coefficient (a constant), l is the path length, c is the concentration of the solution, I_0 is the incoming light intensity and I is the final light intensity.

Bioavailable Fe(II) and Fe_{total}

To determine bio-available Fe(II) concentrations, 50 μL of sample slurry, which was collected from relevant microcosm experiments by use of a syringe and needle, was digested for at least one hour in 2.45 mL 0.5 M HCl. To determine bio-available Fe_{total} concentrations, 50 μL of sample slurry was

digested for at least one hour in a solution of 0.5 M HCl (2.35 mL) and 6.25 M hydroxylamine hydrochloride (100 μ L). After digestion, the dissolved Fe^{2+} is mixed with Ferrozine solution in HEPES buffer (80 μ L sample mixed with 920 μ L Ferrozine solution respectively), the solution is mixed and absorbance at 562.0 nm is measured on a UV-vis spectrophotometer after 1 minute of standing time. Calibration standards were measured daily using standards at 0, 1, 5, 10 and 20 mM Fe(II). Total bio-available Fe does not represent the total Fe, but is a useful parameter as it represents the portion of Fe that is susceptible microbial metabolic activities (Lovley and Phillips, 1987).

The colourless Ferrozine solution can be prepared by dissolving Ferrozine[®] (3-(2-pyridyl)-5,6-bis(4-phenylsulfonic acid)-1,2,4-triazine; 1 g, 2.03 mM, Figure 36) and HEPES (4-(2-Hydroxyethyl)piperazine-1-ethanesulphonic acid; 11.96 g, 50.19 mM) in 1 L DI water. The pH was adjusted to 7 and the resulting solution was stored in the fridge until use. Ferrozine binds to Fe(II) forming a $[\text{FeL}_3^{2+}]$ (L = Ferrozine) species, which is a water-soluble and strongly purple coloured complex that absorbs UV-light centred at 562 nm (Stookey, 1970).

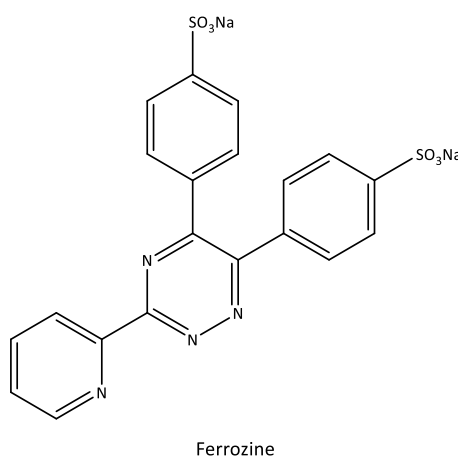


Figure 36: the chemical structure of Ferrozine.

U(VI)

Aqueous U(VI) concentrations were determined in Chapter 5 using the BromoPADAP assay. Prior to analysis supernatant (16,160 g, 5 mins) samples were diluted to appropriate concentrations in DI water. Then, the following components were added to a semi-micro cuvette (Johnson and Florence, 1971): 260 mL de-ionised water, 100 of supernatant sample (diluted in DI-water as appropriate), 80 μ L of complexing solution, 80 μ L of buffer solution, 400 μ L of absolute ethanol and, 80 μ L of indicator solution. Each cuvette was individually covered with parafilm, shaken and left for 40 minutes to ensure U(VI) complexation. The absorbance (578 nm) was measured and compared to a standard calibration curve with U(VI) concentrations of 0, 2.5, 5, 10, 15 and 25 ppm. A calibration curve was drawn for each day that the measurement was taken (Figure 37 below).

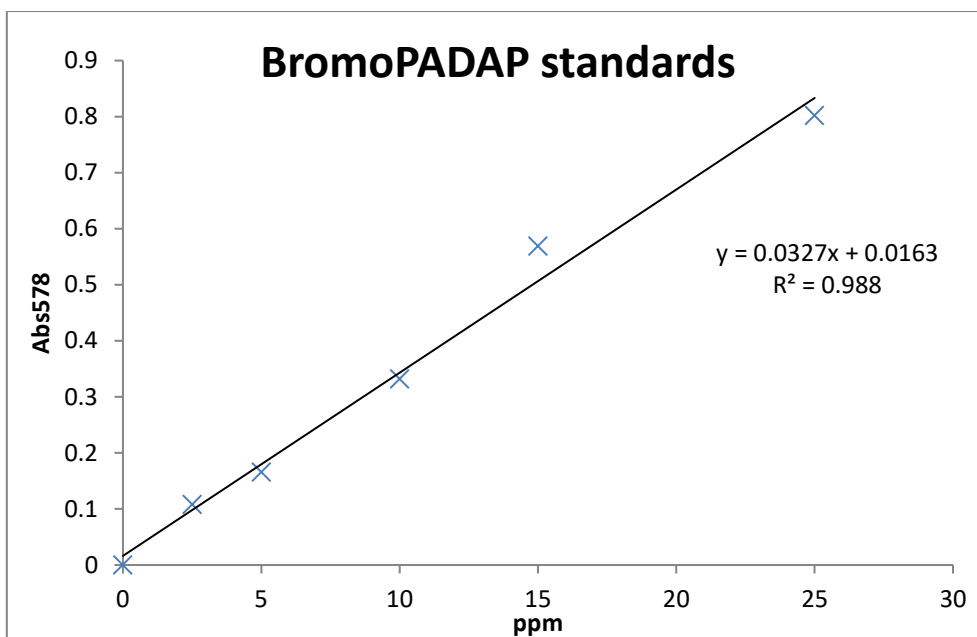


Figure 37: BromoPADAP assay: the standards (blue crosses) are 0, 2.5, 5, 10, 15 and 25 ppm UO_2^{2+} . The analyte concentration (red cross) was calculated by inserting the absorbance value into the line of best fit equation.

The complexant solution (100 mL) is prepared by: dissolving of CY-DTA(trans-1,2-diaminocyclohexane- $\text{NN},\text{N}',\text{N}'$ -tetraacetic acid, 2.63 g, 76.01 mM, Figure 38), sodium fluoride (0.5 g, 119.05 mM) and sulphosalicylic acid (6.5 g, 298.17 mM) in 100 mL of DI-water with pH adjusted to 7.85. The buffer solution (100 mL) is prepared by: dissolving triethanolamine (14.9 g, 1 M) in 100 mL of DI-water with pH adjusted to 7.85 using perchloric acid. The indicator solution (100 mL) is prepared by: dissolving Bromo-PADAP (0.05 g, 1.43 mM) in 100 mL absolute ethanol (This solution must be stored in the fridge). Each of these were prepared by the author, stored appropriately and used within 6 months.

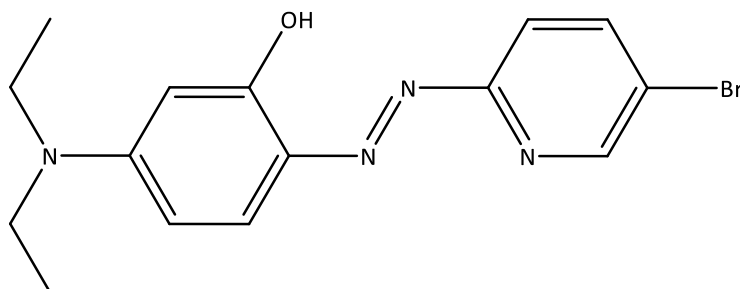


Figure 38: Chemical structure of 2-(5-bromo-2-pyridylazo)-5-diethylaminophenol for spectrophotometric determination of Uranium(VI) in solution.

Nitrite

Aqueous nitrite concentrations in supernatant samples were determined spectrophotometrically in Chapter 6. Supernatant samples were collected from relevant experiments by use of syringe and needles followed by centrifugation at 16,160 g for 5 minutes in a microfuge. The following were added into a semi-micro cuvette in the order given; 750 μl deionised water, 100 μl buffer solution (1 g ammonium chloride in 90 ml deionised water, adjusted to pH 8.5 with 30 % ammonia and made up to 100 ml with deionised water), 100 μl sample, 25 μl SAN solution (0.25 g sulphanilamide in 80 ml deionised water, 2.5 ml 36 % HCl, 100 μl Brij 35 solution, then diluted to 100 ml with deionised water), and 25 μl NED solution (0.25 g naphthylethylenediamine dihydrochloride in 100 ml deionised water)

(Harris and Mortimer, 2002). Each cuvette was mixed and then left for 10 minutes. Absorbance was measured at 536.5 nm, and a calibration curve was drawn up daily using standards of 50, 100, 150, 200 and 300 μM , the blank was made up with deionised water.

Urea

The urea assay, adapted from Knorst *et al.*, was used to monitor urea hydrolysis in Chapter 8.1 (Knorst *et al.*, 1997). Supernatant samples were collected from relevant experiments by use of syringe and needles followed by centrifugation at 16,160 g for 5 minutes in a microfuge. 80 μL of supernatant sample (containing 0-25 mM urea), 720 μL of 18 MQ DI water and 200 μL of complexing agent were mixed into a semi-micro cuvette. The samples were left for 5 minutes, shaken and then absorbance at 422 nm was measured in triplicate. Results were compared to a set of known standards fitted to a calibration curve with $R^2 \geq 0.99$ taken each time the bottles are sampled. Standards ran in artificial groundwater and de-ionised water showed little difference in absorbance (Figure 39).

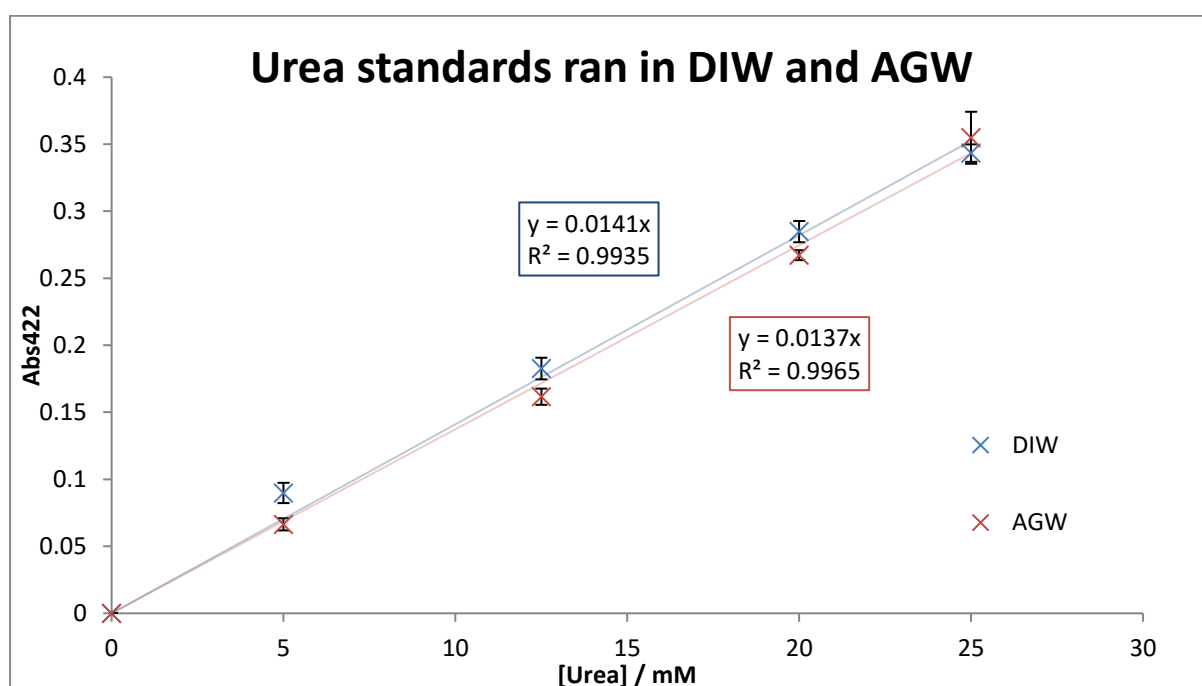


Figure 39: Comparison of the Urea standards ran in DIW (blue) and AGW (red).

100 mL of the complexing agent was made by mixing 92 mL of EtOH (100 %), 4 g of 4-Dimethylamino benzaldehyde and 4 mL of H_2SO_4 (lab grade >95 %). The reaction of urea with the 4-Dimethylamino benzaldehyde forms a yellow coloured solution. This is due to the reversible formation of a Schiff base hydrochloride (Figure 40).

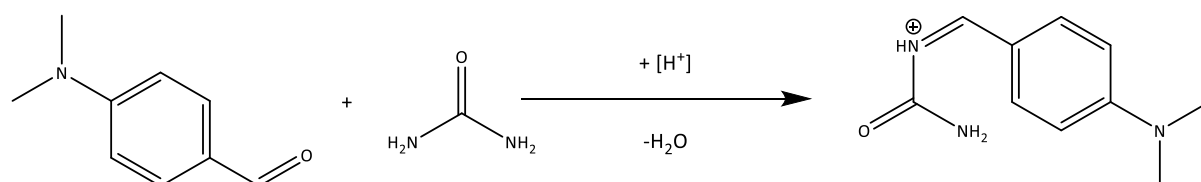


Figure 40: Schiff base hydrochloride formation, the product is responsible for the yellow coloured solution measured.

3.25 Luminescence Spectroscopy

Uranyl(VI)_{aq} concentrations were assessed using luminescence spectroscopy (both fluorescence and phosphorescence) in Chapter 5. The absorption, emission or scattering of a photon causes electronic excitations or relaxations in the form of changing rotational or vibrational states, as such information relating to bond strengths, lengths and angles can be obtained in addition to molecular compositions. In luminescence spectroscopy, where fluorescence refers to an allowed radiative decay from an excited state S_1 to a ground state S_0 of the same degeneracy, it usually occurs on a nano-second timescale (Figure 41 below); phosphorescence refers to a spin-forbidden radiative decay from a triplet excited state to the ground state, it usually occurs on longer timescales.

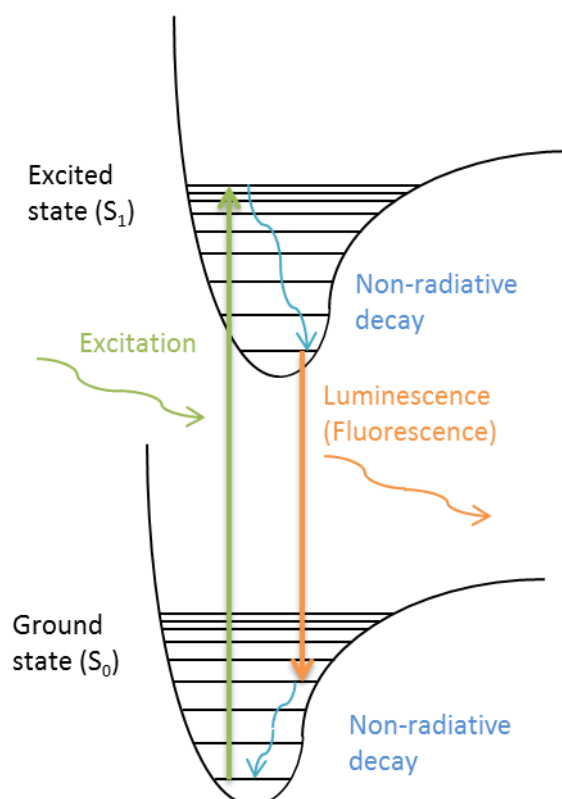


Figure 41: Describing molecular fluorescence. (blue) a molecule is electronically excited from a ground state to an excited state; often by absorption of energy in the form of light. (yellow) Non-radiative decay processes lower the molecules energy to the vibrational ground state of the current state. (red) In order to jump from the excited state back to the ground state the molecule loses radiative energy in the form of a photon. If the two electronic states have the same degeneracy it is fluorescence, if they do not it is phosphorescence.

Uranyl(VI) is known to luminesce after excitation due to a ligand-to-metal charge transfer transition, this is caused by excitation of an electron from an axial oxygen bonding orbital to a the un-occupied non-bonding uranyl(VI) orbital. Uranyl luminescence absorption occurs around 420 nm and the resulting emission is observed around 520 nm, fine structure reveal up to 6 characteristic bands (Figure 42); attributable to coupling of the Raman active total symmetric $U=O_{ax}$ stretching vibration (ν_1) with the excited state. Although uranyl(VI) luminescence is generally accepted to be fluorescence, a little phosphorescence is also likely as in protic solvents hydrogen bonding can stabilise the excited triplet (T_1) state; as such luminescence better describes the process (Denning, 1992; Natrajan, 2012). Due to the core-like behaviour of the f -elements, peaks tend to be sharper as electronic transitions are predominantly localised on single atomic centres. To achieve sharper peak resolution, and to

minimalize quenching effects, samples were run at 77 K, this slows down molecular vibrations and rotations which broaden peaks.

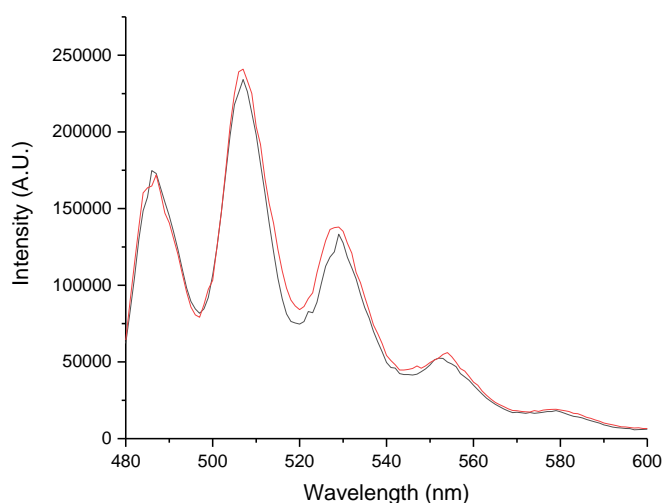


Figure 42: The steady state emission profile of UO_2^{2+} (3 mM) in HCO_3 (30 mM) and lactate (10 mM) in the absence (red line) and presence (black line) of *Shewanella oneidensis* MR1 ($\lambda_{\text{ex}} = 420 \text{ nm}$).

Luminescence emission spectra were analysed using an Edinburgh Instrument FP920 Phosphorescence Lifetime Spectrometer equipped with a 5 watt microsecond pulsed Xe flash lamp and a 450 watt steady state Xe lamp. Lifetime data were recorded on the same instrument but using a 5 watt Xe flash lamp using multichannel scaling. Sample analysis was performed by the author.

3.26 Raman Spectroscopy

Raman spectroscopy was carried out in Chapter 5 to monitor the changes in $\text{U}=\text{O}_{\text{ax}}$, dioxygenyl bond lengths between uranyl(VI) and uranyl(V). Infrared (IR) and Raman spectroscopies investigate transitions between molecular vibrational energy states. Where IR active modes are due to changes in dipole moments, Raman active modes are due to changes in polarity; symmetry labels and character tables can be used to identify bands in both IR and Raman spectroscopies. Vibrational spectroscopies offer a non-destructive method of chemical identification, compatible with air-sensitive and solid or solution phase samples.

When a molecule absorbs infrared radiation of frequency ν_0 , most of the radiation scatters without loss of energy (*Rayleigh scattering*). A small amount of the scattered radiation has a frequency of $\nu_0 + \nu$, where ν is the fundamental frequency of a vibrating mode of a molecule (*Raman scattering*). Since only a small fraction of the scattered light is due to the Raman effect, Raman spectrometers often use a Fourier Transform to increase sensitivity. Covalent bonds stretch as anharmonic oscillations, behaving like springs, with only defined possible energies; the vibrational energy state with $\nu = 0$ describes the zero point energy (vibrational ground state) of the molecule (Figure 43). As we are only (*mostly*) concerned with interactions between the vibrational ground state and an excited state then the motion can be approximated using a simple harmonic oscillation (Equation 10 below).

$$E_{\nu} = \left(\nu + \frac{1}{2} \right) h\nu$$

Equation 10: a simple harmonic oscillation; where v represents the energy state change, h is the planck constant and ν is the frequency of the vibration. ($h = 6.626 \times 10^{-34}$ Js, E_v given in J)

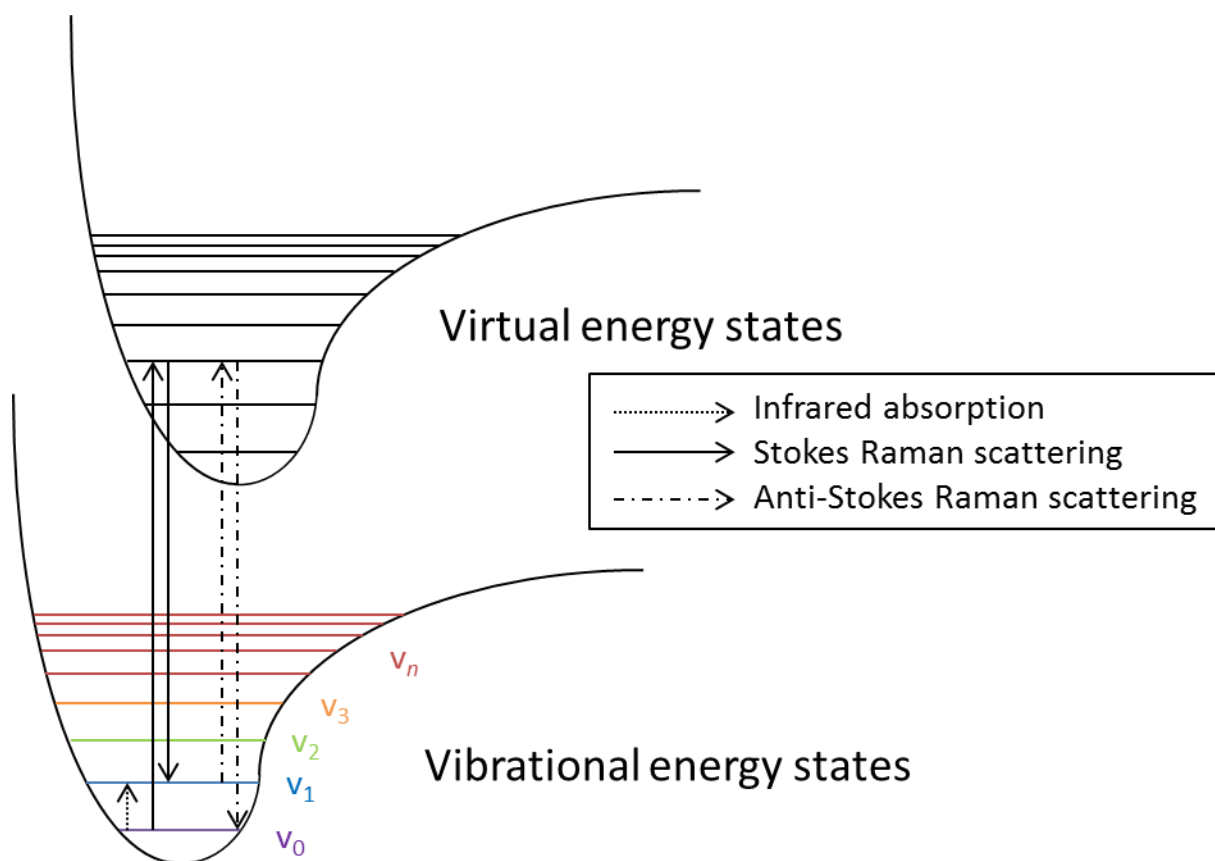


Figure 43: Jablosnki energy diagram for Raman scattering.

The $U=O_{ax}$ bond length in uranyl(VI) cations, is relatively indifferent to the equatorial ligands that bind to the U centre and only varies in small amounts, e.g. from 1.78-1.83 Å in mineral and aqueous samples (Catalano and Brown, 2004; Cejka, 1999). A free uranyl ion (point group $D_{\infty h}$) has three fundamental stretching modes: the symmetric stretch, ν_1 ; the doubly degenerate bending vibration (it is doubly degenerate as it can happen in two mutually perpendicular planes), ν_2 ; and the antisymmetric stretch ν_3 (Figure 44). Lowering the symmetry of the molecule through ligand binding activates all three fundamental modes in the Raman and IR spectra. Once coordinated all three vibrational modes are active in both Raman and IR spectra with ν_1 being the most intense in Raman.

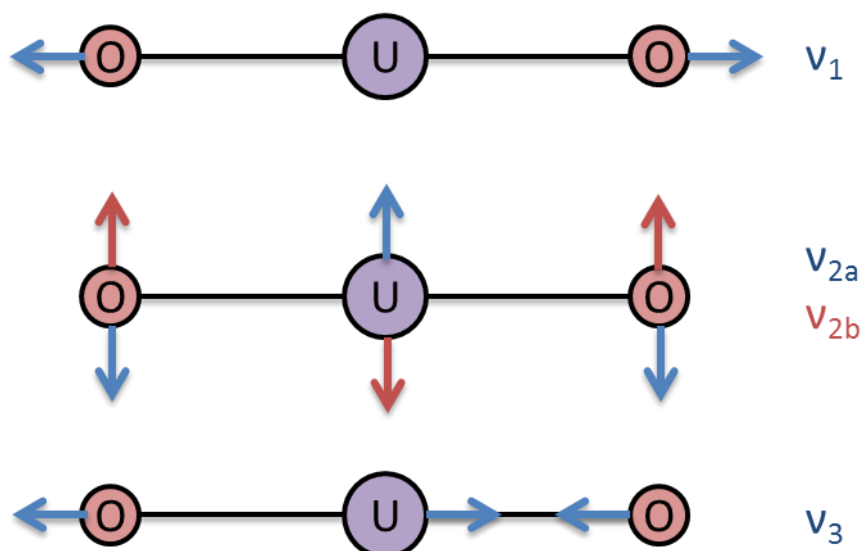


Figure 44: the 3 fundamental vibration modes of the free uranyl ion. Note v_{2a} and v_{2b} signify the two possible planes of vibration making the bending vibration doubly degenerate.

3.27 PHREEQC Computational Analysis

PHREEQC is a geochemical modelling software provided by the U.S. Geological Survey. Where mentioned, PHREEQC was used to calculate the speciation of solutions and saturation indices for solid phases within the experiment. The Andra SIT database was used for all geochemical calculations and additional thermodynamic data was acquired from other sources where necessary. PHREEQC was used in Chapter 5 to understand U speciation in solution.

The speciation of uranyl cations in solution affects spectroscopic analyses; specifically Raman and luminescent spectra. Having more than 1 significant species results in peak broadening. Thermodynamic modelling was carried out using PHREEQC (version 3.0.0) in order to approximate the start point uranyl speciation in the reaction containing UO_2Cl_2 (3 mM), NaHCO_3 (10 mM) and sodium lactate (10 mM). With regard to spectroscopic analysis of solutions, the relative molalities (units mol/kg) and activities are of interest. The results showed that $\text{UO}_2(\text{CO}_3)_3^{4-}$ was the dominant species in solution (94 %)(Table 9). Interestingly $\text{UO}_2(\text{CO}_3)_2^{2-}$ showed a similar activity to $\text{UO}_2(\text{CO}_3)_3^{4-}$ despite representing only 4.9 % of the solution by molality; this is likely attributed to steric effects around the equatorial plane, $\text{UO}_2(\text{CO}_3)_2^{2-}$ has one less ligand and hence has more room to react (Figure 45).

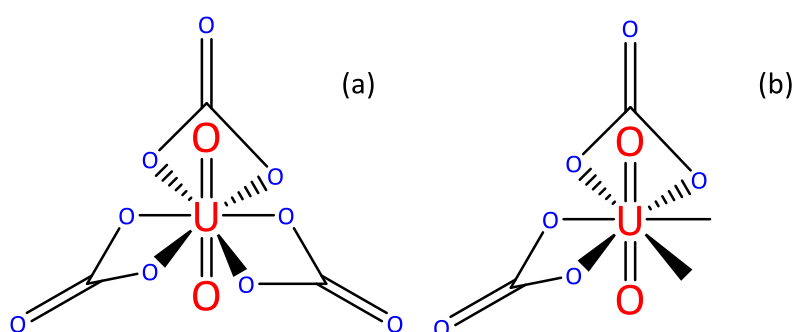


Figure 45: (a) $\text{UO}_2(\text{CO}_3)_3^{4-}$, and (b) $\text{UO}_2(\text{CO}_3)_2^{2-}$, displaying how the partially bounded system in (b) has unbound sites ready to react.

Table 8 and Table 9 (below) describe the parameters used and speciation results, respectively. Data for Na^+ , CO_3^{2-} , UO_2^{2+} and Cl^- were obtained from the ANDRA SIT database (Andra, 2015). As lactate was not available, Log K_{f0} constants for the lactate binding to uranyl(VI) were taken from Ulrich *et al.* 2011 to define the following reactions (Table 10)(Ulrich *et al.*, 2011). PHREEQC has provided computational data that correlates well with scientific expectations and literature (Clark *et al.*, 1995; Krestou and Panyas, 2004).

Parameter	Definition	Species	Molality / mmol (kgwater) ⁻¹
Temperature	298 /K	U(VI)	3
pH	7.6	Cl	6
pe	4	C	30
Density	1	Na	30
		Lac	10

Table 8: parameters used for the PHREEQC calculation.

Species	Molality	Activity	% molality of total U(VI)
$\text{UO}_2(\text{CO}_3)_3^{4-}$	2.821e-03	9.551e-05	94.0
$\text{UO}_2(\text{CO}_3)_2^{2-}$	1.747e-04	7.521e-05	4.9
$(\text{UO}_2)_3(\text{CO}_3)_6^{-6}$	1.240e-06	6.058e-10	4.1e-03
UO_2^{2+}	2.217e-12	9.784e-13	7.4e-08
UO_2Lac^+	1.204e-11	9.810e-12	4e-07

Table 9: Uranyl(VI) speciation as described by PHREEQC calculations, displaying the 3 most significant species, the free uranyl(VI) ion and uranyl(VI) bound to lactate.

Shorthand	Equation	Log K_f
(a)	$\text{Lac}^- + \text{H}^+ = \text{HLac}$	3.86
(b)	$\text{Lac}^- + \text{UO}_2^{2+} = \text{UO}_2(\text{Lac})^+$	3.09

Table 10: Describing formation constants for: (a) the formation of Lactic acid from lactate and a proton; and (b) the formation of lactate bound to uranyl(VI). Both are under aqueous conditions, at 298.15 K, extrapolated to zero ionic strength.

3.3 Solid Phase Analyses

Analyses on solid phases were carried out using the following techniques.

3.3.1 Powder X-ray Diffraction (P-XRD)

Powder X-ray Diffraction (P-XRD) was used to characterise and assess the purity of minerals produced chemically and biotically; it was also used as a tool to characterise sediments used in microcosm and column experiments. XRD is a non-destructive method to analyse crystalline samples by both qualitative and quantitative means. It works due to Bragg's law, which states that when energy, with a wavelength (λ) comparable to the inter-planar atomic spacing in a crystalline system (d), is scattered by atoms it will undergo constructive interference at the appropriate angle of incidence (θ); in accordance with the Bragg equation (Equation 11 and Figure 46 below). The two waves remain in phase when $2d\sin\theta$ is equal to a multiple of the wavelength. The angle of incidence between the sample and the X-ray tube and detector are rotated so that the angle of incidence can be measured from 5° - 70° , analysing a range of diffraction angles and thus crystal lattice d -spacings. As a result of this, XRD can only identify well-ordered crystal structures present at significant ($\geq 5\%$) concentrations (Cullity, 1978).

$$n\lambda = 2d\sin\theta$$

Equation 11: Bragg's law / the Bragg equation.

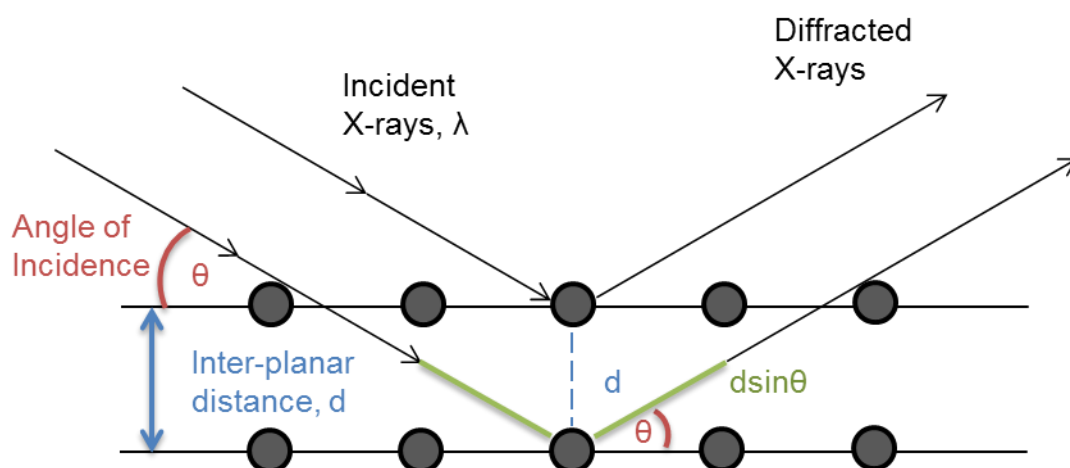


Figure 46: Bragg diffraction, showing two beams of incident X-rays with identical wavelength (λ) and phase being scattered by a crystalline solid with inter-planar distance (d). The lower beam travels a further $2d\sin\theta$ than the top, constructive interference occurs when $d\sin\theta$ is a multiple of the wavelength of the radiation.

Samples were ground using a pestle and mortar, the wet slurry was then pipetted onto a silicon glass mount. Air-sensitive samples were prepared and dried in an anaerobic chamber, using de-gassed DI water and were mounted in anaerobic sample holders. Unless stated otherwise a range of 5° to 70° was used, with increments of 0.02 and a scan speed of 0.5 s^{-1} . Samples were analysed by the Author and Dr John Waters at the University of Manchester using a Bruker D8 advance diffractometer ($\lambda = 1.5406 \text{ \AA}$; Cu K α), equipped with a Göbel Mirror and Lynxeye detector. Data processing and background subtraction of XRD patterns used DIFFRAC.EVA software with peak matching using according to the International Centre for Diffraction Data (ICDD) Powder Diffraction File (PDF) database for references.

3.32 Loss On Ignition (LOI)

LOI was used to determine organic C concentrations in sediments. By measuring the mass difference at after 1 hr incubation of dry sample at 100°C we can calculate the proportion of organic C lost as CO_2 . LOI was carried out by the author and by Mr A. Bewsher at the University of Manchester.

3.33 X-ray Fluorescence (XRF)

X-ray fluorescence (XRF) is a non-destructive method used to determine the elemental composition of the sediment used in microcosm and column experiments, and in this thesis it was also used to track elemental compositions in a 1-dimensional vertical line along the columns. Sediment samples collected from the same site but at different occasions were run to ensure consistency with the given samples; furthermore, the samples were compared to data collected by Law *et al.* (2010) in a similar location (Law *et al.*, 2010a).

When an atom is struck by an incoming X-ray of energy that is greater than or equal to the binding energy of a core electron of the absorber (K or L shell) it is ejected; leaving a core hole where the electron was (Figure 47). To regain stability an electron from a higher shell fills the hole and excess energy is lost as a secondary fluorescent X-ray of energy equal to the difference in energy of the two orbital shells. Thus each element emits a unique 'fingerprint' of X-rays in accordance with possible

energy transitions, where peak position describes the element and peak intensity describes concentration (Jenkins, 1999).

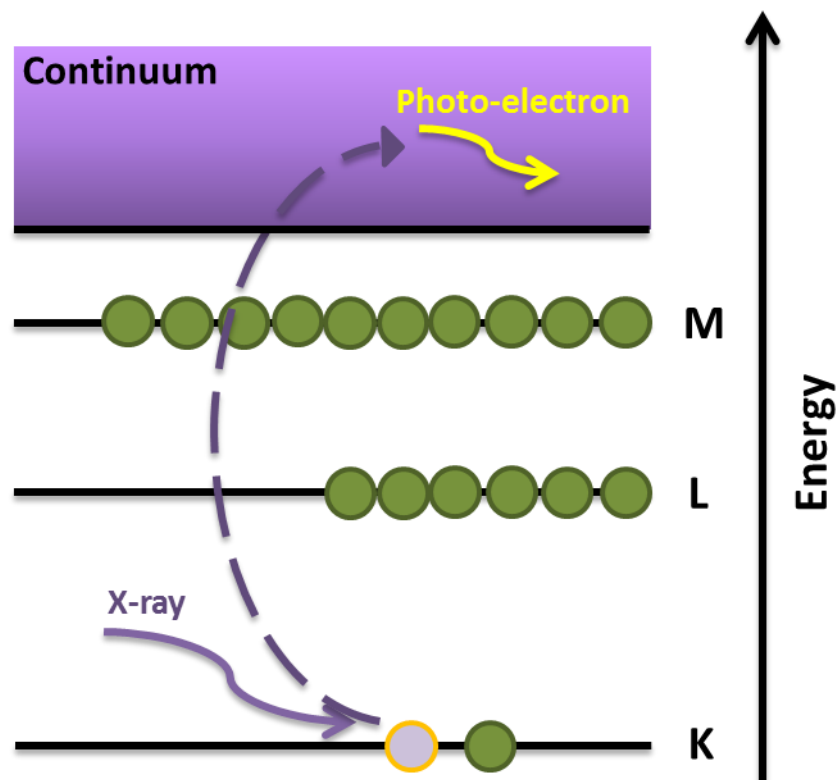


Figure 47: The photoelectric effect, describing the ejection of a core electron from the absorbing atom.

For sediment characterisation, 12 g of samples were dried (80 °C) then ground into a fine powder and mixed with 3 g carboxymethyl cellulose wax using a ball mill, and were pressed into a pellet for XRF analyses. Samples for XRF were dried then ground by Steve Stockley (UoM), XRF was carried out by the author and Paul Lythgoe using a PANalytical Axios system. Elemental analysis along sediment columns were also performed using an Itrax scanner, its setup, in a simplified manner is described in Figure 48 below. Here, sample preparation and data analysis was carried out by the author and Thomas Bishop and the data was used in a qualitative and semi-quantitative manner.

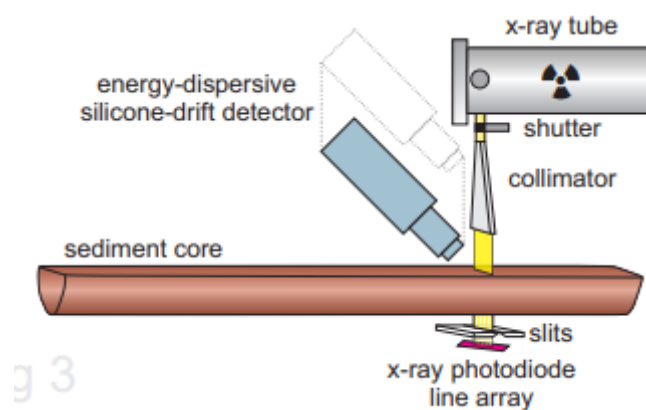


Figure 48: Simplified schematic of the Itrax core scanner. Taken from (Bishop, 2017).

3.34 X-ray Absorption Spectroscopy (XAS)

X-ray Absorption Spectroscopy (XAS) is a synchrotron based technique that fires high energy X-rays onto a sample of interest. In a similar fashion to XRF some X-rays are absorbed by atoms within the sample causing excitation and/or ejection of a core electron. Upon electron ejection or excitation an electron of higher energy moves from a higher shell to the now-vacant core hole, to balance the energy excess energy is lost as a secondary fluorescent X-ray (*Auger electron*). We can measure either the transmission of the incoming X-ray as a function of energy or measure the fluorescence at right angles to yield information on samples. X-ray Absorption Near Edge Structure (XANES) describes oxidation state and bond angles for local geometry and, Extended X-ray Absorption Fine Structure (EXAFS), by comparison, can describe interatomic distances and local coordination number (Alp et al., 1990).

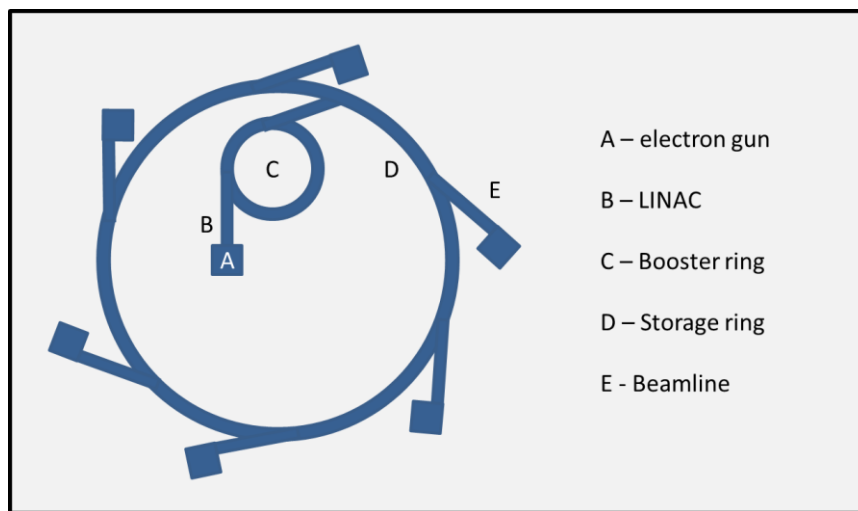


Figure 49: Simplified schematic of a synchrotron.

In synchrotrons (Figure 49) an electron gun is first used to generate said electrons, they are then fed under vacuum into a linear accelerator (LINAC) where they are accelerated by microwave frequency fields. In the booster ring the electrons are further accelerated as they interact with two types of magnets. Dipole magnets direct electrons around the ring and quadrupole magnets refine the electrons into a beam. Once the electrons have enough energy to produce synchrotron light they are transferred from the booster ring to the storage ring; although the booster ring looks circular, it is in fact a polygon consisting of a series of straight sections where the electrons emit light every time the dipole magnets steer their motion. At each corner there is a photon port where photons can travel firstly through the optics hutch for light filtering, optimisation and focussing. This is followed by the experimental hutch, where the experiment takes places and finally control cabin for data collection and analysis and where no X-rays are present. An experimental hutch set up, based on beamline B.18 at the Diamond Light Source, is illustrated in Figure 50.

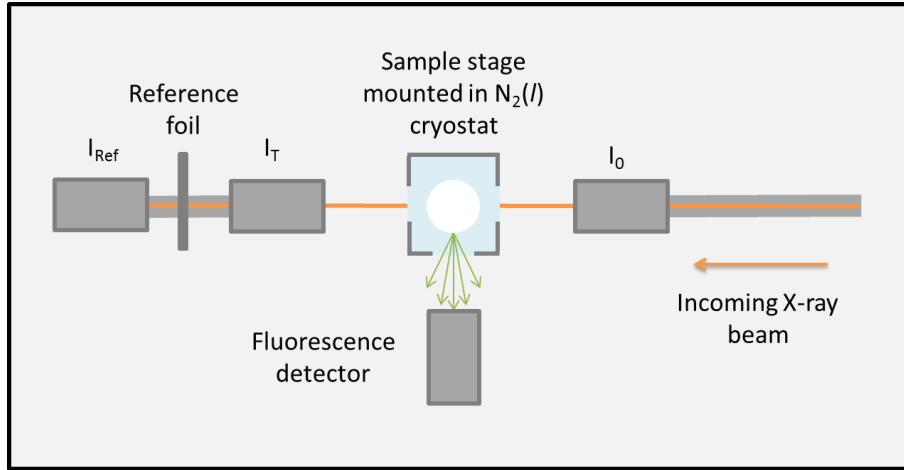


Figure 50: Simplified diagram of the experimental hutch, beamline B.18 at the Diamond Light Source. Image adapted from (Dent et al., 2009).

I_0 , I_T and I_{Ref} are ion chambers; they define the initial beam intensity (I_0), the transmitted intensity (I_T) and the reference intensity (I_{Ref}) before, after transmission through the sample, and after transmission through the reference respectively. The relationship between intensity and transmission is described in Equation 12 below. Transmission spectra are the difference between I_0 and I_T , and spectra collected in fluorescence mode are calculated by normalising the counts in the fluorescence detector to I_0 . Data is calibrated using an in-line reference foil according to Equation 14.

$$a) T = \frac{I_T}{I_0}, A = \log_{10} \frac{I_0}{I_T}, A = -\log_{10} T$$

Equation 12: Transmission (T), where absorbance (A) equals 1-T.

$$b) \text{Flourescence} = \frac{FF}{I_0}$$

Equation 13: Fluorescence mode, where FF = counts measured.

$$c) R = \frac{I_{Ref}}{I_0}$$

Equation 14: Energy calibrations using the in-line reference foil.

$$d) \ln \frac{I_0}{I_t} = \mu(E)x$$

Equation 15: XAS absorption described by the Beer-Lambert law.

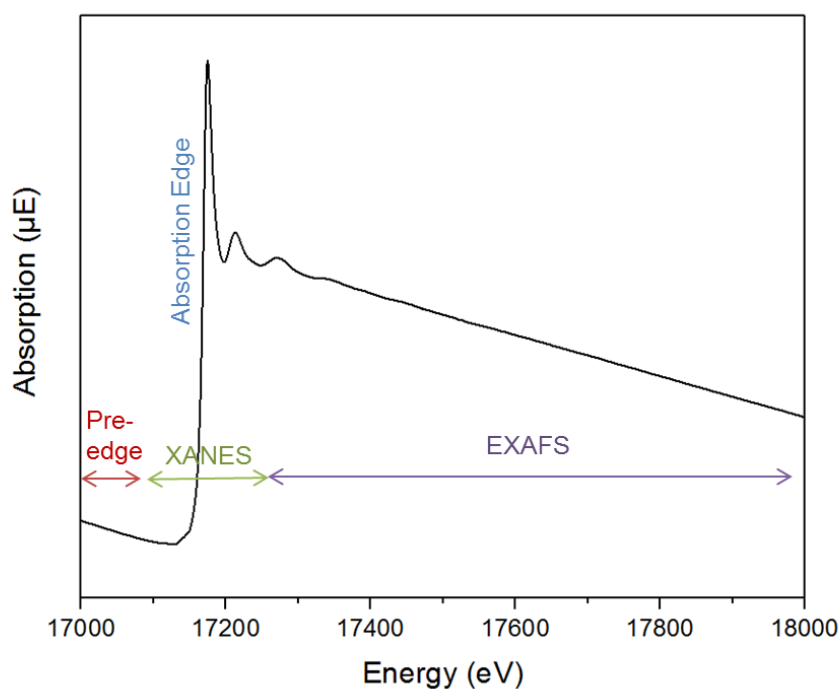


Figure 51: A typical absorption cross section, plotting absorption (μE) vs. energy at the U L_{III} -edge of bio-UO_2 ($E^0 = 17,169$ eV). Pre-edge, XANES, absorption edge and EXAFS regions are labelled in red, green, blue and purple respectively.

The resulting XAS spectrum is divided into three sections (Figure 51). Data collected before the absorption edge is known as the pre-edge, its slope is used to normalise data after collection. The next ~ 50 eV following from the absorption edge is the XANES region. The position and shape of XANES is diagnostic for the oxidation state and yields some, but slightly limited, information on the local coordination environment. Differentiating between U(VI) and U(IV) is clear (Figure 52 below); however distinguishing U(V) amongst U(VI) and U(IV) is difficult in U L_3 -edge XAS spectroscopy (Bès et al., 2016; Kvashnina et al., 2013).

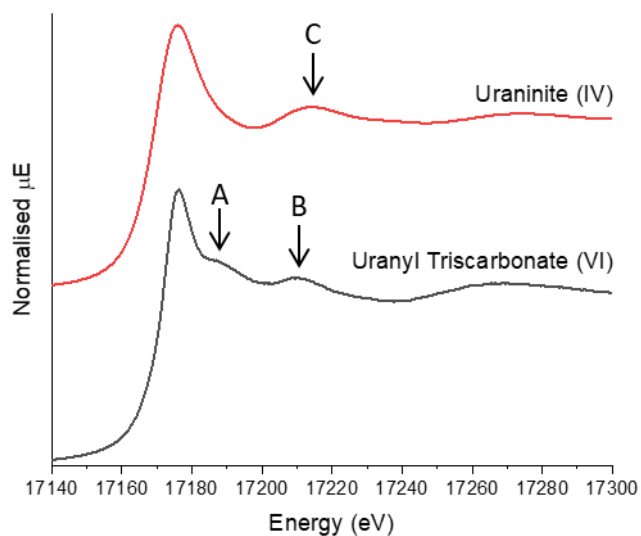


Figure 52: Comparison of Uranium L₃-edge XANES spectra of uraninite (red) and uranyl triscarbonate (grey) (Brookshaw et al., 2015). Point a indicates the presence of a U-O_{ax} bond, points B and C indicate the presence of longer U(VI)-O_{eq} and U(IV)-O bonds.

Whilst the absorption edge and XANES define the element and its oxidation state; features present in the post-edge or EXAFS region characterises the local geometry of the absorber. The interactions of secondary X-rays with the neighbouring atoms. The expelled photoelectron from the central absorber atom radiates in all directions (like a pebble splash in a pond) and scatters off adjacent atoms before returning to the central atom. This backscatter from a shell of a set distance yields a sinusoidal oscillation in the EXAFS spectra, or its relative Fourier transform. EXAFS are often presented in k^3 weighted spectra or in the Fourier transform; the former applies a weighting which presents oscillations at a greater distance with a greater weighting so they are more visible. The latter uses a Fourier transform which yields an approximate radial distribution function where peaks represent backscattering shells at a given radius; this is defined by the EXAFS equation.

$$\chi(k) = \sum_j \frac{N_j S_0^2 f_j(k) e^{-2k^2 \sigma_j^2}}{k R_j^2} \sin[2kR_j + \delta_j(k)]$$

Equation 16: The EXAFS equation.

Where $f(k)$ and $\delta(k)$ are the scattering amplitude and phase shift respectively, they are both constants defined by scattering properties of the neighbouring atom in question and are dependent on the atomic number of the neighbour atom. Per shell, N is the number of neighbouring atoms, R is the average distance from the absorber to the neighbour, and σ^2 is the Debye-Waller factor, a measure of disorder of distance. σ^2 values are usually low for highly crystalline structures and increase with disorder and distance from the absorber. In order to account for electron relaxation incomplete absorption of the incident X-rays and other dampening factors we use an amplitude reduction factor S_0^2 . Through application of the EXAFS equation you can determine N , R and σ^2 .

XAS data fitting and analysis

The analysis of EXAFS and XANES were performed using an array of computing programmes including Athena (in which we could do linear combination fitting [LCF]), Artemis and PyMCA.

For U L₃-edge and Sr K-edge XAS data initial data processing was carried out using Athena; in which individual scans were imported with their corresponding reference files (Y foil, K-edge) before being calibrated, aligned and then merged in $\mu(E)$ to form one spectrum. Still in Athena, the absorption edge is selected, this is defined as the top of the peak in the first derivative of the spectra and the data $y=0$ intercept in the second derivative. By eye, it is roughly the energy point halfway up the absorption edge. Next, background interference can be removed by fitting the pre-edge range with a linear regression line by selecting two points in the pre-edge region, one at the start and one near the end. This approach is repeated in the post-edge region. After background subtractions, the relative contributions from each component in systems in both XANES and EXAFS spectra can be analysed using standards of known compositions to determine the relative contributions in the data, Linear Combination Fitting, LCF. LCF was carried out by the author, using Athena. As always with XAS analyses results and the standards used must make chemical and physical sense to the spectra being fitted.

EXAFS fitting was carried out by the author, using Artemis on the Fourier transform (R) of the k^3 weighted data. Shells could only be used if they were scientifically sound, meaning they: i) had sensible bond lengths and Debye-Waller factors, both comparable to literature; ii) improved the fit, with realistic statistical gain; and iii) included significantly fewer variables than the number of independent data points.

3.35 High Energy Resolution Fluorescence Detected (HERFD) XANES

As aforementioned, distinguishing the U(V) edge amongst U(IV) and U(VI) using U L_3 -edge spectroscopy can be difficult due to the similarity in edge position and shape (Bès et al., 2016; Kvashnina et al., 2013). Advances in synchrotron science have permitted a much more improved distinction between the U(IV), (V) and (VI) edges using U M_4 -edge HERFD XANES (Figure 53)(Bès et al., 2016; Kvashnina et al., 2013; Pidchenko et al., 2017; Roberts et al., 2017). According to the dipole selection rule ($\Delta l = \pm 1$), XANES spectra taken at the U M_4 -edge provide more information about the valence $5f$ states, which play a key role in chemical bonding, compared to U L_3 -edge XANES which probe U $6d$ states. U M_4 -edge XANES also has sharper spectral features because it has a shorter core-hole lifetime broadening than the U L_3 -edge. In HERFD-XANES, the best data is obtained by tuning the crystal analysers to the maximum of the X-ray emission line. Here, the sample, detector and analysing crystals are positioned on a Rowland circle which this allows the spectral data of specific energies only to converge on a detector (Vitova et al., 2013). One difficulty associated with U M_4 -edge HERFD-XANES is that it requires the use of much softer X-rays (edge 3.7 KeV, compared to 17.2 KeV for the U L_3 -edge), the soft X-rays are heavily absorbed by air making it much more challenging to collect data (Merritt, 2010) and thus the experimental set up is often encased in a He environment to maximise the signal received

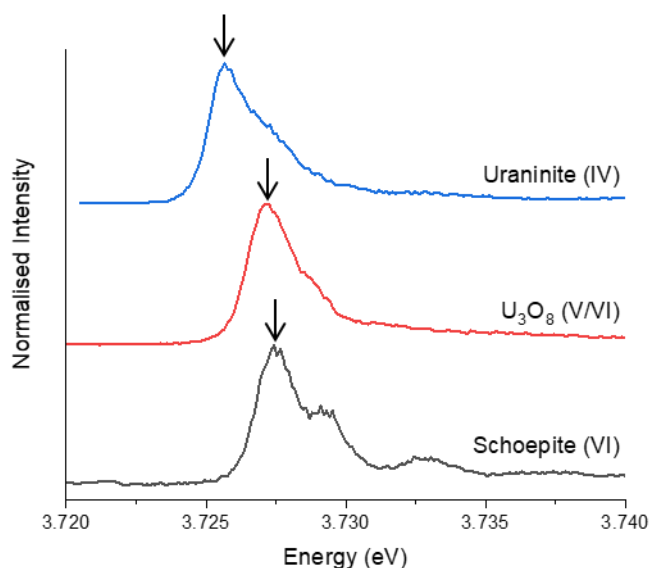


Figure 53: Uranium M_4 -edge HERFD-XANES spectra for uraninite (blue), U_3O_8 (red) and schoepite (grey), with arrows indicating the increase in peak position with increasing oxidation state.

U M_4 -edge HERFD-XANES was used in Chapter 5, spectra were collected on the ANKA light source, beamline CAT-ACT (Zimina et al., 2016). Samples were stored and transported at -80 °C and data were collected in a He(l) cooled cell at approximately -10 °C. XANES spectra were analysed using linear

combination fitting in Athena to determine the proportion of U (IV), (V) and (VI) in the samples (Ravel and Newville 2005).

3.36 Environmental Scanning Electron Microscopy and Energy Dispersive X-ray Spectroscopy

Environmental Scanning Electron Microscopy (SEM) was used in Chapter 6 to obtain images of sediment and the minerals produced in reactions; Energy Dispersive X-ray Spectroscopy (EDX) was used for bulk and spot elemental mapping and identification. SEM directs a focussed electron beam towards a sample in a vacuum or in a water vapour atmosphere. Electrons emitted back to the detector are used to produce an image, this can be done in two ways. Secondary electron emission mode monitors low energy electrons emitted from the sample surface, this leads to varying brightness of peaks correlated with their proximity to the detector. In backscatter mode, higher energy electrons are fired at the sample, heavier atoms with a higher Z (atomic number) backscatter more than lighter elements and so appear brighter. The low vacuum and lack of need for samples to be fixed, means that hydrated environmental samples can be analysed with relative ease.

During sample preparation solid phases were separated from the aqueous phase by centrifugation (16160 *g*, 5 mins), the solid phase was then ground using a mortar and pestle and left to dry under anaerobic conditions on ESEM stubs before mounting. Imaging was performed using a Phillips XL30 ESEM-FEG and assistance was provided by Dr John Waters at The University of Manchester.

3.37 Microbial Analysis – 16S rRNA Gene Sequencing

Chapter 6 and Chapter 7 use 16S rRNA (ribosomal ribonucleic acid) gene sequencing to assess the changes in the bacterial and archaeal community. Here, DNA is extracted from samples and then amplified by a Polymerase Chain Reaction (PCR), using primers for the 16S ribosomal RNA (rRNA) gene. This gene encodes a component of ribosomes that are present in all prokaryotes (bacteria and archaea). The 16S rRNA gene contains approximately 1,500 base pairs. Whilst some regions of the gene are highly conserved across all phylogenetic groups, others vary substantially at a species level and can therefore be used as a genetic 'fingerprint'; through comparison to a database of known 16S rRNA gene sequences we can identify the range of organisms present.

DNA was extracted from sediment slurry using a Powersoil DNA Isolation Kit (MO BIO Laboratories Inc, Calsbad, CA, USA). PCR was then used to amplify a 250 base pair region of the the 16S rRNA gene for high throughput sequencing. PCR replicates the DNA template using the Taq polymerase enzyme and the process occurs in 3 repeatable steps (Figure 54). First, double stranded DNA is split apart by heating to 96 °C; this is denaturation. During the second step, the reaction mix is cooled and the primers are attached at either end of the DNA region of interest; this is annealing. The third and final step of PCR is called extension. Here, the temperature is brought up to 72 °C and the Taq polymerase enzyme synthesises new DNA between the primers that are replicating the original DNA chain. The PCR process is then repeated, usually between 20 and 30 times; as each cycle doubles the quantity of DNA, 20 repeats will typically yield a 10⁶ fold increase in DNA concentration.

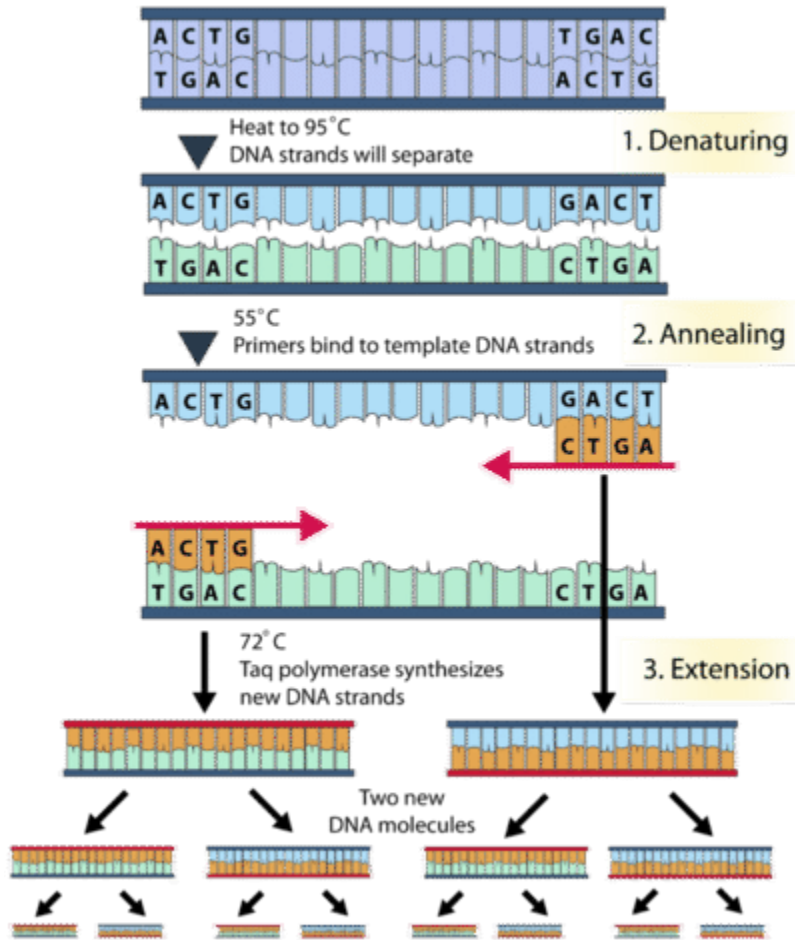


Figure 54: The Polymerase Chain Reaction (PCR). Taken from (CK-12.org, 2016).

The amplified gene fragments from PCR are referred to as amplicons, these were then sequenced with the Illumina MiSeq platform (Illumina, San Diego, Ca, USA). Sediment samples were selected and prepared by the author for 16S rRNA gene analysis in Chapters 5 and 6. All DNA extractions, amplifications and sequencing reactions were carried out by Christopher Boothman, and data analysis was performed by the author and Christopher Boothman.

Chapter 4: Multiple Lines of Evidence Identify U(V) as a Key Intermediate during U(VI) Reduction by *Shewanella oneidensis* MR1

This chapter is a manuscript published in the journal Environmental Science and Technology in January 2020. The supporting information that was published with this manuscript is included in this chapter.

The full citation for this published manuscript is:

Vettese, Gianni F., Katherine Morris, Louise S. Natrajan, Samuel Shaw, Tonya Vitova, Jurij Galanzew, Debbie L. Jones, and Jonathan R. Lloyd. 2020. "Multiple Lines of Evidence Identify U(V) as a Key Intermediate during U(VI) Reduction by *Shewanella Oneidensis* MR1 ." Environmental Science & Technology, January. <https://doi.org/10.1021/acs.est.9b05285>.

Multiple Lines of Evidence Identify U(V) as a Key Intermediate during U(VI) Reduction by *Shewanella oneidensis* MR1

Gianni F. Vettese, Katherine Morris, Louise S. Natrajan, Samuel Shaw, Tonya Vitova, Jurij Galanzew, Debbie L. Jones, and Jonathan R. Lloyd*

Cite This: *Environ. Sci. Technol.* 2020, 54, 2268–2276

Read Online

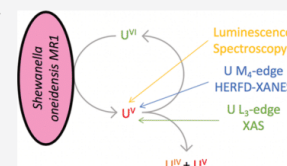
ACCESS |

Metrics & More

Article Recommendations

Supporting Information

ABSTRACT: As the dominant radionuclide by mass in many radioactive wastes, the control of uranium mobility in contaminated environments is of high concern. U speciation can be governed by microbial interactions, whereby metal-reducing bacteria are able to reduce soluble U(VI) to insoluble U(IV), providing a method for removal of U from contaminated groundwater. Although microbial U(VI) reduction is widely reported, the mechanism(s) for the transformation of U(VI) to relatively insoluble U(IV) phases are poorly understood. By combining a suite of analyses, including luminescence, U M₄-edge high-energy resolved fluorescence detection–X-ray absorption near-edge structure (XANES), and U L₃-edge XANES/extended X-ray absorption fine structure, we show that the microbial reduction of U(VI) by the model Fe(III)-reducing bacterium, *Shewanella oneidensis* MR1, proceeds via a single electron transfer to form a pentavalent U(V) intermediate which disproportionates to form U(VI) and U(IV). Furthermore, we have identified significant U(V) present in post reduction solid phases, implying that U(V) may be stabilized for up to 120.5 h.



INTRODUCTION

Highly soluble U(VI), as uranyl(VI), is a significant contaminant in soils and sediments associated with uranium mining, processing, and storage in nuclear sites worldwide. Reduction of mobile U(VI) to poorly soluble U(IV) can be achieved via enzymatic electron transfer mediated by anaerobic metal-reducing bacteria. This metabolism will contribute to a decrease in U mobility in the cases of “natural attenuation”, and can be further enhanced via electron donor injections, which have been proposed as a bioremediation technique for U-contaminated land and water.¹ In field-scale tests at the Rifle Field Research Site, Colorado, the potential for U(VI) removal from contaminated groundwater by indigenous Fe(III)-reducing bacteria was assessed over a 3 month period. Here, “biostimulation”, promoted by the injection of the electron donor acetate, resulted in soluble U dropping to below levels prescribed by the Environmental Protection Agency within 50 days.² Here, a marked increase in numbers of *Geobacter* species, a subsurface metal-reducing bacterium known to respire U(VI), accompanied reduction and precipitation of U(IV).^{2–5} However, subsequent re-oxidation processes lead to remobilization of the U, highlighting that the longevity of bioreduced end-points require optimization.

A series of *c*-type cytochromes traverse the outer compartments of the Gram-negative *Geobacter* cell and terminate at the surface of the outer membrane where metals, including U(VI), are reduced.⁶ In addition, conductive pili, which extend from the cell surface reportedly play a role in metal reduction.^{7,8} These reactions can also be accelerated by the addition of extracellular electron shuttles including humic acids.^{7,8}

Fluorescence spectroscopy, density functional theory, and U L₃-edge X-ray absorption spectroscopy (XAS) have all suggested that the reduction mechanism is via single electron transfer forming an intermediary uranyl(V) state which then disproportionates to more stable U(IV) and uranyl(VI) in *Geobacter sulfurreducens*.^{9–11} Furthermore, uranyl(V/VI) microparticles have been identified in a multispecies biofilm through the combined use of confocal laser scanning microscopy and fluorescence spectroscopy.¹² Other well-studied model metal-reducing bacterial species are found in the genus *Shewanella*, and here the electron transfer proteins are again well characterized. A combination of outer membrane-associated *c*-type cytochromes and extracellular electron shuttles govern U(VI) reduction.^{13–16} However, to date, no published studies have provided direct unequivocal analytical evidence of the pentavalent U(V) intermediate in the enzymatic reduction of U(VI) by *Shewanella*, or indeed any other metal-reducing bacterium.

Pu(V), as plutonyl(V), has been identified as a significant environmental species in water^{17,18} and more recently has been identified as a meta-stable intermediate in the reduction of plutonyl(VI) to form Pu(IV)O₂ nanoparticles.¹⁹ While other actinyl(V) species, specifically [Np(V)O₂]⁺ and [Pu(V)O₂]⁺, are expected to be environmentally significant,^{9,20,21} the

Received: September 2, 2019

Revised: January 6, 2020

Accepted: January 14, 2020

Published: January 14, 2020

uranyl(V) cation is relatively unstable with respect to disproportionation.²² Recent advances in ligand synthesis have permitted the isolation and characterization of several uranyl(V) compounds,^{22–30} and in aqueous media, uranyl(V) is reported as a transient species with some stabilization afforded by, for example, complexation with CO_3^{2-} species.^{31–34} While uranyl(V) triscarbonate solutions have been reported to be stable in carbonate (>0.8 M as Na_2CO_3) solutions in the pH range 10.5–12.0 for up to two weeks,^{32,33,35,36} uranyl(V) has recently been stabilized in aqueous conditions at circumneutral pH over month time-scales, via a polydentate amino-carboxylate ligand.³⁷ In the natural environment, U(V) exists in the mixed valence mineral wyartite and in the mixed oxidation state U-oxides U_3O_8 and U_4O_9 , where U(V) is incorporated in a nonuranyl-like coordination.^{38,39} Recent work also suggests that U(V) phases can show enhanced stability in the presence of iron-bearing phases typically by the incorporation of U(V) into the mineral lattice in a uranate-like coordination.^{40–48} This suggests that a single electron transfer pathway to uranyl(VI) in iron-rich environments may lead to the formation and stabilization of U(V) in the resultant iron-bearing mineral phases.

Despite its potential environmental relevance, the role of U(V) in the microbial reduction of U(VI) is still poorly understood in organisms outside the *Geobacter* genus. Even with *Geobacter* species, only a restricted number of analyses have inferred the presence of U(V); they have been conducted using extended X-ray absorption fine structure (EXAFS)⁹ and fluorescence spectroscopy.¹⁰ Here, we build on this past work to define the mechanism of U(VI) bioreduction using cultures of the model metal-reducing bacterium *Shewanella oneidensis* MRI. Through the application of luminescence spectroscopy, U M_4 -edge HERFD–XANES (high-energy resolved fluorescence detection–X-ray absorption near-edge structure, also called high-energy resolution XANES, HR-XANES^{49,50}), and U L_3 -edge XANES/EXAFS, we demonstrate unequivocally that enzymatic reduction of U(VI) by *S. oneidensis* MRI proceeds via a U(V) intermediate state, and our study is the first to provide direct analytical evidence for U(V) via the U M_4 -edge HERFD–XANES technique. Furthermore, during a 5-day bioreduction experiment, up to 60% U(V) was identified in cell suspensions between 2.5 and 4.5 h. Interestingly, U M_4 -edge HERFD–XANES analyses identified approximately 20–30% U(V) as a persistent species at the 120.5 h bioreduction end-point, and further U L_3 -edge EXAFS analysis for this end-point sample, suggest that it was present as uranyl(V). These multitechnique observations drawing upon the state of the art U M_4 -edge HERFD–XANES analysis approach, confirm that U(V) is a key intermediate during the bioreduction of U(VI) by organisms outside the *Geobacter* genus. They also suggest that U(V) may persist as a long-lived intermediate for up to 120.5 h in addition to well characterized U(IV) bioreduction end products such as uraninite.^{51,52}

EXPERIMENTAL METHODS

Microbial Culture Preparation. *S. oneidensis* MRI was obtained from the University of Manchester Geomicrobiology group culture collection. Starter cultures were grown aerobically in tryptic soy broth (Oxoid CM0876) overnight (30 °C, 100 rpm) before transfer to an anaerobic *Shewanella* minimal medium.^{14,53} The bacteria were grown to mid-exponential growth in the *Shewanella* minimal medium which contains lactate (10 mM) as the electron donor and fumarate (10 mM)

as the electron acceptor for 24 h (30 °C).^{14,53} Late log phase cultures were collected by centrifugation and washed three times in anaerobic NaHCO_3 (30 mM) buffer solution (pH 7). An aliquot of the final washed cell suspension was added to a sterile solution of 3 mM (714 ppm) U(VI) (as UO_2^{2+} in 0.001 M HCl) in NaHCO_3 (30 mM, pH 7) and was supplied with lactate (10 mM) as an electron donor. Experiments were sampled periodically over 5 days. The following samples were collected for further analysis; cell suspensions were sampled directly and included the whole reaction mixture; sub-aliquots were also centrifuged (16,160g, 5 min) and the resultant supernatant (U_{aq}) and precipitate, (U_{ppt}), samples analyzed. The total U and uranyl(VI) concentrations in the supernatant were determined by inductively coupled plasma mass–spectrometry (ICP–MS) analysis of the acidified (2% HNO_3) supernatant using an Agilent 7500CX (ICP–MS), and by luminescence spectroscopy of the frozen supernatant, respectively. Cell suspensions were measured using U L_3 -edge XAS at 2.5 and 4.5 h. At 4.5 h, we also analyzed the cell suspension and a cell pellet using U M_4 -edge HERFD–XANES. Finally, cell pellets made at 120.5 h were measured using both U L_3 -edge XAS and U M_4 -edge HERFD–XANES.

Spectroscopic Analyses. All samples were handled under anaerobic conditions throughout, and for X-ray absorption spectroscopy/luminescence spectroscopy samples were harvested and frozen immediately in liquid N_2 and stored at -80 °C under an Ar atmosphere prior to analysis. Aqueous geochemical samples were prepared at 30 min time points for luminescence spectroscopy, hourly time points for ICMS analysis for total aqueous U, and XAS samples were prepared at approximately 2.5, 4.5, and 120.5 h.

Steady-state emission spectra were recorded on an Edinburgh Instruments FP920 phosphorescence lifetime spectrometer equipped with a finger dewar liquid N_2 cryostat, a 450 W steady state xenon lamp (with single 300 mm focal length excitation and emission monochromators in Czerny Turner configuration), and a red sensitive photomultiplier in a Peltier (air cooled) housing (Hamamatsu R928P) detector.¹⁰ Each scan was run in triplicate at -196 °C using an excitation wavelength 405 nm, and identical parameters throughout. All spectra were corrected for the excitation source and the detector response using the correction files provided in software.

U M_4 -edge HERFD–XANES measurements were performed at the ACT station of the CAT-ACT beamline at the Karlsruhe Research Accelerator (KARA), KIT lightsource.^{54,55} Again, samples were stored at -80 °C prior to analysis on the beam line and during data acquisition, samples were analyzed in a cooled cell under a $\text{He}_{(g)}$ flow. During data acquisition, beam damage was assessed by measuring several short HERFD–XANES over the white line, exposing the sample and analyzing the white line intensity in order to assess any evidence for the oxidation state drift. Throughout, we did not see any evidence for beam damage effects. The resultant U M_4 -edge HERFD–XANES spectra were normalized according to their maxima, before analysis using Athena linear combination fitting to further quantify the likely proportion of U(VI), (V), and (IV) in the samples⁵⁶ and the best results from linear combination fitting had a *R*-factor < 0.02 (Figure S5, Table S2).

U L_3 -edge XAS samples were prepared from cell suspensions and/or centrifuged solid precipitates which had been stored at -80 °C after harvesting for analysis. Samples were maintained

at $-80\text{ }^{\circ}\text{C}$ during transport to Diamond Light Source, Harwell, UK for XAS analysis on B18.⁵⁷ U L_{3} -edge spectra were collected in a liquid N_2 cryostat in either fluorescence or transmission mode using a 36 element Ge detector, with in-line yttrium foil reference for energy calibration. During data acquisition, beam damage was assessed by measuring several quick EXAFS spectra, exposing the sample and analyzing the spectral features (peak height, position, and intensities) in order to assess any evidence for oxidation state drift. Throughout, we did not see any evidence for beam damage effects. Software packages ATHENA and ARTEMIS were used to analyze the EXAFS spectra⁵⁶ (Supporting Information Section S3).

RESULTS AND DISCUSSION

Aqueous Geochemistry and Luminescence Spectroscopy. When supplied with U(VI) and electron donor (lactate), washed cell suspensions of *S. oneidensis* MR1 removed up to 90% of the initial aqueous U(VI) from solution after 24 h and 99.5% after 120 h, as shown by ICPMS and luminescence spectrometry (Figure 1). The solution changed

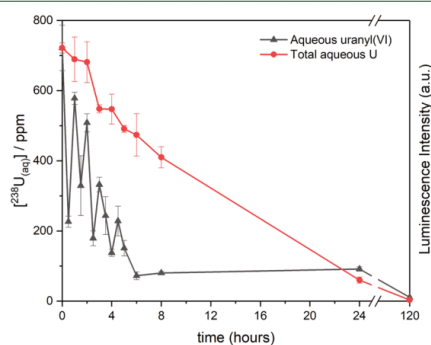


Figure 1. Aqueous uranyl(VI) (grey) and total aqueous U (red). Aqueous uranyl(VI) concentrations were determined by the luminescence intensity at $-196\text{ }^{\circ}\text{C}$ ($\lambda_{\text{ex}} = 405\text{ nm}$), and the total aqueous U concentrations were determined by ICPMS. Both measurements were recorded on the supernatant after centrifugation (16,160g, 5 min). Luminescence intensity was normalized to the initial $\text{U}_{(\text{aq})}$ concentration and the error bars represent 1 standard deviation on triplicate measurements.

from yellow to grey suggesting reduction of soluble U(VI). U sorption to autoclaved cells was quantified in a control experiment, after 2 and 4 h, 9 and 17% U was removed by adsorption to the *S. oneidensis* MR1 cells, respectively (Figure S1). Thermodynamic modeling, carried out using the PHREEQC software package, and UV-vis spectroscopy of the reaction medium suggested that under the conditions employed, uranyl(VI) trisulfate dominates solution (Table S1, Figure S5).^{58,59} Luminescence spectroscopy of supernatant samples yielded diagnostic, vibrationally resolved U(VI), as uranyl(VI), emission spectra centered at 525 nm.¹⁰ As emission intensity is directly proportional to the uranyl(VI) concentration (provided that the uranyl(VI) speciation is unchanged), luminescence spectroscopy was used semi-quantitatively to assess the change in uranyl(VI) concentrations present in the supernatant.^{60,61} Over 24 h incubation, the luminescence emission intensity showed a decreasing

trend, but with noticeable fluctuations within the first 5 h which is consistent with a saw-tooth uranyl(VI) signal. The significant difference in concentrations of aqueous U, as determined by ICPMS, and aqueous uranyl(VI), as determined by luminescence spectroscopy, also suggests the presence of a significant fraction of nonuranyl(VI), nonluminescent (under the conditions employed) U-containing species. These results are likely due to a single electron transfer mechanism generating transient, nonluminescent (under the conditions employed) uranyl(V),⁶² followed by disproportionation to luminescent uranyl(VI) and nonluminescent (under the conditions employed) U(IV),⁶³ as observed for *Geobacter*.¹⁰ (Figure 1). The fluctuations in uranyl(VI) concentrations are consistent with the previous literature suggesting a uranyl(V) intermediate proceeding via a disproportionation mechanism,^{9,10,37,41,64} and the saw-tooth pattern is not consistent with U(IV) reoxidation which generally occurs on much longer timescales (weeks–months).^{65–67}

In the current work, this implies that enzymatic reduction mediated by cells of *S. oneidensis* MR1 is occurring in a similar way to the *Geobacter* system, and via the reduction of uranyl(VI) to an intermediate U(V) species, which is not emissive in the 450–600 nm window employed following a 405 nm excitation.^{10,62} The decrease and subsequent increase in the uranyl(VI) signal steps are consistent with dynamic uranyl(V) disproportionation to luminescent uranyl(VI) and nonluminescent U(IV) species (Figures 1 and S4) and the relevant literature.^{9,10} The clear fluctuations and difference in total U versus uranyl(VI) assessed using luminescence intensity were broadly reproducible over the first 120 h of bioreduction and the kinetics are discussed in the Supporting Information (Figure S4).

X-ray Absorption Spectroscopy: U M_4 -Edge HERFD-XANES. U M_4 -edge analysis has recently been shown to be highly diagnostic for U(VI), U(V), and U(IV) species in complex systems.^{38,40,44,68} Here, U M_4 -edge HERFD-XANES data were collected at 4.5 h (on the cell suspension and cell pellet) and 120.5 h (cell pellet) to further explore the U-oxidation state distribution in the bioreduction experiment. For the 4.5 h cell pellet and cell suspension samples, the U M_4 -edge HERFD-XANES spectra were intermediate between the U(VI) and U(IV) standards (Table S2, Figure S6). We first performed a linear combination fitting of the HERFD-XANES spectra for all samples using only U(VI) and U(IV) standards; however, this yielded unsatisfactory results (Figures S6 and S7, Table S3). The linear combination fits for all samples were improved using either a uranyl(V)^{30,69} or a uranate(V)^{70,71} standard with the U(IV) and U(VI) standards (Figures S6 and S7, Table S3). Our data confirmed U(V) as a major reaction product in the reduction of U(VI) by *S. oneidensis* MR1, although as fits using uranyl(V) only provided marginally better fits than uranate(V), the exact geometry of U(V) at 4.5 h remains inconclusive (Figure S7, Table S3). Linear combination fits for the 4.5 h cell suspension showed either 59% uranyl(V) or 36% uranate(V), with the remaining uranium present as uranyl(VI), consistent with luminescence data and literature.⁹ The 4.5 h cell pellet was fitted with either 71% uranyl(V) or 47% uranate(V) and 23–24% UO_2 , with the remaining uranium present as uranyl(VI). This suggests that U(V) can remain associated with the biomass during bioreduction/disproportionation. Interestingly, the U(IV) signal observed on solids was below the detection limit in the cell suspension due to different contributions from the

solution and the solid phase in these two samples (Figures 1 and 2, Table S3). For the 120.5 h sample, a cell pellet was

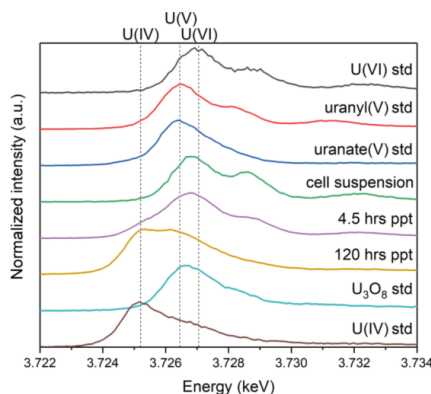


Figure 2. Normalized U M_4 -edge HERFD-XANES spectra for the solid phase: U(IV) O_2 standard (brown); U_3O_8 (2 U(V):1 U(VI)) standard (turquoise); 120.5 h end-point (yellow); 4.5 h cell precipitate (purple); 4.5 h cell suspension (green); uranate(V) standard (blue), uranyl(V) standard (red), and U(VI) O_3 standard (black) (std and ppt are used as abbreviations for standard and precipitate, respectively).

analyzed and the M_4 -edge HERFD-XANES showed clear differences to the chemically precipitated U(IV) O_2 standard. Here, linear combination fitting between U(VI), (V), and (IV) estimated approximately 26–28% U(V) and 72–74% U(IV)- O_2 was present in the sample for both uranyl(V) and uranate(V) fits, respectively (Figures S6 and S7, Table S3). Again, this suggests a significant fraction of U(V) in the cell pellet over 120.5 h (Figure S7, Table S3). Typically, the accuracy of oxidation state determination from XANES data is ± 10 –15%.⁷²

X-ray Absorption Spectroscopy: U L_3 -Edge. U L_3 -edge XANES and EXAFS data collected on cell suspensions from cultures of *S. oneidensis* MR1 supplied with uranyl(VI) were collected after 2.5 and 4.5 h, and on the cell pellet collected at 120.5 h. The edge position for the samples at 2.5 and 4.5 h

were in between the U(VI) and U(IV) standards, which suggested that the cell suspensions contained a mixture of U-oxidation states (Table S4, Figure S7). The structure is also different from the U(VI) and U(IV) standards, which may be due to the presence of other U species. By the 120.5 h end point, the U L_3 -edge XANES matched the U(IV) standard, suggesting that U(IV) dominated in the sample (Figure S6 and Table S3). Unlike U M_4 -edge HERFD-XANES, U L_3 -edge XANES cannot fully quantify the uranium oxidation state in complex samples with mixed U(VI), (V), and (IV) oxidation states.^{38,73} Specifically in the case of complex spectra of the type expected in these bioreduction experiments, quantifying U(VI), (V), and (IV) contributions with U L_3 -edge XANES is challenging.^{38,73}

Fitting of the U L_3 -edge EXAFS data was used to further explore the speciation of U and the distribution of U(VI), (V), and (IV) in the samples. Although EXAFS fitting does not provide direct information regarding the oxidation state, the fitting parameters obtained can be used to indirectly infer U-oxidation states. Here, the characteristic presence and extension of the uranyl $U=O_{ax}$ bond length from 1.8 Å for uranyl(VI) to 1.9 Å for uranyl(V),^{9,22,32,35} and the lack of a U–O, uranate(V), bond length at 2.1–2.2 Å^{40,44,74,75} were particularly pertinent in fitting. Any attempts of fitting using a uranate-like speciation proved unsuccessful. Overall the EXAFS and associated Fourier transforms for the 2.5 and 4.5 h cell suspension samples were remarkably consistent (Figure 3). Informed by the relevant literature, the 2.5 h cell suspension was fitted as uranyl triscarbonate species.^{9,10} Here, the best fit was consistent with an average $U=O_{ax}$ bond length of 1.86 Å (Table 1), supporting an approximately 40 \pm 10%:60 \pm 10% contribution from uranyl(VI) (1.8 Å^{9,32,35,76}) and uranyl(V) (1.9 Å^{9,32,35,76}). We note that this ratio should be treated as an estimate as it will be affected by the number of species and their relative Debye–Waller factors; although the Debye–Waller factors for both uranyl(V/VI) species have been shown to be very similar.^{32,35} Nonetheless, this suggests a significant reduction from the uranyl(VI) species in this sample. The dioxygenyl bond length is significantly longer than values for uranyl(VI) (1.79–1.80 Å^{32,35,76}), it is also significantly shorter than U–O bond lengths in uranate(V/VI) complexes (2.11–2.18 and 2.36–2.42 Å for uranate(V/VI), respectively^{40,44,74,75}), suggesting a mixed valence, uranyl(V/VI)

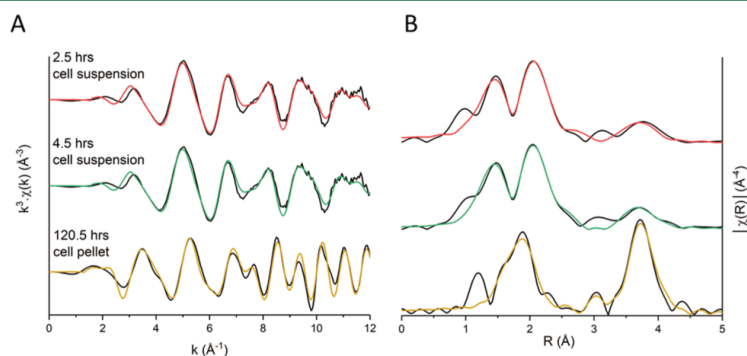


Figure 3. U L_3 -edge EXAFS spectra for uranyl(VI) reduced by *S. oneidensis* MR1 after 2.5 h (cell suspension) (red), 4.5 h (cell suspension) (green) and 120.5 h (precipitate, with uranyl(V) contribution) (yellow). Panel (A) k^3 -weighted EXAFS; panel (B) Fourier transform of k^3 -weighted EXAFS. Black lines show experimental data and colored lines show the fits described in Table 1.

Table 1. Fitting Parameters Obtained from U L₃-Edge EXAFS Spectroscopy^a

sample	scattering path	N	R (Å)	σ^2 (Å ²)	S ₀ ^c	R-factor	α^b
2.5 h cell suspension	U=O _{ax}	2	1.86(1)	0.008(1)	1	0.014	99.9 ^f
	U-O _{eq}	4	2.37(3)	0.012(7)			
	U-O _{eq}	2	2.48(1)	0.004(1)			
	U...C	3	2.93(2)	0.003(2)			
	U...O _{dist}	3	4.22(2)	0.006(2)			
	(MS) U...O _{dist}	6	4.21(2)*	0.006(2)*			
4.5 h cell suspension	(MS) U...O _{dist}	3	4.21(2)*	0.006(2)*	1	0.016	100.0 ^f
	U=O _{ax}	2	1.86(1)	0.008(2)			
	U-O _{eq}	4	2.36(3)	0.010(6)			
	U-O _{eq}	2	2.49(1)	0.003(1)			
	U...C	3	2.92(2)	0.005(2)			
	U...O _{dist}	3	4.23(1)	0.007(2)			
120.5 h cell pellet with U(V)	(MS) U...O _{dist}	6	4.21(2)*	0.007(2)*	1	0.017	99.9 ^d
	(MS) U...O _{dist}	3	4.21(2)*	0.007(2)*			
	U=O _{ax}	0.4	1.92(5)	0.008(5)			
	U-O	7	2.36(0)	0.012(1)			
	U-U	12	3.86(1)	0.008(0)			
	U-O _{dist}	24	4.44(0)	0.009(1)			

^aN, R, σ^2 , S₀^c and the R-factor refer to the coordination number, radial distance, Debye–Waller factor, amplitude correction factor, and the goodness of fit, respectively. Uncertainty in interatomic distances is quoted in brackets for the last decimal place (Å). Spectra have been plotted in R and k^3 in Figure 3. * Parameters fixed during fitting. ^bF-test results; $\alpha > 0.95$ statistically improves the fit with 2 σ confidence. ^cF-test results for adding the U–O_{dist} feature and associated multiple scatterers at 4.2 Å. ^dF-test results for adding the U(V)=O_{ax} feature at 1.9 Å.

system at 2.5 and 4.5 h. The equatorial shell was fitted as a split shell with 2 O backscatterers at approximately 2.4 Å (consistent with uranyl(VI) equatorial oxygen 2.42–2.45 Å^{9,32,35,76}) and four O backscatterers at approximately 2.5 Å (consistent with uranyl(V) equatorial oxygen 2.47–2.50 Å^{9,32,35}) (Table 1). Additional features in the EXAFS and Fourier transform were successfully modeled by inclusion of 3 C backscatterers at approximately 2.9 Å, and 3 O backscatterers at approximately 4.2 Å. Again, these are consistent with contributions from uranyl(VI) and uranyl(V) triscarbonate species (U(VI, V)–C = 2.88–2.94 Å, and U(VI, V)–O_{dist} = 4.13–4.28 Å^{9,32,35,76}) and support significant reduction to uranyl(V) at 2.5 h. This is consistent with the luminescence data which showed significant reduction in uranyl(VI) luminescence at 2.5 h. For both the 2.5 and 4.5 h samples, the EXAFS and Fourier transform data were similar (Figure 3) and here, the 4.5 h sample could be fitted with essentially the same coordination environment as the 2.5 h sample (Table 1). The EXAFS fits for the data at 4.5 h were consistent with the 4.5 h U M₄-edge HERFD–XANES LCF analysis using a uranyl(V) standard showing approximately ~60% U(V), present as uranyl(V) (Figure 3). Interestingly, the geochemical data and U M₄-edge linear combination fitting results suggest that up to 10% U(IV) may be present at 4.5 h (Figures 1 and 2). A fit containing 10% U(IV) contribution improved the results, although the additional shell did not contribute statistically to the fit and was thus not included. Overall, EXAFS fitting for the 2.5 and 4.5 h cell suspensions showed evidence for the extension of the dioxygenyl bond length in uranyl(VI) (1.8 Å;^{9,32}) to 1.86 Å. These fits are consistent with approximately 40% uranyl(VI) and 60% uranyl(V) in the samples, which agreed with the luminescence data (Figure 1), the U M₄-edge HERFD–XANES LCF using a uranyl(V) standard (Figure 2), and with past work, where approximately 60% reduction to uranyl(V) was reported for bioreduction with *G. sulfurreducens* at 4 h.⁹ This suggested uranyl(V) as a transient bioreduction product in agreement with micro-

biological studies,^{9,10,12} and in contrast to recent work on U(V) stabilization in Fe-oxides where uranate(V)-like incorporation dominates.^{40,44}

Finally, the 120.5 h cell pellet EXAFS data were first fitted with 8 O backscatterers at 2.36 Å and 12 U backscatterers at 3.86 Å, consistent with crystalline uraninite and in agreement with past work.^{51,52} However, because of unsatisfactory σ^2 values in the U–O scattering paths (Table S2), and with the new information suggesting a U(V) state in the end-point, we further considered a contribution from U(V) in the U L₃-edge EXAFS fitting for the end-point sample again informed by the relevant literature.^{9,32} The Fourier transform showed a feature at ~1.9 Å before the U(IV)–O shell in uraninite at 2.36 Å. Here, we attempted a fit with approximately 20% of uranyl(V), which statistically contributed to the fit (F-test 99.9%). The resulting fit with a modest 0.4 axial U=O_{ax} backscattering contribution at 1.92 Å and with a reduced U–O contribution of 7 O was consistent with an approximately 20% contribution from uranyl(V) in the bioreduction end point (Tables 1, S4 and Figure 3). This estimate is consistent with the linear combination fitting value of approximately 28% uranyl(V) estimated with U M₄-edge HERFD–XANES. Our interpretation of these data suggests, for the first time, the presence of a long-lived 20–30% uranyl(V) intermediate associated with the biomass/precipitate after 5-days of bioreduction.

Where most work on U(V) under environmentally relevant conditions has addressed the role of Fe in stabilizing U(V),^{40,41,44,78} the combined approach presented here increases the understanding and importance of U(V) in biological systems by demonstrating that *S. oneidensis* MRI operates a one electron transfer mechanism for uranyl(VI) bioreduction. In the supernatant, the difference in total U_(aq), as determined by ICPMS, and the uranyl(VI) concentrations, as determined by luminescence spectroscopy, suggested that up to ~60% of the U was present as a nonuranyl(VI) species in solution at 2.5 and 4.5 h. Here, further analysis of cell suspensions, where the U signal is dominated by aqueous U,

using U M_4 -edge HERFD–XANES defined a significant portion of the species as pentavalent U; although it was not possible to distinguish between uranyl(V) and uranate(V)-like speciation. In the U L_3 -edge EXAFS, the characteristic extension of the $U=O_{ax}$ bond and the lack of a uranate U–O bond are consistent with uranyl(V) after 2.5 and 4.5 h of bioreduction, although this requires further investigation. In agreement with previous findings, this work suggests that biological uranyl(VI) reduction pathways preferentially reduce via 1 electron transfer mechanisms. Given that *S. oneidensis* MR1 reduces U(VI) via the Mtr extracellular pathway which transfers one electron at a time, the results published here are consistent with relevant literature.^{13,14,79,80} Also, this is similar to the single electron transfer mechanisms observed in U(VI) reduction pathways in iron-rich geological systems.^{40,44} The presence of U(V) in both the cell suspension and the cell precipitate suggests that the U(V) was not associated exclusively with the cells, in agreement with similar *Geobacter* systems.^{9,10} This suggests that the mechanism(s) of electron transfer from *S. oneidensis* MR1 to U(VI) could involve multiple (intracellular and extracellular) electron transfer pathways, as supported by the relevant literature.^{13–16,81} Furthermore, we have established that U(V) can persist for appreciable lifetimes (at least 120.5 h) under environmentally relevant conditions in contrast to past studies, where it has been considered transient (less than 24 h).^{9,10} The discovery of a potentially persistent U(V) species in the endpoint sample suggests that it could play a previously unrecognized role in the remobilization of “bioreduced” U. In turn, this greatly improves the mechanistic understanding of environmental U speciation and it further broadens the field of stability for U(V) at circumneutral pH. Indeed, U(V) behavior in environmental conditions has not yet been fully explored, and thus further work in more environmentally relevant settings are merited.

■ ASSOCIATED CONTENT

Supporting Information

The Supporting Information is available free of charge at <https://pubs.acs.org/doi/10.1021/acs.est.9b05285>.

Additional information on U sorption to autoclaved cells, aqueous and luminescence analyses and X-ray absorption spectroscopy: (U L_3 -edge XANES; U L_3 -edge EXAFS; and, M_4 -edge HERFD–XANES) (PDF)

■ AUTHOR INFORMATION

Corresponding Author

Jonathan R. Lloyd – Williamson Research Centre for Molecular Environmental Science and Research Centre for Radwaste Disposal, Department of Earth and Environmental Science, School of Natural Sciences, The University of Manchester, Manchester M13 9PL, England; Email: jon.lloyd@manchester.ac.uk

Authors

Gianni F. Vettese – Williamson Research Centre for Molecular Environmental Science and Research Centre for Radwaste Disposal, Department of Earth and Environmental Science, School of Natural Sciences, The University of Manchester, Manchester M13 9PL, England; orcid.org/0000-0003-0510-9542

Katherine Morris – Williamson Research Centre for Molecular Environmental Science and Research Centre for Radwaste

Disposal, Department of Earth and Environmental Science, School of Natural Sciences, The University of Manchester, Manchester M13 9PL, England; orcid.org/0000-0002-0716-7589

Louise S. Natrajan – Centre for Radiochemistry Research, Department of Chemistry, School of Natural Sciences, The University of Manchester, Manchester M13 9PL, England; orcid.org/0000-0002-9451-3557

Samuel Shaw – Williamson Research Centre for Molecular Environmental Science and Research Centre for Radwaste Disposal, Department of Earth and Environmental Science, School of Natural Sciences, The University of Manchester, Manchester M13 9PL, England; orcid.org/0000-0002-6353-5454

Tonya Vitova – Institute for Nuclear Waste Disposal (INE), Karlsruhe Institute of Technology, Karlsruhe 76131, Germany; orcid.org/0000-0002-3117-7701

Jurij Galanzew – Institute for Nuclear Waste Disposal (INE), Karlsruhe Institute of Technology, Karlsruhe 76131, Germany

Debbie L. Jones – College of Environmental Sciences and Engineering, Bangor University, Bangor LL57 2DG, U.K.

Complete contact information is available at: <https://pubs.acs.org/10.1021/acs.est.9b05285>

Author Contributions

The manuscript was written through contributions of all authors. All the authors have given approval to the final version of the manuscript.

Notes

The authors declare no competing financial interest.

■ ACKNOWLEDGMENTS

This work was funded by the Nuclear Decommissioning Authority (NDA) managed by the National Nuclear Laboratory (NNL). We also acknowledge funding from the NERC funded OPTIUM (Optical Imaging of Uranium Biotransformations by Microorganisms) grant (NE/R011230/1), Diamond Light Source (DLS) for beamtime awards (SP17243 and SP13559), and the KIT synchrotron radiation source for beamtime access. The KIT Institute for Beam Physics and Technology (IBPT) is acknowledged for the operation of the storage ring, the Karlsruhe Research Accelerator (KARA), and provision of beamtime at the KIT synchrotron source. We thank Steven Parry and Giannantonio Cibin for beamtime assistance at DLS and Bianca Schacherl at the KIT synchrotron radiation source. We also thank Luke Townsend, Kurt Smith, and Thomas Neill for assistance with data analysis, Paul Lythgoe for data acquisition, and Pieter Bots and Thomas Neill for the XAS spectra of synthetic UO_2 and $[UO_2(CO_3)_3]^{4-}$, respectively.

■ REFERENCES

- (1) Lovley, D. R.; Phillips, E. J. P.; Gorby, Y. a.; Landa, E. R. Microbial Reduction of Uranium. *Nature* **1991**, *350*, 413–416.
- (2) Anderson, R. T.; Vrionis, H. A.; Ortiz-Bernad, I.; Resch, C. T.; Long, P. E.; Dayvault, R.; Karp, K.; Marutzky, S.; Metzler, D. R.; Peacock, A.; White, D. C.; Lowe, M.; Lovley, D. R. Stimulating the In Situ Activity of *Geobacter* Species to Remove Uranium from the Groundwater of a Uranium-Contaminated Aquifer. *Appl. Environ. Microbiol.* **2003**, *69*, S884–S891.
- (3) Williams, K. H.; Long, P. E.; Davis, J. a.; Wilkins, M. J.; N'Goussan, a. L.; Steefel, C. I.; Yang, L.; Newcomer, D.; Spane, F. a.; Kerkhof, L. J.; McGuinness, L.; Dayvault, R.; Lovley, D. R. Acetate

1 **Multiple lines of evidence identify U(V) as a key intermediate during U(VI) reduction**
2 **by *Shewanella oneidensis* MR1 – Supporting Information**

3

4 Gianni F. Vettese,[‡] Katherine Morris,[‡] Louise S. Natrajan,[§] Samuel Shaw,[‡] Tonya Vitova,[#] Jurij
5 Galanzew,[#] Debbie L. Jones,[†] and Jonathan R. Lloyd*[‡]

6

7 [‡]*Williamson Research Centre for Molecular Environmental Science and Research Centre for Radwaste*
8 *Disposal, Department of Earth and Environmental Science, School of Natural Sciences, The University of*
9 *Manchester, Oxford Road, Manchester, England, M13 9PL*

10 [§]*Centre for Radiochemistry Research, Department of Chemistry, School of Natural Sciences, The*
11 *University of Manchester, Oxford Road, Manchester, England, M13 9PL*

12 [#]*Institute for Nuclear Waste Disposal (INE), Karlsruhe Institute of Technology, Karlsruhe, Germany*

13 [†]*College of Environmental Sciences and Engineering, Bangor University, Bangor, UK*

14

15 **Summary:** The supporting information contains further details on methodology and analyses. The
16 specific sections that follow are: S1 U sorption to cells; S2 Aqueous and luminescence analyses;
17 X-ray Absorption Spectroscopy: (U L₃-edge XANES; U L₃-edge EXAFS; and, M₄-edge HERFD-
18 XANES).

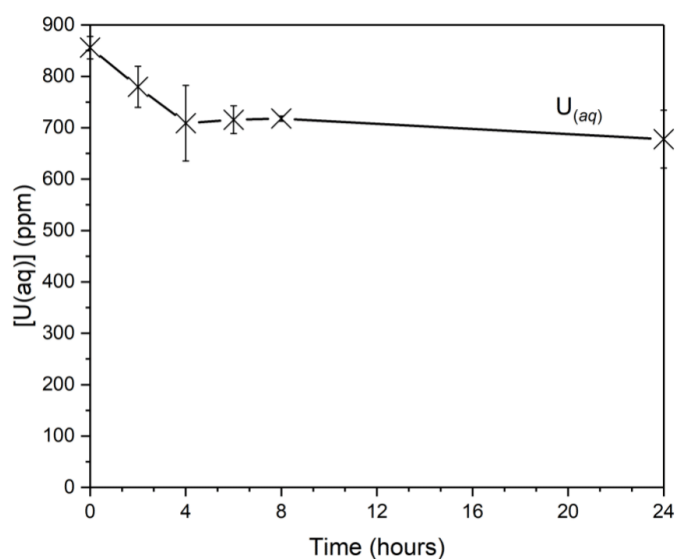
19

20

21 **S1: U sorption to cells**

22 Uranyl(VI) (850 ppm) was added in triplicate to autoclaved cells of *Shewanella oneidensis* MR1
23 in buffer solution (NaHCO₃ 30 mM, lactate 10 mM). U_(aq) in the supernatant of centrifuged (16160
24 g, 5 mins) samples were monitored periodically for U_(aq) removal.

25 Figure S1 shows U bio-sorption to dead cells of *Shewanella oneidensis* MR1. The slight decrease
26 in U_(aq) concentrations suggests that U first sorbs to cells of *Shewanella oneidensis* MR1 before
27 reduction and further removal from solution. By 4 hours up to 17 % of U adsorbs to the autoclaved
28 cells, and this number peaks at 21 % after 24 hrs. By comparison, living cells removed up to 92 %
29 U_(aq) after 24 hrs (Figure S4); thus extensive removal of U_(aq) can be attributed to microbial
30 metabolisms.

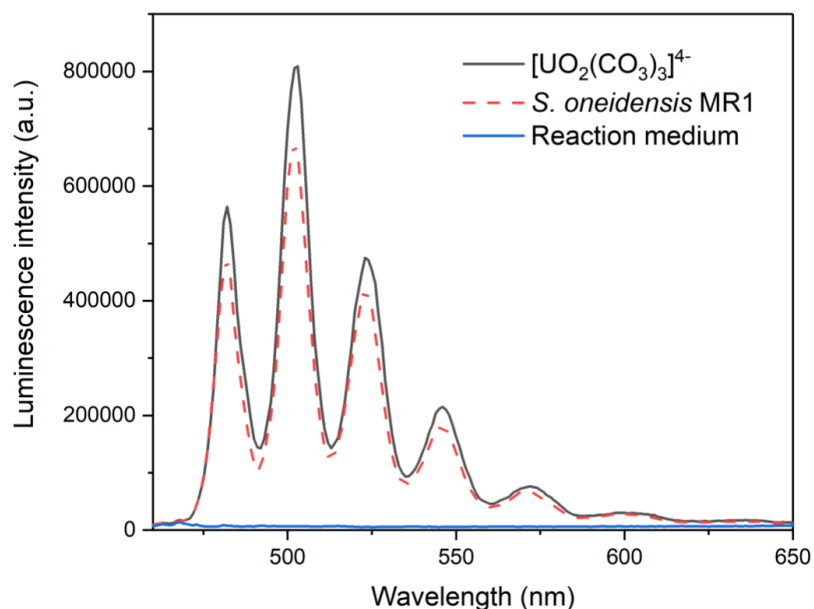


31

32 Figure S1: U_(aq) in solution upon contact with autoclaved cells of *Shewanella oneidensis* MR1, determined
33 by ICPMS. At time = 0, 2, 4, 6, 8 and 24 hrs removal from solution was 0 %, 9%, 17%, 16%, 16% and
34 21 % respectively. Errors represent one standard deviation; the experiment was run in triplicate.

35 **S2: Aqueous and luminescence analyses**

36 Figure S2 below shows the emission spectra taken for uranyl(VI) in solution as $[\text{UO}_2(\text{CO}_3)_3]^{4-}$, the
37 emission spectra taken after the addition and centrifugation of cells of *S. oneidensis* MR1, and the
38 emission spectra for the reaction medium (including cells) without the presence of U. The distinct
39 emission bands between 450 and 600 nm are characteristic of uranyl(VI) emission ¹, and the
40 reaction medium containing cells of *S. oneidensis* MR1 in the absence of U show little auto-
41 fluorescence or scattering (Figure S2).



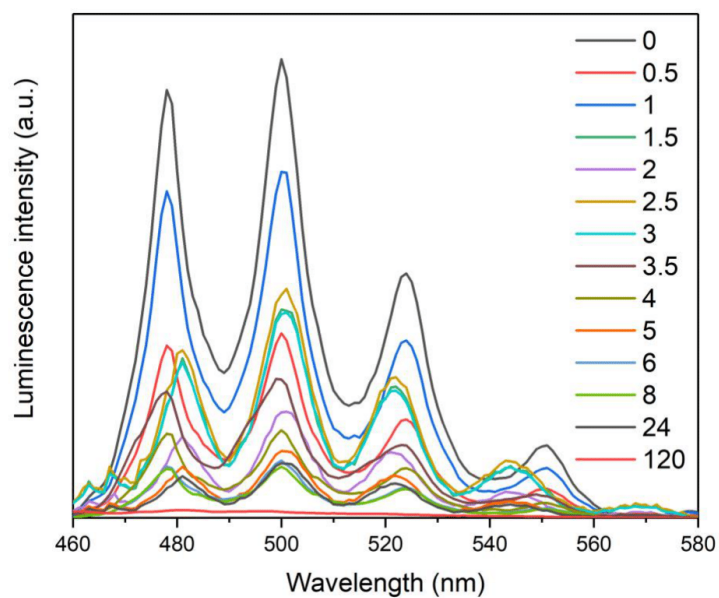
42

43 **Figure S2:** Steady state emission profile of 77 K solution of uranyl(VI) dichloride (3 mM) in sodium
44 carbonate buffer (30 mM) and lactate (10 mM) before the addition of *S. oneidensis* MR1 (grey), after the
45 addition and centrifugation of *S. oneidensis* MR1 (red), and of the reaction medium (blue) ($\lambda_{\text{ex}} = 405 \text{ nm}$).

46

47 The decrease and subsequent increase in the uranyl(VI) emission in the supernatant with time over
48 the course of the bioreduction is a result of the consumption of uranyl(VI) corresponding to
49 enzymatic reduction. This approximately follows first order kinetics with respect to uranyl(VI),
50 resulting in a steady decrease in the uranyl(VI) luminescence intensity corresponding to a one
51 electron reduction event to non-emissive uranyl(V). Since the disproportionation of uranyl(V) has
52 been studied experimentally² and calculated computationally³, it is now widely accepted to be a
53 second order reaction with respect to uranyl(V) concentration via the formation of a bimetallic
54 uranyl(V)-uranyl(V) adduct which provides the path way for inner sphere electron transfer to re-
55 form uranyl(VI) and form U(IV). As such the rate of re-formation of uranyl(VI)/consumption of
56 uranyl(V) should increase quadratically with increasing uranyl(V) concentration. Furthermore the
57 presence of unreduced uranyl(VI) in solution alongside uranyl(V), has been shown to retard the
58 rate of uranyl(V) disproportionation due to the formation of uranyl(V)-uranyl(VI) bimetallic
59 adduct complexes which cannot disproportionate in the same fashion according to the above
60 mechanism². The additive effect of these suggests that as more uranyl(VI) is consumed, the rate
61 of disproportionation should increase as the relative concentration of the uranyl(V)-uranyl(VI)
62 adduct decreases (i.e. more productive uranyl(V)-uranyl(V) encounters). This is consistent with
63 the experimental observations and dynamic uranyl(V) disproportionation to luminescent
64 uranyl(VI) and non-luminescent U(IV) species (Figure 1, Figure S2) and also with the relevant
65 literature^{1,4}. Interestingly, in the 2-3 hour region the emission spectra maxima are shifted to
66 slightly longer wavelengths compared to the other spectra (Figure S3). From these bathochromic
67 shifts it can be concluded that during the bioreduction process there may be some variation in
68 uranyl(VI) speciation although it is not possible to define the change in species and relative
69 contributions to the overall emission intensities at this time^{5,6}. Measurements on the aqueous and

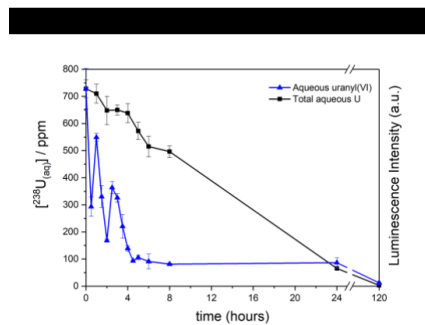
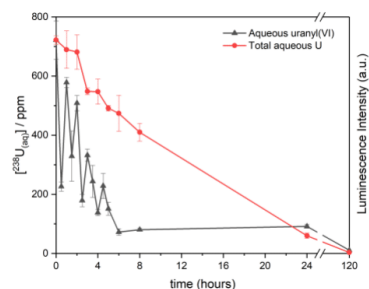
70 luminescence data from the same reaction but set up on different days show reproducible patterns
71 but due to changes in the microbial preparation exact timings may change to some extent (Figure
72 S4).



73

74 **Figure S3:** The varying intensity of uranyl(VI) emission with time, in the supernatant steady-state
75 emission spectrum of anaerobic solutions containing *Shewanella oneidensis* MR1 challenged with
76 uranyl(VI) ($\lambda_{\text{ex}} = 405 \text{ nm}$, $-96 \text{ }^\circ\text{C}$ [77 K]).

77



78

79 **Figure S4:** Aqueous uranyl(VI) and Total aqueous U. Aqueous uranyl(VI) concentrations were determined
 80 by the luminescence intensity at -196 °C ($\lambda_{\text{ex}} = 405 \text{ nm}$), and the Total aqueous U concentrations were
 81 determined by ICPMS. Both measurements were recorded on the supernatant after centrifugation (16160
 82 *g*, 5 mins). Luminescence intensity was normalised to the initial $U_{(\text{aq})}$ concentration and the error bars
 83 represent 1 standard deviation based on triplicate measurements. A) run 1; and B) run 2.

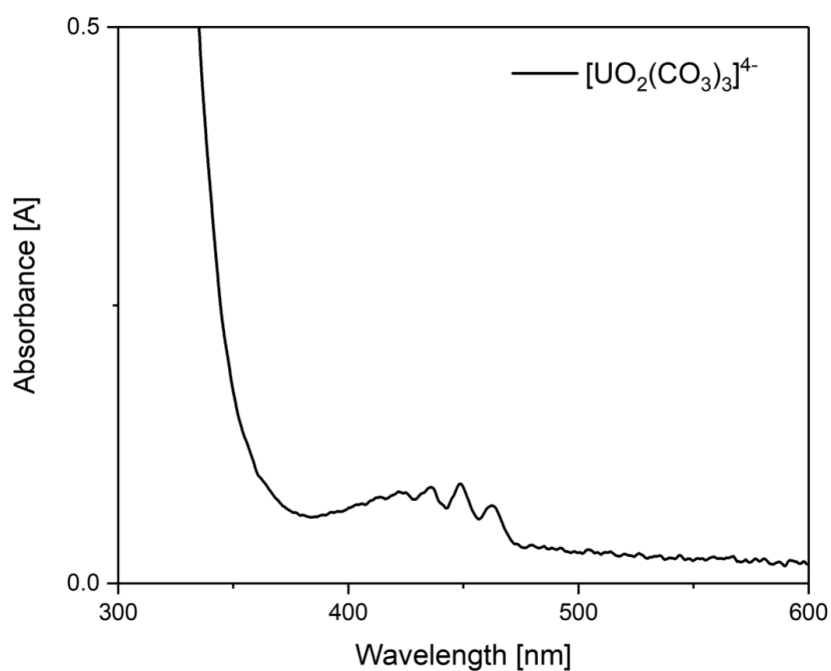
84 Thermodynamic modelling was carried out using PHREEQC (version 3.0.0) coupled to the
 85 ANDRA SIT database⁷ and supplemented with data from Ulrich *et al.*, 2011⁸ to calculate uranyl
 86 speciation in the reaction medium containing UO_2Cl_2 (3 mM, 714 ppm U), NaHCO_3 (10 mM)
 87 sodium lactate (10 mM) (298 K). The results showed that $\text{UO}_2(\text{CO}_3)_3^{4-}$ was the dominant species
 88 in solution (94 %) (Table S1: Uranyl(VI) speciation as described by PHREEQC calculations Table
 89 S1) consistent with relevant literature^{1,9,10}. These data are also supported by the absorption spectra
 90 taken of the reaction medium containing (UO_2Cl_2 (3 mM, 714 ppm U), NaHCO_3 (10 mM) sodium
 91 lactate (10 mM) (298 K) (Figure S5), which is consistent with the published absorption spectra of
 92 $[\text{UO}_2(\text{CO}_3)_3]^{4-}$ ¹¹.

93 **Table S1:** Uranyl(VI) speciation as described by PHREEQC calculations

Species	Molality	Activity	% Molality of total U(VI)
---------	----------	----------	---------------------------

$\text{UO}_2(\text{CO}_3)_3^{4-}$	2.821e-03	9.551e-05	94.0
$\text{UO}_2(\text{CO}_3)_2^{2-}$	1.747e-04	7.521e-05	4.9
$(\text{UO}_2)_3(\text{CO}_3)_6^{-6}$	1.240e-06	6.058e-10	4.1e-03
UO_2^{2+}	2.217e-12	9.784e-13	7.4e-08
UO_2Lac^+	1.204e-11	9.810e-12	4e-07

94



95

96 **Figure S5:** Absorption spectrum of UO_2Cl_2 (3 mM, 714 ppm U), NaHCO_3 (10 mM) sodium lactate (10 mM)
 97 (298 K), consistent with the published absorption spectrum of $[\text{UO}_2(\text{CO}_3)_3]^{4-11}$.

98 **S3: X-ray Absorption Spectroscopy:**

99 **U M_4 -edge HERFD-XANES**

7

100 A Si 111 Double crystal monochromator was used to measured the U M₄-edge (3728 eV) using
101 the M beta emission (3339.8 eV) with a Johann-type spectrometer with 4 analyser crystals (Si 110;
102 Bending radius 1 m; Bragg angle 75.2°) along a Rowland geometry with 1 m radius and a Ketek
103 SDD detector. The incident energy was monochromatised by a Si(111) double crystal
104 monochromator (DCM). The beam was focused to ~0.5 mm vertically and ~0.5 mm horizontally
105 onto the sample. The Johann type X-ray emission spectrometer installed at the CAT-ACT
106 beamline was applied for the HERFD-XANES experiments. Five analyser crystals and a single
107 diode VITUS silicon drift detector (VITUS SDD KETEK) were arranged in a vertical Rowland
108 geometry. The U M₄ edge HR-XANES spectra were obtained by recording the maximum intensity
109 of the U M_β (M4N6, E = 3337.0 eV) emission line ¹². The emitted photos were diffracted by the
110 five spherically bent Si(220) crystal analysers (SAINT-GOBAIN) with 1m bending radius and
111 focused onto a single diode VITUS SDD. A box encompassing the spectrometer and maintaining
112 constant He flow was installed to avoid intensity losses due to scattering and absorption of photons.
113 The DCM was calibrated by assigning 3.7252 eV to the white line maximum of the U M₄ HR-
114 XANES spectrum of a UO₂ sample. Linear Combination Fitting (LCF) was carried out using
115 Athena, from the Demeter suite using a uranyl (VI), (V) and uraninite sample as standards ¹³. The
116 uranyl(V), [K(Crypt)]₂[UO₂{N(SiMe₃)₂}₂] ¹⁴, and uranate(V), [Li(THF)₂U(POSS^{iBu})] (H₃POSS^{iBu}
117 = [(i-C₄H₉)₇Si₇O₉(OH)₃], POSS = partially oligomerised silsesquioxane) ¹⁵, standards were
118 synthesised and characterised according to the following publications respectively ^{14,15}.

119 We used the following standards for the linear combination fitting of the U M₄-edge HERFD-
120 XANES data: For U(VI) uranyl, schoepite; for U(IV), a well characterized uraninite standard was
121 use ¹⁶; for U(V), we used a synthetic U(V) uranyl compound ¹⁴, and a synthetic U(V) uranate
122 species ¹⁵. We also measured a U₃O₈ standard with a contribution from 1/3 U(VI) and 2/3 U(V).

123 The values obtained for linear combination fits are subject to uncertainty, typically the accuracy
 124 of oxidation state determination for XANES is 10-15 %¹⁷.

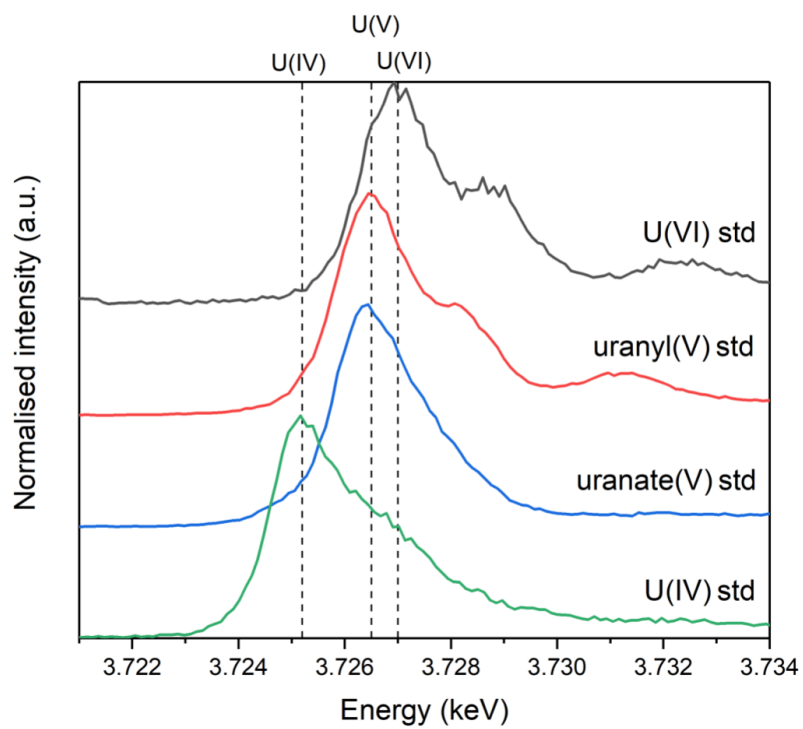
125

126 **Table S2:** U M₄-edge HERFD-XANES E₀ energies compared to published standards

Compound	U composition	E₀ position (first resonance) / eV	E₀ position (second resonance) / eV	Reference
UO ₃	U(VI)	3.7270	3.7285	This work
UO ₃ , UO ₂ (acac) ₂	U(VI)	3.7269 - 3.7270,	3.7286 - 3.7288	¹⁸⁻²¹
Cell suspension (4.5 hours)	U (IV, V and VI)	3.7267	3.7285	This work
Cell pellet (4.5 hours)	U (IV, V and VI)	3.7267	3.7285	This work
Cell pellet	U (IV, V and VI)	3.7253	3.7261	This work

(120.5 hrs)				
U ₃ O ₈	67 % U(V), 33 % U(VI)	3.7266		This work
U ₃ O ₈	67 % U(V), 33 % U(VI)	3.7264 - 3.7265		19,20
U(V)	U(V)	3.7264		18
U(V)O ₂ ⁺	U(V)	3.7264	3.7314	14
U(V)	U(V)	3.7264		15
U ₄ O ₉	50 % U(IV), 50 % U(V)	3.7251 - 3.7252	3.7262- 3.7263	19-21
UO ₂	U(IV)	3.7252		This work
UO ₂	U(IV)	3.7252 - 3.7253		18-20

127



128

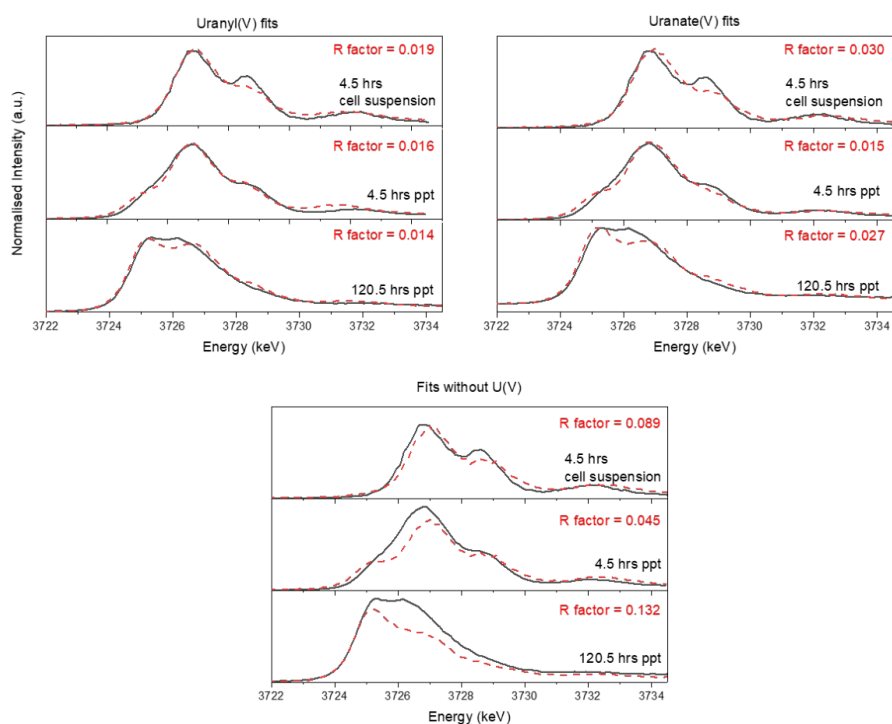
129 **Figure S6:** Standards used for U M₄-edge HERDF-XANES linear combination fitting; U(IV) standard
130 (green), uranate(V) standard (blue), uranyl(V) standard (red) and U(VI) standard (black). Fits were
131 performed in a range from 3.722-3.7335.

132

133 **Table S3:** Linear combination fit results for U M₄-edge HERFD-XANES

Contribution	U(V) -yl fits				U(V) -ate fits				Fits without U(V)		
	VI	V	IV	R- Factor	VI	V	IV	R- Factor	VI	IV	R- Factor
4.5 hrs	41	59	0	0.019	63	36	0	0.030	70	30	0.089
Cell suspension (%)											
4.5 hrs	6	71	24	0.016	30	47	23	0.015	96	4	0.045
Precipitate (%)											
120.5 hrs	0	28	72	0.013	0	26	74	0.027	12	88	0.132
Precipitate (%)											
Sum of R-factors				0.049				0.072			0.266

134



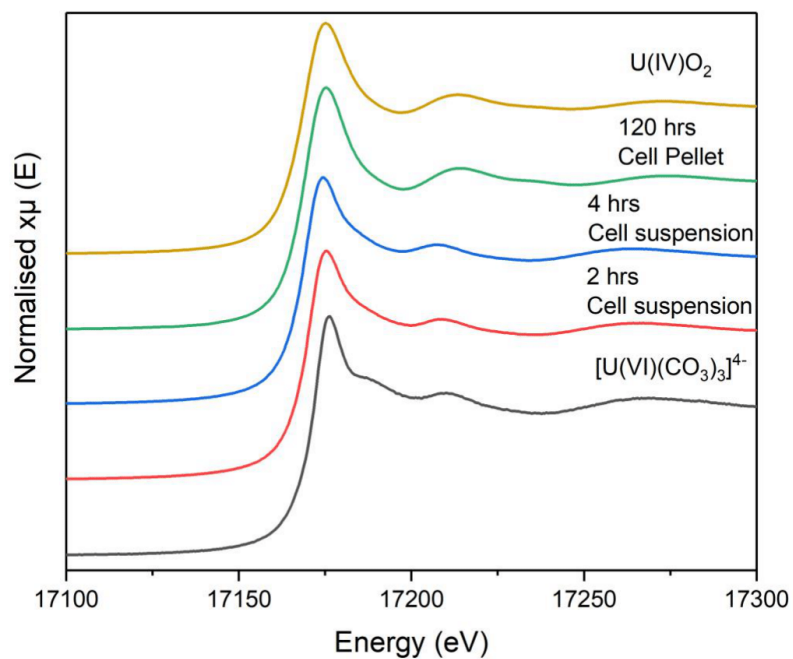
135

136 **Figure S7:** Linear combination fits for U M₄-edge HERFD-XANES, showing the data (black)
 137 combination fits (red dashed lines). In the top two diagrams, all fits were performed using a U(VI), U(V)
 138 and U(IV) standard, fits calculated using a uranyl(V) standard are on the left and fits calculated using a
 139 uranate(V) standard are on the right. On the bottom, fits were calculated using only U(VI) and U(IV)
 140 standards.

141 U L₃-edge XANES

142 U L₃-edge XANES spectra and E⁰ positions for each spectra are given in Figure S8 and

143 Table S4; model compounds of UO_2 , U_3O_8 , U_4O_9 and $\text{UO}_2(\text{CO}_3)_2$ are included^{19,22,23}. As time
144 progressed a general trend in E^0 values are noticeable as the uranyl(VI) is reduced to U(IV).



145

146 **Figure S8:** L₃-edge XANES spectra collected at 77 K of the 2hrs (red) and 4 hrs (blue) cell suspension, and
147 end-point pellet (green) compared to $[\text{U}^{\text{VI}}\text{O}_2(\text{CO}_3)_3]^{4-}$ (black) and UO_2 (yellow) standards from²² and²³
148 respectively.

149

150 **Table S4:** U L₃-edge E⁰ energies compared to published standards

Compound	U composition	E₀ position / eV	Reference
UO ₂ (CO ₃) ₃] ⁴⁻	U(VI)	17172.2	²²
Cell suspension (2.5 hours)	U (IV, V and VI)	17171.8	This work
Cell suspension (4.5 hours)	U (IV, V and VI)	17171.3	This work
Cell pellet (120.5 hrs)	U (IV, V and VI)	17169.8	This work
UO ₂	U(IV)	17170.2	²³
U ₃ O ₈	67 % U(V), 33 % U(VI)	17171.9-17172.2	¹⁹
U ₄ O ₉	50 % U(IV), 50 % U(V)	17171.4	¹⁹

151

152

153 **U L₃-edge EXAFS**

154 The EXAFS spectra were quantitatively fitted using the phase shift and backscattering functions
155 obtained using published reference structures of liebigite, Ca₂[UO₂(CO₃)₃] · ~11H₂O²⁴; and
156 uraninite, UO₂²⁵. Throughout analysis, coordination numbers (N) were fixed based on the relative
157 proportion of each U phase informed by crystallographic data; σ^2 (a Debye-Waller-type factor
158 based on Gaussian distribution of interatomic distances), R (interatomic distance / Å), and ΔE_0 (the
159 difference between the threshold Fermi level of the theoretical phase shift and backscattering
160 amplitude functions and the experimental data) values were allowed to refine. The amplitude
161 reduction factor, S_0^2 was fixed to 1 as preliminary fits converged to this value. The number of
162 degrees of freedom, defined as $N_{\text{idp}} \approx 2\Delta k\Delta r/\pi$ ²⁶, was always greater than the number of
163 parameters allowed to vary in the fitting process. Here, the fits at 2.5 and 4.5 hrs both used 11
164 variables, out of 17.2 and 18.2 independent points respectively; and the fit at 120.5 hours used 9
165 variables out of 19.9 independent points. All obtained fitting values were consistent with published
166 crystal structures. Details of the fitting routine and an explanation of the statistics reported can be
167 found in²⁷. The R-factor value was used in this study to evaluate the quality of fits. This method
168 of EXAFS fitting is consistent with previously published literature e.g.^{16,18,23,28,29}. The Fourier
169 transform of the samples at 2.5 and 4.5 hrs yield 4 well resolved peaks which can be qualitatively
170 assigned as a complex mixed valence species³⁰. Assignments are consistent with uranyl carbonate
171 solutions as well as EXAFS spectra for uranyl incorporated into other uranium-carbonate minerals
172 such as Cejkaite, Rutherfordine, Zellerite, Calcite and Aragonite^{28,30-32}. The 120.5 hrs end-point
173 can be fitted as biogenic U(IV) by U L₃-edge spectroscopy, results correspond well with³³.
174 Addition of a U(V)=O_{ax} shell with an occupancy of 0.4 yields a bond length of 1.9 Å, indicative
175 of a uranyl(V) contribution. This shell statistically contributes to the fit; f-test yielded 99.9 %³⁴.

176 **Table S5: Fitting parameters obtained from U L₃-edge EXAFS**

Sample	Scattering path	N	R (Å)	σ^2 (Å ²)	S0 ²	R-factor	α ^a
120.5 hrs	U-O	8	2.36(0)	0.014(1)	1	0.032	
Cell Pellet	U-U	12	3.86(1)	0.008(0)			
	U-O _{dist}	24	4.44(0)	0.009(1)			
120.5 hrs	U=O _{ax}	0.4	1.92(5)	0.008(5)	1	0.017	99.9 ^d
Cell pellet	U-O	7	2.36(0)	0.012(1)			
With U(V) *	U-U	12	3.86(1)	0.008(0)			
	U-O _{dist}	24	4.44(0)	0.009(1)			

^a N, R, σ^2 , S0² and the R-factor refer to the coordination number, radial distance, Debye-Waller factor, amplitude correction factor, and the goodness of fit, respectively. Uncertainty in interatomic distances is quoted in brackets for the last decimal place (Å). ^a F-test results; $\alpha > 0.95$ statistically improves the fit with 2 σ confidence ³⁴. Spectra marked with an asterisk have been plotted in R and k^3 in Figure 3. ^b F-test results for adding the U-O_{dist} feature and associated multiple scatterers at 4.2 Å. ^c F-test results for adding the 10 % U(IV)-O feature at 2.30 Å and reducing the U(VI) contributions to 90 %. ^d F-test results for adding the U(V)=O_{ax} feature at 1.9 Å.

177

178

17

179 **References**

- 180 (1) Jones, D. L.; Andrews, M. B.; Swinburne, A. N.; Botchway, S. W.; Ward, A. D.; Lloyd, J. R.;
181 Natrajan, L. S. Fluorescence Spectroscopy and Microscopy as Tools for Monitoring Redox
182 Transformations of Uranium in Biological Systems. *Chem. Sci.* **2015**, *6* (9), 5133–5138.
183 <https://doi.org/10.1039/C5SC00661A>.
- 184 (2) Ekstrom, A. Kinetics and Mechanism of the Disproportionation of Uranium(V). *Inorg.*
185 *Chem.* **1974**, *13* (9), 2237–2241. <https://doi.org/10.1021/ic50139a035>.
- 186 (3) Steele, H.; Taylor, R. J. A Theoretical Study of the Inner-Sphere Disproportionation
187 Reaction Mechanism of the Pentavalent Actinyl Ions. *Inorg. Chem.* **2007**, *46* (16), 6311–
188 6318. <https://doi.org/10.1021/ic070235c>.
- 189 (4) Renshaw, J. C.; Butchins, L. J. C.; Livens, F. R.; May, I.; Charnock, J. M.; Lloyd, J. R.
190 Bioreduction of Uranium: Environmental Implications of a Pentavalent Intermediate.
191 *Environ. Sci. Technol.* **2005**, *39* (15), 5657–5660. <https://doi.org/10.1021/es048232b>.
- 192 (5) Reeves, B.; Beccia, M. R.; Solari, P. L.; Smiles, D. E.; Shuh, D. K.; Berthomieu, C.; Marcellin,
193 D.; Bremond, N.; Mangialajo, L.; Pagnotta, S.; Monfort, M.; Moulin, C.; Den Auwer, C.
194 Uranium Uptake in Paracentrotus Lividus Sea Urchin, Accumulation and Speciation.
195 *Environ. Sci. Technol.* **2019**. <https://doi.org/10.1021/acs.est.8b06380>.
- 196 (6) Brockmann, S.; Arnold, T.; Bernhard, G. Speciation of Bioaccumulated Uranium(VI) by
197 Euglena Mutabilis Cells Obtained by Laser Fluorescence Spectroscopy. *Radiochim. Acta*
198 **2014**, *102* (5), 411–422. <https://doi.org/10.1515/ract-2013-2162>.

- 199 (7) Andra. Thermo-Chimie (version applicative 4.3.0) <https://www.thermochimie-tdb.com/>
200 (accessed Jun 14, 2017).
- 201 (8) Ulrich, K.-U.; Veeramani, H.; Bernier-Latmani, R.; Giammar, D. E. Speciation-Dependent
202 Kinetics of Uranium(VI) Bioreduction. *Geomicrobiol. J.* **2011**, *28* (5–6), 396–409.
203 <https://doi.org/10.1080/01490451.2010.507640>.
- 204 (9) Clark, D. L.; David Hobart, I. E.; Neda, M. P. Actinide Carbonate Complexes and Their
205 Importance in Actinide Environmental Chemistry. *Chem. Rev* **1995**, *95*, 25–48.
- 206 (10) Krestou, C. A.; Panias, D. Uranium (VI) Speciation Diagrams in the $UO_2^{2+}/CO_3^{2-}/H_2O$
207 System at 25. *Eur. J. Miner. Process. Environ. Prot.* **2004**, *4* (2), 1303–1868.
- 208 (11) Watanabe, T.; Ikeda, Y. A Study on Identification of Uranyl Complexes in Aqueous Solutions
209 Containing Carbonate Ion and Hydrogen Peroxide. In *Energy Procedia*; Elsevier Ltd, 2013;
210 Vol. 39, pp 81–95. <https://doi.org/10.1016/j.egypro.2013.07.194>.
- 211 (12) Solé, V. A.; Papillon, E.; Cotte, M.; Walter, P.; Susini, J. A Multiplatform Code for the
212 Analysis of Energy-Dispersive X-Ray Fluorescence Spectra. *Spectrochim. Acta - Part B At.*
213 *Spectrosc.* **2007**, *62* (1), 63–68. <https://doi.org/10.1016/j.sab.2006.12.002>.
- 214 (13) Ravel, B.; Newville, M. ATHENA, ARTEMIS, HEPHAESTUS: Data Analysis for X-Ray
215 Absorption Spectroscopy Using IFFFIT. In *Journal of Synchrotron Radiation*; 2005; Vol. 12,
216 pp 537–541. <https://doi.org/10.1107/S0909049505012719>.
- 217 (14) Reta, D.; Ortu, F.; Randall, S.; Mills, D. P.; Chilton, N. F.; Winpenny, R. E. P.; Natrajan, L.;
218 Edwards, B.; Kaltsoyannis, N. The Performance of Density Functional Theory for the

- 219 Description of Ground and Excited State Properties of Inorganic and Organometallic
220 Uranium Compounds. *J. Organomet. Chem.* **2018**, *857*, 58–74.
221 <https://doi.org/10.1016/j.jorganchem.2017.09.021>.
- 222 (15) Randall, S. Preparation and Investigation into the Optical Properties of Air Sensitive F-Block
223 Complexes, The University of Manchester, 2015.
- 224 (16) Neill, T. S.; Morris, K.; Pearce, C. I.; Abrahamsen-Mills, L.; Kovarik, L.; Kellet, S.; Rigby, B.;
225 Vitova, T.; Schacherl, B.; Shaw, S. Silicate Stabilisation of Colloidal UO₂ Produced by
226 Uranium Metal Corrosion. *J. Nucl. Mater.* **2019**, *526*, 151751.
227 <https://doi.org/10.1016/j.jnucmat.2019.151751>.
- 228 (17) Boyanov, M. I.; O'Loughlin, E. J.; Roden, E. E.; Fein, J. B.; Kemner, K. M. Adsorption of Fe(II)
229 and U(VI) to Carboxyl-Functionalized Microspheres: The Influence of Speciation on Uranyl
230 Reduction Studied by Titration and XAFS. *Geochim. Cosmochim. Acta* **2007**, *71* (8), 1898–
231 1912. <https://doi.org/10.1016/J.GCA.2007.01.025>.
- 232 (18) Roberts, H. E.; Morris, K.; Law, G. T. W.; Mosselmans, J. F. W.; Bots, P.; Kvashnina, K.; Shaw,
233 S. Uranium(V) Incorporation Mechanisms and Stability in Fe(II)/Fe(III) (Oxyhydr)Oxides.
234 *Environ. Sci. Technol. Lett.* **2017**, *4* (10), 421–426.
235 <https://doi.org/10.1021/acs.estlett.7b00348>.
- 236 (19) Bès, R.; Rivenet, M.; Solari, P. L.; Kvashnina, K. O.; Scheinost, A. C.; Martin, P. M. Use of
237 HERFD-XANES at the U L₃- and M₄-Edges to Determine the Uranium Valence State on
238 [Ni(H₂O)₄]₃[U(OH,H₂O)(UO₂)₈O₁₂(OH)₃]. *Inorg. Chem.* **2016**, *55* (9), 4260–4270.

- 239 <https://doi.org/10.1021/acs.inorgchem.6b00014>.
- 240 (20) Kvashnina, K. O.; Butorin, S. M.; Martin, P.; Glatzel, P. Chemical State of Complex Uranium
241 Oxides. *Phys. Rev. Lett.* **2013**, *111* (25). <https://doi.org/10.1103/PhysRevLett.111.253002>.
- 242 (21) Smith, A. L.; Raison, P. E.; Martel, L.; Prieur, D.; Charpentier, T.; Wallez, G.; Suard, E.;
243 Scheinost, A. C.; Hennig, C.; Martin, P.; Kvashnina, K. O.; Cheetham, A. K.; Konings, R. J. M.
244 A New Look at the Structural Properties of Trisodium Uranate
245 Na_3UO_4 . *Inorg. Chem.* **2015**, *54* (7), 3552–3561.
246 <https://doi.org/10.1021/acs.inorgchem.5b00136>.
- 247 (22) Brookshaw, D. R.; Patrick, R. A. D.; Bots, P.; Law, G. T. W.; Lloyd, J. R.; Mosselmans, J. F.
248 W.; Vaughan, D. J.; Dardenne, K.; Morris, K. Redox Interactions of Tc(VII), U(VI), and Np(V)
249 with Microbially Reduced Biotite and Chlorite. *Environ. Sci. Technol.* **2015**, *49* (22), 13139–
250 13148. <https://doi.org/10.1021/acs.est.5b03463>.
- 251 (23) Neill, T. S.; Morris, K.; Pearce, C. I.; Sherriff, N. K.; Burke, M. G.; Chater, P. A.; Janssen, A.;
252 Natrajan, L.; Shaw, S. Stability, Composition, and Core-Shell Particle Structure of
253 Uranium(IV)-Silicate Colloids. *Environ. Sci. Technol.* **2018**, *52* (16), 9118–9127.
254 <https://doi.org/10.1021/acs.est.8b01756>.
- 255 (24) Mereiter, K. The Crystal Structure of Liebigite, $\text{Ca}_2\text{UO}_2(\text{CO}_3)_3 \cdot 11\text{H}_2\text{O}$. *TMPM*
256 *Tschermaks Mineral. und Petrogr. Mitteilungen* **1982**, *30* (4), 277–288.
257 <https://doi.org/10.1007/BF01087173>.
- 258 (25) Wyckoff, R. W. G. Crystal Structures 1. *Cryst. Struct.* **1963**, *1*, 239–444.

- 259 (26) Teo, B. K. *EXAFS: Basic Principles and Data Analysis*; New York, 1986.
- 260 (27) Newville, M. EXAFS Analysis Using FEFF and FEFFIT. *J. Synchrotron Radiat.* **2001**, *8* (2), 96–
261 100. <https://doi.org/10.1107/S0909049500016290>.
- 262 (28) Catalano, J. G.; Brown, G. E. Analysis of Uranyl-Bearing Phases by EXAFS Spectroscopy:
263 Interferences, Multiple Scattering, Accuracy of Structural Parameters, and Spectral
264 Differences. *Am. Mineral.* **2004**, *89* (7), 1004–1021. [https://doi.org/10.2138/am-2004-](https://doi.org/10.2138/am-2004-0711)
265 0711.
- 266 (29) Marshall, T. A.; Morris, K.; Law, G. T. W.; Livens, F. R.; Mosselmans, J. F. W.; Bots, P.; Shaw,
267 S. Incorporation of Uranium into Hematite during Crystallization from Ferrihydrite.
268 *Environ. Sci. Technol.* **2014**, *48* (7), 3724–3731. <https://doi.org/10.1021/es500212a>.
- 269 (30) Allen, P. G.; Bucher, J. J.; Clark, D. L.; Edelstein, N. M.; Ekberg, S. A.; Gohdes, J. W.; Hudson,
270 E. A.; Kaltsoyannis, N.; Lukens, W. W.; Neu, M. P.; Palmer, P. D.; Reich, T.; Shuh, D. K.; Tait,
271 C. D.; Zwick, B. D. Multinuclear NMR, Raman, EXAFS, and X-Ray Diffraction Studies of
272 Uranyl Carbonate Complexes in Near-Neutral Aqueous Solution. X-Ray Structure of
273 $[\text{C}(\text{NH}_2)_3]_6[(\text{UO}_2)_3(\text{CO}_3)_6] \cdot 6.5\text{H}_2\text{O}$. *Inorg. Chem.* **1995**, *34* (19), 4797–4807.
274 <https://doi.org/10.1021/ic00123a013>.
- 275 (31) Kelly, S. D.; Newville, M. G.; Cheng, L.; Kemner, K. M.; Sutton, S. R.; Fenter, P.; Sturchio, N.
276 C.; Spötl, C. Uranyl Incorporation in Natural Calcite. *Environ. Sci. Technol.* **2003**, *37* (7),
277 1284–1287. <https://doi.org/10.1021/es025962f>.
- 278 (32) Reeder, R. J.; Nugent, M.; Lambie, G. M.; Tait, C. D.; Morris, D. E. Uranyl Incorporation into

- 279 Calcite and Aragonite: XAFS and Luminescence Studies. *Environ. Sci. Technol.* **2000**, *34* (4),
280 638–644. <https://doi.org/10.1021/es990981j>.
- 281 (33) Schofield, E. J.; Veeramani, H.; Sharp, J. O.; Suvorova, E.; Bernier-Latmani, R.; Mehta, A.;
282 Stahlman, J.; Webb, S. M.; Clark, D. L.; Conradson, S. D.; Ilton, E. S.; Bargar, J. R. Structure
283 of Biogenic Uraninite Produced by *Shewanella Oneidensis* Strain MR-1. *Environ. Sci.*
284 *Technol.* **2008**, *42* (21), 7898–7904. <https://doi.org/10.1021/es800579g>.
- 285 (34) Downward, L.; Booth, C. H.; Lukens, W. W.; Bridges, F.; Division, C. S.; Berkeley, L. A
286 Variation of the F- Test for Determining Statistical Relevance of Particular Parameters in
287 EXAFS Fits. *X-Ray Absorpt. Fine Struct. - XAFS13 13th Int. Conf.* **2007**, *882* (2), 2–4.
- 288

Chapter 5: Comparison of Radionuclide End-Points; the Long-Term Stabilities of U and Sr Co-Treated Sediments after Oxygen and Nitrate Perturbations

Paper in preparation for Earth and Space Chemistry.

Comparison of Radionuclide End-Points; the Long-Term Stabilities of U and Sr Co- Treated Sediments after Oxygen and Nitrate Perturbations

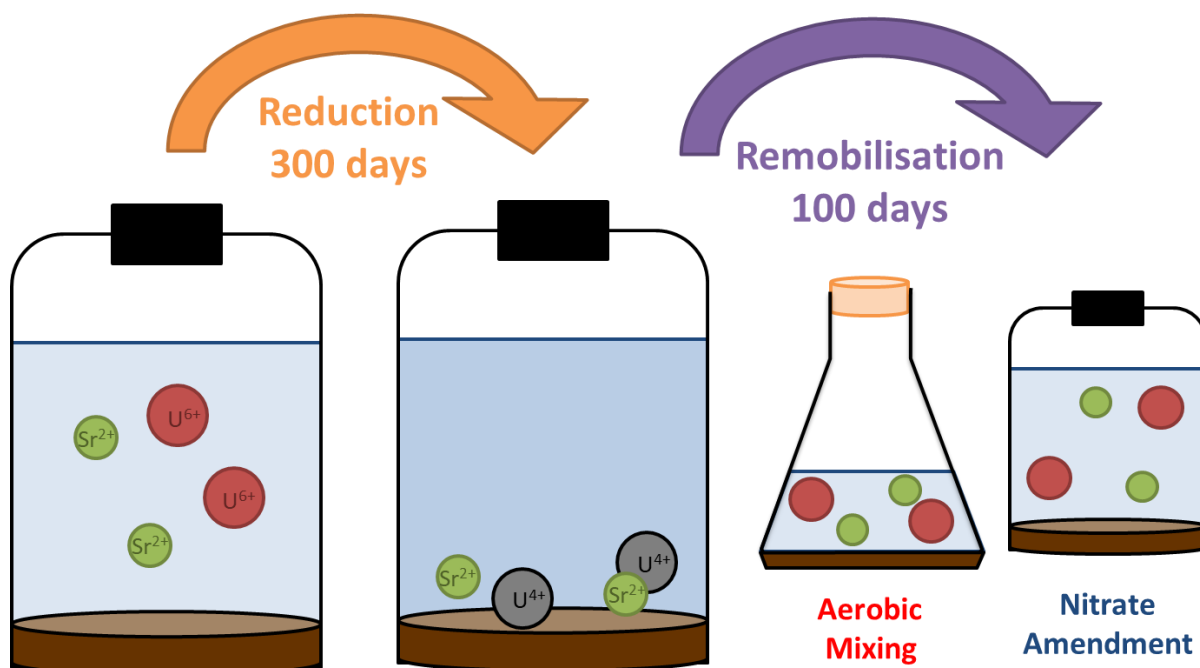
Gianni F. Vettese¹, Katherine Morris¹, Matthew White-Pettigrew¹, Luke Townsend¹, Samuel Shaw¹ and Jonathan R. Lloyd*¹.

¹Williamson Research Centre for Molecular Environmental Science and Research Centre for Radwaste Disposal, School of Earth and Environmental Science, The University of Manchester, Manchester, England

Keywords: Uranium, Strontium, Biogeochemistry, Bioremediation, Zero-Valent Iron, Glycerol phosphate, XAS.

5.1 Abstract

The stability of U and Sr in batch sediment microcosms treated using a range of bioremediation and chemical treatments was assessed during re-oxidation of sediment microcosms with oxygen or nitrate. The co-treated U and Sr phases were immobilised over a 300 day incubation using 7 different treatments resulting in up to 100 % and 95 % removal efficiencies for U and Sr respectively. Included in the 7 treatments were two commercially available nZVI-based products: NanoFeR 25s and Carbo-Iron; a commercially available slow release electron donor (MRC), and glycerol-3-phosphate. These were compared to systems containing added electron donors (lactate and acetate), excess sulphate and finally, a natural attenuation control. After 300 days, the incubated end-points were characterised by U L₃-edge and Sr K edge EXAFS, and the microbial communities were assessed using 16S rRNA gene sequencing. These end-points were then transferred to triplicate batch remobilisation experiments, which examined the long-term stabilities of the U and Sr following 100 days perturbation with an excess of either oxygen (air:sediment ratio 5:1) or nitrate (10 mM). Oxygen ingress consistently resulted in increased U remobilisation compared to nitrate amendments and the most recalcitrant treatments used glycerol phosphate, NanoFeR 25s and Carbo-Iron. Neither oxygen nor nitrate had a significant effect on Sr mobility. After oxygen or nitrate amendments, glycerol phosphate, NanoFeR 25s and Carbo-Iron systems demonstrated substantially more recalcitrant end-points compared to control experiments. The potential use of these three for in-situ treatments for co-contaminated U and Sr sites could provide a more stable method for radionuclide containment. U L₃-edge EXAFS data were collected on 60 day oxygen-remobilised NanoFeR 25s and Carbo-Iron samples; interestingly, despite re-oxidation of any bio-reduced U(IV) to U(VI), the residual U fraction remained in the solid phase.



5.2 Introduction

Groundwater monitoring at nuclear sites worldwide reveals concentrations of redox active U and non-redox active ^{90}Sr that are significantly above acceptable levels, posing a risk to the surrounding biosphere (Mckinley et al., 2001; NDA, 2019b; Stamper et al., 2014; Standring et al., 2002; Watson et al., 2004; Zachara et al., 2007). In-situ site treatment may require intervention in order to control U and Sr mobility, and as such, treatments would ideally remediate multiple high priority radionuclides forming end-points which remain stable over long timescales. Considering these requirements for safe site remediation, this study investigates the long term effectiveness of a range of bioremediation, biostimulation and chemical end-points relevant to U and Sr contaminated lands and provides, for the first time, thorough comparisons between each method.

U remediation strategies can be achieved via microbial reduction processes whereby soluble U(VI), as uranyl(VI), is enzymatically reduced to relatively insoluble U(IV) by addition of simple electron donors (Lovley et al., 1991; D R Lovley and Phillips, 1992). Indeed, the enzymatic reduction of soluble U(VI) to sparingly-soluble U(IV) has been thoroughly demonstrated in a range of laboratory experiments and field scale studies (Anderson et al., 2003; Istok et al., 2016, 2004; Vrionis et al., 2005; Williams et al., 2011; Wu et al., 2006), in addition to being observed in the natural environment when electron donors are already present (Campbell et al., 2012). Aqueous U(VI) immobilisation can be achieved via abiotic reduction (Brookshaw et al., 2015; Ilton et al., 2004; Latta et al., 2012a); aqueous U(VI) can also sorb strongly to the surface of organics, iron (oxy)hydr-oxides and clays under environmentally relevant conditions (Brookshaw et al., 2015; Ching-kuo and Langmuir, 1985; Gu et al., 2005; Newsome et al., 2014a; Winstanley et al., 2019). Furthermore, U can be incorporated into some reduced Fe minerals during their formation; in which more recent evidence suggests that U is present as U(V) (Marshall et al., 2015; Pidchenko et al., 2017; Roberts et al., 2017; Tsarev et al., 2016a). This U(V) state has also been suggested in biogenic pathways for U(VI) reduction by *Geobacter sulfurreducens* (Jones et al., 2015; Renshaw et al., 2005), and it has been identified recently in *Shewanella oneidensis* MR1 (Vettese

et al., 2020). Whilst the bioreduction of U(VI) is an attractive route, it is widely accepted that reduced U(IV) phases are susceptible to oxidative remobilisation after exposure to oxidants, such as dissolved oxygen (Abdelouas et al., 1999; Bi et al., 2013; Komlos et al., 2008b; Law et al., 2011; Moon et al., 2007; Newsome et al., 2015b; Senko et al., 2002), nitrate (Beller, 2005; Finneran et al., 2002; Istok et al., 2016, 2004; Law et al., 2011; Moon et al., 2009; Newsome et al., 2015b; Senko et al., 2002), Fe-oxides (Ginder-Vogel et al., 2010, 2006; Nevin and Lovley, 2000; Sani et al., 2005, 2004; Spycher et al., 2011), Mn-oxides (Liu et al., 2002; Wang et al., 2014, 2013; Zachara et al., 2002) and oxidised humic matter (Newsome et al., 2015a). Of these, oxygen and nitrate are of particular concern in radioactively contaminated land scenarios, with the potential for dissolved oxygen to ingress into reduced sediments, and nitrate being ubiquitously present throughout the subsurface (Law et al., 2010a). A field-scale test at the Rifle Field Research site, Colorado, tested the possibility of U remediation via in-situ injections of electron donor. Whilst the short scale experiments showed a drop in soluble U to below levels prescribed by the Environmental Protection Agency, re-oxidation processes after acetate amendments ceased demonstrated that electron donor injections could not sustain the bioremediation of U (Anderson et al., 2003). This led to the conclusion that for active bioremediation to succeed the longevity of U end-points need optimisation.

Under environmental conditions, ^{90}Sr is present as the aqueous Sr^{2+} cation which is highly insensitive to redox changes and as a result, its environmental mobility is largely governed by sorption to negatively-charged mineral surfaces. At low ionic strengths and acidic to circum-neutral conditions, Sr^{2+} sorbs to mineral surfaces which have a large cation exchange capacity and surface area; mainly Fe-oxides and clays (Balek et al., 1996; Carroll et al., 2008; Dyer et al., 2000; Karasyova et al., 1999). Here, Sr often forms outer-sphere complexes to minerals in competition with other cations (such as H^+ , Na^+ , K^+ , Mg^{2+}) (Axe et al., 1998; Dyer et al., 2000, 1999; Dyer and Umar, 1999; Fuller et al., 2016; O'day et al., 2000; Thorpe et al., 2014, 2012b; Wallace et al., 2012). Sr bound via outer sphere sorption is, however, susceptible to desorption, and thus remobilisation (Handley-Sidhu et al., 2014, 2011; Wallace et al., 2012). More recalcitrant Sr^{2+} phases can be formed in several ways. Under highly alkaline conditions (pH >12.5), Sr^{2+} forms inner-sphere complexes on mineral surfaces where desorption does not occur despite high ionic strengths (Fuller et al., 2016). Alternatively, Sr^{2+} can isomorphically substitute or incorporate into Ca-carbonate or Ca-phosphate minerals, such as calcite (Fujita et al., 2004) or (hydroxyl-)apatite (Cleary et al., 2019; Handley-Sidhu et al., 2011; Macaskie and Dean, 1985b). Simple electron donors (such as acetate, lactate or glycerol) have a limited effect on Sr removal from solution (Brookshaw et al., 2016; Cleary et al., 2019; Thorpe et al., 2012b). In-situ Sr incorporation into Ca-phosphates was proven in the field at the Hanford site, USA, via the simultaneous addition of Ca-citrate and Na-phosphate (Moore et al., 2004). The results showed increased Sr uptake, and increased recalcitrance in desorption experiments compared to untreated soils; further investigation found that this was due to slow substitution of Sr into the apatite structure over a 15 month period (Szecsody et al., 2009; Vermeul et al., 2014). Following on from positive experiments (Cleary et al., 2019; Newsome et al., 2015c, 2015a) we have accordingly chosen to test Sr incorporation into Ca-phosphate minerals using glycerol-3-phosphate.

The stability of the immobilised phases is key to the success of the long-term stewardship of contaminated wastes; this ultimately warrants the need to research and develop alternate U and Sr immobilisation strategies which are effective over extended timescales. Here, we have selected 7 [numbered in square brackets throughout] methods of co-treatment for U and Sr contaminated land, the first 5 methods use biostimulation and they are: a natural attenuation control [1]; an electron

donor experiment [2]; a system with electron donor and excess sulphate [3]; a slow release, commercially available electron donor, MRC [4] and; glycerol phosphate [5]. The remaining 2 systems are both Zero Valent Iron (ZVI)-based treatments; NanoFeR 25s [6] and Carbo-Iron [7]. We explore not only the reactivity of a series of treatments for co-treating U and Sr, but we also define the longevity of each system in the event of aerobic or nitrate induced remobilisation. Our experiments provide clear and direct comparisons between the different treatments under a range of possible scenarios; here, the best results for both U and Sr were found after amendments with glycerol phosphate [5], NanoFeR 25s [6] and Carbo-Iron [7]. This manuscript will first cover the biogeochemical changes during batch incubation phase of the experiment, it will then discuss the changes in the microbial community and the solid phase analysis using EXAFS. Following this, the remobilisation studies will be discussed in a similar order.

5.3 Materials and methods

5.3.1 Sediment Characterisation

Bulk samples of subsurface sediments were acquired from the Calder Valley, Cumbria, UK, in December 2017. The Calder Valley is up-stream from the Sellafield site and is thus representative of its soil (Law et al., 2010a). The sediments were sampled near the surface (approximately 5-10 cm depth) and were transferred directly to Manchester in sealed sterile containers and stored at 7 °C prior to use. X-Ray Fluorescence (XRF) was used to ascertain the elemental composition of the sediment (SI 1: Sediment and Synthetic Groundwater Composition) and the microbial community was analysed using 16S rRNA analysis before and after incubation, as well as after remobilisation studies.

5.3.2 Batch Microcosm Experiments

Batch microcosm experiments were set up anaerobically with a 1:10 sediment to water ratio. Each experiment was prepared in a sterile 2 L Schott bottle and contained 1.5 L of modified, sterile and anaerobic, artificial groundwater representative of the Sellafield groundwater (Wilkins et al., 2007)(SI 1: Sediment and Synthetic Groundwater Composition) and 150 ± 0.5 g of sediment. The 7 systems were set up as above with the following amendments: [1] no treatment; [2] sodium acetate (5 mM) and sodium lactate (5 mM); [3] sodium acetate (5 mM), sodium lactate (5 mM) and sodium sulphate (10 mM); [4] MRC (5 gL⁻¹) (Regenesis, 2015); [5] glycerol-3-phosphate (10 mM by anhydrous mass); [6] NanoFeR 25s (5 gL⁻¹), supplied as an aqueous suspension of nZVI particles suspended in a bio-degradable stabiliser (Newsome et al., 2019) and; [7] Carbo-iron (5 gL⁻¹), stabilised with carboxymethylcellulose (20 wt%) (Mackenzie et al., 2012; Newsome et al., 2019). U, as U(VI)O₂²⁺ in 0.001 M HCl, was spiked into the artificial groundwater to give a final concentration of 44 ppm and the bottles were sealed with self-healing butyl rubber stoppers. The experiments were incubated in the dark, at room temperature and were swirled periodically over the course of the experiment.

Sediment slurry was extracted at set time points using Ar flushed syringes and aseptic technique. An aliquot of slurry was immediately added to 0.5 M HCl for analysis of bioavailable Fe(II) and total bioavailable Fe using the ferrozine assay (Lovley and Phillips, 1987; Stookey, 1970; Viollier et al., 2000). The solid phase was then separated from the aqueous phase via centrifugation (14,800 g, 5 min) and the resulting supernatant was used to monitor total aqueous U, Sr and Fe by Inductively Coupled Plasma – Mass Spectrometry (ICP-MS). Surplus supernatant was frozen at -80 °C and stored for 16S rRNA analysis and Ion Chromatography (IC) for analysis of sulphate, thiosulphate, nitrate, nitrite,

phosphate, glycerol phosphate and volatile fatty acids. The remaining sample was used to determine Eh and pH.

5.33 Oxidative Remobilisation of U and Sr

After 300 days of incubation, the end-points were transferred into smaller experiments in order to examine the stability of the immobilised U and Sr upon exposure to excess air or nitrate. Remobilisation experiments were set up, in triplicate, by removing 20 mL of sample slurry from each microcosm under anaerobic conditions. In aerobic remobilisation studies the removed sample was added to a 100 mL conical flask resulting in a 1 : 5, sample : air ratio and was stoppered with a porous sponge and Al foil. The sponge and foil were removed periodically and the flasks were gently agitated to ensure that the re-oxidation process was not oxygen limited. For nitrate remobilisation studies the removed sample slurry was added to serum bottles filled with Ar and spiked to a final concentration of 10 mM nitrate. This concentration was chosen as an excess to ensure that the re-oxidation process was not nitrate limited; additionally, this value is significantly higher than the maximum concentration of nitrate reported in Sellafield groundwater (3 mM) (Sellafield Ltd., 2015). Again, the samples were agitated periodically throughout the course of the experiment. Aliquots for each experiment were taken in triplicate and all measurements were assessed using the same methodology as before and the microbial community of the end-points were analysed using 16S rRNA gene sequencing. A fourth set of each experiment was set up alongside the triplicate remobilisation studies and was destructively sampled after 60 days for bulk X-ray Absorption Spectroscopy (XAS) analysis.

5.34 Solid-phase Analysis

X-Ray Absorption Spectroscopy

U L₃-edge and Sr K-edge EXAFS analysis assessed the local coordination environment and geometries of the analytes after 300 days of incubation and for selected systems U EXAFS were measured after 60 days of aerobic remobilisation (Figure 57). All XAS samples were prepared anaerobically, frozen immediately in liquid N₂ and maintained at -80 °C under an inert atmosphere prior to analysis. U L₃- and Sr K-edge spectra were recorded in a liquid N₂ cryostat in fluorescence mode using a 36 element Ge detector with an in-line yttrium reference foil for energy calibration. Software packages ATHENA and ARTEMIS were used to analyse the XAS spectra (Ravel and Newville, 2005) (SI 7: Additional X-ray Absorption Spectroscopy Data and Analysis). Geochemical data and relevant literature were used to inform the fits obtained and further details about the EXAFS fitting procedures, including shell-by-shell fits, are in the SI (SI 7: Additional X-ray Absorption Spectroscopy Data and Analysis).

Microbial Analysis

In order to examine changes in the microbial community, DNA was extracted from each system after 0 and 300 days of incubation and after 100 days of remobilisation via oxygen and nitrate addition. Further details for microbial community analysis (16S rRNA gene sequencing) are provided in the Supporting Information (SI 6: Microbial Community Characterisation).

5.35 Proprietary substrates

The commercially available treatments were: Metals Release Compound (MRC) [4] , UK, supplied by Regenesis; NanoFeR 25s [6] supplied by NANO IRON, Czech Republic (“NANOFEER 25S | NANOIRON,” n.d.); and Carbo-Iron [7] supplied by the Helmholtz Centre for Environmental Research, Germany (“Neue Seite - Helmholtz-Centre for Environmental Research,” n.d.). Both nZVI treatments were supported by the NanoRem project.

5.4 Results and Discussion

This manuscript will first cover the biogeochemical changes during the incubation phase, followed by solid phase analysis of the incubated phases using XAS and 16S rRNA gene sequencing. Proceeding these discussions the manuscript discusses the remobilisation of the incubated end-points by both oxygen and nitrate amendments in a similar manner. Here, 2 of the best performing end-points were also studied by XAS to understand the effects of oxygen ingress.

5.4.1 Batch Microcosm Experiments

Sediment microcosms were set up using 7 treatments to investigate their potential for removal of aqueous U and Sr from contaminated sediments and to assess their impacts on biogeochemical behaviour. In the natural attenuation control [1], an increase in the bioavailable Fe(II) as well as significant U removal from solution (41 ppm, 92 %) suggested the consumption of organic carbon already present in the sediment (Figure 1)(SI 1: Sediment and Synthetic Groundwater Composition). 56 ppm (69 %) Sr was rapidly removed from solution within 7 days, presumably due to Sr sorption to sediment (Figure 1)(O' day et al., 2000; Patterson and Spoel, 1981). Following this, there was no significant variation in Sr concentrations over the 300 days consistent with past work under similar conditions (Cleary et al., 2019; Thorpe et al., 2012b; Wallace et al., 2012). Sulphate concentrations did not change throughout the experiment (Figure 64).

The electron donor experiment [2] showed near complete U removal (41 ppm, 94 %) coupled with the reduction of bioavailable Fe(III) (Figure 1). Sr behaved similarly to the natural attenuation control experiment, with 53 ppm (65 %) Sr removed from solution (Figure 55), suggesting that electron donor amendments had limited impact on Sr mobility, consistent with previous studies (Brookshaw et al., 2016; Cleary et al., 2019; Thorpe et al., 2012b). Complete sulphate removal was observed after 300 days concomitant with the darkening of the sediments (Figure 59, Figure 70).

The third system, containing electron donor and excess sulphate [3], assessed the effects of inducing sulphate-reducing conditions on U and Sr biogeochemistry. This system is of interest as iron sulphide minerals are reportedly capable of buffering the re-oxidation and remobilisation rates of radionuclides by scavenging oxidants and acting as a reducing agent (Abdelouas et al., 1999; Bi et al., 2013; Bi and Hayes, 2014; Carpenter et al., 2015; Istok et al., 2016; Moon et al., 2009). Here, significant U was removed from solution (40 ppm, 90 %) concurrent with the reduction of bioavailable Fe(III); although U removal and bioavailable Fe(III) reduction occurred at a slower rate compared to other experiments (Figure 55). Excess sulphate has previously retarded Fe(III) and U(VI) reduction rates (Bower et al., 2019; Yabusaki et al., 2007). Sr removal levels saw a marked increase (66 ppm, 82 %, Figure 1), consistent with previous work (Thorpe et al., 2017). Sediments also reached sulphate-reducing conditions as evident by numerous physical and geochemical observations, including a noticeable blackening of sediment (Figure 59), a detectable sulphide odour, Eh values below -400 mV (Figure 61), sulphate was consumed and thiosulphate was produced (Figure 70).

The fourth system, MRC [4], used a commercially available organo-sulphur ester compound with slow release properties. MRC supplies the subsurface with electron donor over extended periods of time which sustains reducing conditions and minimises the need for repeat amendments, it has an estimated activity of 12-18 months (Regenesis, 2015). MRC has already been successfully identified as a treatment for the long-term immobilisation of Tc and Cr in the laboratory and its capabilities for Cr remediation have been extended to the field (Newsome et al., 2017; Regenesis, 2016a, 2016b);

however, to date, it has not been tested as a treatment for U or Sr. MRC amendments had little effect on U or Sr removal compared to control experiments; removing 39 ppm U (89 %) and 56 ppm Sr (69 %) (Figure 55) and although near complete reduction of bioavailable Fe(III) was observed, this occurred at a much slower rate than the other experiments, likely due to the lower pH (approximately 4, Figure 60). Slower rates of Fe(III)-reduction have previously been linked to low pH sediments using samples representative of the Sellafield site and the Oak Ridge Field Research Centre (TN) (Law et al., 2010a; Petrie et al., 2003b). In other publications MRC did not induce such a drastic change in pH, which suggests that the buffering capacity in these sediments is reduced (Newsome et al., 2017). MRC had little effect on Sr mobility, as this treatment is designed to remediate redox active metal contaminants and therefore it was not expected to have a significant effect on Sr (Regenesis, 2015). This system did not reduce sulphate in the 300 day period (Figure 72) and all IC samples treated with MRC contained an unresolved organic mixture, suggesting a large number of volatile fatty acids, as seen previously (Newsome et al., 2017).

In the glycerol phosphate amended system [5] U and Sr removal progressed in two stages consistent with the previously described mechanisms where, U first sorbed to the sediments and, in the case of U(VI), was then reduced (Figure 55 & Figure 57) (Cleary et al., 2019; Newsome et al., 2015c). Following this, a slower removal of aqueous contaminants was observed which was simultaneous with phosphate mineralisation upon the release of inorganic phosphate into solution in accordance with the relevant literature (Figure 73)(Cleary et al., 2019; Newsome et al., 2015a). After 35 days, 44 ppm (100 %) U and 71 ppm (87 %) Sr was removed from solution before significant Fe(III)-reduction, implying that enzymatic U(VI) removal was achieved by biogeochemical processes other than those induced by Fe(III)-reducing bacteria (Figure 55)(Newsome et al., 2015c). These values increased over incubation period where U and Sr removal increased from 44 ppm (100 %) and 77 ppm (95%) respectively; this has previously been attributed in Sr-phosphate systems as slow Sr uptake into apatite-like structures (Szecsody et al., 2009; Vermeul et al., 2014). The formation of acetate confirmed the oxidation of glycerol (Figure 74) and Fe(III) reduction was observed at similar rates to the electron donor system [2] (Figure 55), as seen previously in literature (Cleary et al., 2019; Newsome et al., 2015c, 2015a). Sulphate was removed from solution (Figure 76) and residual inorganic phosphate (approximately 2 mM) was found in solution until day 400 (Figure 73).

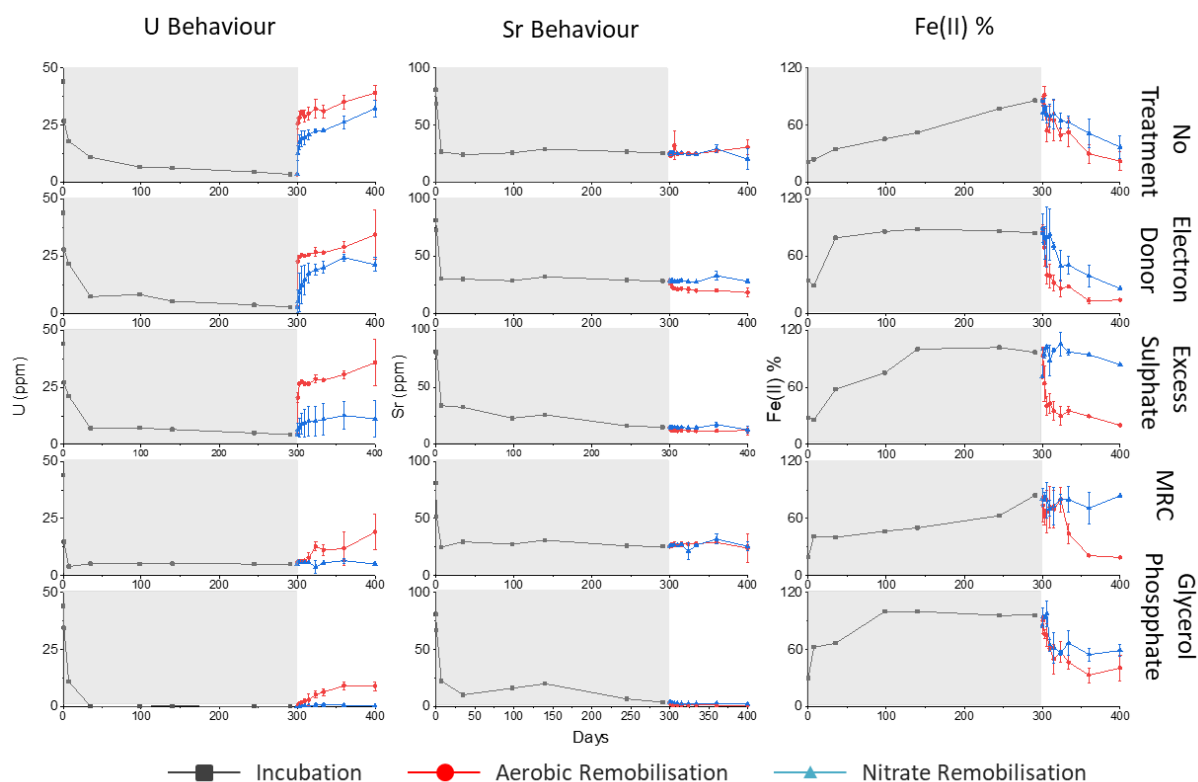


Figure 55: Aqueous U (left) and Sr (middle) concentrations in ppm, and bioavailable Fe(II) as a percentage of total bioavailable Fe (right). With data for the incubation period (black lines, also marked by the grey area) and remobilisation data for each species after aeration (red lines) or when amended with nitrate (blue lines). Measurements were performed in triplicate with error bars representing 1 standard deviation (σ). Incubation phases are highlighted in grey and remobilisation phases are left blank.

U was rapidly removed from solution in the presence of NanoFeR 25s [6] and Carbo-Iron [7] as seen previously using ZVI-based treatments in both the field and laboratory (Crane et al., 2011; Farrell et al., 1999; Tsarev et al., 2017). Within a week both NanoFeR 25s and Carbo-Iron removed 44 ppm (99 %) U; similarly Sr was rapidly removed from solution in both systems reporting 70 ppm (86 %) and 64 ppm (79 %) removal within a week in NanoFeR 25s and Carbo-Iron respectively. After 300 days incubation, these figures increased to 71 ppm (87 %) and 69 ppm (85 %) by day 300. Both systems found elevated concentrations of aqueous and total bioavailable Fe compared to other experiments (Figure 83), and both saw near complete reduction of bioavailable Fe(III) over 300 days (Figure 56). Both completely reduced sulphate in 300 days (Figure 79 and Figure 82) and NanoFeR 25s also produced quantities of acetate and propionate (Figure 77); whereas Carbo-Iron did not.

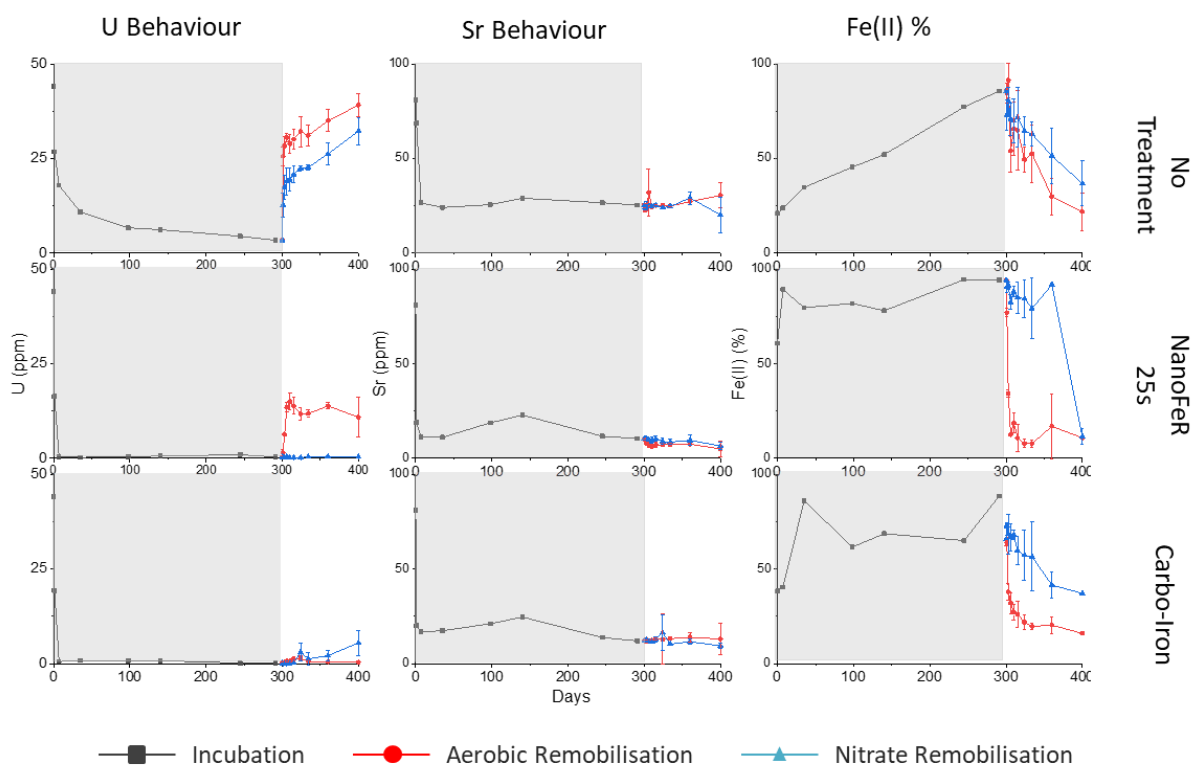


Figure 56: Aqueous U (left) and Sr (middle) concentrations in ppm, and Fe(II) as a percentage of total bioavailable Fe (right). With data for the incubation period (black lines, also marked by the grey area) and remobilisation data for each species after aeration (red lines) or when amended with nitrate (blue lines). Measurements were performed in triplicate with error bars representing 1 standard deviation (σ). Incubation phases are highlighted in grey and remobilisation phases are left blank.

5.42 Microbial Analysis After Batch Incubation

16S rRNA gene analysis was used to investigate the changes in composition of the microbial community during the incubation experimental phase. Before the experiments commenced a relatively diverse range of soil bacteria and archaea was identified (Figures 30-36).

After 300 days of bioreduction the microbial community present in the no treatment [1] and electron donor [2] systems were remarkably similar (Figure 84 & Figure 85). Compared to the control sample, both saw significant increases in the relative abundance of *Alphaproteobacteria*, consistent with the biological reduction of Fe(III). In addition, *Methanobacteria* were also detected (9% of OTUs) in the electron donor supplemented system [2], confirming that the redox cascade had progressed to methanogenesis consistent with the geochemical data (Figure 1). They were not present in the no treatment system [1].

The microbial community in the third system, containing excess sulphate [3], was noticeably different to the no treatment [1] and electron donor [2] systems (Figures 30-32). There were significant increases in the relative abundance of *Deltaproteobacteria* and *Clostridia*, including representatives of the genera *Desulfobulbus* and *Sporobacter*, consistent with Fe(III)- and sulphate-reduction. In addition close relatives to members of the phylogenetic class *Ignavibacteria* were detected in the system [3]; these are green sulphur bacteria with common metabolic characteristics of sulphide-oxidation and carbon-fixation (Lino et al., 2010; Liu et al., 2012). Their presence suggests a full sulphur redox cycle in these systems. Moreover, compared to the electron donor system [2] there was a

significant decrease in *Methanobacteria*, representing 2 % of the microbial OTUs compared to 9 % in the electron donor system [2], suggesting that the addition of sulphate maintained sulphate-reducing conditions over methanogenesis (Figure 85 & Figure 86).

A significantly lower number of OTUs were detected in system [4], added MRC, after 300 days of incubation compared to the other systems, suggesting that MRC may have some toxic effect on the microbial community, although as previous experiments using MRC did not show any negative effect on the diversity of the microbial community this is unlikely (Figure 87)(Newsome et al., 2017). More likely is that incubation with MRC led to the selective enrichment of fewer, but key organisms. After 300 days of incubation, the MRC amended system [4] *Bacilli* dominated, comprising 52 % of the microbial community, with 48 % belonging to the genus *Sporolactobacillus* (spore-forming lactic acid bacteria) (Doores, 2014; McClure, 2006). No methanogens were detected.

Following biostimulation with glycerol phosphate, a diverse microbial community was detected including sequences closely related to known Fe(III)- and sulphate-reducing bacteria *i.e.* *Geobacter*, *Geothrix* and *Desulfosporosinus spp.* (Figure 88), consistent with data from previous experiments using glycerol phosphate amendments (Cleary et al., 2019; Newsome et al., 2015c). Although organisms studied in laboratory investigations of phosphate release from organic substrates *e.g.* *Serratia* or *Chryseobacterium spp.* were not detected, other organisms were probably involved in the release of orthophosphate from glycerol phosphate. Again *Methanobacteria sp.* (7 % of the OTUs) were detected in this treatment by day 300, suggesting that the microbial community present in these sediments eventually formed methane from the added carbon-rich substrate.

Similar to the MRC amended system, the NanoFeR 25s system had significantly lower OTUs than the other systems consistent with toxicity effects on the microbial community (Figure 89). This was previously observed in systems amended with nanoscale ZVI (Kumar et al., 2014b; Newsome et al., 2019, 2016). The results after 300 days of incubation using NanoFeR 25s were broadly similar to previous experiments using this material (Newsome et al., 2019), supporting a community rich in *Clostridia*. In this sample, an organisms most closely related to a *Thermincola sp.* (Class *Clostridia*) represented 30 % of the OTUs, consistent with Fe(III) reduction (Carlson et al., 2012; Zavarzina et al., 2007). After 300 days of incubation with NanoFeR 25s, archaea of the genus *Methanomassiliicoccus* represented 3 % of the OTUs. *Methanomassiliicoccus spp.* are reported to produce methane using H₂ as an electron donor suggesting that the H₂ generated from the anaerobic decomposition of zerovalent iron was stimulating the growth of H₂-utilising microorganisms (Dridi et al., 2012; Gorlas et al., 2012).

The Carbo-Iron amended system [7] showed a comparable microbial diversity to other treatments (Figure 90). This contrasts to previous batch microcosms using Carbo-Iron, which found significant decreases in the microbial community diversity (usually 30-40 % less OTUs with treatment) (Newsome et al., 2019, 2016). The microbial community may have been stimulated by the addition of carboxymethylcellulose (20 wt%). Here, at the phylogenetic class level *Clostridia* and *Deltaproteobacteria* (including *Geobacter*, *Desulfovibrio* and *Desulfobulbus spp.*) and *Methanobacteria*, were detected, consistent with a full cascade of biogeochemical reduction including Fe(III) and sulphate reduction as well as methane production, consistent with other batch experiments using Carbo-Iron or other nanoscale iron particles (Kumar et al., 2014b; Mackenzie et al., 2016; Newsome et al., 2019, 2016).

5.43 Speciation of Solid Phase U and Sr: XAS

Due to the large amount of XAS data collected across the 7 experiments, this section will only briefly discuss the XAS data obtained for each system. For a more in depth and thorough discussion of fits and how conclusions have been drawn, please see the Supporting Information (SI 7: Additional X-ray Absorption Spectroscopy Data and Analysis).

U L₃-edge XAS Data

Linear combination fitting of the natural attenuation system [1] identified U present as both U(VI) and U(IV), suggesting U removal of solution through a combination of sorption and reduction processes (Figure 91). Accordingly, the best fit for the EXAFS suggested that 30 % of the U was present as U(IV), with the rest present as U(VI) sorbed to Fe (Figure 3).

In the electron donor system [2] all U was present as U(IV) (Figure 91), with the best fitting model suggesting that the U was present as a non-crystalline/ biogenic U(IV) phase with 2 P shells at approximately 3.1 and 3.7 Å. In similar work biogenic UO₂ is commonly assigned with U-P interactions through P-containing ligands present on biomass preventing crystallisation to form uraninite (Alessi et al., 2014; Bargar et al., 2013; Bernier-Latmani et al., 2010; Boyanov et al., 2011).

The excess sulphate system [3] found only partial reduction of U(VI), confirming that the presence of excess sulphate hindered the rate and extent of U(VI) reduction (W. Luo et al., 2007; Williams et al., 2011) (Figure 91). Here, the data were best fit with a 40:60 U(VI):(IV) ratio for the U-O shells, and with a small contribution attributable to U-U backscatterers. The remaining shell was fitted as P at 3.15 Å, which has previously been assigned to U-P interactions found in biomass under sulphate-reducing conditions (Bargar et al., 2013; Bernier-Latmani et al., 2010; Bone et al., 2017; Boyanov et al., 2011; Campbell et al., 2012; Fletcher et al., 2010; Sharp et al., 2011).

In the MRC amended system [4] all the U persisted as U(VI) (Figure 91). The system was initially fit with a dioxygenyl O backscatterer at 1.8 Å and an equatorial U-O_{eq} shell at 2.4 Å; following this the fit could be improved by including either a P or S shell at approximately 3.2 Å (Figure 92). S was chosen as a more likely backscatterer based on the significantly better fit (determined by lower R-factor), and the presence of excess S in the MRC system (Figure 92). Furthermore, S interactions with radionuclides have also previously been observed in MRC microcosm experiments, via the formation of TcS₂ in contaminated sediments (Newsome et al., 2017). In either case a S/P shell at 3.15 Å is consistent with bidentate coordination complexation (Alessi et al., 2014; Bargar et al., 2013; Bernier-Latmani et al., 2010; Boyanov et al., 2011; Hennig et al., 2007; Walter et al., 2003).

Inspection of the XANES for the glycerol phosphate system [4] showed that all U was present as U(IV) (Figure 91). Here, the Fourier transform of the U EXAFS on the glycerol phosphate system lacked both U=O_{ax}, typical of uranyl dioxygenyl bonds at 1.8 Å, and an edge-sharing U-U feature at 3.9 Å found in UO₂-like phases (Figure 57). Given this, the shape of the XANES and the relevant literature (Newsome et al., 2015c, 2015a), we proceeded to fit the EXAFS data using the crystal structure on a U(IV)-phosphate ningyoite (Dusausoy et al., 1996; Rui et al., 2013). The resulting fit was highly comparable to other biostimulated U(IV)-phosphates with the central U bound first to 8 O atoms: 4 at ~2.3 Å and 4 at ~2.4 Å. The following shell is constituted by 2 bidentate P atoms and then 4 monodentate P atoms at 3.13 and 3.67 Å respectively (Alessi et al., 2014; Boyanov et al., 2011; Khijniak et al., 2005; Newsome et al., 2015c).

In the NanoFeR 25s system [6] XANES analysis identified a 20:80 U(VI):U(IV) ratio (Figure 91), which was confirmed in the EXAFS fitting; this shows a U(VI)=O_{ax} shell with coordination number 0.4 and a U(IV)-O shell with coordination number 6.4 (Figure 57, Figure 91).

After treatment with Carbo-Iron [7] all U was present as U(IV) (Figure 3, Figure 91). The resulting EXAFS spectra could be fit with a mixture of non-crystalline UO₂ and U(IV) bound to both C and Fe via oxygen ligands with bond lengths of approximately 2.4 Å. These fitting parameters are logical given the structure of Carbo-Iron (Mackenzie et al., 2012); they are also consistent with other literature discussing U(VI) reduction by ZVI (Crane et al., 2011; Dickinson and Scott, 2010; Tsarev et al., 2017, 2016a). Similarly Tc(VII) phases reduced by Carbo-Iron also found Tc-Fe interactions (Newsome et al., 2019).

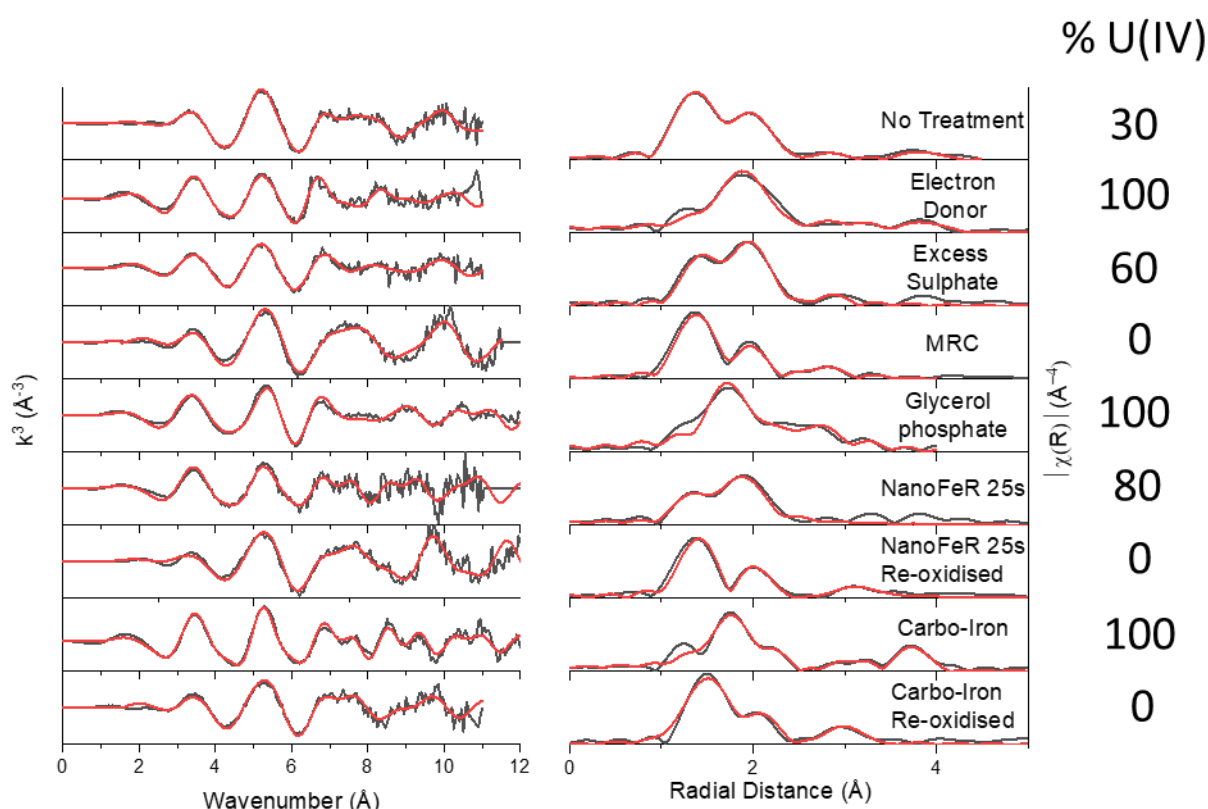


Figure 57: U L₃-edge EXAFS data and fits (red) for bio-reduced species in k^3 (left) and the respective Fourier transforms (right) with calculated contributions from U(IV) (%).

Sr K-edge XAS Data

Sr K-edge EXAFS fitting yields a single shell of O backscatterers representative of O ligands involved in sorption to amorphous silica, Fe-oxides and clays at circumneutral pH (Axe et al., 1998; Carroll et al., 2008; Chen and Hayes, 1999; Fuller et al., 2016). The fitting parameters obtained for the natural attenuation [1], electron donor [2], excess sulphate [3] and NanoFeR 25s [6] systems reflect this as they could all be fit with 9 Sr-O backscatterers at 2.6 Å consistent with outer sphere sorption of Sr to a variety of mineral phases (Axe et al., 1998; Carroll et al., 2008; Chen and Hayes, 1999; Fuller et al., 2016).

The Fourier transform of the bioreduced MRC system [4] has 3 shells (Figure 3). The first can be fit as 9-coordinate Sr-O backscatterers. The second shell was fit as a U-Fe backscatterer, but the third shell could not be fit using sensible parameters *i.e.* Fe, K, Al, Si, Sr.

The Fourier transform of the glycerol phosphate treated sediments [5] has an oxygen shell at 2.6 Å as well as an additional shell at 3.3 Å (Figure 4). This second shell was fit as a partial Sr-P shell ($N = 1.3$) which statistically improved the fit (F-test 96.3 %). Here, the resultant fit and parameters were very similar to published Sr-doped hydroxyapatite like structures (Bazin et al., 2013; Cleary et al., 2019; Handley-Sidhu et al., 2014, 2011; O'day et al., 2000). As the best fit yielded 1.3 out of a possible 3 Sr-P interactions from hydroxyapatite, this suggests that approximately 43 % of the Sr was incorporated into phosphate minerals such as hydroxyapatite. This ratio is significantly higher than the value obtained in previous experiments (Cleary et al., 2019) and is likely due to the longer incubation period used here, consistent with slow uptake of Sr into Ca-phosphate minerals (Szecsody et al., 2009; Vermeul et al., 2014). Sr incorporated into hydroxyapatite has been suggested as a sink for radionuclides because of its resistance to radiation damage and exceedingly low solubility ($K_{sp} = 10^{-44}$) (Fuller et al., 2002; Handley-Sidhu et al., 2011).

Interestingly, for Carbo-Iron [7], a single O shell at 2.6 Å did not resolve the spectra, instead, the best fit contained 3 shells as O, C and Fe (Table 1). The resulting fit suggests that after treatment with Carbo-Iron both U and Sr were precipitated into similar forms. The addition of the C and Fe shell contributed significantly to the fit (F-test 95.2 %) with the C shells within range for Sr-C distances in SrCO_3 (3.1-3.4 Å) (Littlewood et al., 2017; O'day et al., 2000; Sahai et al., 2000; Wallace et al., 2013) and the Fe shell similar to reported values for sorption to goethite (3.56-3.60 Å) (Fuller et al., 2016).

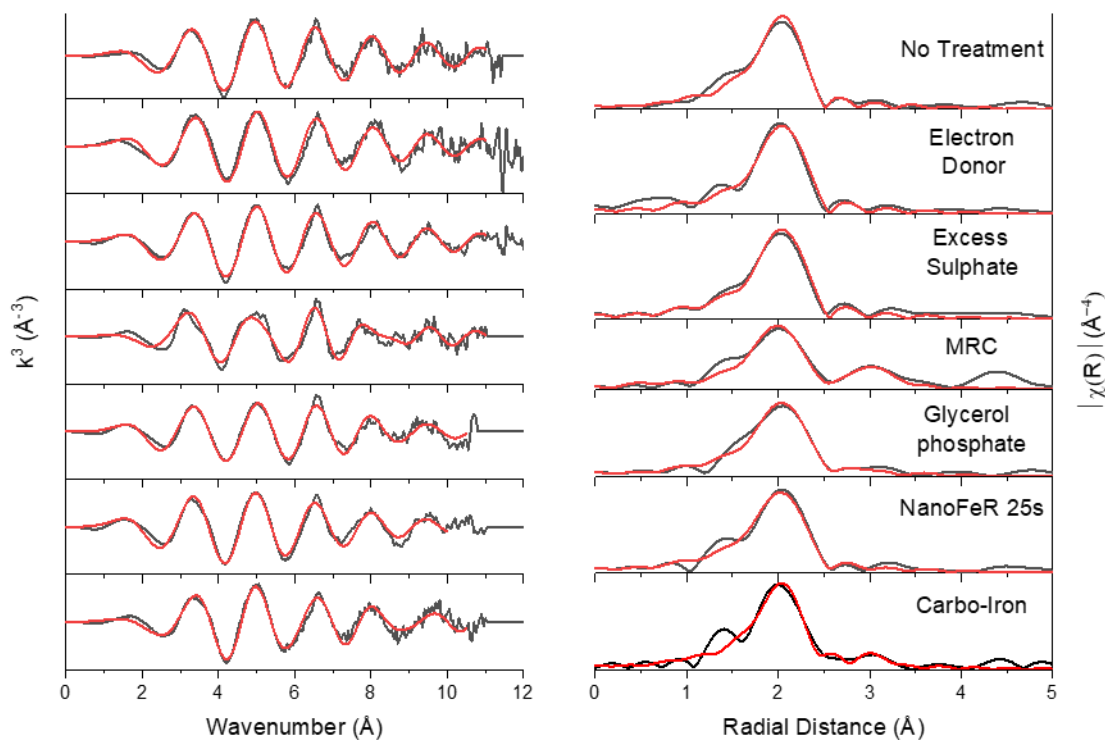


Figure 58: Sr K-edge EXAFS spectra and fits, k^3 weighted data (left) and the Fourier transforms (right).

5.44 Oxidative Remobilisation of U and Sr

Remobilisation experiments were used to determine the stability of U and Sr end-points after 300 days of incubation. The most stable end-points are those which do not re-dissolve into solution after being subject to oxygen ingress or the addition of excess nitrate (10 mM). Under these conditions the re-oxidation of bioavailable Fe(II), as well as the remobilisation of U and Sr was assessed. The results demonstrate that U end-points formed using glycerol phosphate [5] and Carbo-Iron [7] were more recalcitrant to oxidative remobilisation than other methods (Figure 55 & Figure 56). Additionally, all Sr phases were recalcitrant to oxidative remobilisation by oxygen or nitrate and thus comparisons between each technique should only be drawn based upon their Sr removal during the incubation stages. In each experiment, the geochemical monitoring of Eh (Figure 61), bioavailable Fe(II) (Figure 55), nitrate, nitrite and sulphate concentrations (SI 4: Ion Chromatography) and significant changes in microbial community (SI 6: Microbial Community Characterisation) confirmed that oxidising conditions had been re-established.

In the no treatment [1], the electron donor [2] and the excess sulphate [3] systems, U was highly susceptible to oxidative remobilisation via oxygen ingress. After 100 days of aeration, these systems showed all showed similar levels of U remobilisation; all 3 systems remobilised between 77-87 % U; aqueous U concentrations on day 400 were 39 ppm (89 %) [1], 34 ppm (78 %) [2] and 36 ppm (81 %) [3] (Figure 1). This suggests that the reduced S minerals (likely iron-sulphides) associated with sulphate-reducing bacteria activity did not hinder U reoxidation and remobilisation upon oxygen ingress, consistent with literature (Sani et al., 2004). However, after addition of 10 mM nitrate the levels of solid phase U retention varied dramatically. Here, the systems remobilised 32 ppm (73 %), 21 ppm (48 %) and 11 ppm (25 %) of U in the no treatment [1], the electron donor [2] and the excess sulphate [3] systems, respectively (Figure 55). This is consistent with the formation of biogenic U phases, as characterised by EXAFS spectroscopy (Figure 57), which are widely accepted as highly susceptible to oxidative remobilisation (Law et al., 2011; Newsome et al., 2015b; Senko et al., 2002; Wang et al., 2014; Zhong et al., 2005). Interestingly, the excess sulphate system did significantly inhibit Fe(II)-oxidation and U remobilisation in the nitrate amended experiments (Figure 55), suggesting this treatment may have positive, but limited effects on the longevity of bio-reduced U. This result contrasts with previous findings from dynamic sediment column studies which found that sulphate-reducing systems were more effective at limiting bio-reduced U remobilisation upon infiltration of dissolved oxygen rather than nitrate (Moon et al., 2009).

MRC [4] was a reasonably effective agent in creating a more recalcitrant form of U. Here, the MRC system only re-released 19 ppm (43 %) U upon aerobic remobilisation despite evidence of comprehensive re-oxidation of the system *i.e.* the full re-oxidation of bioavailable Fe(II) and the observed changes in the microbial community (Figure 1 & Figure 87). This is consistent with forming a U(VI) end-point after 300 days of incubation which would be less prone than U(IV) to remobilise as oxic conditions developed. After aerobic remobilisation the pH increased over 100 days, during which time electron donor was consumed, as seen previously in other MRC treated sediment studies that were subject to aerobic remobilisation (Newsome et al., 2017). In contrast, nitrate remobilisation caused no change in U solubility after 100 days of perturbations, and MRC did not consume nitrate or sulphate (Figure 75, Figure 76). These results suggest that MRC is an effective treatment to combat nitrate induced remobilisation of U and Sr. Although upon comparison with the glycerol phosphate or

the ZVI-based systems, MRC is not suitable to treat U or Sr contaminated lands in contrast to research using MRC to treat Tc that found near complete and sustained removal of Tc from contaminated groundwater (Newsome et al., 2017).

Glycerol phosphate treated sediments [5] showed significant recalcitrance to remobilization and re-oxidation caused by nitrate addition or oxygen ingress. After 100 days of aerobic perturbations only 9 ppm (20 %) U was found in solution. Additionally, 0 ppm (<1 %) U and 2 ppm (3 %) Sr remobilised after the addition of 10 mM nitrate. Although this could be attributed to the presence of excess phosphate (Latta et al., 2016), which could be re-precipitating and remobilised U, it is unlikely as during the remobilisation study excess phosphate levels did not decrease substantially. The stability is more likely due to formation of highly stable 'nigyoite-like' structures, as identified in the EXAFS fitting. These mineral phases are highly insensitive to oxidative remobilisation and the results of this study are consistent with the relevant literature (Newsome et al., 2015c). The re-oxidised U(IV) phosphate mineral was previously studied by XAS (Newsome et al., 2015c), here they found that after 100 days of oxidative remobilisation the structure was remarkably similar to the bioreduced U(IV) phosphate, demonstrating the high level of oxidation recalcitrance exhibited by the U(IV) phosphate phases. Interestingly, although analysis of the EXAFS of the electron donor [2] and the excess sulphate [3] systems also identified U-phosphate phases, the experiments amended with glycerol phosphate were much more recalcitrant to oxidative remobilisation. This is because the glycerol phosphate amendments formed highly stable U(IV)-phosphate minerals as opposed to weaker amorphous U(IV)-P phases, often bound to inorganic phosphate, which are highly susceptible to oxidative remobilisation (Alessi et al., 2014; Bargar et al., 2013; Bernier-Latmani et al., 2010; Boyanov et al., 2011; Fletcher et al., 2010; Latta et al., 2016; Sharp et al., 2011).

Both ZVI based systems created highly recalcitrant U and Sr phases. After 100 days of aerobic re-oxidation, 11 ppm (25 %) U and 5 ppm (6 %) Sr was present in the aqueous phase after treatment with NanoFeR 25s and 0 ppm (0 %) U and 13 ppm (16 %) Sr was found in the aqueous phase after treatment with Carbo-Iron. U treated with NanoFeR 25s was completely insensitive to nitrate induced remobilisation and the U treated with Carbo-Iron was also highly recalcitrant. After nitrate induced remobilisation 0 ppm (0 %) of U and 7 ppm (8 %) Sr remained in the solid phase in the presence of NanoFeR 25s and 6 ppm (12 %) of U and 9 ppm (12 %) Sr remained in the solid phase in the presence of Carbo-Iron. Both systems showed increased U recalcitrance to remobilisation compared to previous publications for U removal by ZVI, which found that long-term immobilisation was only maintained under simple conditions and that the presence of ligands (predominantly carbonate) led to preferential re-release of U (Crane et al., 2011). U re-oxidation after aeration was significantly slower in the presence of Carbo-Iron compared to NanoFeR 25s. This may be due to the formation of U-C or U-Fe phases as identified in the EXAFS (Figure 57); or the presence of oxidised C-OH and C=O functional groups, which have been suggested to act as redox buffers to contaminant species such as the ones in the activated carbon framework of Carbo-Iron (Newsome et al., 2019; Wu et al., 2017). This suggests that U and Sr phases reduced by Carbo-Iron and NanoFeR 25s are significantly more recalcitrant to oxidative remobilisation, as seen with Tc (Newsome et al., 2017). Treatments of Carbo-Iron and NanoFeR 25s both saw sustained Sr removal from solution, which did not remobilise after perturbation, in contrast to previous literature (Efecan et al., 2009).

5.45 Microbial Analysis of the Remobilised Samples

The microbial community that developed after aerobic remobilisation demonstrated that oxic conditions had been re-established and also suggested that fermentation was occurring. *Actinobacteria* of the order *Micrococcales* and *Micromonosporales*, which have been known as Fe(II)-oxidisers were observed across the oxic systems in significant quantities (Bryce et al., 2018; Busse, 2016). Here, the genus *Pseudoarthrobacter*, strict aerobes (Busse, 2016) represented 26 % of the OTUs in after aerobic remobilisation of the NanoFeR 25s system. Several *spp.* of other aerobic bacteria such as the class *Anaerolineae* were also present in the re-oxidised samples in significant quantities (Kublanov 2013). Interestingly, in the aerobically remobilised day 400 samples in the MRC system [4], the 16S primers used detected that the microbial community was dominated by a Fungi, specifically the species *Talaromyces stipitatus strain ATCC 10500*. This species is a non-pathogenic saprophyte found in soil and decaying plant matter (Zang et al., 2015) and the large shifts in the microbial community in the day 400 aerobic samples demonstrate that the systems have been driven aerobic, consistent with the geochemical dataset (Figure 1 and Figure 2).

Following nitrate addition the microbial communities in the experiments did not change notably compared to the day 300 bioreduction samples (Figures 30-36), suggesting that many of the organisms that proliferated during the initial bioreduction steps, were also able to respire nitrate, consistent with the biogeochemical data (Figures 1 & 2).

U Speciation in the Remobilised Nanoscale Zero Valent Iron Samples

Because the samples treated with glycerol phosphate [5], NanoFeR 25s [6] and Carbo-Iron [7] showed the most promising results, we prepared EXAFS samples with sediments that had been aerobically agitated for 60 days. As this has already been carried out for glycerol phosphate we did not repeat the experiment (Newsome et al., 2015c). In both the ZVI systems, after re-oxidation XAS showed that all of the U in both samples had completely re-oxidised to U(VI); despite this, the majority of U remained partitioned to the solid phase (Figure 57, Table S1). This is observed as a qualitative change in shape of the XANES that includes an increase in the white line energy (Table 12), and the emergence of a $U=O_{ax}$ shell with the concurrent loss of a U-U shell in the Fourier transforms (Figure 3). In the case of NanoFeR 25s the U EXAFS data and fits were remarkably similar to published structures of uranyl(VI) carbonates that bind through an inner-sphere complexation mechanism to Fe(III) edge sites (Bargar et al., 2000; Catalano and Brown, 2005; Waite et al., 1994; Winstanley et al., 2019). Whilst the re-oxidised Carbo-Iron EXAFS sample could be fit in a similar manner, it lacked a U-C backscatterer suggesting that upon aeration the previously reduced U phases, which were bound to C and Fe, re-oxidised to form U(VI) species that only interact with Fe.

5.5 Conclusions

Batch microcosm experiments investigated the potential for 7 different treatments to remediate U and Sr co-contaminated sediments over a 300 day period. Whilst U removal by the ZVI-based treatments (NanoFeR 25s [6] and Carbo-Iron [7]) was rapid, MRC [4] and glycerol phosphate [5] amendments also lead to enhanced U removal over 300 days. Sulphate rich conditions [3], glycerol phosphate [5], NanoFeR 25s [6] and Carbo-Iron [7] showed enhanced Sr removal from solution compared to both the natural attenuation [1] and electron donor [2] amended sediments. The change in microbial community was assessed using 16S rRNA gene analysis and EXAFS characterised the resulting U and Sr speciation in the incubated sediments. The resulting EXAFS fitting models were used

to understand the behaviour and stability of the treated analytes. Following anaerobic incubations, the co-treated U and Sr end-points were subject to oxidative remobilisation by both oxygen or nitrate ingress. Again, the microbial community was assessed and the changes in microbial community and re-oxidation of bioavailable Fe(II) confirmed where oxidising conditions had been achieved. After remobilisation experiments the least mobile phases were glycerol phosphate [5] and Carbo-Iron [7] for both U and Sr (Figures 56 & 57). The longevity of U end-points in the ZVI systems has demonstrated a clear improvement compared to early ZVI treatments. As previously noted glycerol phosphate amendments proved highly successful, and EXAFS analysis identified U and Sr incorporation into highly recalcitrant phosphate minerals. Although biogenic iron sulphides are reported to protect biogenic U(IV) from re-oxidation (Abdelouas, Lutze, and Nuttall 1999), the excess sulphate system [3] did not provide significant oxidation buffering capacities after oxygen ingress. Neither oxygen nor nitrate had a significant effect on Sr remobilisation after 300 days of incubation in any system. Following aerobic conditions 25% U remobilisation was observed NanoFeR 25S, which was much higher than for Carbo-Iron (0%). Here, the Remobilised EXAFS after aerobic perturbations demonstrated that the immobile phases formed by NanoFeR 25s and Carbo-Iron were not susceptible to oxidative remobilisation despite the U(IV) being re-oxidised back to U(VI). This is dissimilar to the U(IV) phosphate formed by glycerol phosphate amendments which have previously demonstrated that the U(IV) 'ningyoite-like' mineral formed was highly recalcitrant to oxidation (Newsome et al., 2015c).

In conclusion U and Sr contaminated phases co-treated using glycerol phosphate [5] and Carbo-Iron [7] compared to biogenic U(IV) clearly demonstrate the stability of the incubated end-points which are highly recalcitrant to oxidative remobilisation by oxygen and nitrate. The experimental results presented here, combined with previous findings, suggest that these may be suitable as a long-term treatment option for U and Sr -contaminated groundwaters (Cleary et al., 2019; Newsome et al., 2019, 2017). All three systems therefore warrant further analysis in long-term column experiments and eventually field-scale studies to check their stabilities under in-situ conditions.

5.6 Acknowledgements

We thank Alastair Bewsher and Paul Lythgoe (The University of Manchester) for IC and ICP-MS analytical support respectively. We also thank Katrin Mackenzie and Steffen Bleyl (UFZ Leipzig) for providing Carbo-Iron, Petra Skácelová (NANOIRON) for providing NanoFer 25s and Jack Shore (Regenesis) for providing MRC. This work was supported by a PhD bursary from the Nuclear Decommissioning Authority, (R120085) managed by the National Nuclear Laboratory. Beamtime at the beamline B18 was funded by the grant SP13559-2 from the Diamond Light Source.

5.7 Supporting Information

This Supporting Information document discusses: SI 1: Sediment and Synthetic Groundwater Composition, SI 2: Experiment Design and Visible Changes, SI 3: pH and Eh changes, SI 4: Ion Chromatography, SI 5: Total Aqueous Fe, SI 6: Microbial Community Characterisation, SI 7: Additional X-ray Absorption Spectroscopy Data and Analysis, SI 8: Powder X-Ray Diffraction and SI 8: Control Precipitation Experiment.

SI 1: Sediment and Synthetic Groundwater Composition

The sediments used in this study were taken from the same location as (Law et al., 2010a). The sediment mineralogy was composed mostly of silicate minerals including quartz (SiO₂), sheet silicates

(muscovite, $[KAl_2(Si_3Al)O_{10}(OH,F)_2]$ and clinocllore, $[(Mg,Fe^{2+})_5Al_2Si_3O_{10}(OH)_8]$), feldspars (Albite, $[NaAlSi_3O_8]$ and microcline, $[KAlSi_3O_8]$) and iron oxides (hematite, $[Fe^{3+}_2O_3]$). X-ray fluorescence analysis showed that the sediment contained (wt %): Si (63.1), Al (15.7), Fe (6.5), K (4.9), Mg (2.2), Na (1.3), Ca (0.7), Ti (0.7), Mn (0.2), P (0.1) and other trace metals at concentrations below 0.1 wt %. The proportion of organic C lost as CO_2 was determined by loss on ignition, as 4.1 wt %. Prior to starting the experiments the concentration of 0.5 N HCl extractable Fe was measured as 7.35 ± 0.8 mmol/kg with 1.5 ± 0.65 % present as Fe(II) and the pH was determined after equilibrating 1 g of sediment in 1 mL of water for an hour (pH 6.5). The recipe for artificial groundwater was adapted from (Wilkins et al., 2007) and contained (mM): KCl (0.09), $MgSO_4 \cdot 7H_2O$ (0.39), $MgCl_2 \cdot 6H_2O$ (0.39), $CaCO_3$ (1.67), $NaNO_3$ (0.32), NaCl (0.16), $NaHCO_3$ (2.88) and $SrCl_2$ (0.99).

SI 2: Experiment Design and Visible Changes

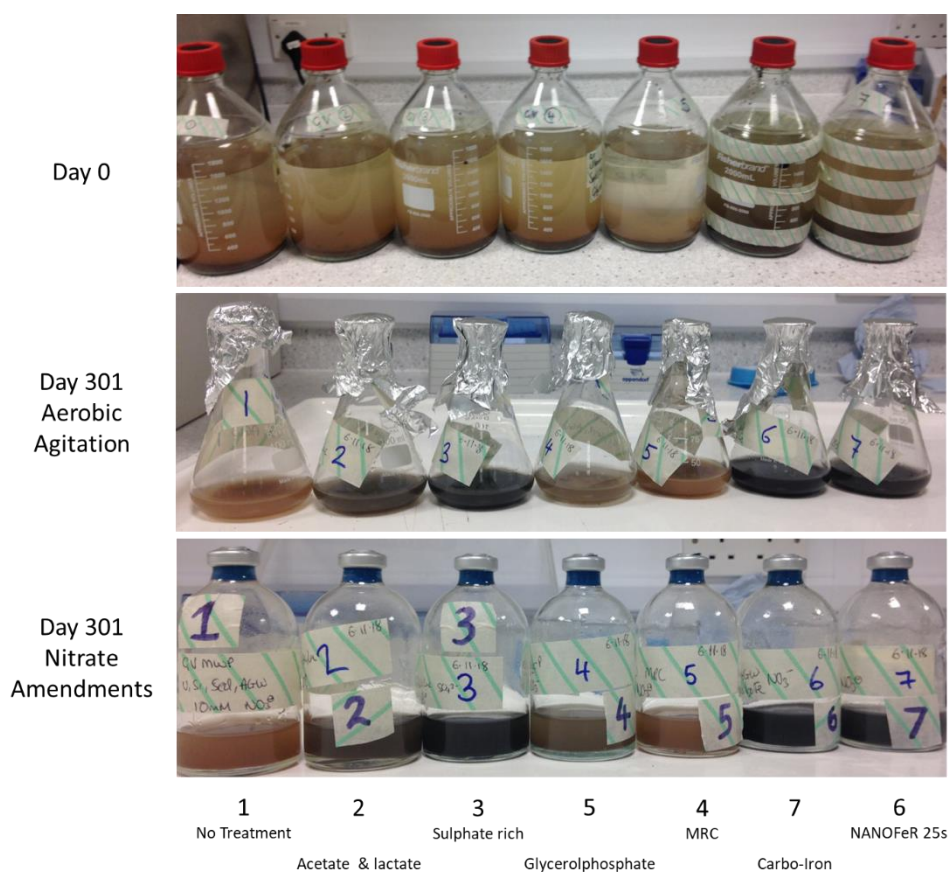


Figure 59: Photographs of: (top) the 1.5 L microcosms at the start of the experiments (day 0) and; the remobilisation experiments following aerobically agitated (middle) and nitrate amended (bottom) systems. At the start of the remobilisation studies (day 300). Note the colour change (darkening) in the electron amended (2) and sulphate rich system (3) between days 0 and 300.

SI 3: pH and Eh changes

All systems showed minor changes in the pH over the 400 with the exception of MRC and the sulphate rich system (Figure 60). The Eh value in the sulphate system had reached -400 mV by 100 days, indicative of sulphate reducing conditions. No other system went as reducing but the NanoFeR 25s system reached almost -200 mV, unlike Carbo-Iron which only reached 0 mV (Figure 61).

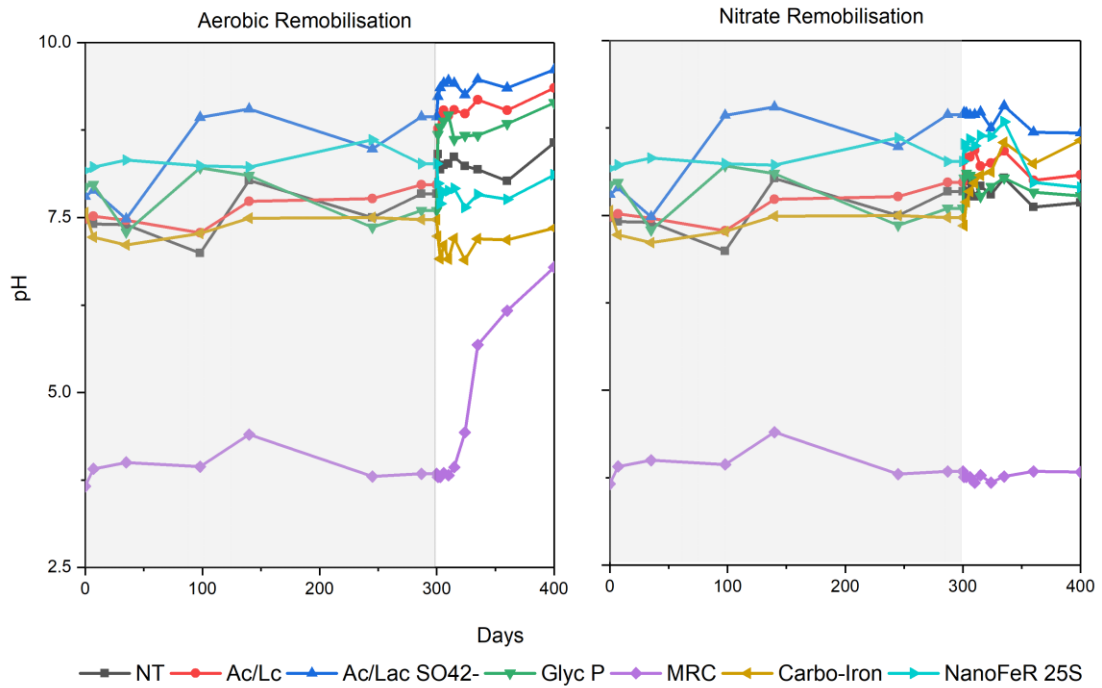


Figure 60: Changes in pH across all experiments. Incubation phases are highlighted in grey and remobilisation phases are left blank.

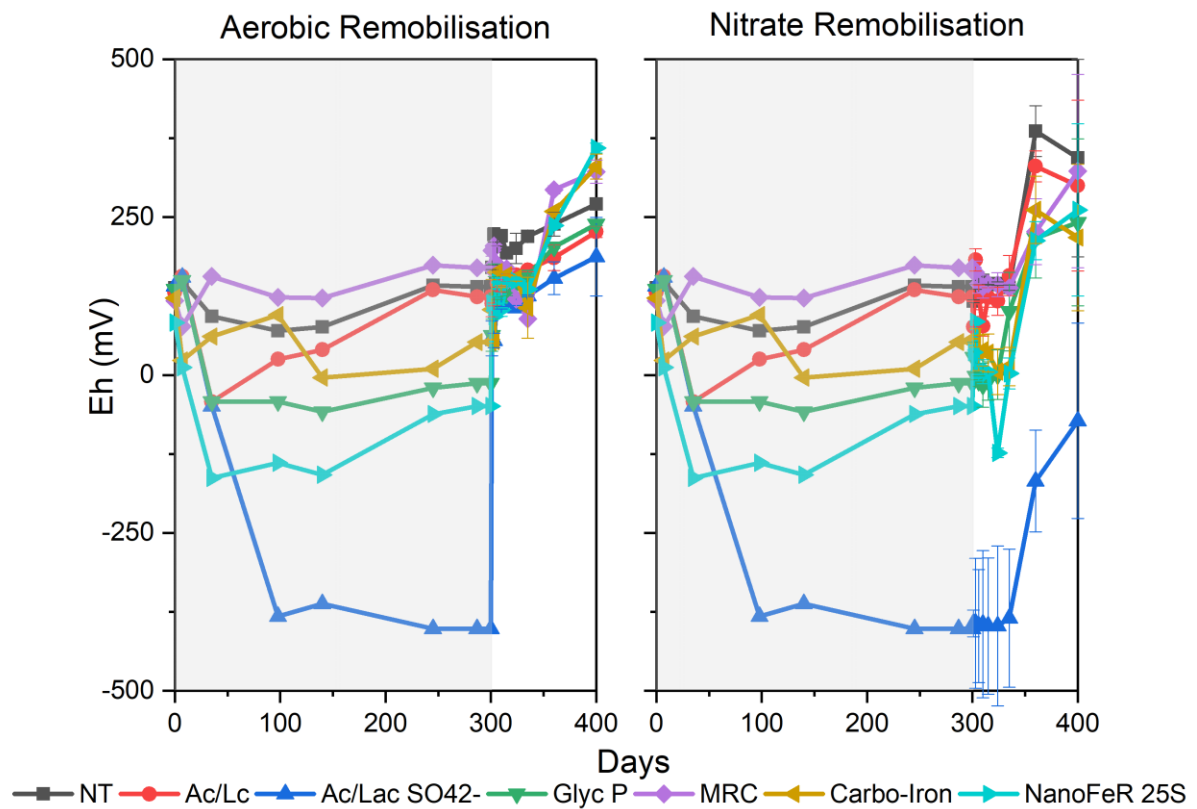


Figure 61: Eh values across all experiments. Incubation phases are highlighted in grey and remobilisation phases are left blank. Error bars represent 1 standard deviation based on triplicate measurements.

SI 4: Ion Chromatography

Here, we present selected IC results from the batch incubation and the remobilisation studies. Each system is presented together and where appropriate multiple species have been plotted on graphs. Monitoring aqueous phosphate and nitrate using a Dionex ICS 5000 with an AS18 2 mm ion exchange column at 0.25 mL/min and monitoring sulphate, nitrite, glycerol phosphate and volatile fatty acids using a Dionex ICS 5000 with an AS11HC 0.4 mm high-capacity ion exchange column at 0.015 mL/min.

System 1: Natural Attenuation

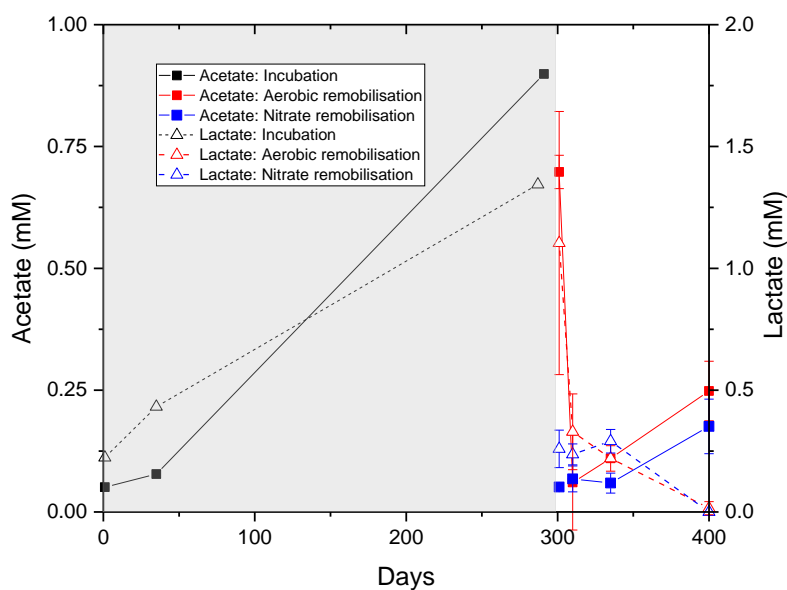


Figure 62: Acetate (left axis) and Lactate (right axis) concentrations in the electron donor system [1]. With data for the incubation phase (black lines) and remobilisation data for each species after aeration (red lines) or when amended with nitrate (blue lines). Measurements were performed in triplicate with error bars representing 1 standard deviation (σ). Incubation phases are highlighted in grey and remobilisation phases are left blank.

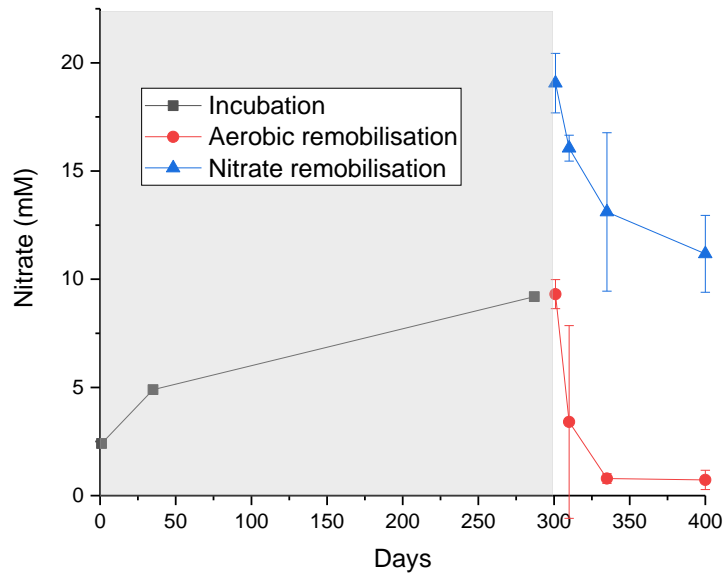


Figure 63: Nitrate concentrations in the no treatment system [1]. With data for the incubation phase (black lines) and remobilisation data for each species after aeration (red lines) or when amended with nitrate (blue lines). Measurements were performed in triplicate with error bars representing 1 standard deviation (σ). Incubation phases are highlighted in grey and remobilisation phases are left blank.

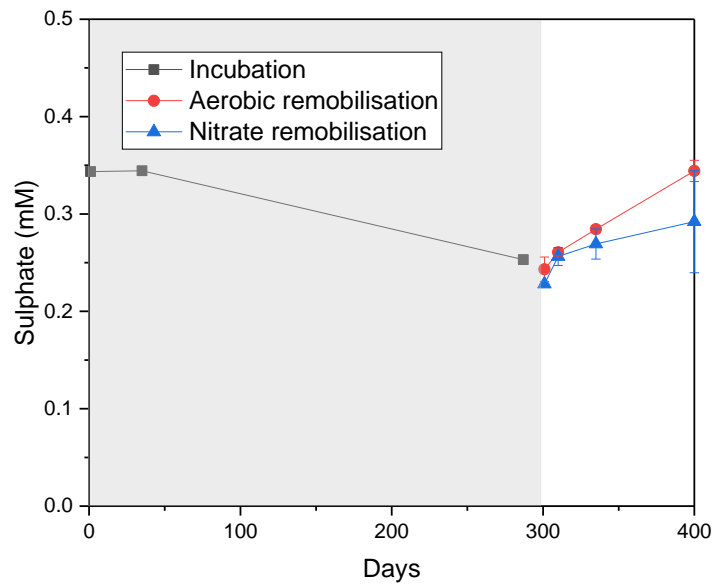


Figure 64: Sulphate concentrations in the no treatment system [1]. With data for the incubation phase (black lines) and remobilisation data for each species after aeration (red lines) or when amended with nitrate (blue lines). Measurements were performed in triplicate with error bars representing 1 standard deviation (σ). Incubation phases are highlighted in grey and remobilisation phases are left blank.

System 2: Electron Donor

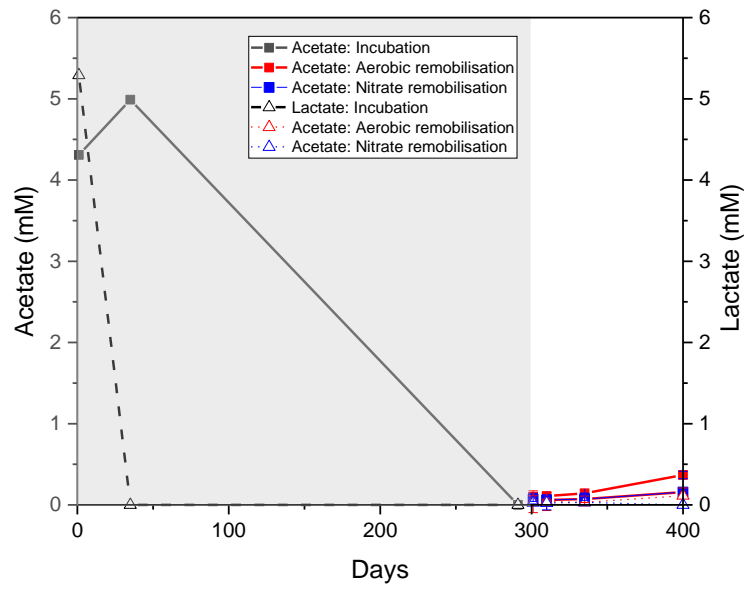


Figure 65: Acetate (left axis) and Lactate (right axis) concentrations in the electron donor system [2]. With data for the incubation phase (black lines) and remobilisation data for each species after aeration (red lines) or when amended with nitrate (blue lines). Measurements were performed in triplicate with error bars representing 1 standard deviation (σ). Incubation phases are highlighted in grey and remobilisation phases are left blank.

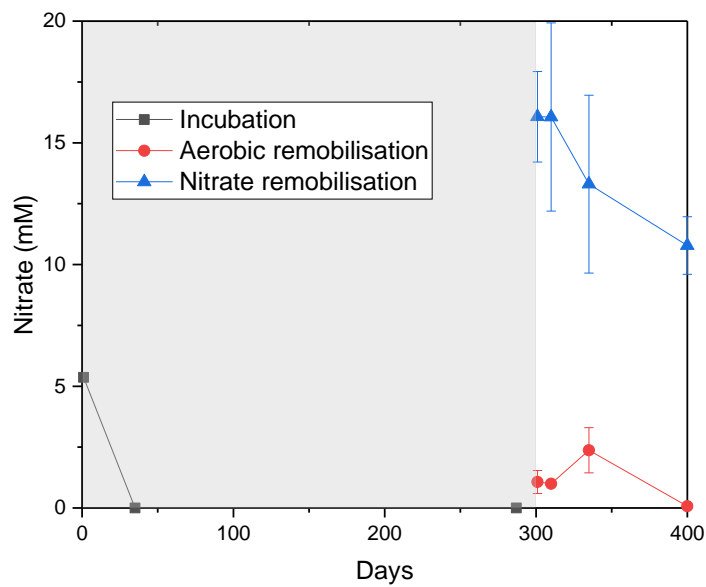


Figure 66: Nitrate concentrations in the electron donor system [2]. With data for the incubation phase (black lines) and remobilisation data for each species after aeration (red lines) or when amended with nitrate (blue lines). Measurements were performed in triplicate with error bars representing 1 standard deviation (σ). Incubation phases are highlighted in grey and remobilisation phases are left blank.

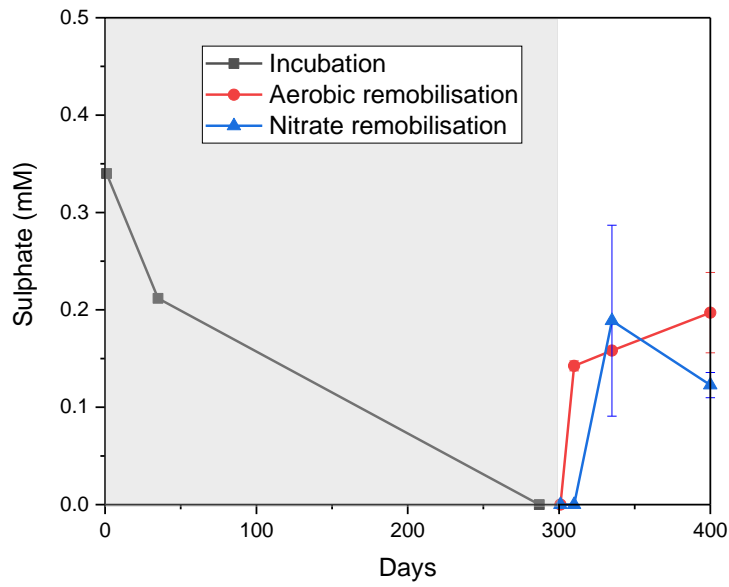


Figure 67: Sulphate concentrations in the electron donor system [2]. With data for the incubation phase (black lines) and remobilisation data for each species after aeration (red lines) or when amended with nitrate (blue lines). Measurements were performed in triplicate with error bars representing 1 standard deviation (σ). Incubation phases are highlighted in grey and remobilisation phases are left blank.

System 3: Excess Sulphate

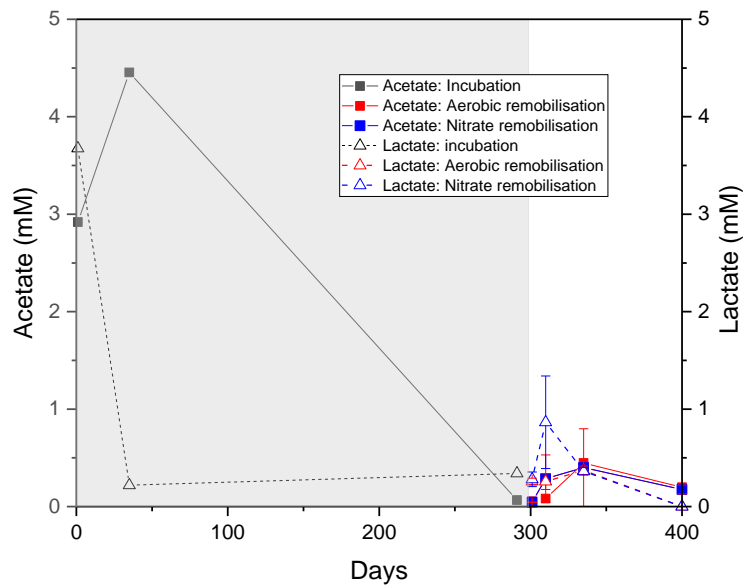


Figure 68: Acetate (left axis) and Lactate (right axis) concentrations in the excess sulphate system [3]. With data for the incubation phase (black lines) and remobilisation data for each species after aeration (red lines) or when amended with nitrate (blue lines). Measurements were performed in triplicate with error bars representing 1 standard deviation (σ). Incubation phases are highlighted in grey and remobilisation phases are left blank.

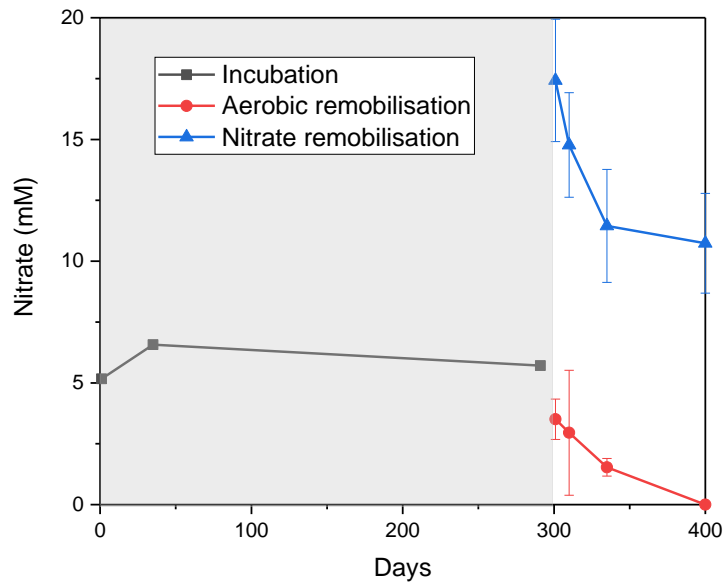


Figure 69: Nitrate concentrations in the excess sulphate system [3]. With data for the incubation phase (black lines) and remobilisation data for each species after aeration (red lines) or when amended with nitrate (blue lines). Measurements were performed in triplicate with error bars representing 1 standard deviation (σ). Incubation phases are highlighted in grey and remobilisation phases are left blank.

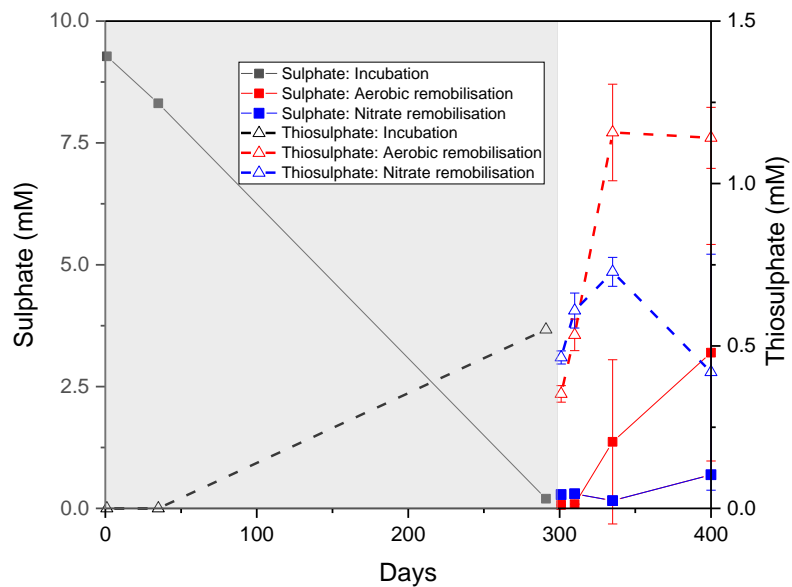


Figure 70: Sulphate (left axis) and thiosulphate (right axis) concentrations in the excess sulphate system [3]. With data for the incubation phase (black lines) and remobilisation data for each species after aeration (red lines) or when amended with nitrate (blue lines). Measurements were performed in triplicate with error bars representing 1 standard deviation (σ). Incubation phases are highlighted in grey and remobilisation phases are left blank.

System 4: MRC

Neither acetate nor lactate were detected at any point in the MRC amended system [4].

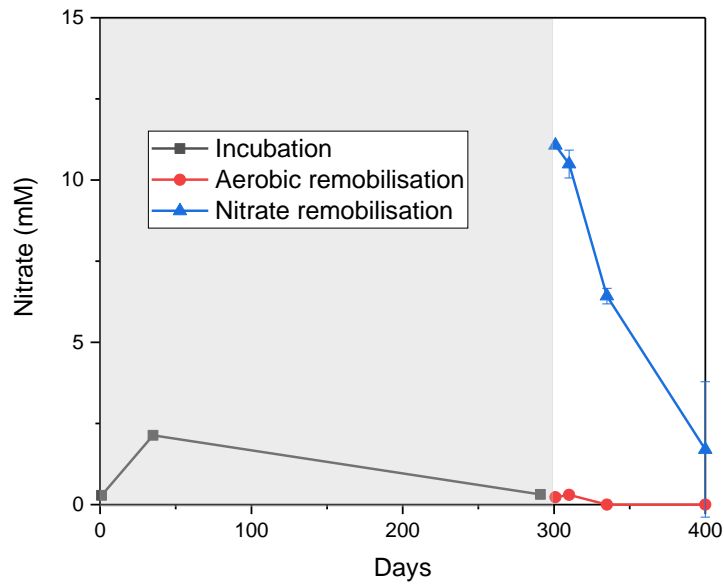


Figure 71: Nitrate concentrations in the MRC system [4]. With data for the incubation phase (black lines) and remobilisation data for each species after aeration (red lines) or when amended with nitrate (blue lines). Measurements were performed in triplicate with error bars representing 1 standard deviation (σ). Incubation phases are highlighted in grey and remobilisation phases are left blank.

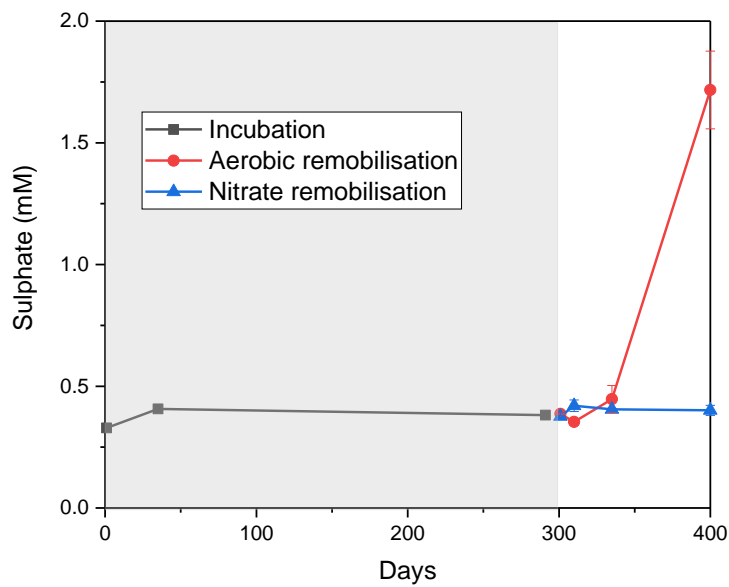


Figure 72: Sulphate concentrations in the MRC system [4]. With data for the incubation phase (black lines) and remobilisation data for each species after aeration (red lines) or when amended with nitrate (blue lines). Measurements were performed in triplicate with error bars representing 1 standard deviation (σ). Incubation phases are highlighted in grey and remobilisation phases are left blank.

System 5: Glycerol Phosphate

In system [5], glycerol phosphate was consumed within 35 days of incubation, during its consumption aqueous phosphate formed and was partially consumed. Aqueous phosphate remained in solution throughout the experiment in the aerobic remobilisation studies but was not detected during nitrate remobilisation studies (Figure 73). Lactate was not observed.

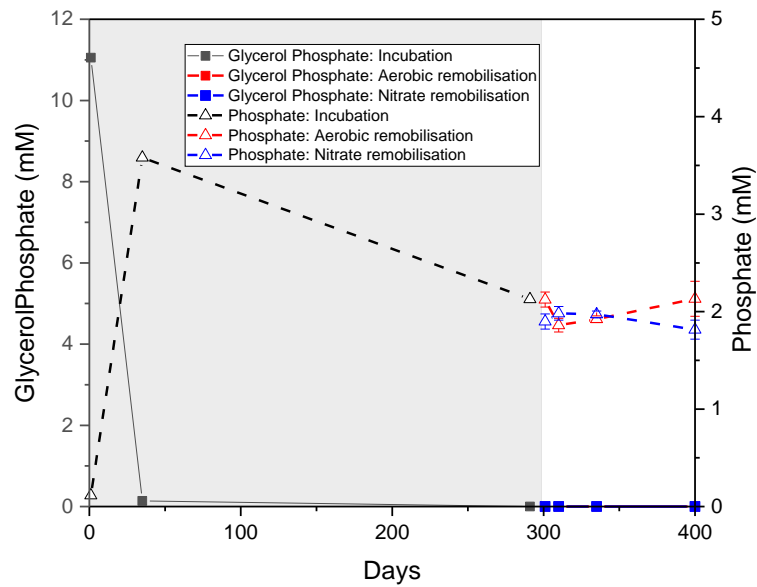


Figure 73: Glycerol Phosphate (left axis) and phosphate (right axis) concentrations in glycerol phosphate system [5]. With data for the incubation phase (black lines) and remobilisation data for each species after aeration (red lines) or when amended with nitrate (blue lines). Measurements were performed in triplicate with error bars representing 1 standard deviation (σ). Incubation phases are highlighted in grey and remobilisation phases are left blank.

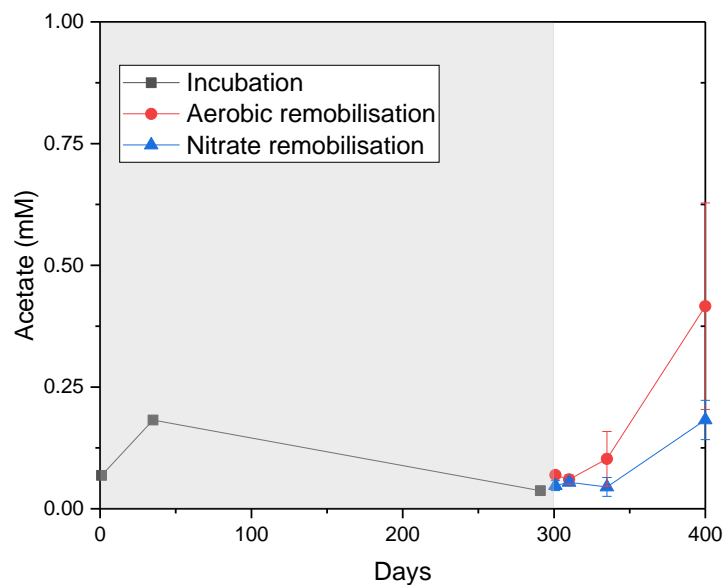


Figure 74: Acetate concentrations in glycerol phosphate system [5]. With data for the incubation phase (black lines) and remobilisation data for each species after aeration (red lines) or when amended with nitrate (blue lines). Measurements

were performed in triplicate with error bars representing 1 standard deviation (σ). Incubation phases are highlighted in grey and remobilisation phases are left blank.

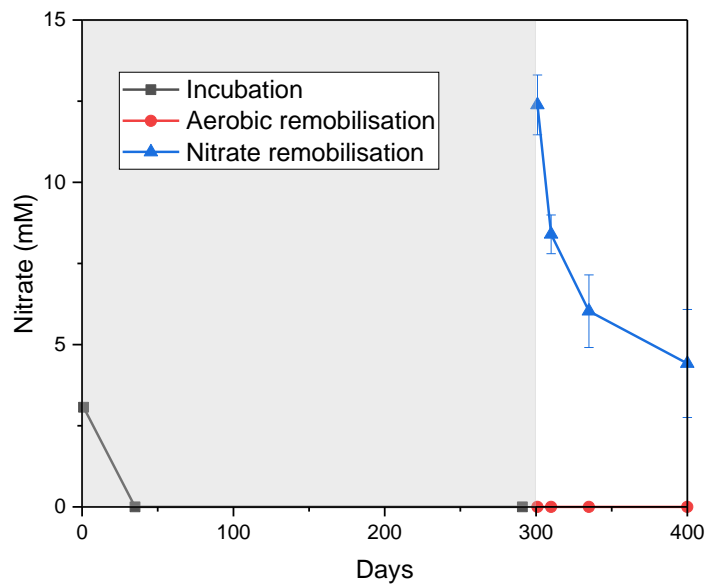


Figure 75: Nitrate concentrations in glycerol phosphate system [5]. With data for the incubation phase (black lines) and remobilisation data for each species after aeration (red lines) or when amended with nitrate (blue lines). Measurements were performed in triplicate with error bars representing 1 standard deviation (σ). Incubation phases are highlighted in grey and remobilisation phases are left blank.

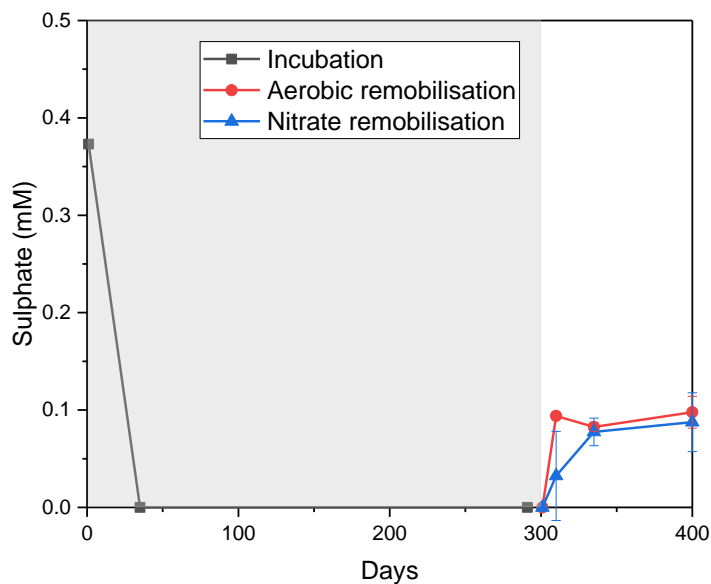


Figure 76: Sulphate concentrations in glycerol phosphate system [5]. With data for the incubation phase (black lines) and remobilisation data for each species after aeration (red lines) or when amended with nitrate (blue lines). Measurements were performed in triplicate with error bars representing 1 standard deviation (σ). Incubation phases are highlighted in grey and remobilisation phases are left blank.

System 6: NanoFeR 25s

No lactate was observed in the NanoFeR 25s system, however, detectable concentrations of propionate were observed (Figure 77). Interestingly this system was the only one which consumed all the added nitrate (Figure 78). Here and in the Carbo-Iron experiment, sulphate was entirely consumed during the incubation phase (Figure 79 & Figure 82). These results are consistent with Newsome *et al.* who observed that nanoscale iron particle treatments did not inhibit sulphate-reducing conditions in contrast to Kumar *et al.* who found the opposite (Kumar *et al.*, 2014b; Newsome *et al.*, 2019).

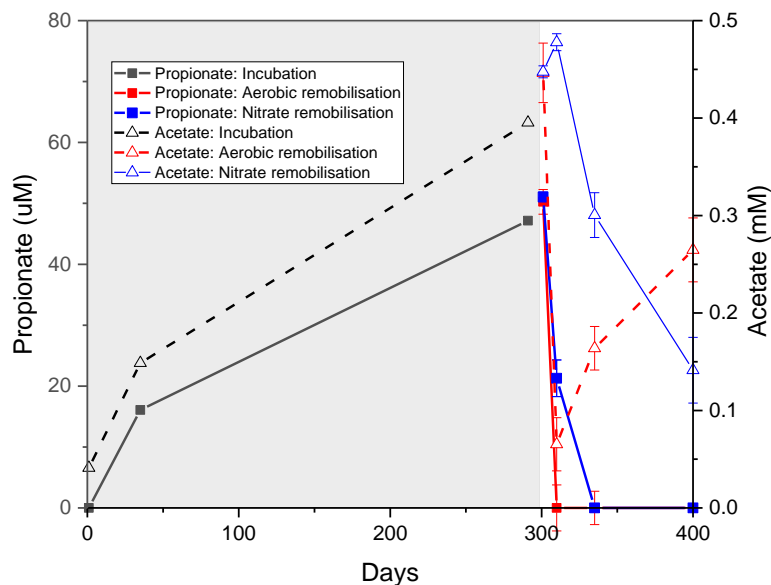


Figure 77: Propionate (left y-axis) and acetate (right y-axis) concentrations in NanoFeR 25s system [6]. With data for the incubation phase (black lines) and remobilisation data for each species after aeration (red lines) or when amended with nitrate (blue lines). Measurements were performed in triplicate with error bars representing 1 standard deviation (σ). Incubation phases are highlighted in grey and remobilisation phases are left blank.

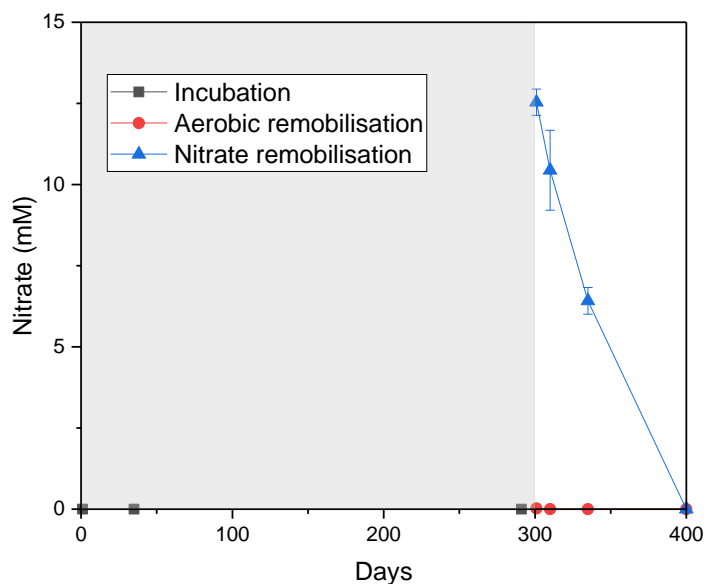


Figure 78: Nitrate concentrations in NanoFeR 25s system [6]. With data for the incubation phase (black lines) and remobilisation data for each species after aeration (red lines) or when amended with nitrate (blue lines). Measurements were performed in triplicate with error bars representing 1 standard deviation (σ). Incubation phases are highlighted in grey and remobilisation phases are left blank.

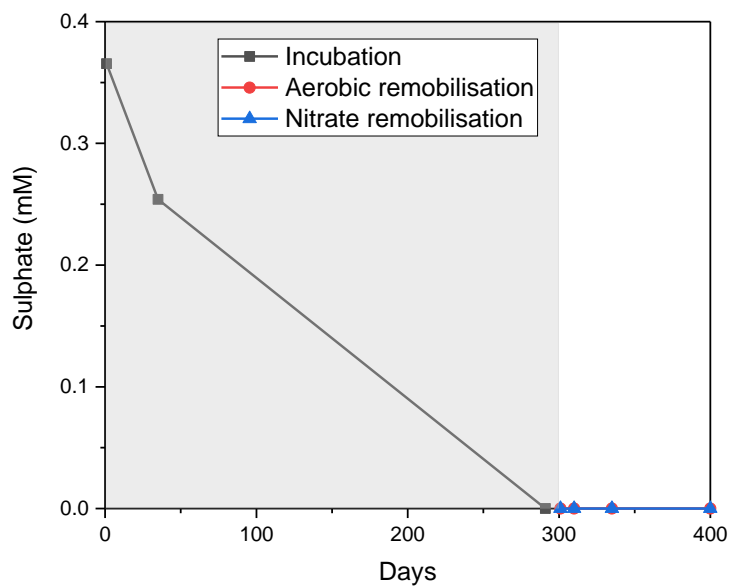


Figure 79: Sulphate concentrations in NanoFeR 25s system [6]. With data for the incubation phase (black lines) and remobilisation data for each species after aeration (red lines) or when amended with nitrate (blue lines). Measurements were performed in triplicate with error bars representing 1 standard deviation (σ). Incubation phases are highlighted in grey and remobilisation phases are left blank.

System 7: Carbo-Iron

The Carbo-Iron system produced measurable levels of nitrite during the nitrate remobilisation period, likely attributable as a denitrification intermediate. Unlike NanoFeR 25s, it did not produce any propionate.

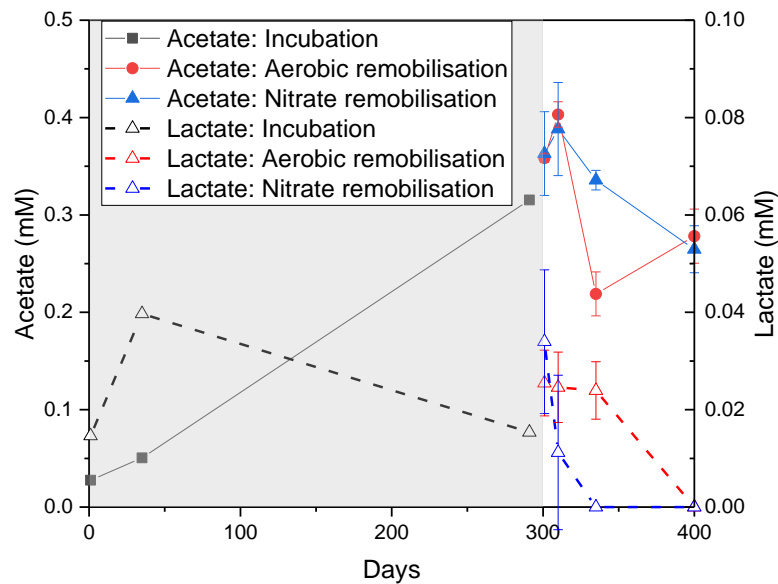


Figure 80: Acetate (left y-axis) and lactate (right y-axis) concentrations in Carbo-Iron system [7]. With data for the incubation phase (black lines) and remobilisation data for each species after aeration (red lines) or when amended with nitrate (blue lines). Measurements were performed in triplicate with error bars representing 1 standard deviation (σ). Incubation phases are highlighted in grey and remobilisation phases are left blank.

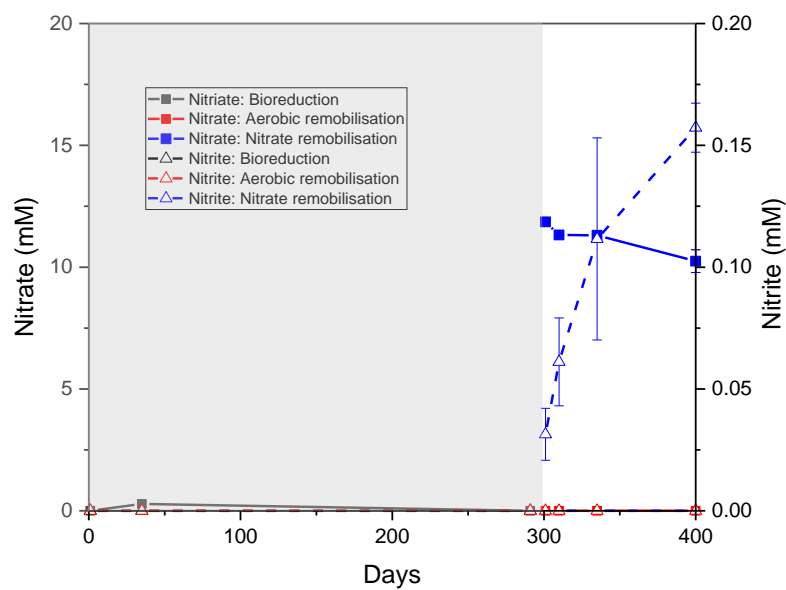


Figure 81: Nitrate (left y-axis) and nitrite (right y-axis) concentrations in Carbo-Iron system [7]. With data for the incubation phase (black lines) and remobilisation data for each species after aeration (red lines) or when amended with nitrate (blue

lines). Measurements were performed in triplicate with error bars representing 1 standard deviation (σ). Incubation phases are highlighted in grey and remobilisation phases are left blank.

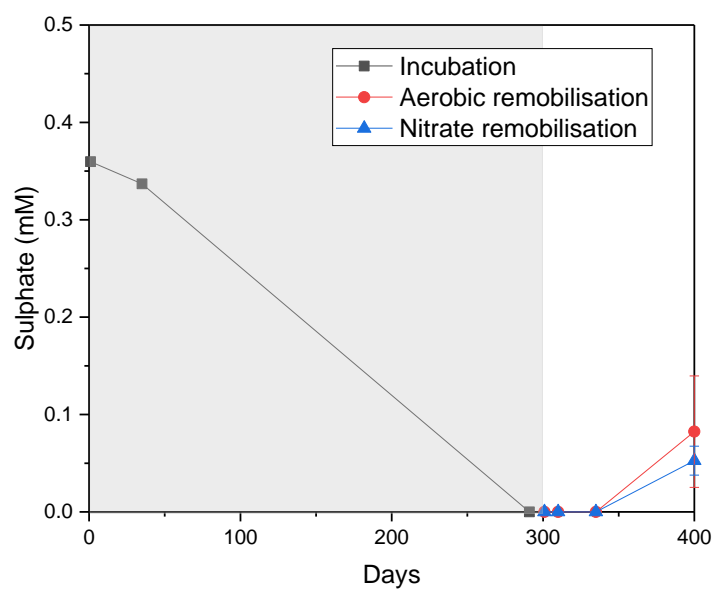


Figure 82: Sulphate concentrations in Carbo-Iron system [7]. With data for the incubation phase (black lines) and remobilisation data for each species after aeration (red lines) or when amended with nitrate (blue lines). Measurements were performed in triplicate with error bars representing 1 standard deviation (σ). Ioreduction phases are highlighted in grey and remobilisation phases are left blank.

SI 5: Total Aqueous Fe

Total aqueous Fe concentrations were determined by ICP-MS.

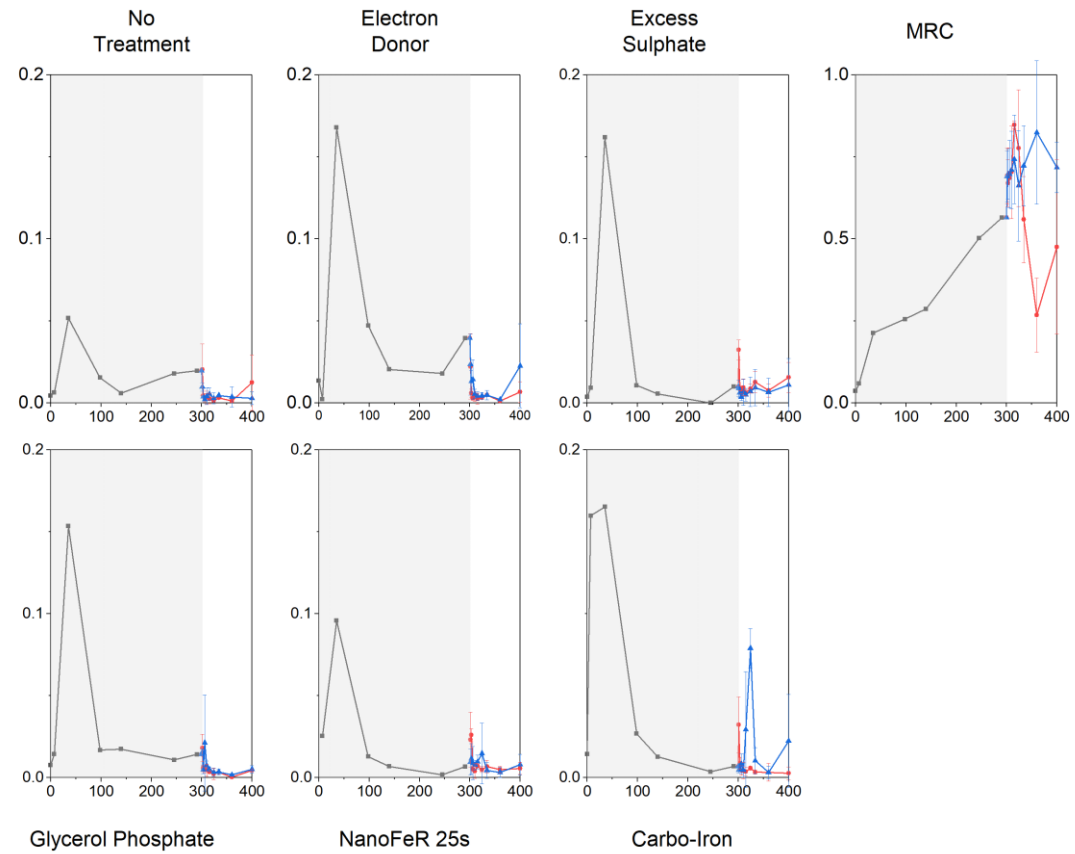


Figure 83: Total aqueous Fe as determined by ICP-MS spectroscopy, x-axes show total aqueous Fe concentrations (mM) and y-axes show time (days) Error bars represent 1 standard deviation based on triplicate measurements. incubation phases are highlighted in grey and remobilisation phases are left blank.

SI 6: Microbial Community Characterisation

The microbial community was assessed using standard procedures (Bassil et al., 2015; Cleary et al., 2019; Foster et al., 2020; Kuipers et al., 2019; Newsome et al., 2019). Here, DNA was extracted from 200 µl of sediment slurry or microcosm sample using a DNeasy PowerLyzer PowerSoil Kit (Qiagen, Manchester, U.K). Sequencing of PCR amplicons of 16S rRNA was conducted with the Illumina MiSeq platform (Illumina, San Diego, CA, USA) targeting the V4 hyper variable region (forward primer, 515F, 5'-GTGYCAGCMGCCGCGTAA-3'; reverse primer, 806R, 5'-GGACTACHVGGGTWTCTAAT-3') for 2 × 250-bp paired-end sequencing (Illumina)(Caporaso et al., 2012, 2011). PCR amplification was performed using Roche FastStart High Fidelity PCR System (Roche Diagnostics Ltd, Burgess Hill, UK) in 50µl reactions under the following conditions: initial denaturation at 95°C for 2 min, followed by 36 cycles of 95°C for 30 s, 55°C for 30 s, 72°C for 1 min, and a final extension step of 5 min at 72°C. The PCR products were purified and normalised to ~20ng each using the SequalPrep Normalization Kit (Fisher Scientific, Loughborough, UK). The PCR amplicons from all samples were pooled in equimolar ratios. The run was performed using a 4 pM sample library spiked with 4 pM PhiX to a final concentration of 10% following the method of Schloss and Kozich (Kozich et al., 2013).

Raw sequences were divided into samples by barcodes (up to one mismatch was permitted) using a sequencing pipeline. Quality control and trimming was performed using Cutadapt (Martin, 2011), FastQC (Bioinformatics, 2019), and Sickle (Joshi and Fass, 2011). MiSeq error correction was performed using SPADes (Nurk et al., 2013). Forward and reverse reads were incorporated into full-length sequences with Pandaseq (Masella et al., 2012). Chimeras were removed using ChimeraSlayer (Haas et al., 2011), and OTUs were generated with UPARSE (Edgar, 2013). OTUs were classified by Usearch (Edgar, 2010) at the 97% similarity level, and singletons were removed. Rarefaction analysis was conducted using the original detected OTUs in Qiime (Caporaso et al., 2010). The taxonomic assignment was performed by the RDP naïve Bayesian classifier version 2.2 (Wang et al., 2007). The OTU tables were rarefied to the sample containing the lowest number of sequences, all samples having less than 5,000 sequences were removed from analyses prior to the rarefaction step. The step size used was 2000 and 10 iterations were performed at each step.

Table 11: Details of molecular ecology sequencing results.

Sample	Day	Number of Reads (OTUs)	Sequences per Sample at 10200 Reads	OTUs that are Archaea (%)	Counts of Archaea (OTUs)
Control		102393	935.7	0.12	17
No Treatment [1]	1	112108	1361.5	51.04	25
	300	122670	1322.8	0.25	36
	400 – Aerobic	342366	1182.8	0.21	17
	400 – Nitrate	117257	1286.9	0.21	22
Electron Donor [2]	1	110064	1213	9.49	17
	300	101360	1372.7	1.79	28
	400 – Aerobic	130270	1293.4	9.30	18
	400 – Nitrate	123907	1132.3	0.42	26
Excess Sulphate [3]	1	102701	1028.3	1.02	14
	300	110927	700.4	0.33	19
	400 – Aerobic	114302	1050.5	12.42	13
	400 – Nitrate	82678	454.7	0.41	19
MRC	1	129797	774.5	0.18	18

[4]	300	86973	423.8	0.26	25
	400 – Aerobic	118171	693.2	0.23	21
	400 – Nitrate	129363	419.2	9.85	25
Glycerol Phosphate [5]	1	121135	299.9	0.20	25
	300	120316	555.2	8.32	6
	400 – Aerobic	15578	214.9	1.51	4
	400 – Nitrate	108666	236.5	0.40	12
NanoFeR 25S [6]	1	48479	254.8	3.56	30
	300	132066	845	0.33	15
	400 – Aerobic	132504	680.6	0.20	5
	400 – Nitrate	146088	566.2	0.38	16
Carbo-Iron [7]	1	387481	792.4	0.43	19
	300	84462	339.1	0.75	8
	400 – Aerobic	134433	592.7	0.47	11
	400 – Nitrate	119357	393.1	14.02	14

System 1: Natural Attenuation

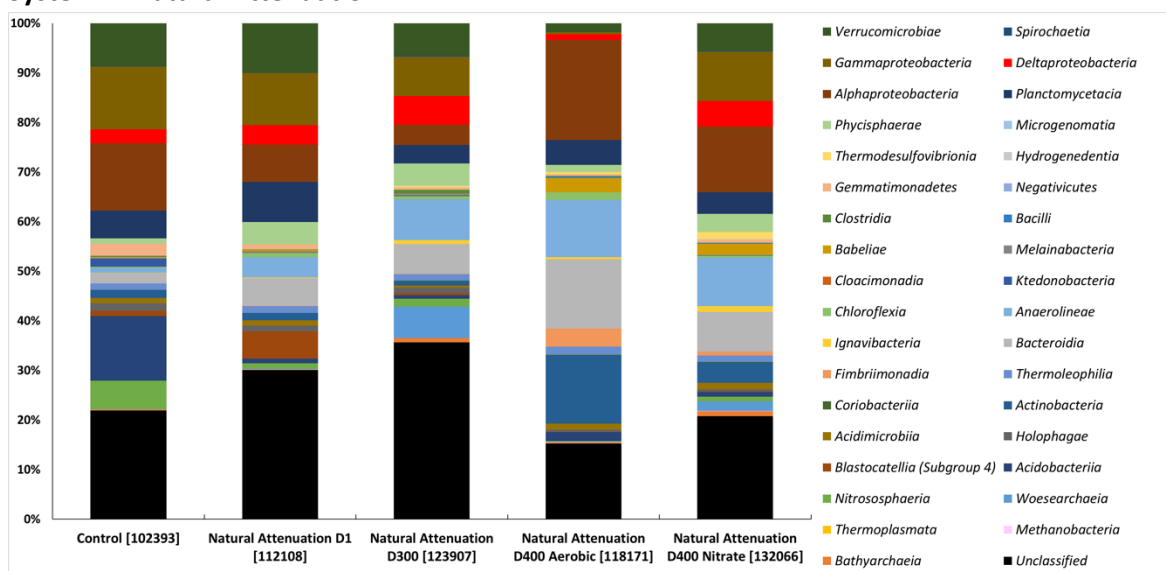


Figure 84: 16S rRNA microbial community by phylogenetic class in the control experiment (left), and the natural attenuation system [1] after: 1 day (second from the left), 300 days (middle), 400 days – aerobic remobilisation (second from the right) and 400 days – nitrate remobilisation (right). With OTUs in square brackets.

System 2: Electron Donor

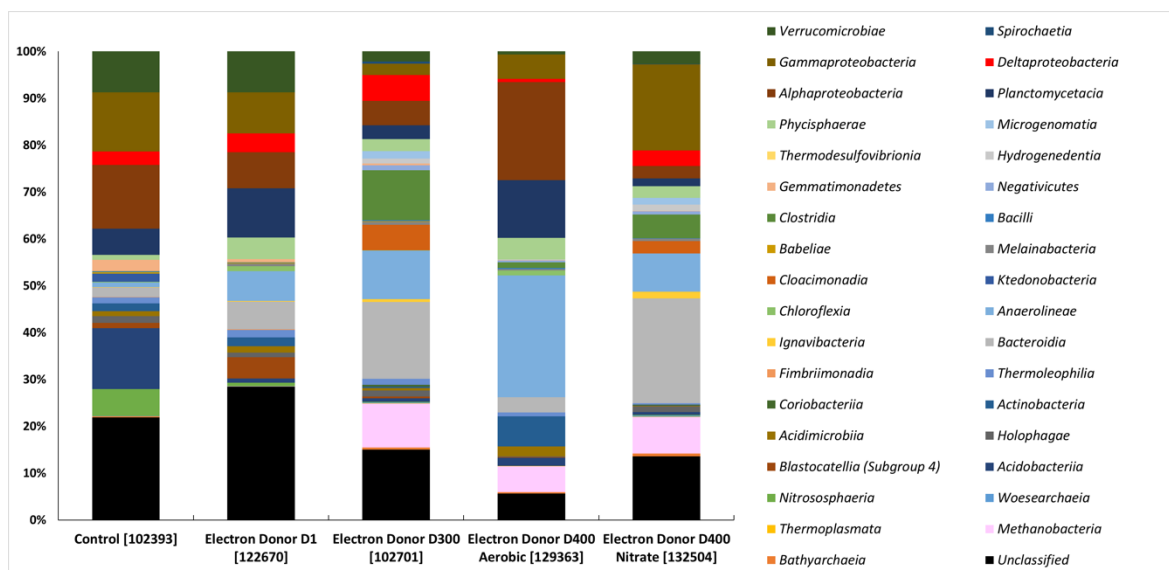


Figure 85: 16S rRNA microbial community by phylogenetic class in the control experiment (left), and the electron donor system [2] after: 1 day (second from the left), 300 days (middle), 400 days – aerobic remobilisation (second from the right) and 400 days – nitrate remobilisation (right). With OTUs in square brackets.

System 3: Excess Sulphate

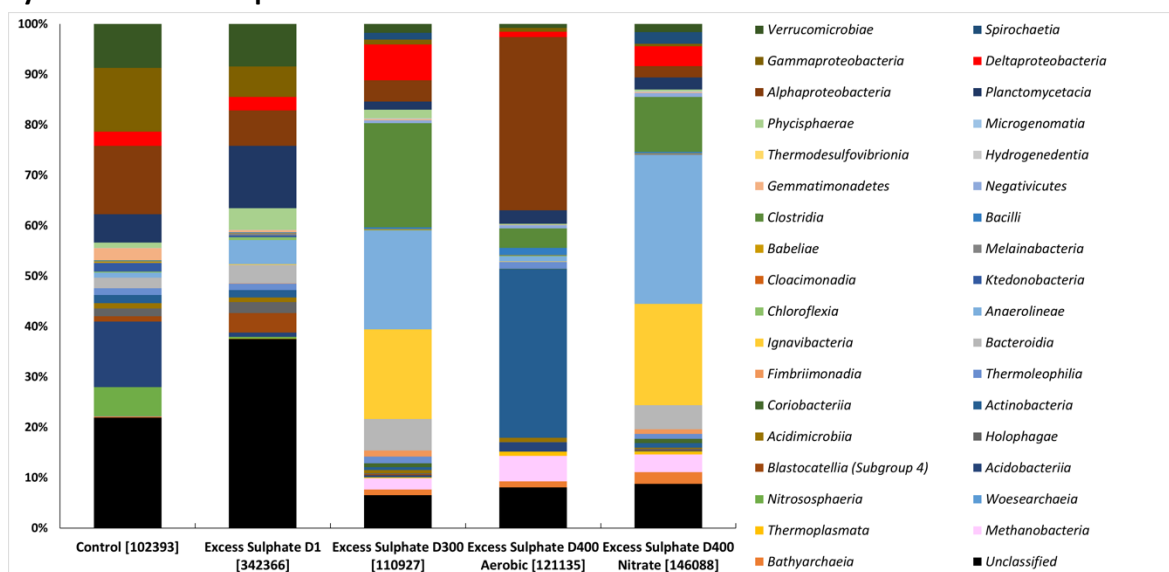


Figure 86: 16S rRNA microbial community by phylogenetic class in the control experiment (left), and the excess nitrate system [3] after: 1 day (second from the left), 300 days (middle), 400 days – aerobic remobilisation (second from the right) and 400 days – nitrate remobilisation (right). With OTUs in square brackets.

System 4: MRC

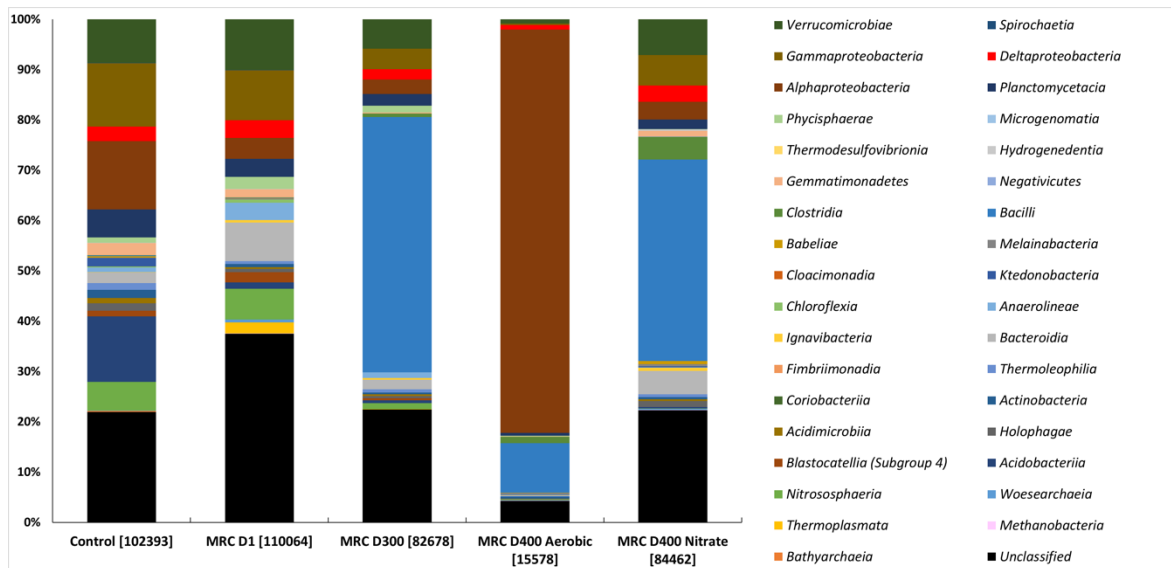


Figure 87: 16S rRNA microbial community by phylogenetic class in the control experiment (left), and the MRC system [4] after: 1 day (second from the left), 300 days (middle), 400 days – aerobic remobilisation (second from the right) and 400 days – nitrate remobilisation (right). With OTUs in square brackets.

System 5: Glycerol Phosphate

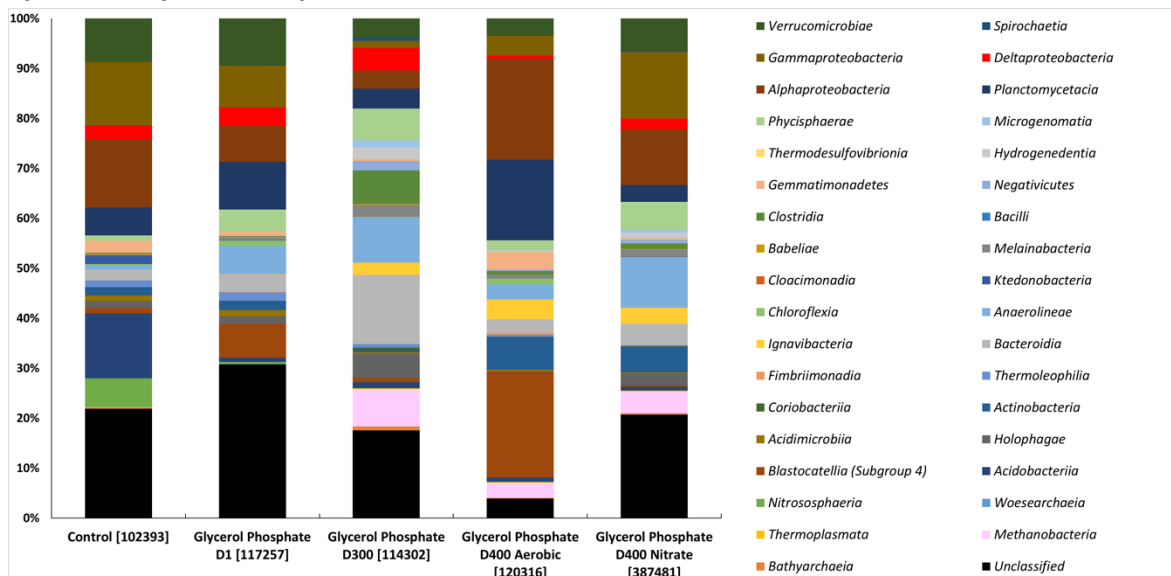


Figure 88: 16S rRNA microbial community by phylogenetic class in the control experiment (left), and the glycerol phosphate system [5] after: 1 day (second from the left), 300 days (middle), 400 days – aerobic remobilisation (second from the right) and 400 days – nitrate remobilisation (right). With OTUs in square brackets.

System 6: NanoFeR 25s

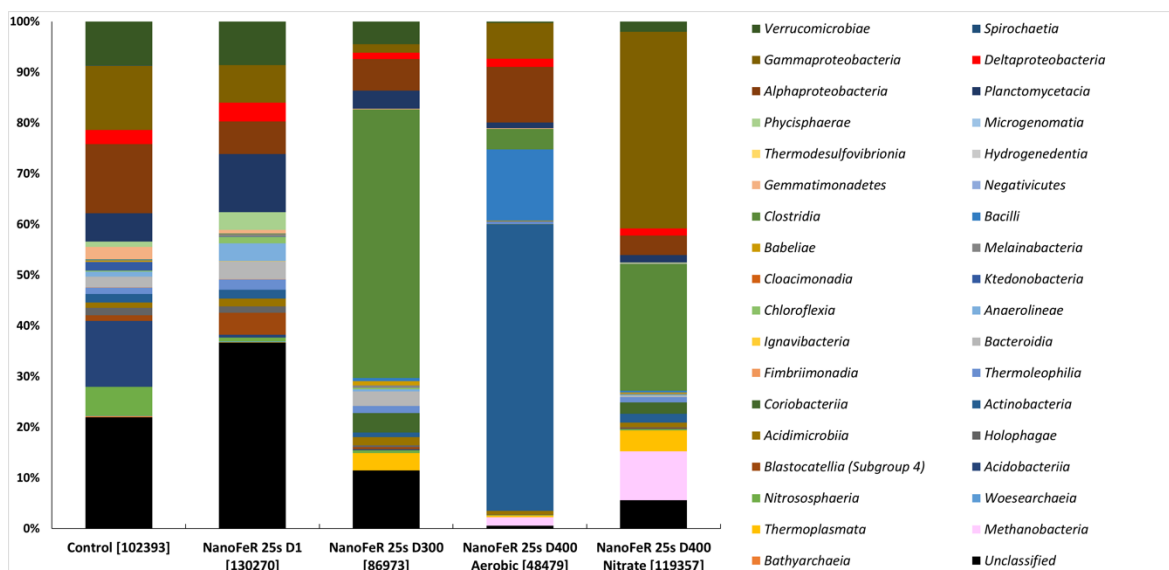


Figure 89: 16S rRNA microbial community by phylogenetic class in the control experiment (left), and the NanoFeR 25s system [6] after: 1 day (second from the left), 300 days (middle), 400 days – aerobic remobilisation (second from the right) and 400 days – nitrate remobilisation (right). With OTUs in square brackets.

System 7: Carbo-Iron

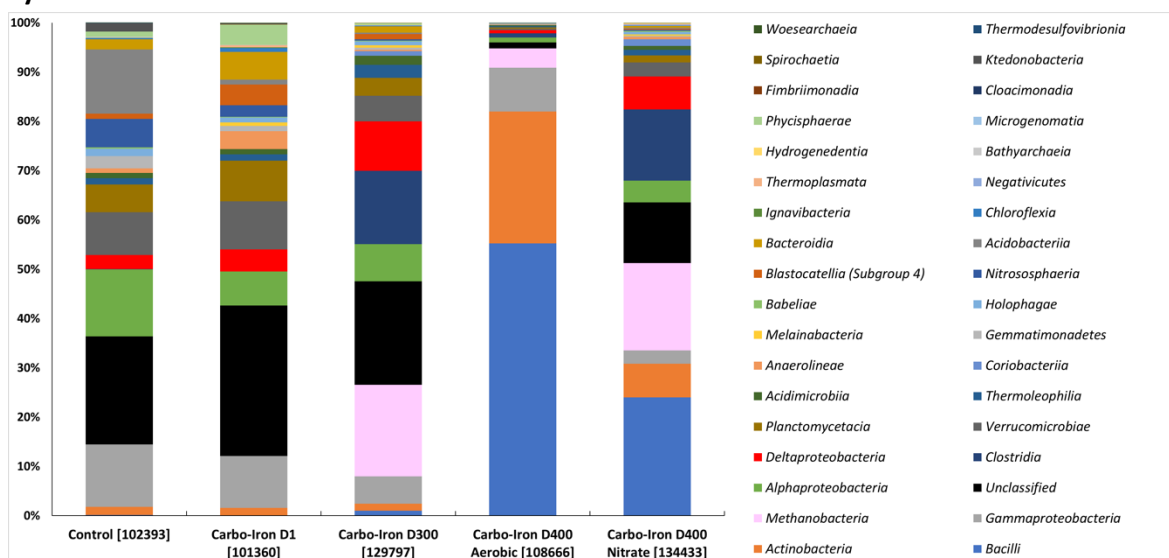


Figure 90: 16S rRNA microbial community by phylogenetic class in the control experiment (left), and the Carbo-Iron system [7] after: 1 day (second from the left), 300 days (middle), 400 days – aerobic remobilisation (second from the right) and 400 days – nitrate remobilisation (right). With OTUs in square brackets.

SI 7: Additional X-ray Absorption Spectroscopy Data and Analysis

During data acquisition beam damage was assessed by measuring several quick X-ray Absorption Near-Edge Structure (XANES) spectra, exposing the sample and analysing the spectral features (peak height, position and intensities) in order to assess any evidence for oxidation state drift. Throughout, we did not see any evidence for beam damage effects.

XANES

Before EXAFS fitting was carried out, linear combination fitting of the U L₃-edge XANES was used to inform the U(VI):U(IV) ratios. Linear combination fitting of all samples was performed using U(VI), as uranyl(VI) triscarbonate (Brookshaw et al., 2015), and U(IV), as uraninite (Neill et al., 2018), except

for the glycerol phosphate amended system which used U(VI) and U(IV) phosphate standards (Newsome et al., 2015c, 2015a). Whilst U(V) has been identified under environmentally relevant conditions (Duff et al., 2002; Grossmann et al., 2009; Jones et al., 2015; Pidchenko et al., 2017; Renshaw et al., 2005; Roberts et al., 2017; Sundararajan et al., 2008; Tsarev et al., 2017, 2016a; Vettese et al., 2020), U L₃-edge analyses are not sufficient to unambiguously identify U(V) (Bès et al., 2016; Kvashnina et al., 2013; Vettese et al., 2020), thus for this data set U has been assumed to be either U(VI), or U(IV). As Sr is non redox active LCF was not carried out and all Sr was assumed to be Sr²⁺.

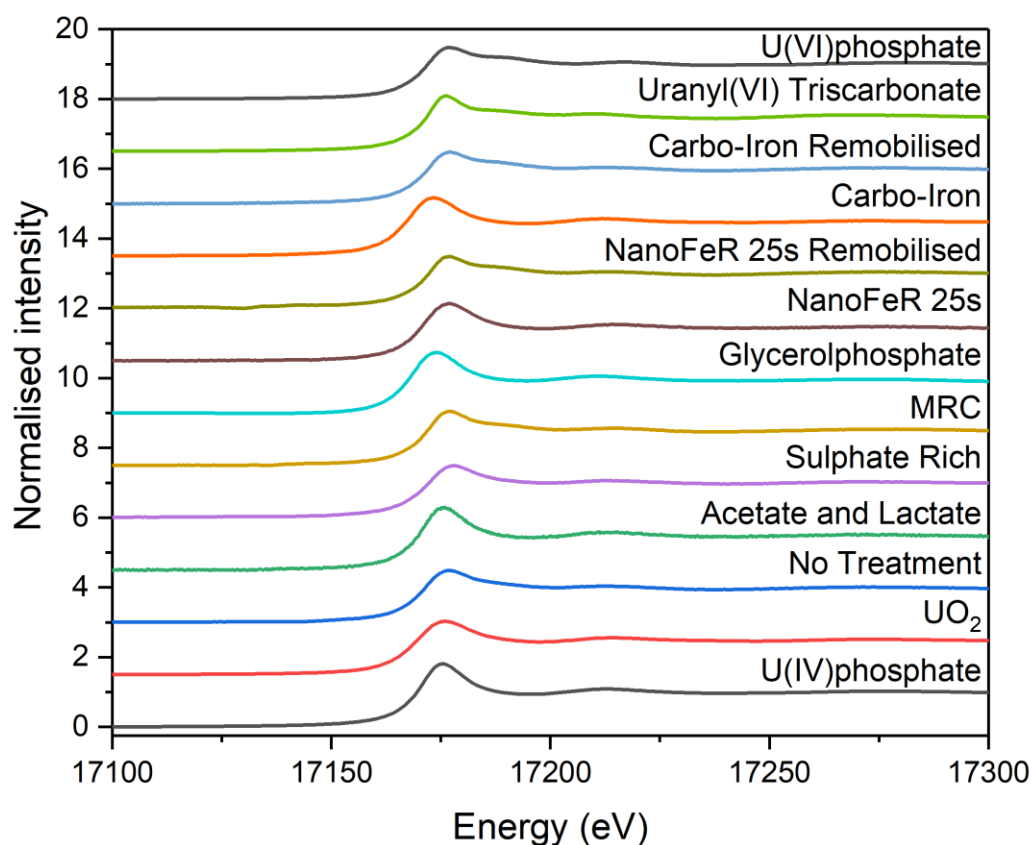


Figure 91: U L₃-edge XANES spectra collected at 77 K. Standards: Uranyl(VI) triscarbonate from (Brookshaw et al., 2015), U(VI) phosphate from (Newsome et al., 2015c) U(IV) phosphate from (Newsome et al., 2015a), synthetic U(IV)O₂ standard from (Neill et al., 2018).

EXAFS Fitting

The U L₃-edge EXAFS spectra were quantitatively fitted using the phase shift and backscattering functions obtained using the published reference structures of liebigite, Ca₂[UO₂(CO₃)₃] · ~11H₂O (Mereiter, 1982); ningyoite [CaU(PO₄)₂·2H₂O] (Muto, 1965); [U(SO₄)₂·4H₂O] (Kierkegaard et al., 1956); Magnetite (Fe₃O₄) (Wechsler et al., 1984); and uraninite, UO₂ (Wyckoff, 1963) were used. The Sr K-edge EXAFS spectra were quantitatively fitted using the phase shift and backscattering functions obtained using published reference structures of strontianite, SrCO₃ (De Villiers, 1971) and strontium hydroxide phosphate, Sr₅(PO₄)₃OH, which is isostructural with hydroxyapatite Ca₅(PO₄)₃OH (Sudarsanan and Young, 1972). Throughout analysis, coordination numbers (N) were fixed based on

the relative proportion of each U phase informed by crystallographic data; σ^2 (Debye-Waller factor s), R (interatomic distance in Å), and ΔE_0 (the difference between the threshold Fermi level of the theoretical phase shift and backscattering amplitude functions and the experimental data) values were allowed to refine. The amplitude reduction factor, S_0^2 , was fixed to between 0.9-1.1 as preliminary fits converged to these values. The number of degrees of freedom, defined as $N_{\text{idp}} \approx 2\Delta k\Delta r/\pi$ (Teo, 1986), was always greater than the number of parameters allowed to vary in the fitting process. All obtained fitting values were consistent with published crystal structures and are scientifically sound. Details of the fitting routine and an explanation of the statistics reported can be found in (Newville, 2001). Shells were only included in the fit if they made a statistically significant improvement to the model fit as determined by the F-test (Downward et al., 2007). The R-factor value was used in this study to evaluate the quality of fits. This method of EXAFS fitting is consistent with previously published literature e.g. (Catalano and Brown, 2004; Marshall et al., 2014; Neill et al., 2019, 2018; Roberts et al., 2017). In the case of the U EXAFS fits, after analysis of the XANES, a U=O_{ax} shell at approximately 1.8 Å was used as a proxy to estimate the presence of U(VI); similarly, in reduced phases a U-U shell at approximately 3.9 Å was used as a proxy to estimate the likely presence of amorphous UO₂. Other backscatterers (C, P, S or Fe) were included if they contributed statistically to the fits (Downward et al., 2007). 9-coordinate outer-sphere sorbed Sr to oxygen ligands was used a reasonable base for Sr EXAFS and similarly, further shells were only added if they contributed statistically to the fits (Downward et al., 2007).

Table 12: Fitting Parameters obtained from Uranium L₃-Edge and Sr-K-edge EXAFS Spectroscopy ^a.

U EXAFS Fits							
	Scattering path	N	R (Å)	σ^2 (Å ²)	E ₀ (eV)	R-factor	Confidence of adding shell (%) ^a
No Treatment [1]	U=O _{ax}	1.4	1.78(2)	0.003(0)	5.85	0.009	90.2
	U(IV)-O	2.4	2.29(1)	0.004(0)			
	U(VI)-O _{eq}	4.2	2.43(6)	0.005(5)			
	U-C	2.1	2.93(5)	0.008(1)			
	U-Fe	1	3.41(8)	0.012(1)			
	U-U	2.4	3.91(1)	0.012(7)			
Electron Donor [2]	U-O	8	2.40(1)	0.013(1)	6.28	0.011	98.9 99.3
	U-P _{Bid}	1	3.13(2)	0.003(2)			
	U-P _{mono}	2	3.68(3)	0.005(3)			
	U-U	3	3.99(4)	0.012(4)			
Sulphate Rich [3]	U=O _{ax}	0.8	1.82(1)	0.005(2)	6.93	0.011	98.8
	U(IV)-O	4.8	2.37(4)	0.016(8)			
	U(VI)-O _{eq}	2.4	2.42(4)	0.006(2)			
	U-P	1	3.15(3)	0.008(4)			
	U-U	1	3.99(4)	0.007(5)			
MRC [4]	U=O _{ax}	2	1.79(1)	0.002(1)	6.96	0.018	96.5
	U-O _{eq}	6	2.39(3)	0.013(4)			
	U-S	1	3.16(4)	0.004(2)			
Glycerol phosphate [5]	U-O	4	2.28(2)	0.003(0)	4.07	0.020	
	U-O	4	2.44(2)	0.003(0)			
	U-P _{bidentate}	2	3.13(2)	0.004(2)			
	U-	4	3.67(3)	0.006(3)			
	P _{monodentate}						

Carbo-Iron [6]	U-O	4	2.29(2)	0.006(2)	3.85	0.008	99.8 ^b 98.0 ^c
	U-O	3	2.46(1)	0.006(1)			
	U-C	2	2.87(5)	0.006(3)			
	U-Fe	1	3.44(3)	0.016(1)			
	U-U	5	3.85(2)	0.011(7)			
Carbo-Iron Aerobically Remobilised [6]	U=O _{ax}	2	1.83(1)	0.006(1)	5.70	0.022	98.2
	U(VI)-O _{eq}	3	2.27(1)	0.003(2)			
	U(VI)-O _{eq}	3	2.45(1)	0.001(1)			
	U-Fe	1	3.45(3)	0.009(3)			
NanoFeR 25s [7]	U=O _{ax}	0.4	1.73(3)	0.004(3)	5.29	0.010	
	U-O	6.4	2.37(2)	0.013(1)			
NanoFeR 25s Aerobically Remobilised [7]	U=O _{ax}	2	1.80(2)	0.003(1)	5.72	0.020	95.7 ^b
	U-O _{eq}	2	2.20(3)	0.003(2)*			
	U-O _{eq}	4	2.40(3)	0.003(2)*			
	U-C	1.6	2.92(5)	0.002(1)			
	U-Fe	1	3.46(4)	0.002(1)			
Sr EXAFS Fits							
	Scattering path	N	R (Å)	σ^2 (Å ²)	E ₀	R-factor	Confidence of adding shell (α) ^a
No Treatment [1]	Sr-O	9	2.60(1)	0.009(1)	-0.03	0.016	
Electron Donor [2]	Sr-O	9	2.61(1)	0.009(1)	-0.37	0.009	
Excess Sulphate [3]	Sr-O	9	2.60(1)	0.009(0)	-0.67	0.009	
Glycerol phosphate [4]	Sr-O	9	2.61(1)	0.011(6)	-0.17	0.008	96.3
	Sr-P	1.3	3.30(3)	0.013(4)			
MRC [5]	Sr-O	9	2.59(2)	0.012(2)	-8.61	0.022	99.8
	Sr-Fe	3	3.52(3)	0.014(3)			
NanoFeR 25s [6]	Sr-O	9	2.60(1)	0.0010(1)	-0.03	0.015	
Carbo-Iron [7]	Sr-O	9	2.58(1)	0.010(0)	-2.42	0.013	96.2 96.2
	Sr-C	4	3.20(3)	0.004(3)			
	Sr-Fe	1	3.42(4)	0.020(4)			
<p>Uncertainty in interatomic distances is quoted in brackets for the last decimal place (Å), points without a value have error less than 0.005 Å. Uncertainty in Debye-Waller factors is quoted in brackets for the last decimal place, points without a value have error less than 0.0005. ^a F-test results; $\alpha > 0.95$ statistically improves the fit with 2 σ confidence. ^b F-test results, shell added first. ^c F-test results, shell added second. Values marked with an * were tied together. S_0^2 was fixed to 1 for all samples, except for the U fits amended with MRC where S_0^2 was fixed to 0.9.</p>							

System 1: Natural Attenuation

U in the end-point of the natural attenuation [1] sample was characterised as a mixed phase species. The presence of both U(VI) and U(IV) is observable in the XANES (Figure 91) and is confirmed by the simultaneous presence of both U=O_{ax} and U-U backscatterers in the Fourier-transform (Figure 57). In the U-U shell, we assumed a N of 8 for biogenic UO₂, hence the resulting value of 2.4 suggests approximately 30 % biogenic UO₂ in the sample. The fit was further optimised by including a U-Fe shell at 3.4 Å (N = 1, F-test 90.2) which is consistent with relevant literature (Bower et al., 2019) and is statistically valid.

System 2: Electron Donor

XANES analysis of the electron donor system [2] showed that the U was completely reduced to U(IV) (Figure 91), as seen previously in the literature (Newsome et al., 2015b, 2014b). The structure was, therefore, initially attempted as biogenic UO_2 . Again the resulting coordination number of 3 for the U-U shell suggests an approximately 40 % UO_2 contribution to the system. Given the relevant literature (Alessi et al., 2014; Bargar et al., 2013; Bernier-Latmani et al., 2010; Boyanov et al., 2011), 2 U-P shells \AA were added to understand the speciation of the remaining U. These were added to the fit, at $\sim 3.1 \text{ \AA}$ and ~ 3.7 representing bi- and monodentate P shells, respectively. The addition of each shell statistically improved the fit (F-Test: U-P_{bid} 98.9, U-P_{mono} 99.3) and the data is consistent with the relevant literature (Alessi et al., 2014; Bargar et al., 2013; Bernier-Latmani et al., 2010; Boyanov et al., 2011).

System 3: Excess Sulphate

In the sulphate system [3], the shape of the XANES (Figure 91), as well as the simultaneous presence of a characteristic U=O_{ax} at 1.8 \AA and a U-U shell at 4.0 \AA , suggested that the U was present as a mixed valence species. Here, the ratio of U(VI) to U(IV) was determined by comparing ratios of U-O shells for U(VI) and U(IV). The best results were obtained using a 40:60 U(VI):(IV) ratio based on 0.8 O scatterers at 1.80 \AA , 2.4 U(VI)- O_{eq} scatterers at 2.43 \AA and 4.8 single O scatterers at 2.34 \AA . Following this, a U-U backscattering shell was added at approximately 4.0 \AA with a low N of 1, suggesting a small contribution of biogenic UO_2 . Finally a U-P the addition of a U-P shell at approximately 3.1 \AA (F-test 98.8) resolved the peak at $R+\Delta = 3 \text{ \AA}$.

System 4: MRC

Inspection of the XANES for the MRC system demonstrate that the U is present as U(VI) (Figure 91). The first two shells of MRC can be fit with a U=O_{ax} dioxygenyl bond at 1.8 \AA (N = 2) and 6 equatorial U- O_{eq} backscatterers at 2.4 \AA . The shell at 2.8 \AA in the Fourier transform was then attempted using either a S or a P shell, both fits are included below (Figure 92). As addition of an S shell yielded a much better fit, determined by a lower R-factor, the P shell was discarded.

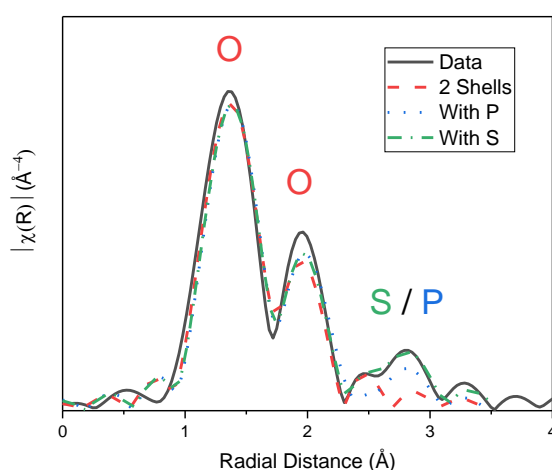


Figure 92: EXAFS fits for bioreduced MRC. Comparing EXAFS data (grey) with fits using just two O shells (red), two O shells + P (blue), and two O shells + S (green). The fit using an S shell is included in Table 12.

The Sr EXAFS of the bioreduced MRC system contains 3 shells (Figure 3). The first shell was fit as Sr-O, and after trying C, Si, P the fit was significantly improved by adding a Fe shell at 3.52 \AA (N = 3) (F-test

99.8 %). Here, the Sr-Fe distances were comparable to Sr sorbed to goethite at high pH (Fuller et al., 2016). The Fourier transform also contains a third shell although this could not be fit using sensible fitting parameters (Fe, K, Sr).

System 5: Glycerol Phosphate

The U XANES for the glycerol phosphate amended system [5] suggested that all U was present as U(IV) (Figure 91); later, the lack of a $U=O_{ax}$ in the Fourier transform (Figure 91) confirmed that U was present as U(IV). Given the lack of a U-U shell, indicative of biogenic UO_2 , and the relevant literature (Newsome et al., 2015a, 2015c) the EXAFS were fit using a ningyoite-like structure as seen previously in similar experiments (Alessi et al., 2014; Dusausoy et al., 1996; Newsome et al., 2015a, 2015c). Ningyoite is a U(IV)-phosphate mineral which lacks an edge-sharing U-U feature typically found in uraninite (UO_2) or coffinite ($U(SiO_4)_9(OH)_4$). As this was not present in the data it further supports the 'ningyoite-like' fit presented (Fletcher et al., 2010; Morin et al., 2016) and this fit has very similar to parameters in the ningyoite crystal structure with only minor variations ($0.06 \pm 0.03 \text{ \AA}$) compared to the published crystal structure. Despite the presence of Ca in the crystal structure of ningyoite (Dusausoy et al., 1996), the expected U-Ca shell at 3.85 Å could not be successfully fit as previously observed in other U-phosphates (Bernier-Latmani et al., 2010; Newsome et al., 2015c).

The Sr K-edge EXAFS fit for the glycerol phosphate system was fit using two shells. The second Sr-P shell was necessary to achieve suitable results, determined by an R-factor close to or below 0.02. The additional P shell contributed statistically to the fit (F-test 96.3) and was consistent with the relevant literature.

System 6: NanoFeR 25s

Analysis of the XANES for the NanoFeR 25s system shows that U is present in a mixed phase system (Figure 91), here linear combination fitting identified a 20 % U(VI) contribution amongst the U(VI). Thus, this ratio was applied to the fitting of the first two shells of the Fourier transform (Figure 3).

NanoFeR 25s Remobilised Sample

Analysis of the XANES for the remobilised NanoFeR 25s sample demonstrates that all U is present as U(VI) (Figure 91). This was confirmed when fitting the first two shells of the EXAFS spectra using 2 $U=O_{ax}$ dioxygenyl and 6 $U-O_{eq}$ equatorial shells at 1.8 Å and 2.2-2.4 Å respectively, confirming a uranyl-like coordination environment (Figure 3, Table 12). Here the best fit was obtained using a split shell for the equatorial oxygens with 2 shorter O at 2.2 Å and 4 longer ones at 2.4 Å. As the EXAFS spectra was not fully resolved at this point we considered additional backscatterers, first a U-C shell was added as 2.9 Å, second a U-Fe shell was added at 3.4 Å with N 1.6, again this shell contributed statistically to the fit (F-test 95.7 %). Debye-Waller factor and bond lengths for the C and Fe shells are consistent with U(VI) bound to Fe(III) (Winstanley et al., 2019). The resulting fit highly resembles other structures indicative of inner-sphere binding of ternary uranyl(VI) carbonate complexes to Fe(III) edge sites (Bargar et al., 2000; Catalano and Brown, 2005; Waite et al., 1994; Winstanley et al., 2019).

System 7: Carbo-Iron

The U XANES for the Carbo-Iron system showed that all U was present as U(IV) (Figure 91), this was further clarified by the presence of a U-U shell and the lack of a $U=O_{ax}$ shell in the Fourier transform (Figure 57). The first U-O shell was best fitted as an under-saturated, split U-O shell, as previously seen in U(IV) reduced by nanoscale ZVI after a year's incubation (Tsarev et al., 2016a). The U-U peak at $R+\Delta = 3.6 \text{ \AA}$ was best fitted with N = 5; considering that nano-uraninite is commonly fit with 8-10 U-U

backscatterers, this suggests that the 50-60 % nano- UO_2 present in the system. As the EXAFS were not fully resolved with this fit, additional backscatterers were considered. Given the likely presence of C in Carbo-Iron (24 wt % C), we added a C shell, this statistically improved the feature at $R+\Delta = 2.2 \text{ \AA}$ (F-Test 99.8) and suggested that U(IV) was bound to C. Finally in order to resolve the peak at $R+\Delta = 2.8\text{-}3.2 \text{ \AA}$, an additional U-Fe shell was considered; applying a range of reasonable constraints for the Debye-Waller factor yielded a coordination number between 1 Fe atom bound to U(IV) atom (F-test 98.0). U-C bond lengths are consistent with U(IV) carbonates (Bhattacharyya et al., 2017; Boyanov et al., 2011; Catalano and Brown, 2004; Hennig et al., 2010; Tsarev et al., 2016a) and U-Fe distances are consistent with U(IV)-Fe bond distances (Bargar et al., 2000; Boyanov et al., 2007; Tsarev et al., 2016a). Interestingly, when Tc(VII) was treated using Carbo-Iron the resulting Tc(IV) speciation was also interacting with Fe (Newsome et al., 2019). The U EXAFS spectrum could be the result of two possible scenarios: if all the U(IV) is in a single phase it can be described as a Fe and C coated uraninite particles, in which an interface between UO_2 with U-Fe and U-C has produced the observed EXAFS spectra. Alternatively, the U(IV) may be partitioned into two or three phases, a UO_2 phase (50-60%) and monomeric U(IV) adsorbed to Fe and C phases. Given that Carbo-Iron retained 99 % of the incubated U phases after 100 days of re-oxidation to form U(VI) bound to Fe (Figure 3, Table 12), the former scenario is more likely.

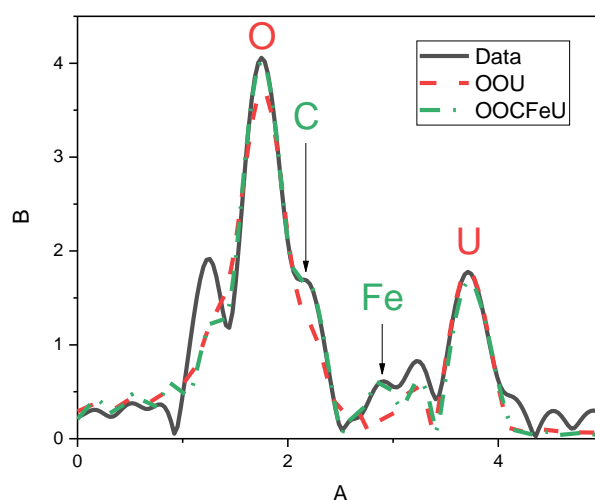


Figure 93: The Fourier transform of the U L_3 -edge EXAFS showing the shell by shell fitting method of the Carbo-iron nanoparticles following reaction with U.

Carbo-Iron Remobilised Sample

Comparison of the XANES and the Fourier transform of the incubated and the re-oxidised Carbo-Iron EXAFS samples clearly demonstrates that upon aeration the U(IV) present in the Carbo-Iron sample completely re-oxidised to U(VI) (Figure 3, Figure 91, Table 12). Interestingly, there is also a considerable increase in the height of the shell at $R+\Delta = 2.8\text{-}3.2 \text{ \AA}$ suggesting an increase in U-Fe interactions re-oxidised Carbo-Iron EXAFS sample. Here, the first shell was fitted as $\text{U}=\text{O}_{\text{ax}}$ ($N = 2$), followed by a split equatorial shell containing two $\text{U}-\text{O}_{\text{eq}}$ bond distances at 2.3 and 2.4 \AA . Next, a C shell was attempted, although excessively large Debye-Waller factor and bond lengths suggested that U-C interactions were no longer present. Here, A U-Fe shell at 3.4 \AA , contributed statistically to the fit (F-test 98.2 %) and was consistent with U bound Fe via mononuclear bidentate inner sphere U(VI)

complexation (Bargar et al., 2000; Catalano and Brown, 2005; Waite et al., 1994; Winstanley et al., 2019). This data collectively suggests that upon aeration the previously reduced U phases which were bound to C and Fe, re-oxidise to form U(VI) species which only bind to Fe.

SI 8: Powder X-Ray Diffraction

PXRD analysis found little difference in the bulk sediment before and after incubation and after remobilisation studies. In all end points and in the starting sediment, U and Sr concentrations were too low to be detected on XRD but U and Sr sorption to these minerals has been documented (Brookshaw et al., 2016, 2015; Carroll et al., 2008; Fuller et al., 2016; Ilton et al., 2004; Karasyova et al., 1999; Kodama et al., 2001; Meleshyn, 2010; Moyes et al., 2000; Nair et al., 2014).

SI 8: Control Precipitation Experiment

A further control system was set up as a 100 mL sediment microcosm. This assessed U and Sr precipitation in the artificial groundwater, this reaction contained 80 ppm Sr and 44 ppm U in AGW. Over the course of the 300 day experiment the pH remained constant, the Eh dropped to 100 mV and no U or Sr precipitated (Figure 94), thus implying that any removal from solution was due to interactions with the sediments and any microorganisms contained within it.

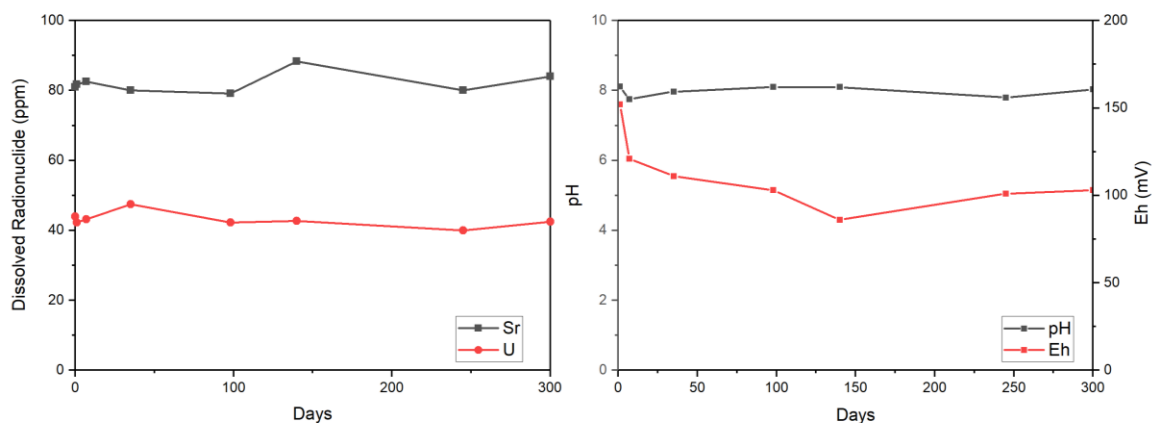


Figure 94: Selected geochemical data in the aqueous precipitation experiments. Left) Aqueous U (red) and Sr (grey) concentrations; and right) pH (grey) and Eh (red).

Chapter 6: Quantifying the Stability of Remediation End-Points for Uranium and Strontium Contaminated Land: Potential Impact of Ground- and Seawater Ingress

Paper in preparation for Chemical Geology.

Quantifying the Stability of Remediation End-Points for Uranium and Strontium Contaminated Land: Potential Impact of Ground- and Seawater Ingress

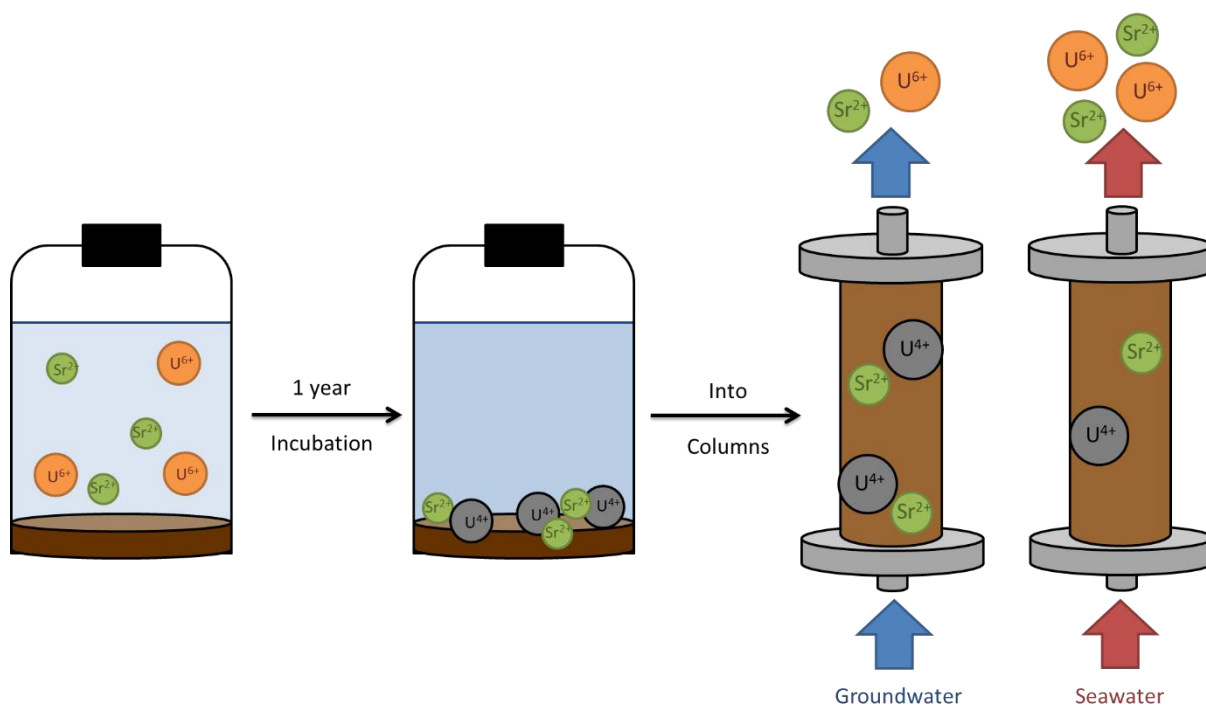
Gianni F. Vettese¹, Katherine Morris¹, Thomas Bishop², Samuel Shaw¹, and Jonathan R. Lloyd*¹.

¹Williamson Research Centre for Molecular Environmental Science and Research Centre for Radwaste Disposal, School of Earth and Environmental Science, The University of Manchester, Manchester, England

²Department of Geography, School of Environment, Education and Development, The University of Manchester, Manchester, England

6.1 Abstract

Following on from a detailed study on the long-term stability of a range of remediation strategies co-treating U and Sr (Vettese *et al.*, 2020, Thesis Chapter 5), 8 parallel flow-through sediment columns examined the remobilisation of previously treated sediments containing U and Sr via the ingress of aerobic ground- and seawater. Duplicate columns were packed with 300 day old contaminated sediments amended with electron donor (acetate and lactate), glycerol phosphate, or 1 of 2 nanoscale Zero Valent Iron (ZVI) treatments: Carbo-Iron or NanoFeR 25s. Once packed, the columns were subjected to a continual flow of aerobic simulated ground- or seawater as the influent. Monitoring of the effluent indicated that the majority of treated U remained in the solid phase following groundwater ingress when treated previously with glycerol phosphate or nanoscale ZVI. Similarly, these systems retained up to twice as much Sr compared to the electron donor experiment following groundwater ingress. Compared to the groundwater experiments, seawater ingress led to a significant increase in U and Sr mobility in all systems. Here, the seawater columns remobilised up to 20 times more U and 4 times more Sr than groundwater. Additionally, glycerol phosphate retained 4 times more U and NanoFeR 25s retained almost 6 times more Sr, compared to the electron donor amended systems following seawater ingress. After 120 days the remaining sediments in the columns were analysed using XRF mapping, acid digestions, EXAFS spectroscopy, SEM-EDX and 16S rRNA gene sequence analysis. XRF mapping displayed elemental distributions along each column in 0.2 mm steps. Unfortunately due to COVID-19 the samples for acid digestions, EXAFS spectroscopy, SEM-EDX and 16S rRNA analysis were not run, although the samples are prepared and stored. Nevertheless, our results confirm that the end-points using targeted injections such as glycerol phosphate, Carbo-Iron or NanoFeR 25s are more stable and resistant to remobilisation compared to electron donor amendments. These data also demonstrate that if groundwater ionic strength increases, by the rise in sea levels or by design, that significant U and Sr remobilisation should be expected.



6.2 Introduction

U and Sr are common contaminant radionuclides in soils, sediments and groundwaters at nuclear sites across the globe including: Sellafield (U.K.), Mayak (Russia) and the Hanford and Rifle sites (U.S.A.) (Mckinley et al., 2001; NDA, 2019b; Stamper et al., 2014; Standing et al., 2002; Watson et al., 2004; Zachara et al., 2007). Targeted remediation is required in these locations, where aqueous U and Sr concentrations are above the limits prescribed by the Environmental Protection Agency.

U mobility under environmentally relevant conditions is generally governed by its oxidation state, where more soluble U(VI) dominates under oxidising conditions and relatively insoluble U(IV) dominates under reducing conditions. The enzymatic reduction of U(VI) therefore has the potential to control the fate of U in contaminated sediments (Anderson et al., 2003; Lovley et al., 1991; Yabusaki et al., 2007). Accordingly, the microbially mediated reduction of U(VI) to U(IV) has been suggested as a means of treating contaminated sediments and has been tested thoroughly in both laboratory and field-scale studies (Anderson et al., 2003; Lovley et al., 1991; Williams et al., 2013, 2011; Yabusaki et al., 2007). Whilst multiple pathways for microbial U(VI) reduction have been identified, the most common method of “biostimulation” for this process in contaminated land studies is via the activation of Fe(III)-reducing bacteria following the addition of organic carbon (Anderson et al., 2003; Lovley et al., 1991; Newsome et al., 2014a; Wildung et al., 2000; Williams et al., 2013, 2011; Yabusaki et al., 2007). Bioreduced U(IV) is, however, known to re-oxidise and remobilise upon contact with various oxidants such as; dissolved oxygen (Abdelouas et al., 1999; Bi et al., 2013; Komlos et al., 2008b; Law et al., 2011; Moon et al., 2007; Newsome et al., 2015b; Senko et al., 2002) (Vettese *et al.*, 2020, Thesis Chapter 5), nitrate and its relevant denitrification intermediates (nitrite, nitric oxide and nitrous oxide) (Beller, 2005; Finneran et al., 2002; Istok et al., 2016, 2004; Law et al., 2011; Moon et al., 2009; Newsome et al., 2015b; Senko et al., 2002) (Vettese *et al.*, 2020, Thesis Chapter 5), oxidised Fe- and Mn-oxides (Ginder-Vogel et al., 2010, 2006; Liu et al., 2002; Nevin and Lovley, 2000; Sani et al., 2005, 2004; Spycher et al., 2011; Wang et al., 2014; Zachara et al., 2002) and humics (Newsome et al., 2015a). To the best of our knowledge there is no literature that directly discusses the effect of ionic

strength on U(IV) re-oxidation and remobilisation. Consequently, the long-term stability of a variety of U end-points must therefore be considered. These should involve a range of strategies for U immobilisation whilst also regarding methods of mitigating its oxidative remobilisation over extended timescales.

Sr mobility in contaminated soils and sediments, present as non-redox active Sr^{2+} , is dictated by sorption to charged surfaces; principally Fe-oxides and clays (Balek et al., 1996; Carroll et al., 2008; Dyer et al., 2000; Karasyova et al., 1999). Unlike U, the transport of Sr is largely unaffected by simple electron donor additions (Brookshaw et al., 2016; Cleary et al., 2019; Thorpe et al., 2012b)(Vettese et al., 2020, Thesis Chapter 5). Instead, the rate and extent of Sr sorption is dependent on the groundwater geochemistry and sediment mineralogy where it often forms weakly bound, outer-sphere complexes in competition with other cations (Axe et al., 1998; Dyer et al., 2000, 1999; Dyer and Umar, 1999; Fuller et al., 2016; O 'day et al., 2000; Thorpe et al., 2014, 2012b; Wallace et al., 2012). Evidence suggests that, if environmental conditions remain unchanged, these weakly bound surface complexes also remain largely unaffected over extended timescales (Wallace et al., 2012). Although, as ionic strength increases so do cation exchange processes, which, in turn lower Sr uptake and sorption. A study carried out by Wallace *et al.* found that 80 % of Sr, present as mostly surface bound Sr, was exchangeable with 1 M MgCl_2 . This suggests, that if groundwater ionic strength increases (e.g. by seawater ingress caused by a rise in sea level rise or by any other means) then substantial Sr remobilisation is expected. More recalcitrant Sr phases can be formed at high pH (> 12.5), where Sr binds to mineral surfaces via inner-sphere complexation (Fuller et al., 2016; Wallace et al., 2013). Alternatively, Sr can incorporate into solid phase Ca-carbonate or Ca-phosphate minerals, which remain stable over extended timescales (Cleary et al., 2019; Fujita et al., 2004; Handley-Sidhu et al., 2011; Macaskie and Dean, 1985b).

Although there are many different methods proposed to promote the immobilisation of radioactive contaminants, direct comparisons between multiple treatments are still uncommon (Newsome et al., 2019, 2017, 2015c) and there are even fewer studies that consider more than one radionuclide (Cleary et al., 2019)(Vettese *et al.*, 2020, Thesis Chapter 5). In a previous study, batch experiments assessed the co-precipitation of U and Sr following 7 biostimulation or chemical treatments. This work showed that sediments amended with glycerol phosphate or nanoscale ZVI not only removed the most U and Sr from solution during treatment, but they also formed the most recalcitrant phases following re-oxidation by oxygen or nitrate ingress (Vettese *et al.*, 2020, Thesis Chapter 5). Accordingly, we have taken these 3, best performing systems and used flow-through column studies to evaluate the long-term stabilities of immobilised U and Sr following re-oxidation regimes facilitated by ground- or seawater ingress. Given the rise of global sea levels as a result of climate change, and the potential for coastal erosion near UK nuclear sites, we chose to study the effects of the ingress of highly saline seawater as well as groundwater. Here, we expected that the ingress of aerobic seawater would displace weakly bound surface complexes for both U and Sr to a greater extent than in groundwater (Catalano and Brown, 2005; Wallace et al., 2012), even after biostimulation or chemical treatment.

In the experiment described in this chapter, we simultaneously ran aerobic simulated ground- or seawater through 8 treated columns and we monitored the effluent geochemistry. Upon completion of the experiments we studied the elemental composition along each column using ICP-MS and XRF. We also examined the change in U and Sr speciation using X-ray Absorption Spectroscopy (XAS) and Scanning Electron Microscopy - Energy Dispersive X-ray spectroscopy (SEM-EDX) and the change in

the microbial community using 16S rRNA gene sequencing. We selected 2 nanoscale Zero Valent Iron (ZVI) based chemical treatments (Carbo-Iron and NanoFeR 25s), a combined bioreduction and phosphate mineralisation approach (glycerol phosphate) and a standard electron donor, bioreduction method (acetate and lactate) as our 4 experimental systems. We chose to use column studies in this experiment rather than batch microcosm experiments as they are open systems and therefore are subject to water flow and they have a more environmentally relevant solid:solution ratio; and they also better account for heterogeneity in the subsurface (Gu et al., 2005; Komlos et al., 2008b; Thorpe et al., 2017, 2016).

6.3 Materials and Methods

6.3.1 Sediment Characterisation and Batch Treatment Phase

The sediment used for all experiments was acquired from the Calder Valley, Cumbria, UK. The sampling location was upstream from the Sellafield site and thus representative of its sediments and it has previously been characterised (Vettese *et al.*, 2020, Thesis Chapter 5)(Law et al., 2010a). The incubation phase was carried out in batch sediment microcosms and its related biogeochemical dynamics have been described and analysed elsewhere in detail (Vettese *et al.*, 2020, Thesis Chapter 5).

6.3.2 Column Design and Operation

Following a 300 day treatment period 2 parallel sets of 4 columns were packed with the following systems: electron donor, glycerol phosphate, Carbo-Iron and NanoFer 25s. The resulting 8 acrylic columns (11.6 cm long by 2.8 cm inner-diameter), were packed with 3 cm (approximately 40 g) of treated (300 days) sediment on top of a 6 cm bed of acid washed quartz sand (mesh size 50-70). A plug of glass wool (1 cm) was used as a cap on the top and bottom of the columns to optimise fluid flow in the columns and prevent blockages in the effluent (Figure S1). The artificial ground- or seawater was pumped upward through the columns with a flow rate similar to average groundwater flow (1.2 mL hr⁻¹) using a Watson-Marlow 205S peristaltic pump (Thorpe et al., 2017). Flow was established into the columns using filtered (<22 µm) synthetic regional ground- or seawater. The artificial groundwater was composed of (g per litre of de-ionised water): KCl (0.0066), MgSO₄·7H₂O (0.0976), MgCl₂·6H₂O (0.081), CaCO₃ (0.1672), NaNO₃ (0.0275), NaCl (0.0094) and NaHCO₃ (0.2424), and the ionic strength was 0.017 M (Wilkins et al., 2007). The artificial seawater was composed of (g per litre of de-ionised water): NaCl (23.9968), KCl (0.8772), MgCl₂·6H₂O (11.4427), CaCl₂·2H₂O (1.570), Na₂SO₄ (4.3635) and NaHCO₃ (0.1707) and the ionic strength was (0.67 M) (Todd and Yuan, 1992). The columns and sterile water reservoirs were maintained at room temperature in the dark using cardboard boxes covered in Al foil to prevent the growth of photosynthetic microorganisms. Throughout the experiment the influent pH was maintained between pH 6.8-7.2. The pore volume of the column was determined by use of Br⁻ as a tracer which was used to define the breakthrough curve (Figure S102).

The column influents and effluents were monitored at regular intervals. In the effluent, pH, Eh and the concentrations of U, Sr and Fe were monitored by Inductively Coupled Plasma-Mass Spectrometry (ICP-MS). Surplus supernatant samples were frozen immediately at -80 °C and stored for Ion Chromatography (IC). Here the changes in aqueous, nitrate, sulphate and chloride were tracked using IC. Bioavailable Fe(II) was measured spectrophotometrically to assess terminal electron accepting

processes (Stookey, 1970; Viollier et al., 2000). Eh and pH were measured immediately using calibrated electrodes.

6.33 Column Sacrifice

At the experimental end-point (120 days), the columns were uncapped and sliced vertically in half in a Coy glovebox under an anaerobic atmosphere. 1 half was then dissected into 3 fractions labelled as inflow, middle and outflow. At each third, we analysed; the total U and Sr, bioavailable Fe(II) and the microbial community using ICP-MS, the Ferrozine method and 16S rRNA gene sequencing respectively. For the ICP-MS analysis, approximately 0.5 g of dry sediment (dried in a 40 °C oven for 24 hrs) was digested in boiling aqua regia for 4 hrs before dilution into 2 % nitric acid. The portion of bioavailable Fe(II) in the sediments was performed on 0.5 g wet sediment dissolved in 0.5 N HCl (Stookey, 1970; Viollier et al., 2000). Samples for 16S rRNA gene sequencing, SEM-EDX and XAS analysis were prepared at each third of each column and were stored anaerobically at -80 °C until analysis. The remaining half of the column used for 1-dimensional X-Ray Fluorescence (XRF) mapping with a 200 micron resolution along the vertical axes of the columns (S3.5: XRF scanning using the Itrax Core Scanner). Further details for the aqua regia digests, microbial community analyses, XAS and XRF are provided in the Supporting Information (S3.2: Aqua Regia Digests, S3.4: X-ray Absorption Spectroscopy, S3.5: XRF scanning using the Itrax Core Scanner).

6.4 Results and Discussion

6.41 U(VI) and Sr Batch Incubation Experiments

In a previous study U and Sr were removed from solution in 4 sets of anaerobic batch treatments amended with electron donor (acetate and lactate), glycerol phosphate, Carbo-Iron and NanoFeR 25s; here aqueous U concentrations decreased by 93-97 % and Sr concentrations decreased by 66-95 % within 300 days (Figure 95) (Vettese *et al.*, 2020, Thesis Chapter 5). Changes in the biogeochemistry and the microbial community were also studied in detail in this initial 300 day experiment, and the treatment end-points for each of these systems were also characterised using U L₃- and Sr K-edge Extended X-ray Absorption Fine Structure (EXAFS) (Vettese *et al.*, 2020, Thesis Chapter 5). Moreover, the solid phase U and Sr after aerobic treatment in batch microcosms have also been studied for glycerol phosphate, Carbo-Iron and NanoFeR 25s previously via U L₃-edge EXAFS (Vettese *et al.*, 2020, Thesis Chapter 5)(Newsome et al., 2015c).

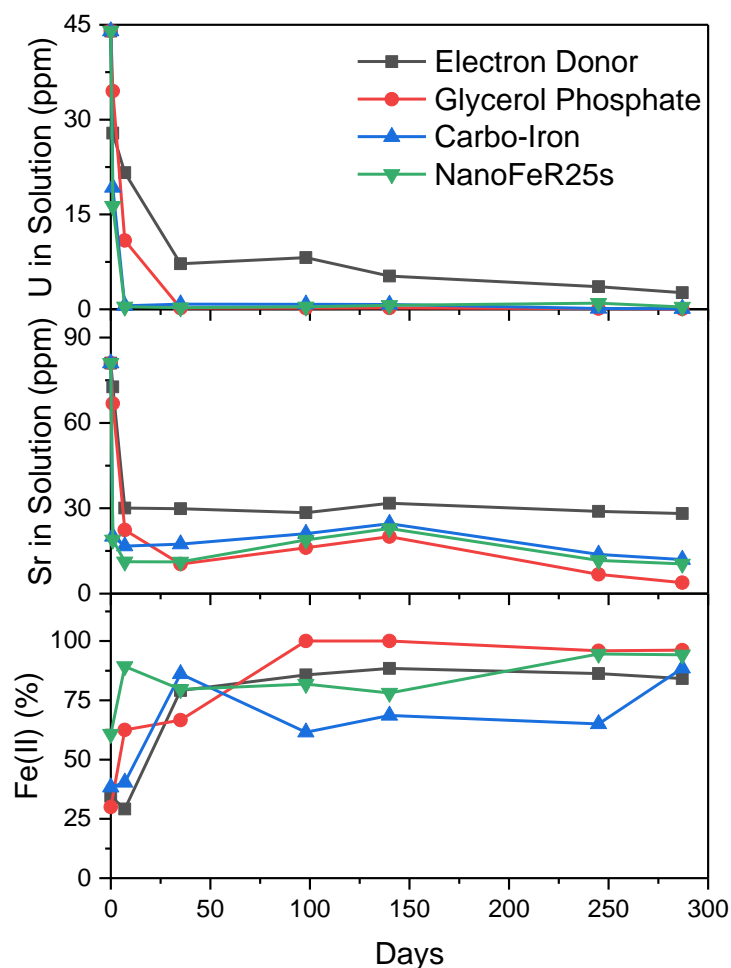


Figure 95: A) U removal, B) Sr removal, and C) Fe(II) as a % of total bioavailable Fe in the incubation phase. System 1: Electron Donor (grey squares), System 2: Glycerol phosphate (red circles), System 3: Carbo-Iron (blue triangles), and System 4: NanoFeR25s (green inverted triangles). Data adapted from and previously discussed in (Vettese *et al.*, 2020, Thesis Chapter 5).

6.42 Column Effluent Geochemistry

8 parallel flow-through columns were packed with the post treatment sediments described above and were subjected to remobilisation experiments via ground- or seawater ingress for 120 days. In this time 106 pore volumes of aerobic ground or seawater was passed through each column and both U and Sr were detected in the effluent of all columns (Figures 97 & 98). Eh measurements, suggested that the column effluents were oxic (Figure S104). This was confirmed by the return of the bioavailable Fe(II) ratios in the effluents to their initial values from the start of the incubation period in 60 days. All 8 columns saw an initial spike in U and Sr over the first 20 days which was especially pronounced in the columns treated with seawater (Figure 96 & Figure 97). This was presumably, due to initial removal of a more mobile fraction, likely present as weakly bound sorption complexes. Analysis of the effluent data indicated that throughout the experiment, all systems that were treated using glycerol phosphate, Carbo-Iron or NanoFeR 25s retained more U and Sr compared to the electron donor (acetate & lactate) system; confirming that the chosen methods provide enhanced retention of solid-phase U and Sr compared to standard electron donor amendments (Vettese *et al.*, 2020, Thesis Chapter 5)(Newsome *et al.*, 2015c). In both ground- and seawater experiments the glycerol phosphate amended system retained the most U; after groundwater ingress glycerol phosphate amended

sediments retained 24 times more U than the electron donor system, and after seawater ingress it retained 4 times more (Figure 2, Table 1). In the case of Sr, both ZVI treatments retained the most Sr; after groundwater ingress Carbo-Iron retained twice as much Sr compared to the electron donor system, and NanoFeR 25s retained almost 5 times more Sr than the electron donor system after seawater ingress (Figure 3, Table 1). The impact of seawater ingress on U efflux was even more pronounced than for Sr (Figures 2 & 3); here, seawater remobilised up to 20 times more U and up to 3.4 times more Sr than groundwater ingress (Figures 2 & 3, Table 1). Surprisingly, these results show that seawater ingress had a greater effect on U remobilisation than Sr; a likely explanation is as follows. Assuming that the ground and seawater have the same concentrations of dissolved O₂ and are therefore equally oxidising, they should re-oxidise equal amounts of U(IV) to U(VI). Under these circumstances, any U(VI) cations bound to exchange sites will be replaced by dominant cations present in higher concentrations in the seawater (Catalano and Brown, 2005). U(VI) sorption to clays and minerals can range from highly sensitive (i.e. clays / bentonite) to completely insensitive to ionic strength (i.e. goethite)(Gao et al., 2015; Guo et al., 2009; Xiao et al., 2013). These data suggest that oxidation state is not the only controlling factor with respect to U mobility although to test this hypothesis we would need EXAFS analysis on the end-points. Although the samples are prepared they were not run due to COVID-19. Interestingly the groundwater has a higher carbonate concentration compared to the seawater, usually carbonate increases U(VI) solubility (Ching-kuo and Langmuir, 1985; Waite et al., 1994; Wazne et al., 2003).

Bioavailable Fe(II) as a percentage of total bioavailable Fe was determined in the column effluents using the ferrozine method (Stookey, 1970; Viollier et al., 2000) and the Eh was also measured. Here, the percentage of bioavailable Fe(II) in the effluents returned to the initial concentrations within a 60 day period and the Eh values suggested that the fluids passing through the columns were oxic (Figure 95, Figure S104, Figure 106) (Vettese *et al.*, 2020, Thesis Chapter 5). Throughout the experiment there were negligible changes in SO₄²⁻ or NO₃⁻ (Figure 105), suggesting that the systems remained predominantly aerobic during these entire reaction period. Characterisation of the microbial community would help clarify the re-establishment of oxic conditions, although the samples are prepared they have not been run to date, due to COVID-19.

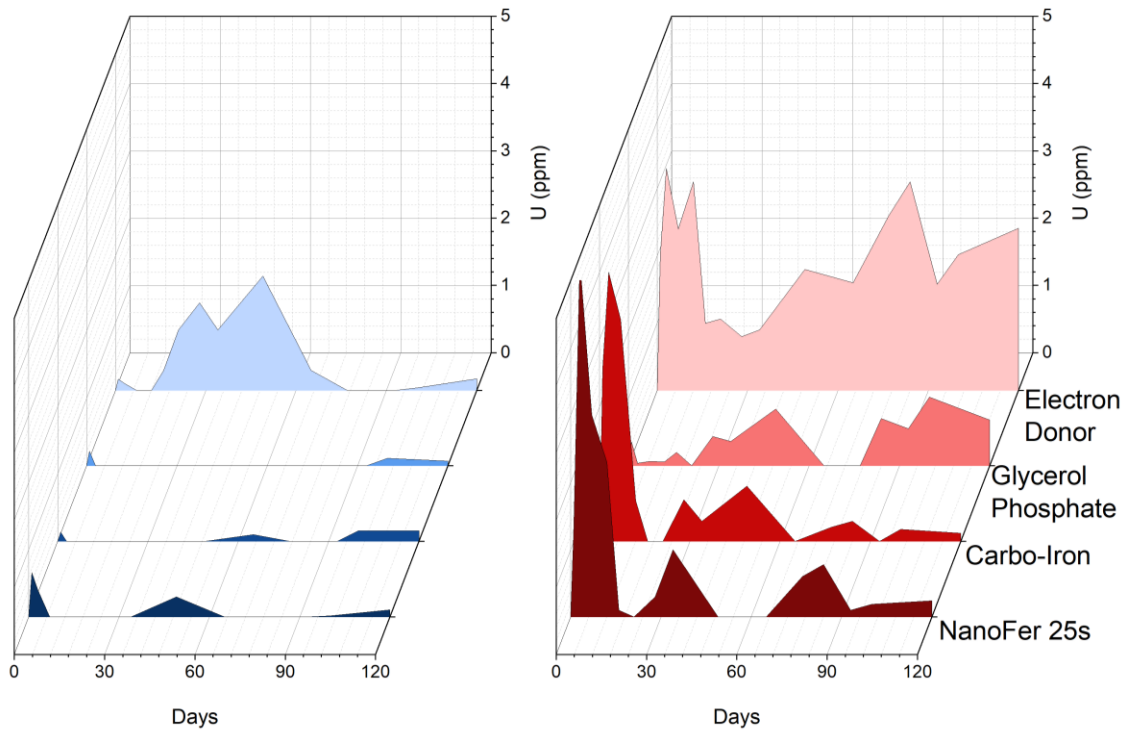


Figure 96: U concentrations in effluents with artificial groundwater treatments (left, blue) and artificial seawater treatments (right, red), with systems in the order from top to bottom: electron door, glycerol phosphate, Carbo-Iron and NanoFer 25s.

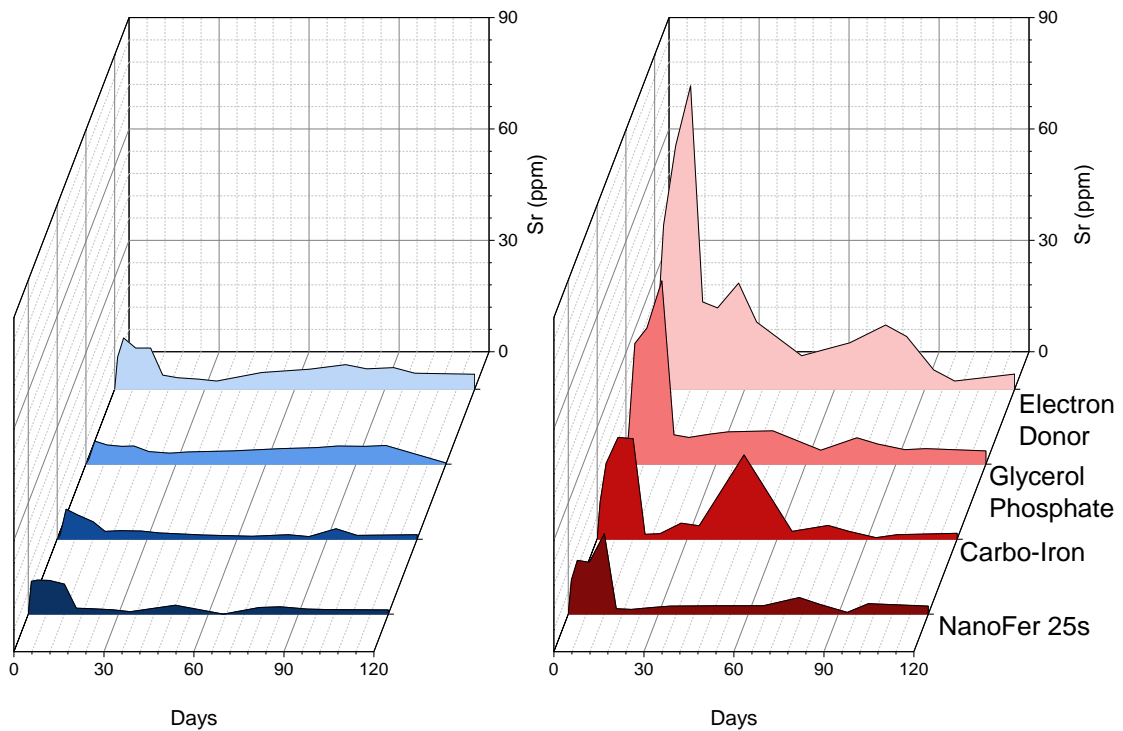


Figure 97: Sr concentrations in effluents with artificial groundwater treatments (left, blue) and artificial seawater treatments (right, red), with systems in the order from top to bottom: electron door, glycerol phosphate, Carbo-Iron and NanoFer 25s.

By subtracting the mass of U and Sr in the effluents from the the initial U and Sr loadings we were able to estimate the amount of each analyte that was remobilised. Although a short summary is provided below (Table 1), the full calculation is available in a larger table in the supporting information (Table S14). Here, it is important that the values provided are regarded as estimates at best. The data provided should be backed up using the absolute U and Sr concentrations determined by acid digests on each third of the column. Unfortunately, although triplicate ICPMS samples were prepared and submitted for analysis, they have been put on hold due to COVID-19.

Table 13: Radionuclide Mass Balance after Re-oxidation.

Column		Concentration of Analyte Remaining in Solution After Bioreduction (ppm) ^a		Initial Mass of Analyte in Column (mg) ^b		Mass of Analyte Remobilised During Experiment (mg) ^c		Amount of Analyte Remobilised During Experiment (%)	
		U	Sr	U	Sr	U	Sr	U	Sr
AGW	Electron Donor	2.6	28.1	15.5	19.9	0.5	5.3	3.1	26.3
	Glycerol Phosphate	> 0.05	3.8	18.7	32.8	> 0.05	3.9	0.1	11.9
	Carbo-Iron	0.1	12.0	17.6	27.6	> 0.05	1.9	0.3	6.8
	NanoFeR 25s	0.4	10.4	14.3	23.1	0.07	2.2	0.5	9.4
ASW	Electron Donor	2.6	28.1	15.9	20.4	1.9	17.8	11.9	87.3
	Glycerol Phosphate	0.0	3.8	16.8	29.5	0.4	9.6	2.6	32.4
	Carbo-Iron	0.1	12.0	17.8	28.0	0.5	7.3	2.9	26.0
	NanoFeR 25s	0.4	10.4	17.8	28.8	0.6	3.9	3.4	13.4

^a Values from (Vettese *et al.*, 2020, Thesis Chapter 5). ^b Estimated using the difference in the ICPMS after 300 days incubation to calculate the radionuclide concentration in ppm. Then using the mass of sediment in each experiment (Vettese *et al.*, 2020, Thesis Chapter 5) (Figure 1). ^c Determined using the cumulative effluent concentrations. Remaining data is in Table S14.

6.43 Solid Phase Geochemistry

During the latter stages of the experiment we observed discrete patches of darkened sediment that were particularly prominent the seawater columns (Figure S101). Although the effluent analysis suggested that the fluids passing through the columns were oxic, we hypothesised that these darker areas may be due to localised areas of anaerobiosis or even localised sulphate-reduction. Indeed, the microbial community present in the sediments for all systems added after the incubation phase contained sulphate-reducing microorganisms and the geochemical data showed complete sulphate removal in all 4 systems (Vettese *et al.*, 2020, Thesis Chapter 5). Although S was detected in all columns using XRF, it accumulated to a greater extent in the columns with seawater ingress (Figure 109). In these systems there was on average more than twice as many counts of S when compared to their groundwater counterparts. Although this was expected, the artificial seawater recipe contains significantly more dissolved sulphate (0.04 g/L in the groundwater recipe vs 2.95 g/L in the seawater

recipe), it would be interesting to determine the speciation of the S and the local mineralogy using SEM-EDX. Bulk Eh measurements were not helpful in diagnosing whether localised sulphate-reducing conditions were achieved (Figure S104). End-point samples were prepared for analysis however have been put on hold due to COVID-19. Without the accompanying 16S rRNA gene sequencing and SEM-EDX data we cannot unambiguously characterise the biogeochemistry of the sediments.

XRF using an Itrax core scanner provided counts of fluorescence at 200 μm steps along the columns for a host of elements, Figure 98 (below) shows selected elements of interest for each column. As the counts provided are a function of multiple parameters, e.g. concentration, particle size, moisture content, elemental fluorescence and background subtraction, the results do not depict the concentrations, rather the relative change in concentrations with height. Therefore the Itrax data displayed in Figure 98 can be used to determine elemental positions in a strictly qualitative manner. Here, we found that generally Sr was distributed evenly throughout the columns (Figure 98). Interestingly, U behaviour was often found in large clusters aggregated at random points in the system. With the current dataset we cannot be sure if these correlate to the dark patches observed in the columns, ICP-MS, SEM-EDX and XAS supported by 16S rRNA gene sequencing will help in answering this. The presence of larger U peaks at the top of the glycerol phosphate and the NanoFeR 25s seawater systems suggests that in these systems U may have been moving out of the columns and therefore would ultimately move to a mobile fraction if given sufficient time. Using the Itrax data, we calculated Pearson correlation coefficients across elements of interest which had significant fluorescence counts (Figure 110 & Figure 111). Analysis of the correlation coefficients only found a strong positive correlation between the positions U and Sr co-location in the glycerol phosphate system treated with groundwater (Figure 110). Interestingly, we did not find any correlations between neither U nor Sr and Fe in the nanoscale ZVI based treatments even though EXAFS analysis suggest that they are bound to each other (Vettese *et al.*, 2020, Thesis Chapter 5). This could be an artefact of the methods used and the local structure around U and Sr should be further investigated combining the Itrax results with EXAFS and SEM-EDX analysis.

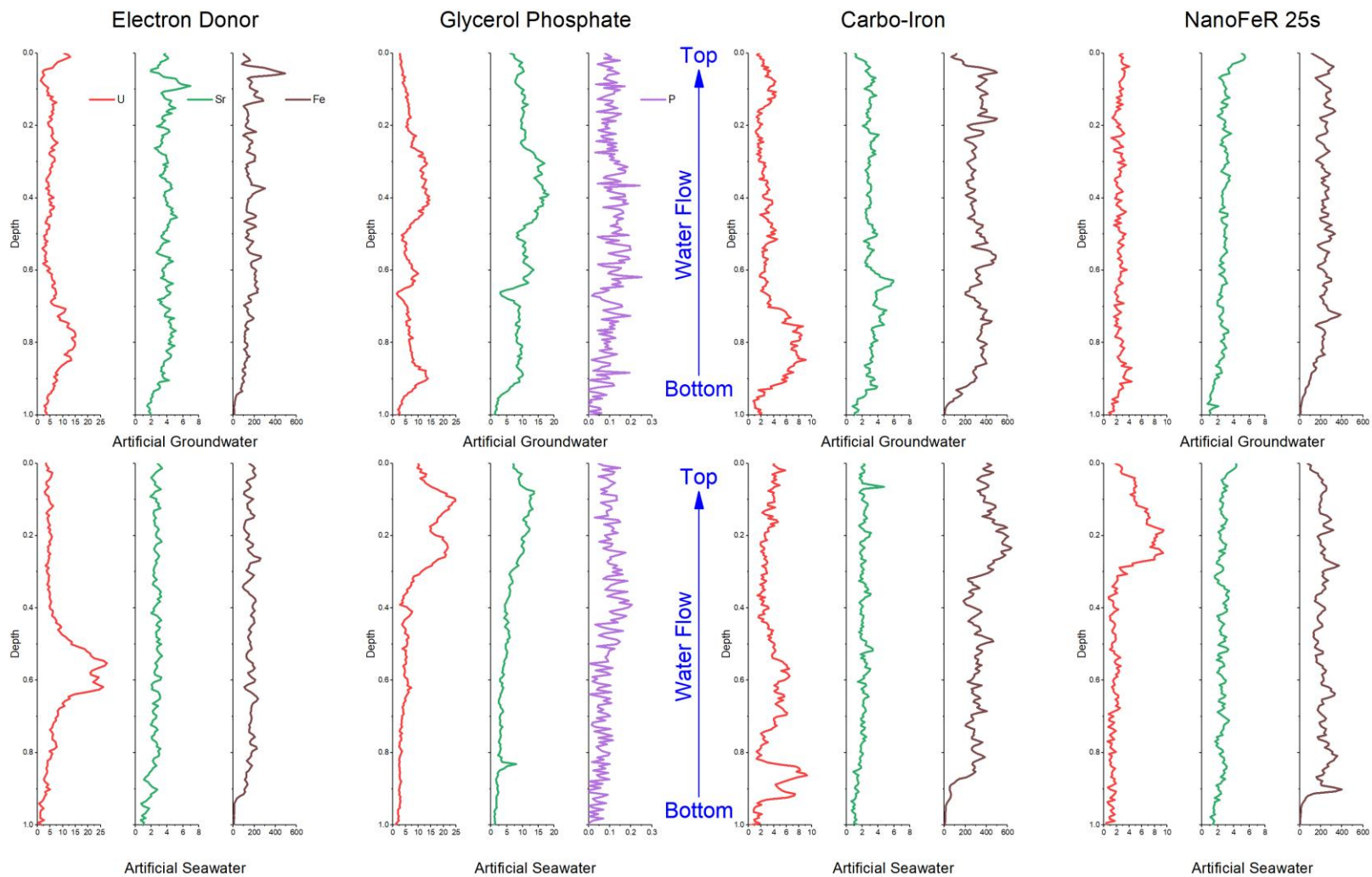


Figure 98: XRF counts against normalised depth, with water flow drawn in blue. The top (0) of each plot represents the outflow section and the bottom (1) of each plot represents the inflow section of the columns, plotted for U (red), Sr (green), and either Fe (brown) or P (purple). Data from the columns subject to artificial groundwater ingress are on the top and to seawater are on the bottom.

6.5 Conclusions

Although the experiment was carried out for 120 days, unforeseen circumstances (COVID-19) meant that the complete assessment of the columns was not complete within the required timeframe as planned. As a result of this, samples for 16S rRNA gene sequencing, SEM-EDX, XAS and ICP-MS have been prepared but were not run. The addition of these analyses would permit a much better understanding of the final biogeochemistry of the columns. However, even without these data we have still demonstrated clear comparisons in the effects of ground and seawater ingress to previously treated sediments. Our flow-through column experiments investigated the potential for 4 different systems to retain co-treated U and Sr in the solid phase following the ingress of ground or seawater. Whilst groundwater ingress had a limited effect on U remobilisation following treatment with glycerol phosphate, Carbo-Iron or NanoFeR 25s, it remobilised significant quantities of sediments that were bioreduced with the electron donors acetate and lactate. U remobilisation was surprisingly susceptible to seawater ingress, suggesting that bioreduced U(IV) is susceptible to remobilisation after intrusion of highly saline waters (e.g. seawater), they also suggest that U mobility is not totally governed by oxidation state. This is likely due to the combined impact of U(IV) oxidation and subsequent cation competition effects limiting U(VI) sorption capacities, although to successfully test this hypothesis further analysis (e.g. EXAFS) on the solid-phase end-points is required. Sr retention following both ground and seawater ingress was maximised with systems amended with nanoscale ZVI. Proof of concept XRF analysis permitted us to monitor the analytes position within the column and perform correlation coefficient analysis. Further work using this tool could provide deeper insights into contaminant mobility in flow-through column experiments, especially when combined with other solid phase analyses (EXAFS, SEM-EDX). Given that many radioactive sites are located by the sea and the continued rise of sea levels there is a surprisingly small amount of work that investigates scenarios of seawater ingress into contaminated land. Following this work the next logical step would test out these targeted treatments via the use of field-scale experiments such as lysimeters or pilot-scale injection wells.

6.6 Acknowledgements

We thank Alastair Bewsher and Paul Lythgoe (The University of Manchester) for IC and ICP-MS analytical support respectively. We also thank Katrin Mackenzie and Steffen Bleyl (UFZ Leipzig) for providing Carbo-Iron and Petra Skácelová (NANOIRON) for providing NanoFer 25s. This work was supported by a PhD bursary from the Nuclear Decommissioning Authority, (R120085) managed by the National Nuclear Laboratory.

6.7 Supporting Information

S1: Experimental Setup

S1.1: Column Setup & Images

In the latter part of the flow-through column experiments discrete dark patches were noticed in the sediments (Figure S101 A - C). They appeared to be randomly distributed but were particularly prominent in the seawater experiments.

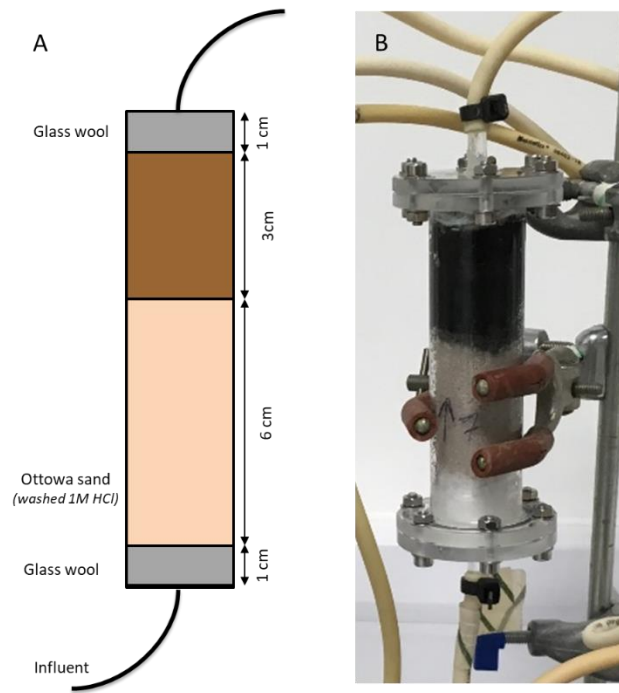


Figure S99: A) schematic depicting the column setup; B) a photo of a column. Influent flowed in to the bottom of the columns and effluent was sampled from the top.

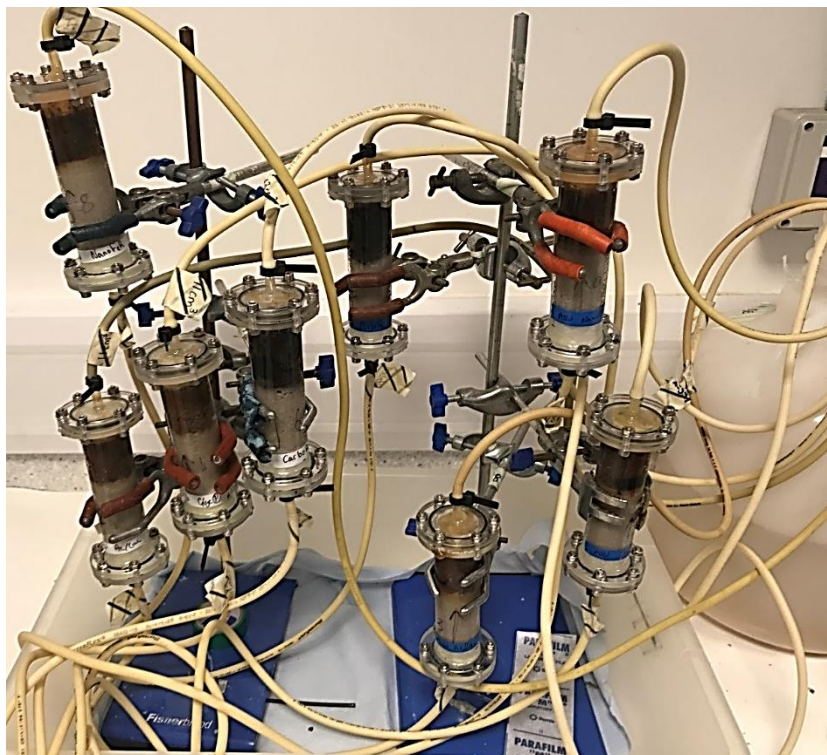


Figure S100: All 8 columns. Influent flowed in to the bottom of the columns and effluent was sampled from the top.

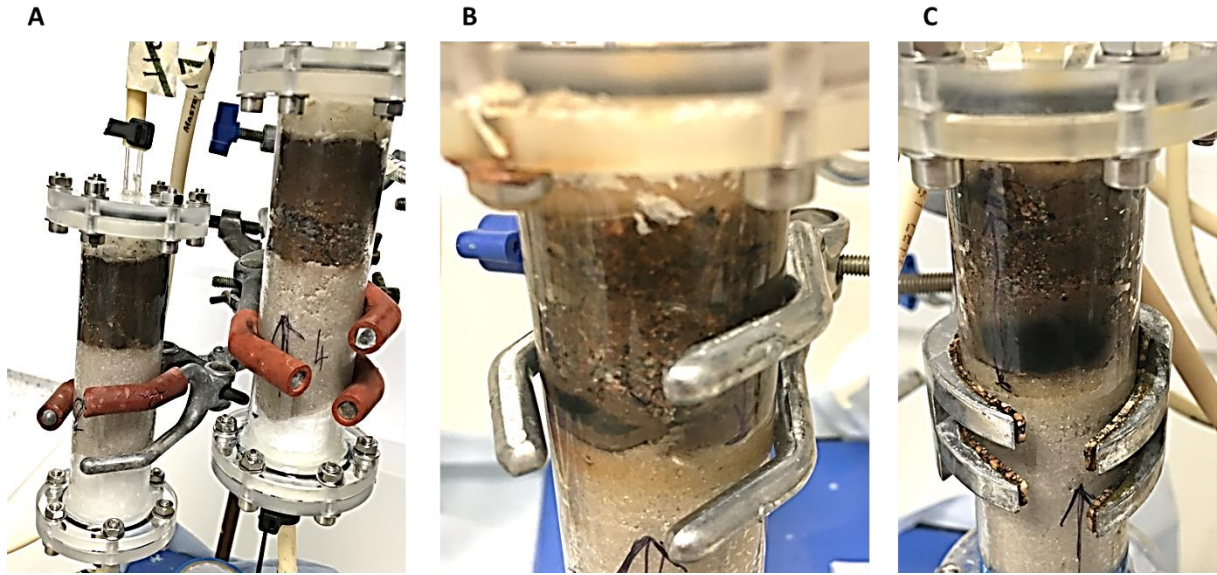


Figure S101 A-C: Photos of the column experiments at day 80, showing: A) the groundwater experiments amended with glycerol phosphate (left) and NanoFeR 25s (right); seawater experiments amended with glycerol phosphate (B) and NanoFeR 25s (C).

S2.2 Bromide Tracer Experiment

A dummy column without any amendments was set up in order to estimate pore volumes in the other columns. A Br⁻ tracer experiment calculated a pore volume of approximately 33 mL for the column experiments. This represented approximately 46 % of the column's volume, giving a flow rate of approximately 0.87 pore volumes a day.

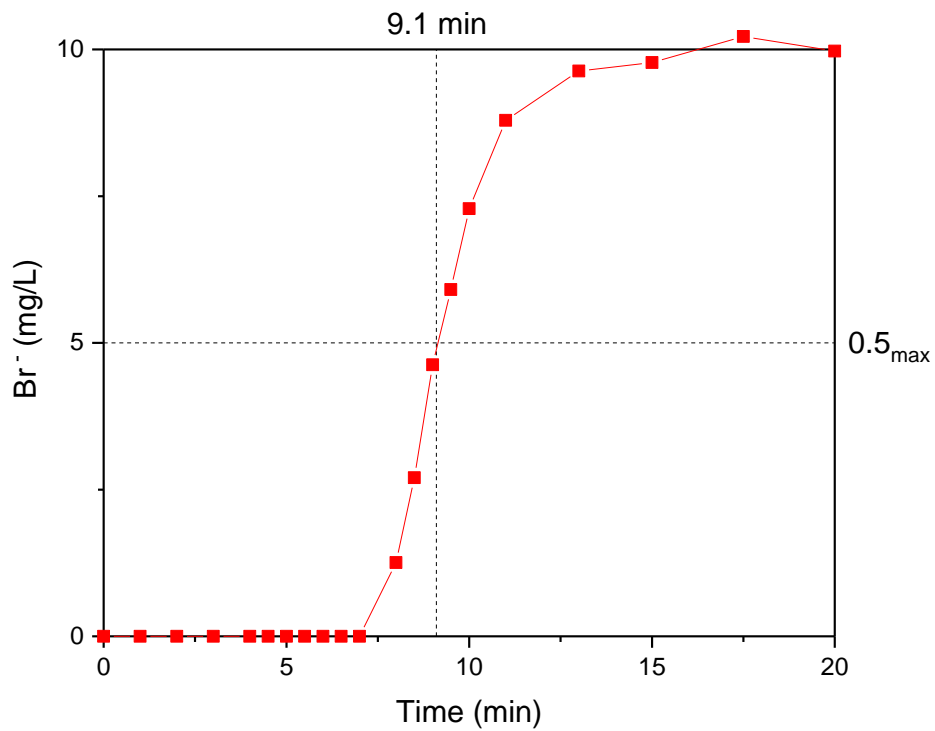


Figure S102: Representative, Br⁻ tracer breakthrough curve from a 3 cm long sediment column at a flow rate of 4.8 mL/min. Influent Br⁻ concentrations (10 mg/L) were reached in the effluent groundwater after 12 min. 'Breakthrough' was therefore determines to be at 50 % of the influent concentration 5 mgL⁻¹ or 9.1 mins.

S2: Column effluents

S2.1: Radionuclide Mass Balance

Table S14: Remaining data needed to calculate the analyte mass balance in Table 1. Integrals were calculated using the analyse function in Origin 2017 64-bit.

Column		Mass of bioreduced sediment packed into Column (g) ^a	Analyte in Effluent / ppm (integrated area under each curve)	
			U	Sr
AGW	Electron Donor	37.6	57.9	628.1
	Glycerol Phosphate	42.5	2.5	468.7
	Carbo-Iron	40.0	5.3	225.6
	NanoFeR 25s	32.7	8.1	259.4
ASW	Electron Donor	38.5	227.0	2138.1
	Glycerol Phosphate	38.3	52.3	1148.8
	Carbo-Iron	40.5	61.3	870.9
	NanoFeR 25s	40.8	72.4	462.7

^a Measured once parafilm sealed before and after packing. 39 g as an average was used on the nuts and bolts and parafilm.

S2.2: Effluent pH & Eh

In all experiments the pH increased during the first 60 days of experiment, following this all of the effluents buffered to a pH of approximately 8 in groundwater experiments and 7.5 in seawater experiments. This was presumably due to bicarbonate alkalinity or microbial activity in the sediment.

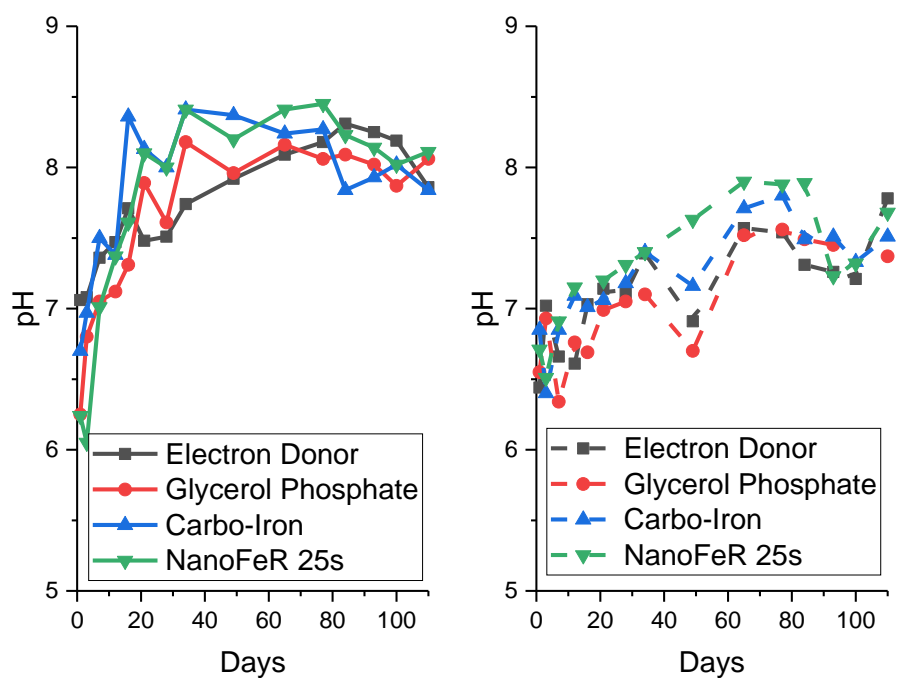


Figure S103: Variation in pH for the 4 columns with aerobic groundwater (left, full lines) and for the 4 columns with aerobic seawater (right, dashed lines). System 1: Electron Donor (grey squares), System 2: Glycerol phosphate (red circles), System 3: Carbo-Iron (blue triangles), and System 4: NanoFeR 25s (green inverted triangles).

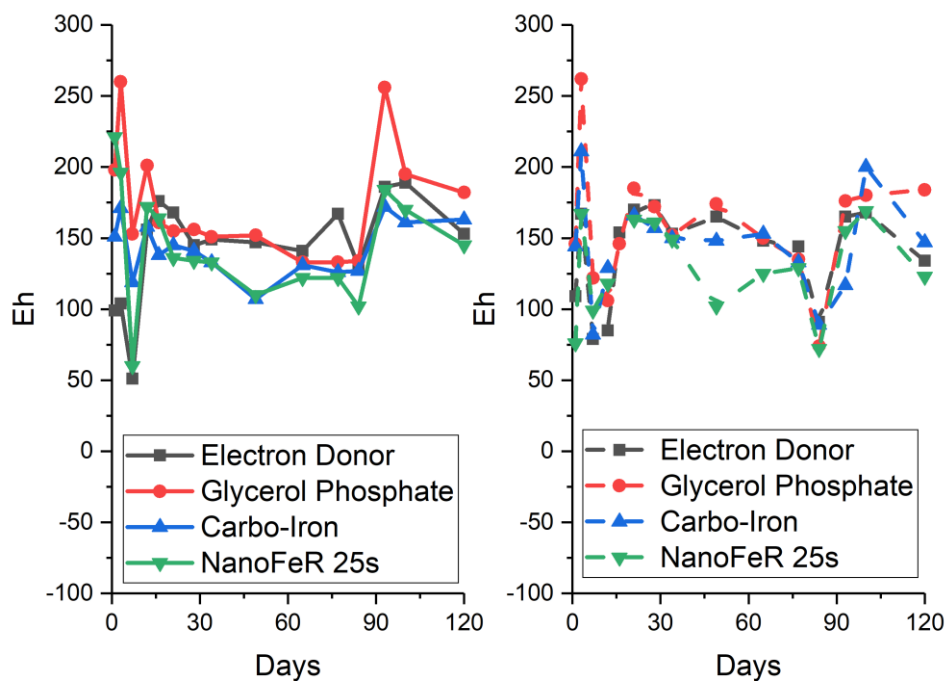
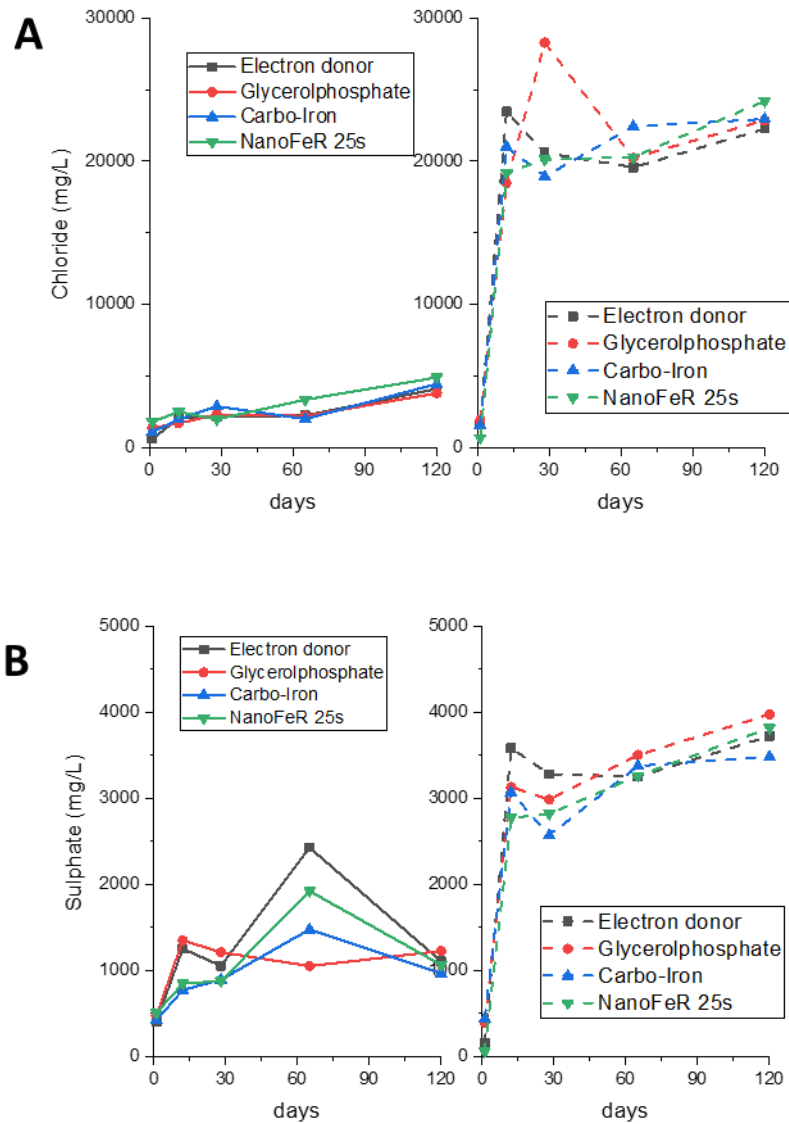


Figure S104: Variation in effluent Eh for the 4 columns with aerobic groundwater (left, full lines) and for the 4 columns with aerobic seawater (right, dashed lines). System 1: Electron Donor (grey squares), System 2: Glycerol phosphate (red circles), System 3 Carbo-Iron (blue triangles), and System 4: NanoFeR 25s (green inverted triangles).

S2.3: Effluent Anions

Sulphate and chloride were present in all effluents, in seawater systems chloride and sulphate concentrations reached a steady state within 12 days (Figure 105 A & B). Nitrate was detected in some of the effluents, despite not being a component in the seawater. This was likely leftover nitrate present in the sediments or the result of oxidation of other intermediates to form nitrate (Figure 105 C).



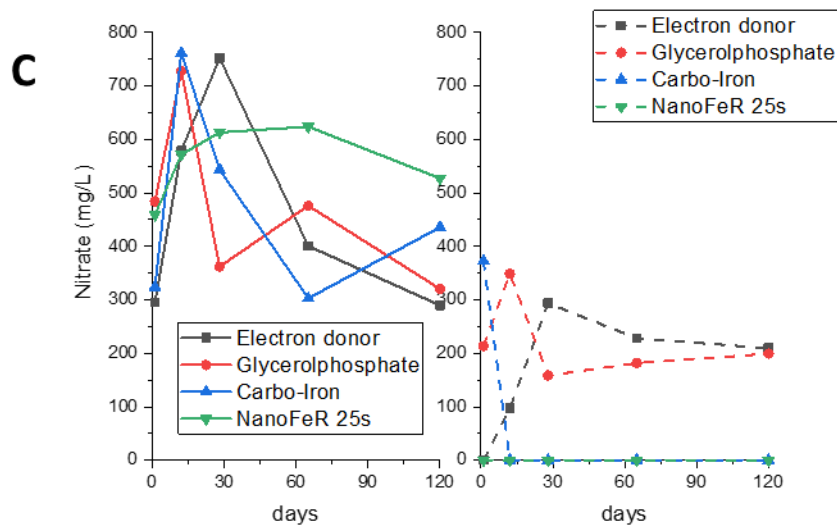


Figure 105: Chloride (A), Sulphate (B) and Nitrate (C) concentrations in column effluents with: Electron donor (grey), Glycerol phosphate (red), Carbo-Iron (blue) and NanoFeR 25s (green). Results from columns 1-4 AGW have full lines (left) and columns 5-8 ASW have dashed lines (right).

S2.4: Bio-available Fe(II) as a % of Total Bio-available Fe in the Effluent

With the exception of electron donor artificial seawater results all bioavailable Fe(II) returned to their original concentrations before incubation (Figure 1). Following seawater ingress the electron donor system did not return to its original bioavailable Fe(II) concentration. This could be attributable to elevated concentrations of S in the column that resulted in the FeS buffering. This theory would be tested using aqua regia digests, XAS and 16S rRNA gene sequencing. *However due to COVID-19 these samples were not run.*

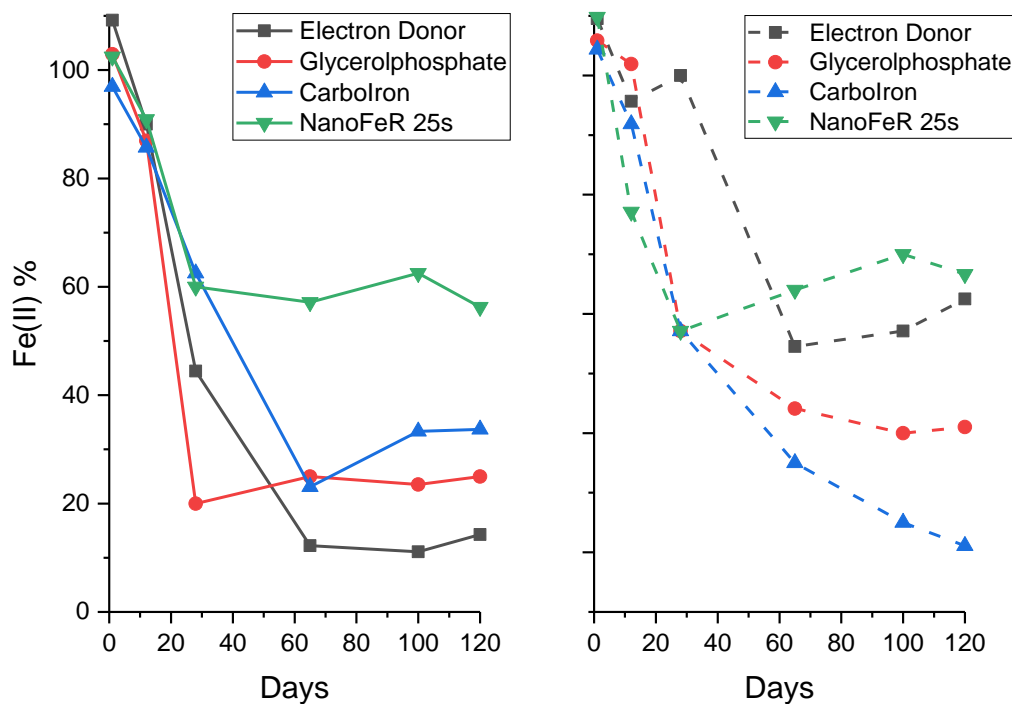


Figure 106: Ferrozine analysis on the effluent columns with aerobic groundwater (left, full lines) and for the 4 columns with aerobic seawater (right, dashed lines). System 1: Electron Donor (grey squares), System 2: Glycerol phosphate (red circles), System 3 Carbo-Iron (blue triangles), and System 4: NanoFeR 25s (green inverted triangles).

S3: Column End-points

S3.1: Bio-available Fe(II) as a Percent of Total Bio-available Fe

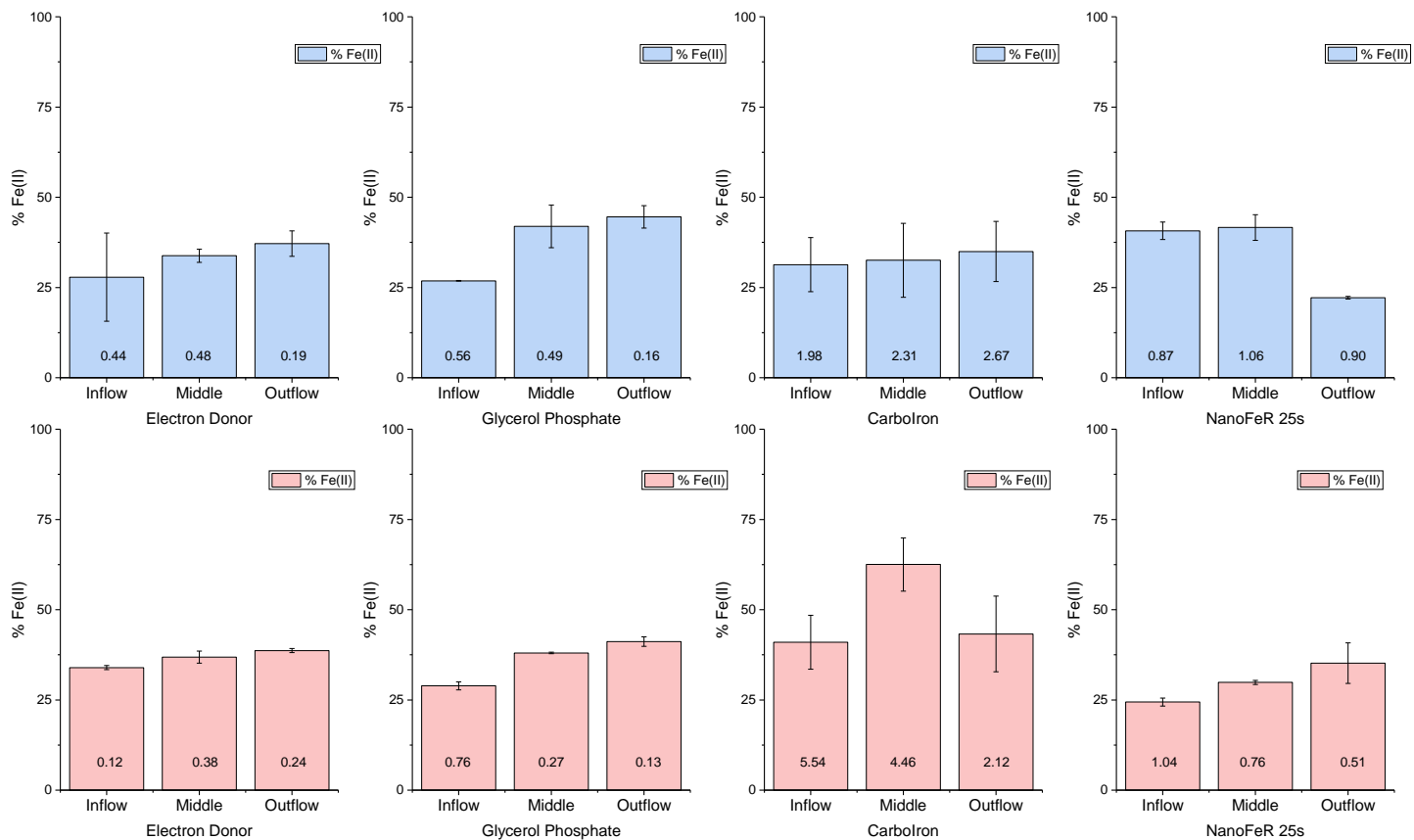


Figure 107: Bio-available Fe(II) as a percentage of total bioavailable Fe taken on the solid phase end-points. Columns in blue were ran with artificial groundwater and columns in red were ran with artificial seawater. The numbers at the bottom of each box represents the bio-available Fe(II) concentration (mM). Error bars represent 1 standard deviation taken from triplicate measurements.

S3.2: Aqua Regia Digests

Sample for acid digests, in aqua regia, were prepared in triplicate along each fraction of the column (inflow, middle and outflow). Here, 0.5 g of pre-weighed wet sediment was dried overnight at 40 °C and the change in mass was noted. The following day the remaining sediments was digested in boiling aqua regia (12.5 mL) for 4 hours until only silica remained. This solution was filtered, and washed with 3 M HNO₃ and the filtered solution was heated until only a film remained. The remaining film was made up to 20 mL in 3 M HNO₃ and was then diluted appropriately into 2 % HNO₃ for ICP-MS analysis.

S3.3: Microbial Analysis

The microbial community was assessed using standard procedures (Bassil et al., 2015; Cleary et al., 2019; Foster et al., 2020; Kuippers et al., 2019; Newsome et al., 2019)(Vettese *et al.* 2020, Chapter 5). Here, DNA was extracted from 200 µl of sediment slurry or microcosm sample using a DNeasy PowerLyzer PowerSoil Kit (Qiagen, Manchester, U.K). Sequencing of PCR amplicons of the 16S rRNA gene was conducted with the Illumina MiSeq platform (Illumina, San Diego, CA, USA) targeting the V4 hyper variable region (forward primer, 515F, 5'-GTGYCAGCMGCCGCGGTAA-3'; reverse primer, 806R, 5'-GGACTACHVGGGTWTCTAAT-3') for 2 × 250-bp paired-end sequencing (Illumina)(Caporaso et al., 2012, 2011). PCR amplification was performed using Roche FastStart High Fidelity PCR System (Roche Diagnostics Ltd, Burgess Hill, UK) in 50µl reactions under the following conditions: initial denaturation at 95°C for 2 min, followed by 36 cycles of 95°C for 30 s, 55°C for 30 s, 72°C for 1 min, and a final extension step of 5 min at 72°C. The PCR products were purified and normalised to ~20ng each using the SequalPrep Normalization Kit (Fisher Scientific, Loughborough, UK). The PCR amplicons from all samples were pooled in equimolar ratios. The run was performed using a 4 pM sample library spiked with 4 pM PhiX to a final concentration of 10% following the method of Schloss and Kozich (Kozich et al., 2013).

Raw sequences were divided into samples by barcodes (up to one mismatch was permitted) using a sequencing pipeline. Quality control and trimming was performed using Cutadapt (Martin, 2011), FastQC (Bioinformatics, 2019), and Sickle (Joshi and Fass, 2011). MiSeq error correction was performed using SPADes (Nurk et al., 2013). Forward and reverse reads were incorporated into full-length sequences with Pandaseq (Masella et al., 2012). Chimeras were removed using ChimeraSlayer (Haas et al., 2011), and OTU's were generated with UPARSE (Edgar, 2013). OTUs were classified by Usearch (Edgar, 2010) at the 97% similarity level, and singletons were removed. Rarefaction analysis was conducted using the original detected OTUs in Qiime (Caporaso et al., 2010). The taxonomic assignment was performed by the RDP naïve Bayesian classifier version 2.2 (Wang et al., 2007). The OTU tables were rarefied to the sample containing the lowest number of sequences, all samples having less than 5,000 sequences were removed from analyses prior to the rarefaction step. The step size used was 2000 and 10 iterations were performed at each step.

S3.4: X-ray Absorption Spectroscopy

Samples for XAS were prepared under anaerobic conditions and were stored anaerobically at -80 °C until analysis.

S3.5: XRF scanning using the Itrax Core Scanner

Elemental distribution was analysed along column cores by XRF using an Itrax Core Scanner at the Geography Department in the University of Manchester. Samples were collected following excitation

using a Mo X-ray Tube at 30 kv / 30 mA with a 15 s dwell time and a step size of 200 microns (Croudace et al., 2006).



Figure S108: 8 core halves prepared for XRF scanning using the Itrax Core Scanner.

Sulphur accumulated in the columns subject to artificial seawater ingress, in these columns the counts of sulphur were on average 2.2 more than their groundwater counterparts.

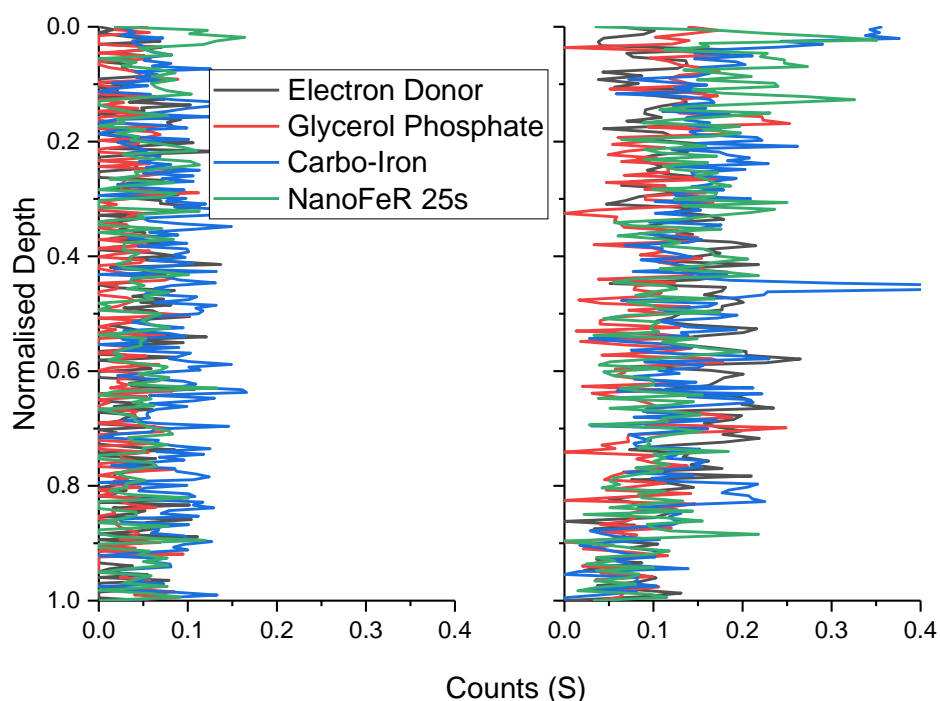


Figure 109: Sulphur counts vs normalised depth for the 4 columns with aerobic groundwater (left) and for the 4 columns with aerobic seawater (right,). System 1: Electron Donor (grey), System 2: Glycerol phosphate (red), System 3 Carbo-Iron (blue), and System 4: NanoFeR 25s (green). Influents flowed in to the bottom of the columns and effluent was sampled from the top.

Elemental Correlation Plots

Pearson correlation coefficients were calculated using the centred log ratios of elemental counts for the Itrax data. In the resulting plots, a full positive correlation gives the value + 1 (blue) and a full negative correlation gives the value - 1 (red). The centred log ratios and Pearson correlation coefficients were calculated using Rscript, with the devtools and itraxR packages (Bishop, 2020; Wickham et al., 2020). Although it is possible to calculate Pearson correlation coefficients for each element, we only used elements which were 1 – of interest to the study, and 2) had average counts greater than 2, as samples with a low signal:noise ratio produced misleading values.

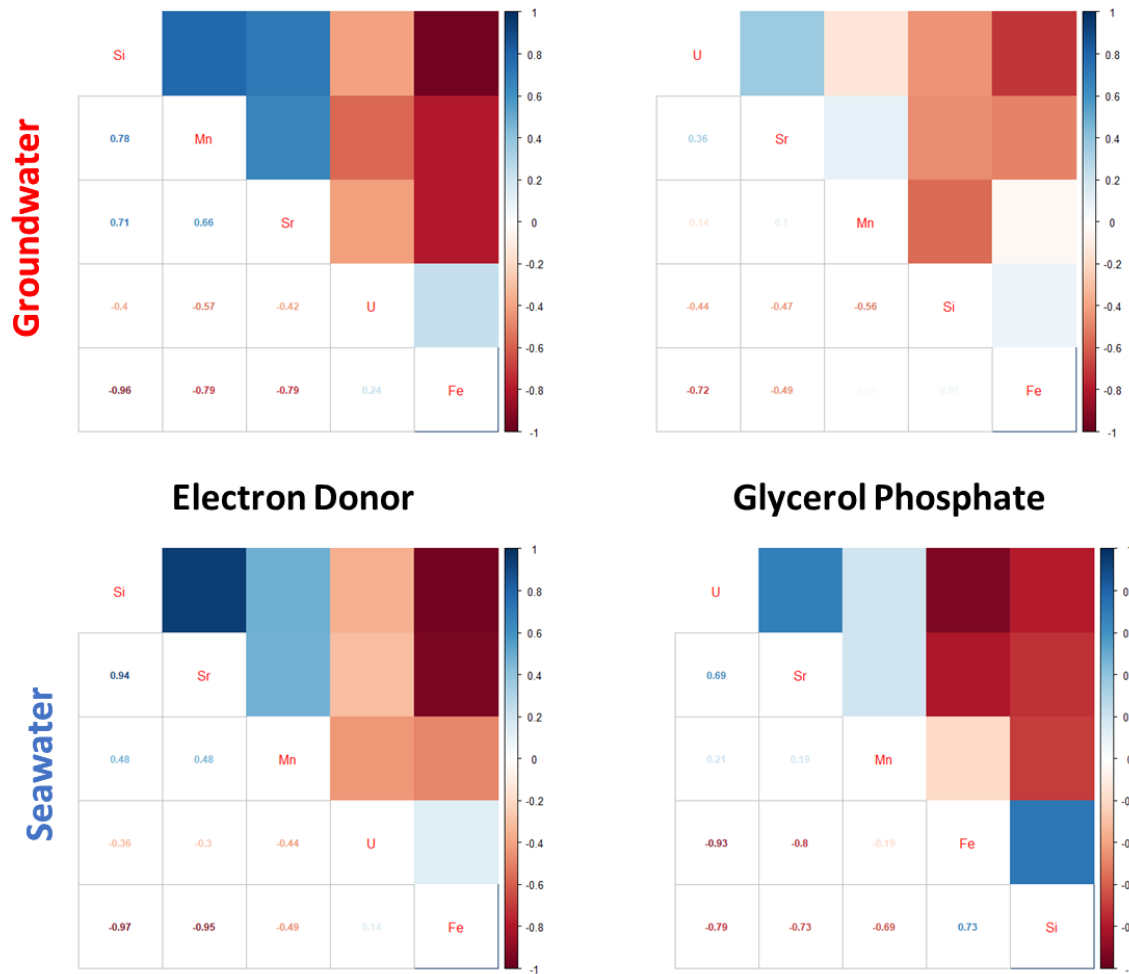


Figure 110: Pearson correlation coefficients plots of the XRF data for U, Sr, Mn, Fe and Si where a value of +1 (blue) represents a full positive correlation, 0 (no colour) represents no correlation and -1 (red) represents a full negative correlation. Data plotted for the electron donor and glycerol phosphate systems with groundwater on top (red) and seawater on bottom (blue).

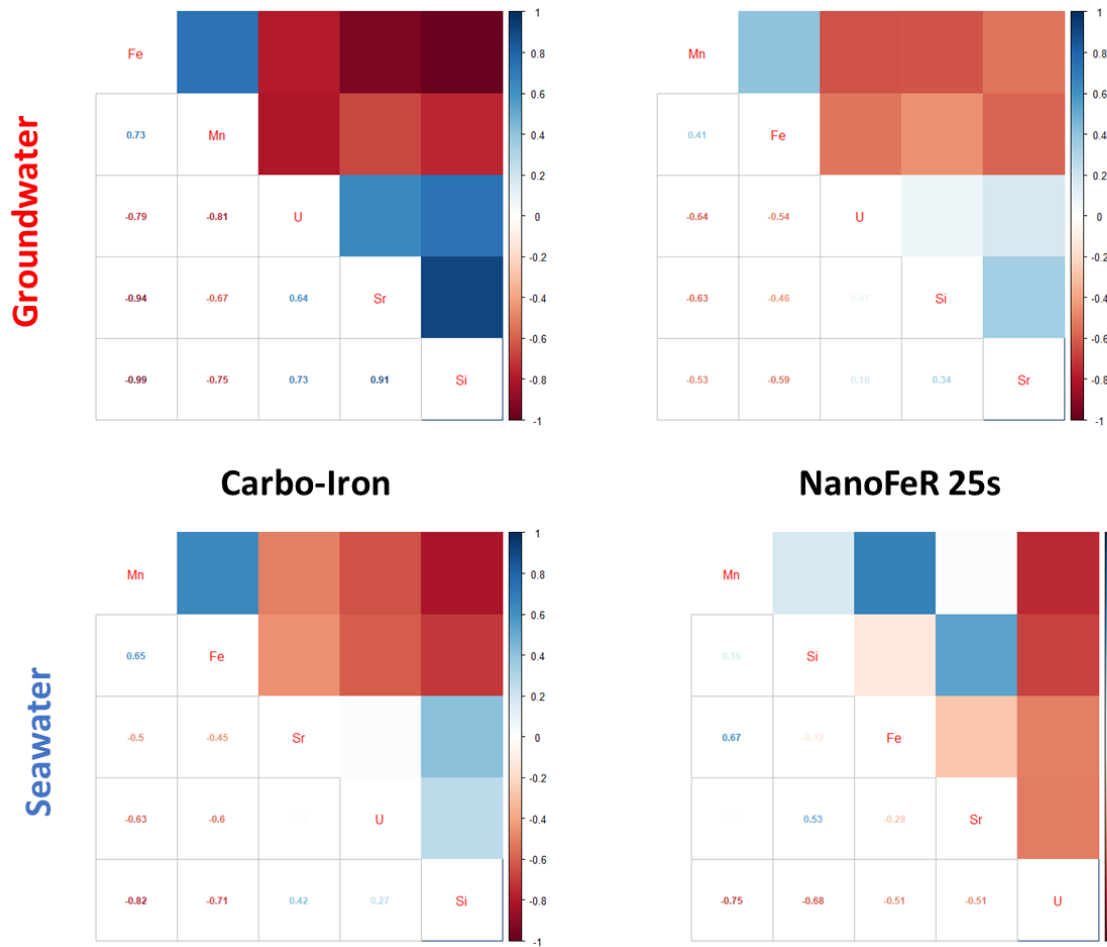


Figure 111: Pearson correlation coefficients plots of the XRF data for U, Sr, Mn, Fe and Si where a value of +1 (blue) represents a full positive correlation, 0 (no colour) represents no correlation and -1 (red) represents a full negative correlation. Data plotted for the Carbo-Iron and NanoFeR 25s systems with groundwater on top (red) and seawater on bottom (blue)

Chapter 7: Thesis Conclusions and Future Work

Bioremediation, as a method of enhanced natural attenuation offers significant advantages over other technologies in the effective and long-term stewardship of land contaminated with radionuclides. Whilst a larger bank of knowledge is still required before bioremediation can be used to treat radioactive contaminated land at scale, this PhD has offered many useful insights to help bridge this gap. The key aims of this project were to identify the fate and prolonged stabilities of U and Sr in contaminated land and GDF scenarios. This led to two areas of investigation; the first combined spectroscopic techniques to study the mechanisms of microbial U(VI) reduction and the second followed the long-term stabilities of targeted remedies co-treating U and Sr sediments during incubation and reoxidation phases. The questions used to guide the research described in Chapters 5-7 were:

- Does the bioreduction of U(VI) by model Fe(III)-reducing bacteria proceed via a U(V) intermediate?
- If the U(V) intermediate exists, what is its speciation, how stable is it and what does this infer about the U(VI) bioreduction mechanism?
- What chemical or bioremediation methods, including stimulated microbial process and nanoparticles, provide the greatest removal of U and Sr from solution, and what is the speciation of the end-points?
- Which end-points are most stable following reoxidation?
- How does the fate of U and Sr compare under Fe(III) and sulphate-reducing conditions?
- Does seawater ingress cause more radionuclide remobilisation than groundwater ingress and why?

Whilst U(VI) bioreduction has been well studied, the mechanism(s) underpinning this were not fully understood prior to this work. For example, in *Geobacter sulfurreducens* a pentavalent intermediate was suggested but was not identified unequivocally (Jones et al., 2015; Renshaw et al., 2005; Sundararajan et al., 2008). In Chapter 5, we present novel contributions towards understanding microbial reduction of U(VI) with respect to not only the mechanism(s) of reduction but also the stability of the U(V) intermediate present in environmentally relevant conditions. Through the combined use of ICP-MS, luminescence spectroscopy, U L₃-edge XAS and (for the first time in biological samples) U M₄-edge HERFD-XANES we have emphatically defined the enzymatic reduction of U(VI) by model Fe(III)-reducing bacteria *Shewanella oneidensis* MR1 which proceeds via a 1 electron transfer mechanism to form a U(V), as uranyl(V), intermediate. This intermediate then disproportionates to form insoluble U(IV) and soluble U(VI). Whilst the biomechanical mechanism(s) of U(VI) bioreduction have been debated in depth for some time (Cherkouk et al., 2016; Kotloski and Gralnick, 2013; Marshall et al., 2006; Suzuki et al., 2010), our work suggests that U(VI) bioreduction likely involves both intracellular and extracellular electron transfer pathways. Moreover we have identified, for the first time, a significant quantity (20-30 %) of persistent U(V) in the solid-phase end-point after up to 120.5 hours of bioreduction, using both U L₃-edge EXAFS and U M₄-edge HERFD-XANES. This stability of U(V) under environmentally relevant conditions has not been documented before. Most work has addressed the stabilisation of U(V) by Fe (Collins and Rosso, 2017; Ilton et al., 2005; Pidchenko et al., 2017; Roberts et al., 2017) and moreover, U(V) was only recently stabilised in water (Faizova et al., 2018). Our work suggests that U(V) may be stabilised for at least 120.5 hours in the presence of bacteria and questions remain regarding its longevity or indeed its existence in the field. These

discoveries were facilitated by the recent growth of U M₄-edge HERFD XANES which has allowed for much more facile identification of U(V) (Bès et al., 2016; Kvashnina et al., 2013; Pidchenko et al., 2017; Roberts et al., 2017). One other technique that stands out as a key tool for identifying U(V) amongst other U oxidation states is Electron Paramagnetic Resonance (EPR). In EPR signals are generated by unpaired electrons; thus U(VI) and U(IV) are silent and U(V), which has one unpaired electron, produces a signal (Lewis et al., 1973). Further investigation of the environmental stability of U(V) is warranted. Indeed, these investigations should aim to identify where the U(V) was bound and why it persisted for 120.5 hours; it would also be interesting to test how long it persists for. A plausible hypothesis could be that ligands present on the cells stabilise the U(V) or provide steric hindrance which prevent disproportionation by cation-cation encounter complexes (Collins and Rosso, 2017; Faizova et al., 2018). The location of the U could be investigated using imaging techniques such as Transmission Electron Microscopy (TEM) or fluorescence microscopy, as was used in the microbial reduction of U(VI) by *G. sulfurreducens* (Jones et al., 2015).

Aqueous U and Sr in contaminated environments are mobile and in some circumstances, need to be targeted for *in-situ* treatments in order to provide a “toolbox” for contaminated land treatment. A wide range of options are available to the practitioner, but to date there is little work which has compared the performance of contrasting chemical and biogeochemical treatment options. Moreover, reoxidation scenarios can significantly impact the rate and extent of remobilisation, and direct comparisons between different studies is often not possible. In Chapter 6, we have used batch microcosm experiments to quantify the stability of the end member treatments and we have explored their behaviour during reoxidation perturbations. These experiments are particularly pertinent because microbially-reduced U(IV) is highly susceptible to oxidative remobilisation. We examined the stability and reoxidation behaviour of U and Sr phases which had been incubated for 300 days using 7 different treatments selected from standard bioremediation methods and commercially available products. These included: a “natural attenuation” control, an electron donor system with acetate and lactate, an electron donor and excess sulphate experiment, a glycerol phosphate system, two nanoscale ZVI treatments (NanoFeR 25s and Carbo-Iron) and a commercially available slow-release electron donor MRC. Remobilisation experiments were set up to quantify radionuclide release during the reoxidation of the incubated systems, with either excess oxygen or nitrate supplied as the oxidant over another 100 days. The incubated end-points were then characterised using U L₃-edge and Sr K-edge EXAFS. In two cases of particular interest the remobilised U products were then examined again using EXAFS spectroscopy. Briefly, the end-point experiments suggested U and Sr are not only removed from solution to the greatest extent, but they are also best retained in systems amended with glycerol phosphate and nanoscale ZVI (both Carbo-Iron and NanoFeR 25s). Our data also suggest that sulphate-reducing conditions limited U(VI) bioreduction and did not inhibit U remobilisation compared to standard electron donor amendments. The two reoxidised end-point samples selected for detailed characterisation were Carbo-Iron and NanoFeR 25s and here, initial analyses suggest U was retained as solid phase U(VI) bound to Fe.

Whilst these experiments have demonstrated that U and Sr can be co-treated in an optimal manner using glycerol phosphate or nanoscale ZVI systems, we still require further knowledge before they can be used in the field. This experiment only tested 2 analytes, U and Sr; however, at radioactive contaminated sites there are many other radionuclides and fission products which must be accounted for. For example, whilst biostimulation via the addition of carbon based electron donors may remove U from groundwater, other toxic contaminants such as As become more mobile (Anderson et al., 2003;

Islam et al., 2004; Lovley et al., 1991) and some radionuclides also have highly complex environmental behaviours and have not been studied in sufficient detail e.g. ^3H , Pu. With regard to U and Sr however, the next logical step was carried out in Chapter 7 where we used the end-points from the 3 best-performing treatments in Chapter 6 in flow-through column experiments. Columns offer more environmentally relevant conditions compared to batch microcosm experiments. Here, the 300 day-old, incubated sediments were packed into flow-through columns and were subject to the ingress of aerobic groundwater or seawater. U and Sr concentrations were analysed in the effluent over a 120 day period using ICP-MS, and the elemental distributions along the columns were assessed using XRF. Although samples were prepared for acid digestions, 16S rRNA gene sequencing and XAS analyses on the end-points of the columns, these analyses were not run due to COVID-19. It is expected that these samples will be run and added to the chapter to form a publication. Nevertheless, using the data already collected it was clear that the ingress of seawater led to increased levels of U and Sr remobilisation compared to groundwater.

Chapters 6 and 7 both provide clear comparisons for multiple radionuclides during a range of treatments. Together they follow the initial changes in biogeochemistry and speciation, they then assess the longevities of the solid-phase U and Sr following a host of remobilisation experiments. These data are novel as there little other work that compares *i*) multiple radionuclides and *ii*) more than 4 treatments, in batch incubation and remobilisation experiments. Given the rise of sea levels and that many radioactive sites are located by the sea there is also a surprisingly small amount of work investigating the effects of seawater ingress to contaminated land, Chapter 7 addresses this. The next step would be to use field lysimeters, such as the ones used at Clemson University (USA) (Peruski et al., 2018; Witmer, 2014) or pilot-scale injection wells, such as the ones used at the US DoE Rifle Site (Anderson et al., 2003), to test out targeted treatments e.g. glycerol phosphate / nanoscale ZVI in the field. Interestingly, some publications have suggested that the abiotic reduction of U(VI) by nanoscale ZVI forms a U(V) intermediate before further reduction to U(IV) (Tsarev et al., 2017, 2016a). In a similar manner to the experiments conducted in Chapter 5, it would be interesting to provide unequivocal proof of a U(V) intermediate during reduction using nanoscale ZVI.

In summary, the work presented in this thesis has examined the mechanisms, speciation and long-term fate of U and Sr following a range of treatments in engineered or natural environments. Chapter 5, used novel approaches to unequivocally conclude that U(V), as uranyl(V), exists as an intermediate in U(VI) bioreduction by *S. oneidensis* MR1. Furthermore, the identification of U(V) after 120.5 hours of bioreduction has broadened the field of stability for U(V) under environmentally relevant conditions. Chapters 6 and 7 assessed the long-term stability for co-targeted U and Sr during incubation and following re-oxidation experiments. These data allowed for novel and quantitative comparisons between a host of treatments and following multiple reoxidation experiments. They highlighted optimum treatments for both U and Sr and addressed the issue of rising sea levels which is highly topical today. Chapter 5 has been published in *Environmental Science and Technology* (Vettese et al., 2020), Chapter 6 is written as ready for submission to *Earth and Space Science*, and Chapter 7 is written with aim for eventual submission to *Chemical Geology* once the remaining data are collected.

Chapter 8: List of References

- Abbasi, W.A., Streat, M., 1994. Adsorption of uranium from aqueous solutions using activated carbon. *Sep. Sci. Technol.* 29, 1217–1230.
- Abdelouas, A., Lu, Y., Lutze, W., Nuttall, H.E., 1998. Reduction of U(VI) to U(IV) by indigenous bacteria in contaminated ground water. *J. Contam. Hydrol.* 35, 217–233.
- Abdelouas, A., Lutze, W., Nuttall, H.E., 1999. Oxidative dissolution of uraninite precipitated on Navajo sandstone. *J. Contam. Hydrol.* 36, 353–375.
- Achal, V., Pan, X., 2011. Characterization of urease and carbonic anhydrase producing bacteria and their role in calcite precipitation. *Curr. Microbiol.* 62, 894–902.
- Achal, V., Pan, X., Zhang, D., 2012. Bioremediation of strontium (Sr) contaminated aquifer quartz sand based on carbonate precipitation induced by Sr resistant *Halomonas* sp. *Chemosphere* 89, 764–768.
- Adamson, D.T., McDade, J.M., Hughes, J.B., 2003. Inoculation of a DNAPL source zone to initiate reductive dechlorination of PCE. *Environ. Sci. Technol.* 37, 2525–33.
- Ahmann, D., Roberts, A.L., Krumholz, L.R., Morel, F.M.M., 1994. Microbe grows by reducing arsenic. *Nature*.
- Ahmed et al., Ahmed, M.F., Ahuja, S., Alauddin, M., Hug, S.J., Lloyd, J.R., Pfaff, A., Pichler, T., Saltikov, C., Stute, M., van Geen, A., 2006. Ensuring Safe Drinking Water in Bangladesh. *Science* (80-.). 314, 1687–1689.
- Aksu, Z., Kutsal, T., 1991. A bioseparation process for removing lead(II) ions from waste water by using *C. vulgaris*. *J. Chem. Technol. Biotechnol.* 52, 109–118.
- Alessi, D.S., Lezama-Pacheco, J.S., Stubbs, J.E., Janousch, M., Bargar, J.R., Persson, P., Bernier-Latmani, R., 2014. The product of microbial uranium reduction includes multiple species with U(IV)-phosphate coordination. *Geochim. Cosmochim. Acta* 131.
- Alessi, D.S., Uster, B., Veeramani, H., Suvorova, E.I., Lezama-Pacheco, J.S., Stubbs, J.E., Bargar, J.R., Bernier-Latmani, R., 2012. Quantitative Separation of Monomeric U(IV) from UO_2 in Products of U(VI) Reduction. *Environ. Sci. Technol.* 46, 6150–6157.
- Alp, E.E., Mini, S.M., Ramanathan, M., 1990. X-Ray Absorption Spectroscopy: EXAFS and XANES-A Versatile Tool to Study the Atomic and Electronic Structure of Materials. *Synchrotron x-ray sources new Oppor. soil Environ. Sci.* 25–36.
- Anderson, R.T., Vrionis, H.A., Ortiz-Bernad, I., Resch, C.T., Long, P.E., Dayvault, R., Karp, K., Marutzky, S., Metzler, D.R., Peacock, A., White, D.C., Lowe, M., Lovley, D.R., 2003. Stimulating the In Situ Activity of *Geobacter* Species to Remove Uranium from the Groundwater of a Uranium-Contaminated Aquifer. *Appl. Environ. Microbiol.* 69, 5884–5891.
- Anderson, S., Appanna, V.D., 1994. Microbial formation of crystalline strontium carbonate. *FEMS Microbiol. Lett.* 116, 43–48.
- Andra, 2015. Thermo-Chimie (version applicative 4.3.0) [WWW Document]. URL <https://www.thermochimie-tdb.com/> (accessed 6.14.17).

- Arnold, P.L., Love, J.B., Patel, D., 2009. Pentavalent uranyl complexes. *Coord. Chem. Rev.* 253, 1973–1978.
- Ashbolt, N.J., 2004. Microbial contamination of drinking water and disease outcomes in developing regions. *Toxicology* 198, 229–238.
- Ashry, A., Bailey, E.H., Chenery, S.R.N., Young, S.D., 2016. Kinetic study of time-dependent fixation of UVI on biochar. *J. Hazard. Mater.* 320, 55–66.
- ASN, 2017. French National Plan for the Management of Radioactive Materials and Waste (PNGMDR).
- Atlas, R.M., Hazen, T.C., 2011. Oil biodegradation and bioremediation: A tale of the two worst spills in U.S. history. *Environ. Sci. Technol.* 45, 6709–6715.
- Axe, L., Bunker, G.B., Anderson, P.R., Tyson, T.A., 1998. An XAFS analysis of strontium at the hydrous ferric oxide surface. *J. Colloid Interface Sci.* 199, 44–52.
- Balek, V., Málek, Z., Šubrt, J., Ždimera, A., 1996. Characterization of iron(III) oxide and oxide-hydroxide as Sr-sorbent. *J. Radioanal. Nucl. Chem.* 212, 321–331.
- Bargar, J.R., Reitmeyer, R., Lenhart, J.J., Davis, J.A., 2000. Characterization of U(VI)-carbonato ternary complexes on hematite: EXAFS and electrophoretic mobility measurements. *Geochim. Cosmochim. Acta* 64, 2737–2749.
- Bargar, J.R., Williams, K.H., Campbell, K.M., Long, P.E., Stubbs, J.E., Suvorova, E.I., Lezama-Pacheco, J.S., Alessi, D.S., Stylo, M., Webb, S.M., Davis, J.A., Giammar, D.E., Blue, L.Y., Bernier-Latmani, R., 2013. Uranium redox transition pathways in acetate-amended sediments. *Proc. Natl. Acad. Sci.* 110, 4506–4511.
- Bassil, N.M., Bryan, N., Lloyd, J.R., 2015. Microbial degradation of isosaccharinic acid at high pH. *ISME J.* 9, 310–320.
- Bauman, G., Charette, M., Reid, R., Sathya, J., 2005. Radiopharmaceuticals for the palliation of painful bone metastases - A systematic review. *Radiother. Oncol.*
- Bazin, D., Dessombz, A., Reguer, S., Lioté, F., Rouzière, S., Nguyen, C., Chappard, C., Thiaudière, D., Rehr, J., Ea, H.K., Daudon, M., 2013. The status of strontium in biological apatites: an XANES/EXAFS investigation. *J. Synchrotron Radiat.* 21, 136–142.
- Beazley, M.J., Martinez, R.J., Sobecky, P.A., Webb, S.M., Taillefert, M., 2007. Uranium biomineralization as a result of bacterial phosphatase activity: Insights from bacterial isolates from a contaminated subsurface. *Environ. Sci. Technol.* 41, 5701–5707.
- Beazley, M.J., Martinez, R.J., Webb, S.M., Sobecky, P.A., Taillefert, M., 2011. The effect of pH and natural microbial phosphatase activity on the speciation of uranium in subsurface soils. *Geochim. Cosmochim. Acta* 75, 5648–5663.
- Begg, J.D.C., Burke, I.T., Lloyd, J.R., Boothman, C., Shaw, S., Charnock, J.M., Morris, K., 2011. Bioreduction behavior of U(VI) sorbed to sediments. *Geomicrobiol. J.* 28, 160–171.
- Beller, H.R., 2005. Anaerobic, nitrate-dependent oxidation of U(IV) oxide minerals by the chemolithoautotrophic bacterium *Thiobacillus denitrificans*. *Appl. Environ. Microbiol.* 71, 2170–2174.
- Belousova, E.A., Griffin, W.L., O'Reilly, S.Y., Fisher, N.I., 2002. Apatite as an indicator mineral for mineral exploration: Trace-element compositions and their relationship to host rock type. *J.*

Geochemical Explor. 76, 45–69.

- Bernier-Latmani, R., Veeramani, H., Vecchia, E.D., Junier, P., Lezama-Pacheco, J.S., Suvorova, E.I., Sharp, J.O., Wigginton, N.S., Bargar, J.R., 2010. Non-uraninite products of microbial U(VI) reduction. *Environ. Sci. Technol.* 44, 9456–9462.
- Berthet, J.C., Nierlich, M., Ephritikhine, M., 2003. Isolation of a uranyl [UO₂]⁺ species: Crystallographic comparison of the dioxouranium(V) and (VI) compounds [UO₂(OPPH₃)₄](OTf)_n (n = 1, 2). *Angew. Chemie - Int. Ed.* 42, 1952–1954.
- Bès, R., Rivenet, M., Solari, P.L., Kvashnina, K.O., Scheinost, A.C., Martin, P.M., 2016. Use of HERFD-XANES at the U L₃- and M₄-Edges to Determine the Uranium Valence State on [Ni(H₂O)₄]₃[U(OH,H₂O)(UO₂)₈O₁₂(OH)₃]. *Inorg. Chem.* 55, 4260–4270.
- Bhattacharya, A.K., Venkobachar, C., 1984. Removal of cadmium (II) by low cost adsorbents. *J. Environ. Eng. (United States)* 110, 110–122.
- Bhattacharyya, A., Campbell, K.M., Kelly, S.D., Roebbert, Y., Weyer, S., Bernier-Latmani, R., Borch, T., 2017. Biogenic non-crystalline U (IV) revealed as major component in uranium ore deposits. *Nat. Commun.* 8.
- Bi, Y., Hayes, K.F., 2014. Nano-FeS inhibits UO₂ reoxidation under varied oxic conditions. *Environ. Sci. Technol.* 48, 632–640.
- Bi, Y., Hyun, S.P., Kukkadapu, R., Hayes, K.F., 2013. Oxidative dissolution of UO₂ in a simulated groundwater containing synthetic nanocrystalline mackinawite. *Geochim. Cosmochim. Acta* 102, 175–190.
- Bioinformatics, B., 2019. FastQC A Quality Control tool for High Throughput Sequence Data [WWW Document]. URL <http://www.bioinformatics.babraham.ac.uk/projects/fastqc/> (accessed 4.23.20).
- Bishop, T., 2017. Principles of X-ray Fluorescence in the Itrax Core Scanner [WWW Document]. URL <https://thomasbishop.uk/wp-content/uploads/2018/01/howitraxworks.pdf> (accessed 2.13.20).
- Bishop, T., 2020. tombishop1 · GitHub.
- Bleyl, S., Kopinke, F.-D., Mackenzie, K., 2012. Carbo-Iron[®]—Synthesis and stabilization of Fe(0)-doped colloidal activated carbon for in situ groundwater treatment. *Chem. Eng. J.* 191, 588–595.
- Bone, S.E., Dynes, J.J., Cliff, J., Bargar, J.R., 2017. Uranium(IV) adsorption by natural organic matter in anoxic sediments. *Proc. Natl. Acad. Sci.* 114, 711–716.
- Borovec, Z., 1981. The adsorption of uranyl species by fine clay. *Chem. Geol.* 32, 45–58.
- Bosch, J., Heister, K., Hofmann, T., Meckenstock, R.U., 2010. Nanosized iron oxide colloids strongly enhance microbial iron reduction. *Appl. Environ. Microbiol.* 76, 184–9.
- Bots, P., Morris, K., Hibberd, R., Law, G.T.W., Mosselmans, J.F.W., Brown, A.P., Douth, J., Smith, A.J., Shaw, S., 2014. Formation of Stable Uranium(VI) Colloidal Nanoparticles in Conditions Relevant to Radioactive Waste Disposal. *Langmuir* 30, 14396–14405.
- Boukhalfa, H., Icopini, G.A., Reilly, S.D., Neu, M.P., 2007. Plutonium(IV) reduction by the metal-reducing bacteria *Geobacter metallireducens* GS15 and *Shewanella oneidensis* MR1. *Appl. Environ. Microbiol.* 73, 5897–903.

- Bower, W.R., Morris, K., Livens, F.R., Mosselmans, J.F.W., Fallon, C.M., Fuller, A.J., Natrajan, L., Boothman, C., Lloyd, J.R., Utsunomiya, S., Grolimund, D., Ferreira Sanchez, D., Jilbert, T., Parker, J., Neill, T.S., Law, G.T.W., 2019. Metaschoepite Dissolution in Sediment Column Systems - Implications for Uranium Speciation and Transport. *Environ. Sci. Technol.* 53, 9915–9925.
- Boyanov, M.I., Fletcher, K.E., Kwon, M.J., Rui, X., O’Loughlin, E.J., Löffler, F.E., Kemner, K.M., O’Loughlin, E.J., Löffler, F.E., Kemner, K.M., 2011. Solution and microbial controls on the formation of reduced U(IV) species. *Environ. Sci. Technol.* 45, 8336–8344.
- Boyanov, M.I., O’Loughlin, E.J., Roden, E.E., Fein, J.B., Kemner, K.M., 2007. Adsorption of Fe(II) and U(VI) to carboxyl-functionalized microspheres: The influence of speciation on uranyl reduction studied by titration and XAFS. *Geochim. Cosmochim. Acta* 71, 1898–1912.
- Brandel, V., Dacheux, N., Genet, M., 2001. Studies on the Chemistry of Uranium and Thorium Phosphates . Thorium Phosphate Diphosphate : A Matrix for Storage of Radioactive Wastes. *Radiochemistry* 43, 16–17.
- Braney, M.C., Haworth, A., Jefferies, N.L., Smith, A.C., 1993. A study of the effects of an alkaline plume from a cementitious repository on geological materials. *J. Contam. Hydrol.* 13, 379–402.
- Brookshaw, D.R., Lloyd, J.R., Vaughan, D.J., Patrick, R.A.D., 2016. Effects of microbial Fe(III) reduction on the sorption of Cs and Sr on biotite and chlorite. *Geomicrobiol. J.* 33, 206–215.
- Brookshaw, D.R., Patrick, R.A.D., Bots, P., Law, G.T.W., Lloyd, J.R., Mosselmans, J.F.W., Vaughan, D.J., Dardenne, K., Morris, K., 2015. Redox Interactions of Tc(VII), U(VI), and Np(V) with Microbially Reduced Biotite and Chlorite. *Environ. Sci. Technol.* 49, 13139–13148.
- Brundage, M.D., Crook, J.M., Lukka, H., 1998. Use of strontium-89 in endocrine-refractory prostate cancer metastatic to bone. Provincial Genitourinary Cancer Disease Site Group. *Cancer Prev Control* 2, 79–87.
- Bryce, C., Blackwell, N., Schmidt, C., Otte, J., Huang, Y.M., Kleindienst, S., Tomaszewski, E., Schad, M., Warter, V., Peng, C., Byrne, J.M., Kappler, A., 2018. Microbial anaerobic Fe(II) oxidation – Ecology, mechanisms and environmental implications. *Environ. Microbiol.*
- Buck, E.C., Brown, N.R., Dietz, N.L., 1996. Contaminant uranium phases and leaching at the Fernald site in Ohio. *Environ. Sci. Technol.* 30, 81–88.
- Burbank, M.B., Weaver, T.J., Williams, B.C., Crawford, R.L., 2012. Urease Activity of Ureolytic Bacteria Isolated from Six Soils in which Calcite was Precipitated by Indigenous Bacteria. *Geomicrobiol. J.* 29, 389–395.
- Burns, P.C., Finch, R.J., 1999. Wyartite: Crystallographic evidence for the first pentavalent-uranium mineral. *Am. Mineral.* 84, 1456–1460.
- Busse, H.J., 2016. Review of the taxonomy of the genus *Arthrobacter*, emendation of the genus *arthrobacter sensu lato*, proposal to reclassify selected species of the genus *Arthrobacter* in the novel genera *Glutamicibacter* gen. nov., *Paeniglutamicibacter* gen. nov., *Pseudoglutamicibacter* gen. nov., *Paenarthrobacter* gen. nov. and *pseudarthrobacter* gen. nov., and emended description of *Arthrobacter roseus*. *Int. J. Syst. Evol. Microbiol.*
- Butler, J.E., He, Q., Nevin, K.P., He, Z., Zhou, J., Lovley, D.R., 2007. Genomic and microarray analysis of aromatics degradation in *Geobacter metallireducens* and comparison to a *Geobacter* isolate from a contaminated field site. *BMC Genomics* 8, 180.

- Byrne, J.M., Muhamadali, H., Coker, V.S., Cooper, J., Lloyd, J.R., 2015. Scale-up of the production of highly reactive biogenic magnetite nanoparticles using *Geobacter sulfurreducens*. *J. R. Soc. Interface* 12.
- Byrne, J.M., Telling, N.D., Coker, V.S., Patrick, R. a D., van der Laan, G., Arenholz, E., Tuna, F., Lloyd, J.R., 2011. Control of nanoparticle size, reactivity and magnetic properties during the bioproduction of magnetite by *Geobacter sulfurreducens*. *Nanotechnology* 22, 455709.
- Caccavo, F., Lonergan, D.J., Lovley, D.R., Davis, M., Stolz, J.F., McInerney, M.J., 1994. *Geobacter sulfurreducens* sp. nov., a hydrogen- and acetate-oxidizing dissimilatory metal-reducing microorganism. *Appl. Environ. Microbiol.* 60, 3752–9.
- Caccin, M., Giacobbo, F., Da Ros, M., Besozzi, L., Mariani, M., 2013. Adsorption of uranium, cesium and strontium onto coconut shell activated carbon. *J. Radioanal. Nucl. Chem.* 297, 9–18.
- Campbell, K.M., Kukkadapu, R.K., Qafoku, N.P., Peacock, A.D., Leshner, E., Williams, K.H., Bargar, J.R., Wilkins, M.J., Figueroa, L., Ranville, J., Davis, J.A., Long, P.E., 2012. Geochemical, mineralogical and microbiological characteristics of sediment from a naturally reduced zone in a uranium-contaminated aquifer. *Appl. Geochemistry* 27, 1499–1511.
- Canfield, D.E., Thamdrup, B., 2009. Towards a consistent classification scheme for geochemical environments, or, why we wish the term “suboxic” would go away: Editorial. *Geobiology*.
- Caporaso, J.G., Kuczynski, J., Stombaugh, J., Bittinger, K., Bushman, F.D., Costello, E.K., Fierer, N., Pěa, A.G., Goodrich, J.K., Gordon, J.I., Huttley, G.A., Kelley, S.T., Knights, D., Koenig, J.E., Ley, R.E., Lozupone, C.A., McDonald, D., Muegge, B.D., Pirrung, M., Reeder, J., Sevinsky, J.R., Turnbaugh, P.J., Walters, W.A., Widmann, J., Yatsunencko, T., Zaneveld, J., Knight, R., 2010. QIIME allows analysis of high-throughput community sequencing data. *Nat. Methods*.
- Caporaso, J.G., Lauber, C.L., Walters, W.A., Berg-Lyons, D., Huntley, J., Fierer, N., Owens, S.M., Betley, J., Fraser, L., Bauer, M., Gormley, N., Gilbert, J.A., Smith, G., Knight, R., 2012. Ultra-high-throughput microbial community analysis on the Illumina HiSeq and MiSeq platforms. *ISME J.* 6, 1621–1624.
- Caporaso, J.G., Lauber, C.L., Walters, W.A., Berg-Lyons, D., Lozupone, C.A., Turnbaugh, P.J., Fierer, N., Knight, R., 2011. Global patterns of 16S rRNA diversity at a depth of millions of sequences per sample. *Proc. Natl. Acad. Sci. U. S. A.* 108, 4516–4522.
- Carlson, H.K., Iavarone, A.T., Gorur, A., Yeo, B.S., Tran, R., Melnyk, R.A., Mathies, R.A., Auer, M., Coates, J.D., 2012. Surface multiheme c-type cytochromes from *Thermincola potens* and implications for respiratory metal reduction by Gram-positive bacteria. *Proc. Natl. Acad. Sci. U. S. A.* 109, 1702–1707.
- Carpenter, J., Bi, Y., Hayes, K.F., 2015. Influence of iron sulfides on abiotic oxidation of UO₂ by nitrite and dissolved oxygen in natural sediments. *Environ. Sci. Technol.* 49, 1078–1085.
- Carpenter, S.J., Lohmann, K.C., 1992. Sr Mg ratios of modern marine calcite: Empirical indicators of ocean chemistry and precipitation rate. *Geochim. Cosmochim. Acta* 56, 1837–1849.
- Carroll, S.A., Roberts, S.K., Criscenti, L.J., O’Day, P.A., 2008. Surface complexation model for strontium sorption to amorphous silica and goethite. *Geochem. Trans.* 9.
- Catalano, J.G., Brown, G.E., 2004. Analysis of uranyl-bearing phases by EXAFS spectroscopy: Interferences, multiple scattering, accuracy of structural parameters, and spectral differences. *Am. Mineral.* 89, 1004–1021.

- Catalano, J.G., Brown, G.E., 2005. Uranyl adsorption onto montmorillonite: Evaluation of binding sites and carbonate complexation. *Geochim. Cosmochim. Acta* 69, 2995–3005.
- Catalano, J.G., McKinley, J.P., Zachara, J.M., Heald, S.M., Smith, S.C., Brown, G.E., 2006. Changes in uranium speciation through a depth sequence of contaminated Hanford sediments. *Environ. Sci. Technol.* 40, 2517–2524.
- Cejka, J., 1999. Infrared spectroscopy and thermal analysis of the uranyl minerals. In: RC, E. (Ed.), *Reviews in Mineralogy*. pp. 521–622.
- Chegrouche, S., Mellah, A., Barkat, M., 2009. Removal of strontium from aqueous solutions by adsorption onto activated carbon: kinetic and thermodynamic studies. *Desalination* 235, 306–318.
- Chen, C.C., Hayes, K.F., 1999. X-ray absorption spectroscopy investigation of aqueous Co(II) and Sr(II) sorption at clay-water interfaces. *Geochim. Cosmochim. Acta* 63, 3205–3215.
- Cherkouk, A., Law, G.T.W., Rizoulis, A., Law, K.A., Renshaw, J.C., Morris, K., Livens, F.R., Lloyd, J.R., 2016. Influence of riboflavin on the reduction of radionuclides by *Shewanella oneidensis* MR-1. *Dalt. Trans.* 45, 5030–5037.
- Childers, S.E., Ciuffo, S., Lovley, D.R., 2002. *Geobacter metallireducens* accesses insoluble Fe(III) oxide by chemotaxis. *Nature* 416, 767–9.
- Ching-kuo, D.H., Langmuir, D., 1985. Adsorption of uranyl onto ferric oxyhydroxides: Application of the surface complexation site-binding model. *Geochim. Cosmochim. Acta* 49, 1931–1941.
- Choppin, G.R., 1989. Soluble rare earth and actinide species in seawater. *Mar. Chem.* 28, 19–26.
- Choppin, G.R., 2006. Actinide speciation in aquatic systems. In: *Marine Chemistry*. pp. 83–92.
- Choppin, G.R., Wong, P.J., 1998. The chemistry of actinide behavior in marine systems. *Aquat. Geochemistry* 4, 77–101.
- Chorover, J., Choi, S., Rotenberg, P., Serne, R.J., Rivera, N., Strepka, C., Thompson, A., Mueller, K.T., O'day, P.A., 2008. Silicon control of strontium and cesium partitioning in hydroxide-weathered sediments.
- CK-12.org, 2016. *Biotechnology* | CK-12 Foundation [WWW Document]. URL <https://www.ck12.org/book/ck-12-biology/r44/section/8.3/> (accessed 4.23.20).
- Cl:Aire, 2004. Mine Water Treatment at Wheal Jane Tin Mine, Cornwall. *Case Study Bull.* 04 4, 1–4.
- Clark, D.L., David Hobart, I.E., Neda, M.P., 1995. Actinide Carbonate Complexes and Their Importance in Actinide Environmental Chemistry. *Chem. Rev* 95, 25–48.
- Clark, D.L., Janecky, D.R., Lane, L.J., 2006. Science-based cleanup of Rocky Flats. *Phys. Today* 59, 34–40.
- Clarke, T.A., Edwards, M.J., Gates, A.J., Hall, A., White, G.F., Bradley, J., Reardon, C.L., Shi, L., Beliaev, A.S., Marshall, M.J., Wang, Z., Watmough, N.J., Fredrickson, J.K., Zachara, J.M., Butt, J.N., Richardson, D.J., 2011. Structure of a bacterial cell surface decaheme electron conduit. *Proc. Natl. Acad. Sci. U. S. A.* 108, 9384–9.
- Cleary, A., 2018. Assessment of natural attenuation and targeted in-situ remediation of radioactively contaminated land.

- Cleary, A., Lloyd, J.R., Newsome, L., Shaw, S., Boothman, C., Boshoff, G., Atherton, N., Morris, K., 2019. Bioremediation of strontium and technetium contaminated groundwater using glycerol phosphate. *Chem. Geol.* 509, 213–222.
- Cohen, D., 1970. The preparation and spectrum of uranium(V) ions in aqueous solutions. *J. Inorg. Nucl. Chem.* 32, 3525–3530.
- Collins, R.N., Rosso, K.M., 2017. Mechanisms and Rates of U(VI) Reduction by Fe(II) in Homogeneous Aqueous Solution and the Role of U(V) Disproportionation. *J. Phys. Chem. A* 121, 6603–6613.
- Cologgi, D.L., Lampa-Pastirk, S., Speers, A.M., Kelly, S.D., Reguera, G., 2011. Extracellular reduction of uranium via *Geobacter* conductive pili as a protective cellular mechanism. *Proc. Natl. Acad. Sci. U. S. A.* 108, 15248–15252.
- Connolly, J., Kaufman, M., Rothman, A., Gupta, R., Redden, G., Schuster, M., Colwell, F., Gerlach, R., 2013. Construction of two ureolytic model organisms for the study of microbially induced calcium carbonate precipitation. *J. Microbiol. Methods* 94, 290–299.
- Conradson, S.D., Manara, D., Wastin, F., Clark, D.L., Lander, G.H., Morales, L.A., Rebizant, J., Rondinella, V. V, 2004. Local Structure and Charge Distribution in the UO₂–UO₄ System. *Inorg. Chem.* 43, 6922–6935.
- Converse, B.J., Wu, T., Findlay, R.H., Roden, E.E., 2013. U(VI) reduction in sulfate-reducing subsurface sediments amended with ethanol or acetate. *Appl. Environ. Microbiol.* 79, 4173–4177.
- Coursolle, D., Baron, D.B., Bond, D.R., Gralnick, J.A., 2010. The Mtr respiratory pathway is essential for reducing flavins and electrodes in *Shewanella oneidensis*. *J. Bacteriol.* 192, 467–474.
- Crane, R.A.A., Dickinson, M., Popescu, I.C.C., Scott, T.B.B., 2011. Magnetite and zero-valent iron nanoparticles for the remediation of uranium contaminated environmental water. *Water Res.* 45, 2931–2942.
- Crossland, I., 2012. *Nuclear Fuel Cycle Science and Engineering*, 1st ed. Woodhead Publishing Limited, Cambridge.
- Croudace, I.W., Rindby, A., Rothwell, R.G., 2006. ITRAX: Description and evaluation of a new multi-function X-ray core scanner. *Geol. Soc. Spec. Publ.* 267, 51–63.
- Cruickshank, J., 2012. The Sellafield Contaminated Land and Groundwater Management Project: Characterisation of a Complex Nuclear Facility, Workshop on “Radiological Characterisation for Decommissioning.”
- Cullity, B.D., 1978. *Elements of X-ray Diffraction*, 2nd ed, Elements of X-ray Diffraction. Addison-Wesley Publishing Company, Reading, Massachusetts, Massachusetts.
- Cuney, M., 2010. Evolution of uranium fractionation processes through time: Driving the secular variation of uranium deposit types. *Econ. Geol.* 105, 553–569.
- Cutting, R.S., Coker, V.S., Telling, N.D., Kimber, R.L., Pearce, C.I., Ellis, B.L., Lawson, R.S., van der Laan, G., Patrick, R.A.D., Vaughan, D.J., Arenholz, E., Lloyd, J.R., 2010. Optimizing Cr(VI) and Tc(VII) Remediation through Nanoscale Biomineral Engineering. *Environ. Sci. Technol.* 44, 2577–2584.
- Dar, M.A., Kaushik, G., Villareal Chiu, J.F., 2019. Pollution status and biodegradation of organophosphate pesticides in the environment. In: *Abatement of Environmental Pollutants: Trends and Strategies*. Elsevier, pp. 25–66.

- Davies, K.J., Sevanian, A., Muakkassah-Kelly, S.F., Hochstein, P., 1986. Uric acid-iron ion complexes. A new aspect of the antioxidant functions of uric acid. *Biochem. J.* 235, 747–54.
- Davis, J.A., Curtis, G.P., Wilkins, M.J., Kohler, M., Fox, P., Naftz, D.L., Lloyd, J.R., 2006. Processes affecting transport of uranium in a suboxic aquifer. *Phys. Chem. Earth* 31, 548–555.
- De Villiers, J.P.R., 1971. Crystal structures of aragonite, strontianite, and witherite. *Am. Mineral.* 56, 758–767.
- DEFRA, 2008. Managing Radioactive Waste Safely A Framework for Implementing Geological Disposal.
- Denning, R.G., 1992. Electronic Structure and Bonding in Actinyl Ions. *Struct. Bond.* 79, 215–276.
- Dent, A.J., Cibin, G., Ramos, S., Smith, A.D., Scott, S.M., Varandas, L., Pearson, M.R., Krumpa, N.A., Jones, C.P., Robbins, P.E., 2009. B18: A core XAS spectroscopy beamline for Diamond. *J. Phys. Conf. Ser.* 190, 012039.
- Dickinson, M., Scott, T.B., 2010. The application of zero-valent iron nanoparticles for the remediation of a uranium-contaminated waste effluent. *J. Hazard. Mater.* 178, 171–179.
- Dirkes, T., JP, P., RL, D., 2009. Hanford Site Environmental Report for Calendar Year 2008, PNNL-18427.
- Docrat, T.I., Mosselmans, J.F.W., Charnock, J.M., Whiteley, M.W., Collison, D., Livens, F.R., Jones, C., Edmiston, M.J., 1999. X-ray Absorption Spectroscopy of Tricarbonatodioxouranate(V), [UO₂(CO₃)₃]⁵⁻, in Aqueous Solution. *Inorg. Chem.* 38, 1879–1882.
- Doinikova, O.A., 2007. Uranium deposits with a new phosphate type of blacks. *Geol. Ore Depos.* 49, 80–86.
- Dong, L., Yang, J., Mou, Y., Sheng, G., Wang, L., Linghu, W., Asiri, A.M., Alamry, K.A., 2017. Effect of various environmental factors on the adsorption of U(VI) onto biochar derived from rice straw. *J. Radioanal. Nucl. Chem.* 314, 377–386.
- Doores, S., 2014. The genus *Sporolactobacillus*. In: *Lactic Acid Bacteria*. John Wiley & Sons, Ltd, Chichester, UK, pp. 543–553.
- Downward, L., Booth, C.H., Lukens, W.W., Bridges, F., Division, C.S., Berkeley, L., 2007. A Variation of the F- Test for Determining Statistical Relevance of Particular Parameters in EXAFS Fits. *X-Ray Absorpt. Fine Struct. - XAFS13 13th Int. Conf.* 882, 2–4.
- Dridi, B., Fardeau, M.L., Ollivier, B., Raoult, D., Drancourt, M., 2012. *Methanomassiliicoccus luminyensis* gen. nov., sp. nov., a methanogenic archaeon isolated from human faeces. *Int. J. Syst. Evol. Microbiol.* 62, 1902–1907.
- Duff, M.C., Coughlin, J.U., Hunter, D.B., 2002. Uranium co-precipitation with iron oxide minerals. *Geochim. Cosmochim. Acta* 66, 3533–3547.
- Dusausoy, Y., Ghermany, N.-E., Podor, R., Cuney, M., 1996. Low-temperature ordered phase of CaU(PO₄)₂: synthesis and crystal structure. *Eur. J. Mineral.* 8, 667–673.
- Dyer, A., Chow, J., Umar, I.M., 2000. The uptake of caesium and strontium radioisotopes onto clays. *J. Mater. Chem.* 10, 2734–2740.
- Dyer, A., James, N.U., Terrill, N.J., 1999. Uptake of cesium and strontium radioisotopes onto pillared clays. *J. Radioanal. Nucl. Chem.* 240, 589–592.

- Dyer, A., Umar, I.M., 1999. The uptake of radioisotopes onto clays and other natural materials. *J. Radioanal. Nucl. Chem.* 242, 329–333.
- Dzik, E.A., Lobeck, H.L., Zhang, L., Burns, P.C., 2017. Thermodynamic properties of phosphate members of the meta-autunite group: A high-temperature calorimetric study. *J. Chem. Thermodyn.* 114, 165–171.
- Edgar, R.C., 2010. Search and clustering orders of magnitude faster than BLAST. *Bioinformatics* 26, 2460–2461.
- Edgar, R.C., 2013. UPARSE: Highly accurate OTU sequences from microbial amplicon reads. *Nat. Methods* 10, 996–998.
- Edwards, M.J., Baiden, N.A., Johs, A., Tomanicek, S.J., Liang, L., Shi, L., Fredrickson, J.K., Zachara, J.M., Gates, A.J., Butt, J.N., Richardson, D.J., Clarke, T.A., 2014. The X-ray crystal structure of *Shewanella oneidensis* OmcA reveals new insight at the microbe-mineral interface. *FEBS Lett.* 588, 1886–1890.
- Edwards, M.J., White, G.F., Norman, M., Tome-Fernandez, A., Ainsworth, E., Shi, L., Fredrickson, J.K., Zachara, J.M., Butt, J.N., Richardson, D.J., Clarke, T.A., 2015. Redox linked flavin sites in extracellular decaheme proteins involved in microbe-mineral electron transfer. *Sci. Rep.* 5: 11677, 1–11.
- Efecan, N., Shahwan, T., Eroğlu, A.E., Lieberwirth, I., 2009. *Desalination* 249, 1048–1054.
- Ekstrom, A., 1974. Kinetics and mechanism of the disproportionation of uranium(V). *Inorg. Chem.* 13, 2237–2241.
- El-Megharbel, S.M., El-Metwaly, N.M., Refat, M.S., 2015. Synthesis of uranyl(II), vanadyl(II) and zirconyl urate complexes, spectral, thermal and biological studies. *Spectrochim. Acta - Part A Mol. Biomol. Spectrosc.* 149, 263–270.
- Elderfield, H., 1996. A biomineralization model for the incorporation of trace elements into foraminiferal calcium carbonate. *Earth Planet. Sci. Lett.* 142, 409–423.
- Faizova, R., Scopelliti, R., Chauvin, A.-S., Mazzanti, M., 2018. Synthesis and Characterization of a Water Stable Uranyl(V) Complex. *J. Am. Chem. Soc.* 140, 13554–13557.
- Farrell, J., Bostick, W.D., Jarabek, R.J., Fiedor, J.N., 1999. Uranium removal from ground water using zero valent iron media. *Ground Water* 37, 618–624.
- Faybishenko, B., Hazen, T.C., Long, P.E., Brodie, E.L., Conrad, M.E., Hubbard, S.S., Christensen, J.N., Joyner, D., Borglin, S.E., Chakraborty, R., Williams, K.H., Peterson, J.E., Chen, J., Brown, S.T., Tokunaga, T.K., Wan, J., Firestone, M., Newcomer, D.R., Resch, C.T., Cantrell, K.J., Willett, A., Koenigsberg, S., 2008. In situ long-term reductive bioimmobilization of Cr(VI) in groundwater using hydrogen release compound. *Environ. Sci. Technol.* 42, 8478–8485.
- Feiveson, H., Mian, Z., Ramana, M.V., von Hippel, F., 2011. Spent Fuel from Nuclear Power Reactors: An Overview of a New Study by the International Panel on Fissile Materials. *Int. Panel Fissile Mater.* 1–21.
- Ferris, F.G., Fratton, C.M., Gerits, J.P., Schultze-Lam, S., Lollar, B.S., 1995. Microbial precipitation of a strontium calcite phase at a groundwater discharge zone near rock Creek, British Columbia, Canada. *Geomicrobiol. J.* 13, 57–67.

- Fields, M.W., Yan, T., Rhee, S.K., Carroll, S.L., Jardine, P.M., Watson, D.B., Criddle, C.S., Zhou, J., 2005. Impacts on microbial communities and cultivable isolates from groundwater contaminated with high levels of nitric acid-uranium waste. *FEMS Microbiol. Ecol.* 53, 417–428.
- Finch, R., Murakami, T., 1999. Uranium: Mineralogy, Geochemistry and the Environment. In: Burns, P.C., Finch, R.J. (Eds.), *Reviews in Mineralogy Volume 38*. Golden, pp. 91–179.
- Finneran, K.T., Housewright, M.E., Lovley, D.R., 2002. Multiple influences of nitrate on uranium solubility during bioremediation of uranium-contaminated subsurface sediments. *Environ. Microbiol.* 4, 510–516.
- Fletcher, K.E., Boyanov, M.I., Thomas, S.H., Wu, Q., Kemner, K.M., Löffler, F.E., 2010. U(VI) reduction to mononuclear U(IV) by desulfitobacterium species. *Environ. Sci. Technol.* 44, 4705–4709.
- Foster, A.W., Dainty, S.J., Patterson, C.J., Pohl, E., Blackburn, H., Wilson, C., Hess, C.R., Rutherford, J.C., Quaranta, L., Corran, A., Robinson, N.J., 2014. A chemical potentiator of copper-accumulation used to investigate the iron-regulons of *Saccharomyces cerevisiae*. *Mol. Microbiol.* 93, 317–330.
- Foster, L., Boothman, C., Ruiz-Lopez, S., Boshoff, G., Jenkinson, P., Sigeo, D., Pittman, J.K., Morris, K., Lloyd, J.R., 2020. Microbial bloom formation in a high pH spent nuclear fuel pond. *Sci. Total Environ.* 720, 137515.
- Francis, A.J., Dodge, C.J., Lu, F., Halada, G.P., Clayton, C.R., 1994. XPS and XANES Studies of Uranium Reduction by *Clostridium* sp. *Society* 28, 11973–11973.
- Fredrickson, J.K., Romine, M.F., Beliaev, A.S., Auchtung, J.M., Driscoll, M.E., Gardner, T.S., Nealson, K.H., Osterman, A.L., Pinchuk, G., Reed, J.L., Rodionov, D.A., Rodrigues, J.L.M., Saffarini, D.A., Serres, M.H., Spormann, A.M., Zhulin, I.B., Tiedje, J.M., 2008. Towards environmental systems biology of *Shewanella*. *Nat. Rev. Microbiol.* 6, 592–603.
- Fredrickson, J.K., Zachara, J.M., Kennedy, D.W., Kukkadapu, R.K., McKinley, J.P., Heald, S.M., Liu, C., Plymale, A.E., 2004. Reduction of TcO_4^- by sediment-associated biogenic Fe(II). *Geochim. Cosmochim. Acta* 68, 3171–3187.
- Fujita, Y., Ferris, F.G., Lawson, R.D., Colwell, F.S., Smith, R.W., 2000. Calcium Carbonate Precipitation by Ureolytic Subsurface Bacteria. *Geomicrobiol. J.* 17, 305–318.
- Fujita, Y., Redden, G.D., Ingram, J.C., Cortez, M.M., Ferris, F.G., Smith, R.W., 2004. Strontium incorporation into calcite generated by bacterial ureolysis. *Geochim. Cosmochim. Acta* 68, 3261–3270.
- Fujita, Y., Taylor, J.L., Wendt, L.M., Reed, D.W., Smith, R.W., 2010. Evaluating the potential of native ureolytic microbes to remediate a ^{90}Sr contaminated environment. *Environ. Sci. Technol.* 44, 7652–7658.
- Fuller, A.J., Shaw, S., Peacock, C.L., Trivedi, D., Burke, I.T., 2016. EXAFS Study of Sr sorption to Illite, Goethite, Chlorite, and Mixed Sediment under Hyperalkaline Conditions. *Langmuir* 32, 2937–2946.
- Fuller, A.J., Shaw, S., Ward, M.B., Haigh, S.J., Mosselmans, J.F.W., Peacock, C.L., Stackhouse, S., Dent, A.J., Trivedi, D., Burke, I.T., 2015. Caesium incorporation and retention in illite interlayers. *Appl. Clay Sci.* 108, 128–134.
- Fuller, C.C., Bargar, J.R., Davis, J.A., Piana, M.J., 2002. Mechanisms of uranium interactions with hydroxyapatite: implications for groundwater remediation. *Environ. Sci. Technol.* 36, 158–65.

- Gabitov, R.I., Watson, E.B., 2006. Partitioning of strontium between calcite and fluid. *Geochemistry, Geophys. Geosystems* 7.
- Gao, Y., Shao, Z., Xiao, Z., 2015. U(VI) sorption on illite: effect of pH, ionic strength, humic acid and temperature. *J. Radioanal. Nucl. Chem.* 303, 867–876.
- Giammar, D.E., Catalano, J.G., Mehta, V.S., Maillot, F., Wang, Z., 2014. Transport of U(VI) through sediments amended with phosphate to induce in situ uranium immobilization. *Water Res.* 69, 307–317.
- Ginder-Vogel, M., Criddle, C.S., Fendorf, S., 2006. Thermodynamic constraints on the oxidation of biogenic UO₂ by Fe(III) (Hydr)oxides. *Environ. Sci. Technol.* 40, 3544–3550.
- Ginder-Vogel, M., Fendorf, S., 2007. Chapter 11 Biogeochemical Uranium Redox Transformations: Potential Oxidants of Uraninite. In: *Developments in Earth and Environmental Sciences*. pp. 293–319.
- Ginder-Vogel, M., Stewart, B., Fendorf, S., 2010. Kinetic and mechanistic constraints on the oxidation of biogenic uraninite by ferrihydrite. *Environ. Sci. Technol.* 44, 163–169.
- Goodwin, C.A.P., Chilton, N.F., Vettese, G.F., Moreno Pineda, E., Crowe, I.F., Ziller, J.W., Winpenny, R.E.P., Evans, W.J., Mills, D.P., 2016. Physicochemical Properties of Near-Linear Lanthanide(II) Bis(silylamide) Complexes (Ln = Sm, Eu, Tm, Yb). *Inorg. Chem.* 55, 10057–10067.
- Goodwin, C.A.P., Réant, B.L.L., Vettese, G.F., Kragoskow, J.G.C., Giansiracusa, M.J., DiMucci, I.M., Lancaster, K.M., Mills, D.P., Sproules, S., 2020. Heteroleptic Samarium(III) Chalcogenide Complexes: Opportunities for Giant Exchange Coupling in Bridging σ - and π -Radical Lanthanide Dichalcogenides. *Inorg. Chem.* [acs.inorgchem.0c00470](https://doi.org/10.1021/acs.inorgchem.0c00470).
- Gorby, Y.A., Lovley, D.R., 1992. Enzymic uranium precipitation. *Environ. Sci. Technol.* 26, 205–207.
- Gorlas, A., Robert, C., Gimenez, G., Drancourt, M., Raoult, D., 2012. Complete genome sequence of *Methanomassiliicoccus luminyensis*, the largest genome of a human-associated Archaea species. *J. Bacteriol.*
- Green, S.J., Taillefert, M., Webb, S.M., Salome, K.R., Kostka, J.E., Beazley, M.J., 2013. The role of anaerobic respiration in the immobilization of uranium through biomineralization of phosphate minerals. *Geochim. Cosmochim. Acta* 106, 344–363.
- Grenthe, I., Fuger, J., Lemire, R.J., Muller, A.B., Wanner, H., Forest, I., 1992. *Chemical Thermodynamics of Uranium*. 1992 715.
- Grossmann, K., Arnold, T., Ikeda-Ohno, A., Steudtner, R., Geipel, G., Bernhard, G., 2009. Fluorescence properties of a uranyl(V)-carbonate species [U(V)O₂(CO₃)₃]⁵⁻ at low temperature. *Spectrochim. Acta - Part A Mol. Biomol. Spectrosc.* 72, 449–453.
- Gu, B., Wu, W.M., Ginder-Vogel, M.A., Yan, H., Fields, M.W., Zhou, J., Fendorf, S., Criddle, C.S., Jardine, P.M., 2005. Bioreduction of uranium in a contaminated soil column. *Environ. Sci. Technol.* 39, 4841–4847.
- Guo, Z., Li, Y., Wu, W., 2009. Sorption of U(VI) on goethite: Effects of pH, ionic strength, phosphate, carbonate and fulvic acid. *Appl. Radiat. Isot.*
- Haas, B.J., Gevers, D., Earl, A.M., Feldgarden, M., Ward, D. V., Giannoukos, G., Ciulla, D., Tabbaa, D., Highlander, S.K., Sodergren, E., Methé, B., DeSantis, T.Z., Petrosino, J.F., Knight, R., Birren, B.W.,

2011. Chimeric 16S rRNA sequence formation and detection in Sanger and 454-pyrosequenced PCR amplicons. *Genome Res.* 21, 494–504.
- Hafenbradl, D., Jannasch, H.W., Stetter, K.O., Blöchl, E., Rachel, R., Burggraf, S., 1997. *Pyrolobus fumarii*, gen. and sp. nov., represents a novel group of archaea, extending the upper temperature limit for life to 113°C. *Extremophiles* 1, 14–21.
- Han, B., Zhang, E., Cheng, G., Zhang, L., Wang, D., Wang, X., 2018. Hydrothermal carbon superstructures enriched with carboxyl groups for highly efficient uranium removal. *Chem. Eng. J.* 338, 734–744.
- Handley-Sidhu, S., Hriljac, J.A., Cuthbert, M.O., Renshaw, J.C., Patrick, R.A.D., Charnock, J.M., Stolpe, B., Lead, J.R., Baker, S., Macaskie, L.E., 2014. Bacterially produced calcium phosphate nanobiominerals: Sorption capacity, site preferences, and stability of captured radionuclides. *Environ. Sci. Technol.* 48, 6891–6898.
- Handley-Sidhu, S., Renshaw, J.C., Moriyama, S., Stolpe, B., Mennan, C., Bagheriasl, S., Yong, P., Stamboulis, A., Paterson-Beedle, M., Sasaki, K., Patrick, R.A.D., Lead, J.R., Macaskie, L.E., 2011. Uptake of Sr²⁺ and Co²⁺ into Biogenic Hydroxyapatite: Implications for Biomineral Ion Exchange Synthesis. *Environ. Sci. Technol.* 45, 6985–6990.
- Harder, E.C., 1919. Iron-depositing bacteria and their geologic relations. In: U.S. Geological Survey. Government Printing Office, Washington.
- Harris, S.J., Mortimer, R.J.G., 2002. Determination of nitrate in small water samples (100 µL) by the cadmium-copper reduction method: A manual technique with application to the interstitial waters of marine sediments. *Int. J. Environ. Anal. Chem.* 82, 369–376.
- Harvard College Review, 2015. How Does Nuclear Energy Work?: A brief scientific introduction | Harvard College Review of Environment and Society [WWW Document]. URL <http://www.hcs.harvard.edu/~res/2015/06/how-does-nuclear-energy-work-a-brief-scientific-introduction/> (accessed 2.7.19).
- Harwood, C.S., Gibson, J., 1997. Shedding light on anaerobic benzene ring degradation: a process unique to prokaryotes? *J. Bacteriol.* 179, 301–9.
- Heidelberg, J.F., Paulsen, I.T., Nelson, K.E., Gaidos, E.J., Nelson, W.C., Read, T.D., Eisen, J.A., Seshadri, R., Ward, N., Methe, B., Clayton, R.A., Meyer, T., Tsapin, A., Scott, J., Beanan, M., Brinkac, L., Daugherty, S., DeBoy, R.T., Dodson, R.J., Durkin, A.S., Haft, D.H., Kolonay, J.F., Madupu, R., Peterson, J.D., Umayam, L.A., White, O., Wolf, A.M., Vamathevan, J., Weidman, J., Impraim, M., Lee, K., Berry, K., Lee, C., Mueller, J., Khouri, H., Gill, J., Utterback, T.R., McDonald, L.A., Feldblyum, T. V., Smith, H.O., Venter, J.C., Nealson, K.H., Fraser, C.M., 2002. Genome sequence of the dissimilatory metal ion-reducing bacterium *Shewanella oneidensis*. *Nat. Biotechnol.* 20, 1118–1123.
- Hennig, C., Ikeda-Ohno, A., Emmerling, F., Kraus, W., Bernhard, G., 2010. Comparative investigation of the solution species [U(CO₃)₅]⁶⁻ and the crystal structure of Na₆[U(CO₃)₅]·12H₂O. *Dalt. Trans.* 39, 3744–3750.
- Hennig, C., Schmeide, K., Brendler, V., Moll, H., Tsushima, S., Scheinost, A.C., 2007. EXAFS investigation of U(VI), U(IV), and Th(IV) sulfato complexes in aqueous solution. *Inorg. Chem.* 46, 5882–5892.
- Higgo, J.J.W., 1987. CLAY AS A BARRIER TO RADIONUCLIDE MIGRATION. *Prog. Nucl. Energy* 1987, 173–207.

- Housecroft, Catherine E.; Sharpe, A.G., 2012. *Inorganic Chemistry*, Fourth. ed. Pearson Education Limited, Harlow.
- Huh, N.W., Berkowitz, P., Hiskey, R.G., Pedersen, L.G., 1991. Determination of strontium binding to macromolecules. *Anal. Biochem.* 198, 391–393.
- Hussain, S.A., Demirci, Ş., Özbayoğlu, G., 1996. Zeta Potential Measurements on Three Clays from Turkey and Effects of Clays on Coal Flotation. *J. Colloid Interface Sci.* 184, 535–541.
- Hutchins, S.R., Davidson, M.S., Brierley, J.A., Brierley, C.L., 1986. MICROORGANISMS IN RECLAMATION OF METALS. *Ann. Rev. Microb.* 40, 311–36.
- Hyun, S.P., Davis, J.A., Hayes, K.F., 2014. Abiotic U(VI) reduction by aqueous sulfide. *Appl. Geochemistry* 50, 7–15.
- IAEA, 2020. PRIS - Home [WWW Document]. URL <https://pris.iaea.org/PRIS/home.aspx> (accessed 2.3.20).
- Ikeda, A., Hennig, C., Tsushima, S., Takao, K., Ikeda, Y., Scheinost, A.C., Bernhard, G., 2007. Comparative study of uranyl(VI) and -(V) carbonate complexes in an aqueous solution. *Inorg. Chem.* 46, 4212–4219.
- Ilton, E.S., Bagus, P.S., 2011. XPS determination of uranium oxidation states. *Surf. Interface Anal.* 43, 1549–1560.
- Ilton, E.S., Haiduc, A., Cahill, C.L., Felmyt, A.R., 2005. Mica surfaces stabilize pentavalent uranium. *Inorg. Chem.* 44, 2986–2988.
- Ilton, E.S., Haiduc, A., Moses, C.O., Heald, S.M., Elbert, D.C., Veblen, D.R., 2004. Heterogeneous reduction of uranyl by micas: Crystal chemical and solution controls. *Geochim. Cosmochim. Acta* 68, 2417–2435.
- Institute for Energy and Environmental Research [WWW Document], n.d. . 2020. URL <http://ieer.org/> (accessed 4.28.17).
- International Atomic Energy Agency, 2005. *Country Nuclear Fuel Cycle Profiles*, 2nd ed. Vienna.
- IPCC, 2014. *Climate Change 2014: Synthesis Report. Contribution of Working Groups I, II and III to the Fifth Assessment Report of the Intergovernmental Panel on Climate Change*. Gian-Kasper Plattner, Geneva, Switzerland, Switzerland.
- Islam, F.S., Gault, A.G., Boothman, C., Polya, D.A., Chamok, J.M., Chatterjee, D., Lloyd, J.R., 2004. Role of metal-reducing bacteria in arsenic release from Bengal delta sediments. *Nature* 430, 68–71.
- Istok, J.D., Park, M., McKay, L.D., Watson, D.B., Hazen, T.C., Jagadamma, S., Paradis, C.J., 2016. In situ mobility of uranium in the presence of nitrate following sulfate-reducing conditions. *J. Contam. Hydrol.* 187, 55–64.
- Istok, J.D., Senko, J.M., Krumholz, L.R., Watson, D., Bogle, M.A., Peacock, A., Chang, Y.J., White, D.C., 2004. In Situ Bioreduction of Technetium and Uranium in a Nitrate-Contaminated Aquifer. *Environ. Sci. Technol.* 38, 468–475.
- James T. Nurmi, †, Paul G. Tratnyek, *†, Vaishnavi Sarathy, †, Donald R. Baer, ‡, James E. Amonette, ‡, Klaus Pecher, ‡, Chongmin Wang, ‡, John C. Linehan, ‡, Dean W. Matson, ‡, R. Lee Penn, § and, Driessen§, M.D., 2004. Characterization and Properties of Metallic Iron Nanoparticles: Spectroscopy, Electrochemistry, and Kinetics.

- Jang, J., Miran, W., Divine, S.D., Nawaz, M., Shahzad, A., Woo, S.H., Lee, D.S., 2018. Rice straw-based biochar beads for the removal of radioactive strontium from aqueous solution. *Sci. Total Environ.* 615, 698–707.
- JCVI: Home [WWW Document], n.d. URL <http://www.jcvi.org/cms/home/> (accessed 4.28.17).
- Jenkins, R., 1999. *X-Ray Fluorescence Spectrometry*. John Wiley & Sons, Inc., NJ, USA.
- Jensen, K.A., Palenik, C.S., Ewing, R.C., 2002. U6+ phases in the weathering zone of the Bangombé U-deposit: Observed and predicted mineralogy. In: *Radiochimica Acta*. pp. 761–769.
- Jensen, M.L., 1958. Sulfur isotopes and the origin of sandstone-type uranium deposits. *Econ. Geol.* 53, 598–616.
- Jensen, S.E., Nonbol, E., 1998. *Nordic nuclear safety research Description of the Magnox Type of Gas Cooled Reactor (MAGNOX)*. Roskilde, Denmark.
- Jerden, J.L., Sinha, A.K., 2003. Phosphate based immobilization of uranium in an oxidizing bedrock aquifer. *Appl. Geochemistry* 18, 823–843.
- Jin, J., Li, S., Peng, X., Liu, W., Zhang, C., Yang, Y., Han, L., Du, Z., Sun, K., Wang, X., 2018. HNO₃ modified biochars for uranium (VI) removal from aqueous solution. *Bioresour. Technol.* 256, 247–253.
- Johnson, D.A., Florence, T.M., 1971. Spectrophotometric determination of uranium(vi) with 2-(5-bromo-2-pyridylazo)-5-diethylaminophenol. *Anal. Chim. Acta* 53, 73–79.
- Jones, D.L., Andrews, M.B., Swinburne, A.N., Botchway, S.W., Ward, A.D., Lloyd, J.R., Natrajan, L.S., 2015. Fluorescence spectroscopy and microscopy as tools for monitoring redox transformations of uranium in biological systems. *Chem. Sci.* 6, 5133–5138.
- Joshi, N., Fass, J., 2011. Sickel: A sliding-window, adaptive, quality-based trimming tool for FastQ files (Version 1.33) [WWW Document]. URL <https://github.com/najoshi/sickle>
- Joshi, N., Liu, F., Watts, M.P., Williams, H., Coker, V.S., Schmid, D., Hofmann, T., Lloyd, J.R., 2018. Optimising the transport properties and reactivity of microbially-synthesised magnetite for in situ remediation. *Sci. Rep.* 8, 4246.
- Kaçan, E., Kütahyalı, C., 2012. Adsorption of strontium from aqueous solution using activated carbon produced from textile sewage sludges. *J. Anal. Appl. Pyrolysis* 97, 149–157.
- Karasyova, O.N., Ivanova, L.I., Lakshtanov, L.Z., Lövgren, L., 1999. Strontium sorption on hematite at elevated temperatures. *J. Colloid Interface Sci.* 220, 419–428.
- Kärnbränslehantering, S., 2019. *Äspö Hard Rock Laboratory Annual Report 2017*.
- Katsenovich, Y.P., Carvajal, D.A., Wellman, D.M., Lagos, L.E., 2012. Enhanced U(VI) release from autunite mineral by aerobic *Arthrobacter* sp. in the presence of aqueous bicarbonate. *Chem. Geol.* 308–309, 1–9.
- Kemmler, S., 1965. Zur Kristallstruktur von LiUO₃. *Zeitschrift für Anorg. und Allg. Chemie* 338, 9–14.
- Kerisit, S., Bylaska, E.J., Massey, M.S., McBriarty, M.E., Ilton, E.S., 2016. Ab initio molecular dynamics of uranium incorporated in goethite (α -FeOOH): Interpretation of X-ray absorption spectroscopy of trace polyvalent metals. *Inorg. Chem.* 55, 11736–11746.
- Khan, R., Patel, V., Khan, Z., 2019. *Bioremediation of dyes from textile and dye manufacturing industry*

- effluent. In: *Abatement of Environmental Pollutants: Trends and Strategies*. Elsevier, pp. 107–125.
- Khijniak, T. V, Slobodkin, A.I., Coker, V., Renshaw, J.C., Livens, F.R., Bonch-Osmolovskaya, E.A., Birkeland, N.K., Medvedeva-Lyalikova, N.N., Lloyd, J.R., 2005. Reduction of uranium(VI) phosphate during growth of the thermophilic bacterium *Thermoterrabacterium ferrireducens*. *Appl. Environ. Microbiol.* 71, 6423–6426.
- Kierkegaard, P., Parck, C., Ulfvarson, U., Stenhagen, E., Thorell, B., 1956. The Crystal Structure of $U(SO_4)_2 \cdot 4H_2O$. *Acta Chem. Scand.* 10, 599–616.
- Knorst, M.T., Neubert, R., Wohlrab, W., 1997. Analytical methods for measuring urea in pharmaceutical formulations. *J. Pharm. Biomed. Anal.* 15, 1627–1632.
- Kodama, T., Harada, Y., Ueda, M., Shimizu, K.I., Shuto, K., Komarneni, S., 2001. Selective exchange and fixation of strontium ions with ultrafine Na-4-mica. *Langmuir* 17, 4881–4886.
- Komlos, J., Moon, H.S., Jaffé, P.R., 2008a. Effect of sulfate on the simultaneous bioreduction of iron and uranium. *J. Environ. Qual.* 37, 2058–2062.
- Komlos, J., Peacock, A., Kukkadapu, R.K., Jaffé, P.R., 2008b. Long-term dynamics of uranium reduction/reoxidation under low sulfate conditions. *Geochim. Cosmochim. Acta* 72, 3603–3615.
- Kotloski, N.J., Gralnick, J.A., 2013. Flavin electron shuttles dominate extracellular electron transfer by *Shewanella oneidensis*. *MBio* 4, 10–13.
- Kozich, J.J., Westcott, S.L., Baxter, N.T., Highlander, S.K., Schloss, P.D., 2013. Development of a dual-index sequencing strategy and curation pipeline for analyzing amplicon sequence data on the miseq illumina sequencing platform. *Appl. Environ. Microbiol.* 79, 5112–5120.
- Krejci, M.R., Finney, L., Vogt, S., Joester, D., 2011. Selective sequestration of strontium in desmid green algae by biogenic co-precipitation with barite. *ChemSusChem* 4, 470–473.
- Krestou, C.A., Panias, D., 2004. Uranium (VI) speciation diagrams in the $UO_2^{2+}/CO_3^{2-}/H_2O$ system at 25. *Eur. J. Miner. Process. Environ. Prot.* 4, 1303–868.
- Kuipers, G., Boothman, C., Bagshaw, H., Beard, R., Bryan, N.D., Lloyd, J.R., 2019. Microbial reduction of Fe(III) coupled to the biodegradation of isosaccharinic acid (ISA). *Appl. Geochemistry* 109, 104399.
- Kumar, N., Auffan, M., Gattacceca, J., Rose, J., Olivi, L., Borschneck, D., Kvapil, P., Jublot, M., Kaifas, D., Malleret, L., Doumenq, P., Bottero, J.Y., 2014a. Molecular insights of oxidation process of iron nanoparticles: Spectroscopic, magnetic, and microscopic evidence. *Environ. Sci. Technol.* 48, 13888–13894.
- Kumar, N., Omoregie, E.O., Rose, J., Masion, A., Lloyd, J.R., Diels, L., Bastiaens, L., 2014b. Inhibition of sulfate reducing bacteria in aquifer sediment by iron nanoparticles. *Water Res.* 51, 64–72.
- Kumar, S., Loganathan, V.A., Gupta, R.B., Barnett, M.O., 2011. An Assessment of U(VI) removal from groundwater using biochar produced from hydrothermal carbonization. *J. Environ. Manage.* 92, 2504–2512.
- Kütahyalı, C., Eral, M., 2004. Selective adsorption of uranium from aqueous solutions using activated carbon prepared from charcoal by chemical activation. *Sep. Purif. Technol.* 40, 109–114.
- Kvashnina, K.O., Butorin, S.M., Martin, P., Glatzel, P., 2013. Chemical state of complex uranium oxides.

Phys. Rev. Lett. 111.

- Lamm, D., Van der Meijden, A.P.M., Morales, A., S.A., B., W.J., C., H.W., H., M.S., S., A., S., F.M.J., D., 1992. Incidence and treatment of complications of bacillus Calmette-Guerin intravesical therapy in superficial bladder cancer. *J. Urol.*
- Langmuir, D., 1978. Uranium solution-mineral equilibria at low temperatures with applications to sedimentary ore deposits. *Geochim. Cosmochim. Acta* 42, 547–569.
- Latta, D.E., Boyanov, M.I., Kemner, K.M., O’Loughlin, E.J., Scherer, M.M., 2012a. Abiotic reduction of uranium by Fe(II) in soil. *Appl. Geochemistry* 27, 1512–1524.
- Latta, D.E., Gorski, C.A., Boyanov, M.I., O’Loughlin, E.J., Kemner, K.M., Scherer, M.M., 2012b. Influence of magnetite stoichiometry on U VI reduction. *Environ. Sci. Technol.* 46, 778–786.
- Latta, D.E., Kemner, K.M., Mishra, B., Boyanov, M.I., 2016. Effects of calcium and phosphate on uranium(IV) oxidation: Comparison between nanoparticulate uraninite and amorphous UIV-phosphate. *Geochim. Cosmochim. Acta* 174, 122–142.
- Law, G.T.W., Geissler, A., Burke, I.T., Livens, F.R., Lloyd, J.R., McBeth, J.M., Morris, K., 2011. Uranium redox cycling in sediment and biomineral systems. *Geomicrobiol. J.* 28, 497–506.
- Law, Geissler, A., Boothman, C., Burke, I.T., Livens, F.R., Lloyd, J.R., Morris, K., 2010a. Role of nitrate in conditioning aquifer sediments for technetium bioreduction. *Environ. Sci. Technol.* 44, 150–155.
- Law, Geissler, A., Lloyd, J.R., Livens, F.R., Boothman, C., Begg, J.D.C., Denecke, M.A., Rothe, J., Dardenne, K., Burke, I.T., Charnock, J.M., Morris, K., 2010b. Geomicrobiological redox cycling of the transuranic element neptunium. *Environ. Sci. Technol.* 44, 8924–8929.
- Law, N., Ansari, S., Livens, F.R., Renshaw, J.C., Lloyd, J.R., 2008. Formation of nanoscale elemental silver particles via enzymatic reduction by *Geobacter sulfurreducens*. *Appl. Environ. Microbiol.* 74, 7090–7093.
- Ledyard, K.M., Butler, A., 1997. Structure of putrebactin, a new dihydroxamate siderophore produced by *Shewanella putrefaciens*. *J. Biol. Inorg. Chem.* 2, 93–97.
- Lewis, J., Sjöstrom, J., 2010. Optimizing the experimental design of soil columns in saturated and unsaturated transport experiments. *J. Contam. Hydrol.*
- Lewis, W.B., Hecht, H.G., Eastman, M.P., 1973. Electron Paramagnetic Resonance and Optical Studies of Pentavalent Uranium¹. *Inorg. Chem.* 12, 1634–1639.
- Li, W., Beard, B.L., Johnson, C.M., 2015. Biologically recycled continental iron is a major component in banded iron formations. *Proc. Natl. Acad. Sci. U. S. A.* 112, 8193–8.
- Li, X., Elliott, D.W., Zhang, W., 2006. Zero-Valent Iron Nanoparticles for Abatement of Environmental Pollutants: Materials and Engineering Aspects. *Crit. Rev. Solid State Mater. Sci.* 31, 111–122.
- Li, X., Krumholz, L.R., 2008. Influence of Nitrate on Microbial Reduction of Per technetate. *Environ. Sci. Technol.* 42, 1910–1915.
- Lino, T., Mori, K., Uchino, Y., Nakagawa, T., Harayama, S., Suzuki, K.I., 2010. *Ignavibacterium album* gen. nov., sp. nov., a moderately thermophilic anaerobic bacterium isolated from microbial mats at a terrestrial hot spring and proposal of *Ignavibacteria* classis nov., for a novel lineage at the periphery of green sulfur bacteria. *Int. J. Syst. Evol. Microbiol.* 60, 1376–1382.

- Littlewood, J.L., Shaw, S., Peacock, C.L., Bots, P., Trivedi, D., Burke, I.T., 2017. Mechanism of Enhanced Strontium Uptake into Calcite via an Amorphous Calcium Carbonate Crystallization Pathway 17, 1214–1223.
- Liu, A., Liu, J., Pan, B., Zhang, W.X., 2014. Formation of lepidocrocite (γ -FeOOH) from oxidation of nanoscale zero-valent iron (nZVI) in oxygenated water. *RSC Adv.* 4, 57377–57382.
- Liu, C., Gorby, Y.A., Zachara, J.M., Fredrickson, J.K., Brown, C.F., 2002. Reduction kinetics of Fe(III), Co(III), U(VI), Cr(VI), and Tc(VII) in cultures of dissimilatory metal-reducing bacteria. *Biotechnol. Bioeng.* 80, 637–649.
- Liu, H., Ramnarayanan, R., Logan, B.E., 2004. Production of Electricity during Wastewater Treatment Using a Single Chamber Microbial Fuel Cell. *Environ. Sci. Technol.* 38, 2281–2285.
- Liu, Z., Frigaard, N.U., Vogl, K., Iino, T., Ohkuma, M., Overmann, J., Bryant, D.A., 2012. Complete genome of *Ignavibacterium album*, a metabolically versatile, flagellated, facultative anaerobe from the phylum Chlorobi. *Front. Microbiol.* 3, 185.
- Lloyd, J.R., 2003. Microbial reduction of metals and radionuclides. *FEMS Microbiol. Rev.* 27, 411–425.
- Lloyd, J.R., Macaskie, L.E., 1996. A novel PhosphorImager-based technique for monitoring the microbial reduction of technetium. *Appl. Environ. Microbiol.* 62, 578–582.
- Lorens, R.B., 1981. Sr, Cd, Mn and Co distribution coefficients in calcite as a function of calcite precipitation rate. *Geochim. Cosmochim. Acta* 45, 553–561.
- Lovley, D.R., 2006. Bug juice: harvesting electricity with microorganisms. *Nat. Rev. Microbiol.* 4, 497–508.
- Lovley, D.R., Coates, J.D., Blunt-Harris, E.L., Phillips, E.J.P., Woodward, J.C., 1996. Humic substances as electron acceptors for microbial respiration. *Nature* 382, 445–448.
- Lovley, D.R., Fraga, J.L., Blunt-Harris, E.L., Hayes, L.A., Phillips, E.J.P., Coates, J.D., 1998. Humic substances as a mediator for microbially catalyzed metal reduction. *Acta Hydrochim. Hydrobiol.* 26, 152–157.
- Lovley, D.R., Giovannoni, S.J., White, D.C., Champine, J.E., Phillips, E.J.P., Gorby, Y.A., Goodwin, S., 1993. *Geobacter metallireducens* gen. nov. sp. nov., a microorganism capable of coupling the complete oxidation of organic compounds to the reduction of iron and other metals. *Arch. Microbiol.* 159, 336–344.
- Lovley, D.R., Holmes, D.E., Nevin, K.P., 2004. Dissimilatory Fe(III) and Mn(IV) reduction, *Advances in Microbial Physiology*.
- Lovley, D.R., Phillips, E.J., 1987. Rapid assay for microbially reducible ferric iron in aquatic sediments. *Appl. Environ. Microbiol.* 53, 1536–40.
- Lovley, D.R., Phillips, E.J., 1992. Reduction of uranium by *Desulfovibrio desulfuricans*. *Appl. Environ. Microbiol.* 58, 850–6.
- Lovley, D.R., Phillips, E.J., 1994. Novel processes for anaerobic sulfate production from elemental sulfur by sulfate-reducing bacteria. *Appl. Environ. Microbiol.* 60, 2394–9.
- Lovley, D.R., Phillips, E.J., Lonergan, D.J., 1989. Hydrogen and Formate Oxidation Coupled to Dissimilatory Reduction of Iron or Manganese by *Alteromonas putrefaciens*. *Appl. Environ. Microbiol.* 55, 700–6.

- Lovley, D.R., Phillips, E.J.P., 1988. Novel Mode of Microbial Energy Metabolism: Organic Carbon Oxidation Coupled to Dissimilatory Reduction of Iron or Manganese. *Appl. Envir. Microbiol.* 54, 1472–1480.
- Lovley, D.R., Phillips, E.J.P., 1992. Bioremediation of uranium contamination with enzymatic uranium reduction. *Environ. Sci. Technol.* 26, 2228–2234.
- Lovley, D.R., Phillips, E.J.P., Gorby, Y. a., Landa, E.R., 1991. Microbial reduction of uranium. *Nature* 350, 413–416.
- Lovley, D.R., Roden, E.E., Phillips, E.J.P., Woodward, J.C., 1993. Enzymatic iron and uranium reduction by sulfate-reducing bacteria. *Mar. Geol.* 113, 41–53.
- Lovley, D.R., Stolz, J.F., Nord, G.L., Phillips, E.J.P.P., 1987. Anaerobic production of magnetite by a dissimilatory iron-reducing microorganism. *Nature* 330, 252–254.
- Lovley, D.R., Ueki, T., Zhang, T., Malvankar, N.S., Shrestha, P.M., Flanagan, K.A., Aklujkar, M., Butler, J.E., Giloteaux, L., Rotaru, A.E., Holmes, D.E., Franks, A.E., Orellana, R., Risso, C., Nevin, K.P., 2011. *Geobacter*. The Microbe Electric's Physiology, Ecology, and Practical Applications. *Adv. Microb. Physiol.* 59, 1–100.
- Lundgren, D.G., Silver, M., 1980. Ore leaching by bacteria. *Annu. Rev. Microbiol.* 34, 263–283.
- Luo, J., Weber, F.A., Cirpka, O.A., Wu, W.M., Nyman, J.L., Carley, J., Jardine, P.M., Criddle, C.S., Kitanidis, P.K., 2007. Modeling in-situ uranium(VI) bioreduction by sulfate-reducing bacteria. *J. Contam. Hydrol.* 92, 129–148.
- Luo, W., Wu, W.M., Yan, T., Criddle, C.S., Jardine, P.M., Zhou, J., Gu, B., 2007. Influence of bicarbonate, sulfate, and electron donors on biological reduction of uranium and microbial community composition. *Appl. Microbiol. Biotechnol.* 77, 713–721.
- Macaskie, L.E., Dean, A.C.R., 1984. Heavy metal accumulation by immobilized cells of a *Citrobacter* sp. *Biotechnol. Lett.* 6, 71–76.
- Macaskie, L.E., Dean, A.C.R., 1985a. Uranium accumulation by immobilized cells of a *Citrobacter* sp. *Biotechnol. Lett.* 7, 457–462.
- Macaskie, L.E., Dean, A.C.R., 1985b. Strontium accumulation by immobilized cells of a *Citrobacter* sp. *Biotechnol. Lett.* 7, 627–630.
- Macaskie, L.E., Empson, R.M., Cheetham, A.K., Grey, C.P., Skarnulis, A.J., 1992. Uranium bioaccumulation by a *Citrobacter* sp. as a result of enzymically mediated growth of polycrystalline HUO_2PO_4 . *Science* (80-.). 257, 782–784.
- MacDonald, M.R., Fieser, M.E., Bates, J.E., Ziller, J.W., Furche, F., Evans, W.J., 2013. Identification of the +2 oxidation state for uranium in a crystalline molecular complex, $[\text{K}(\text{2.2.2-Cryptand})][(\text{C}_5\text{H}_4\text{SiMe}_3)_3\text{U}]$. *J. Am. Chem. Soc.* 135, 13310–13313.
- Mackenzie, K., Bleyl, S., Georgi, A., Kopinke, F.D., 2012. Carbo-Iron - An Fe/AC composite - As alternative to nano-iron for groundwater treatment. *Water Res.* 46, 3817–3826.
- Mackenzie, K., Bleyl, S., Kopinke, F., Bruns, J., 2015. Performance of Carbo-Iron particles in in-situ groundwater plume and source treatment approaches.
- Mackenzie, K., Bleyl, S., Kopinke, F.D., Doose, H., Bruns, J., 2016. Carbo-Iron as improvement of the nanoiron technology: From laboratory design to the field test. *Sci. Total Environ.* 563–564, 641–

648.

- Madic, C., Hobart, D.E., Begun, G.M., 1983. Raman Spectrometric Studies of Actinide(V) and (VI) Complexes in Aqueous Sodium Carbonate Solution and of Solid Sodium Actinide(V) Carbonate Compounds. *Inorg. Chem.* 22, 1494–1503.
- Madigan, M., Martinko, J., Bender, K., Buckley, D., Stahl, D., 2015. *Brock Biology of Microorganisms*, 14th ed. Pearson Education Limited, Harlow.
- Makarova, K.S., Aravind, L., Wolf, Y.I., Tatusov, R.L., Minton, K.W., Koonin, E. V., Daly, M.J., 2001. Genome of the Extremely Radiation-Resistant Bacterium *Deinococcus radiodurans* Viewed from the Perspective of Comparative Genomics. *Microbiol. Mol. Biol. Rev.* 65, 44–79.
- Marshall, M.J., Beliaev, A.S., Dohnalkova, A.C., Kennedy, D.W., Shi, L., Wang, Z., Boyanov, M.I., Lai, B., Kemner, K.M., McLean, J.S., Reed, S.B., Culley, D.E., Bailey, V.L., Simonson, C.J., Saffarini, D.A., Romine, M.F., Zachara, J.M., Fredrickson, J.K., 2006. c-Type Cytochrome-Dependent Formation of U(IV) Nanoparticles by *Shewanella oneidensis*. *PLoS Biol.* 4, 1324–1333.
- Marshall, M.J., Plymale, A.E., Kennedy, D.W., Shi, L., Wang, Z., Reed, S.B., Dohnalkova, A.C., Simonson, C.J., Liu, C., Saffarini, D.A., Romine, M.F., Zachara, J.M., Beliaev, A.S., Fredrickson, J.K., 2008. Hydrogenase- and outer membrane c-type cytochrome-facilitated reduction of technetium(VII) by *Shewanella oneidensis* MR-1. *Environ. Microbiol.* 10, 125–136.
- Marshall, T.A., Morris, K., Law, G.T.W., Livens, F.R., Mosselmans, J.F.W., Bots, P., Shaw, S., 2014. Incorporation of uranium into hematite during crystallization from ferrihydrite. *Environ. Sci. Technol.* 48, 3724–3731.
- Marshall, T.A., Morris, K., Law, G.T.W., W. Mosselmans, J.F., Bots, P., Roberts, H., Shaw, S., 2015. Uranium fate during crystallization of magnetite from ferrihydrite in conditions relevant to the disposal of radioactive waste. *Mineral. Mag.* 79, 1265–1274.
- Martin, M., 2011. Cutadapt removes adapter sequences from high-throughput sequencing reads. *EMBnet.journal* 17, 10.
- Martinez, R.J., Wu, C.H., Beazley, M.J., Andersen, G.L., Conrad, M.E., Hazen, T.C., Taillefert, M., Sobocky, P.A., 2014. Microbial Community Responses to Organophosphate Substrate Additions in Contaminated Subsurface Sediments.
- Masella, A.P., Bartram, A.K., Truszkowski, J.M., Brown, D.G., Neufeld, J.D., 2012. PANDAseq: Paired-end assembler for illumina sequences. *BMC Bioinformatics* 13, 31.
- Masters-Waage, N.K., Morris, K., Lloyd, J.R., Shaw, S., Mosselmans, J.F.W., Boothman, C., Bots, P., Rizoulis, A., Livens, F.R., Law, G.T.W., 2017. Impacts of Repeated Redox Cycling on Technetium Mobility in the Environment. *Environ. Sci. Technol.* 51, 14301–14310.
- McClure, P.J., 2006. Spore-forming bacteria. In: *Food Spoilage Microorganisms*. Elsevier Ltd, pp. 579–623.
- Mckinley, J.P., Zeissler, C.J., Zachara, J.M., Jeffrey Serne, R., Lindstrom, R.M., Schaefer, H.T., Orr, R.D., 2001. Distribution and retention of ¹³⁷Cs in sediments at the Hanford Site, Washington. *Environ. Sci. Technol.* 35, 3433–3441.
- Meleshyn, A., 2010. Adsorption of Sr²⁺ and Ba²⁺ at the cleaved mica-water interface: Free energy profiles and interfacial structure. *Geochim. Cosmochim. Acta* 74, 1485–1497.

- Mereiter, K., 1982. The crystal structure of Liebigite, $\text{Ca}_2\text{UO}_2(\text{CO}_3)_3 \cdot 11\text{H}_2\text{O}$. *TMPM Tschermaks Mineral. und Petrogr. Mitteilungen* 30, 277–288.
- Merritt, E.A., 2010. X-ray absorption edges [WWW Document]. URL http://skuld.bmsc.washington.edu/scatter/AS_periodic.html (accessed 3.19.19).
- Michel, L.J., Macaskie, L.E., Dean, A.C.R., 1986. Cadmium accumulation by immobilized cells of a *Citrobacter* sp. using various phosphate donors. *Biotechnol. Bioeng.* 28, 1358–1365.
- Micić, V., Schmid, D., Bossa, N., Gondikas, A., Velimirovic, M., Von Der Kammer, F., Wiesner, M.R., Hofmann, T., 2017. Impact of Sodium Humate Coating on Collector Surfaces on Deposition of Polymer-Coated Nanoiron Particles. *Environ. Sci. Technol.* 51, 9202–9209.
- Mitchell, A.C., Ferris, F.G., 2005. The coprecipitation of Sr into calcite precipitates induced by bacterial ureolysis in artificial groundwater: Temperature and kinetic dependence. *Geochim. Cosmochim. Acta* 69, 4199–4210.
- Mitchell, A.C., Grant Ferris, F., 2006. The influence of *Bacillus pasteurii* on the nucleation and growth of calcium carbonate. *Geomicrobiol. J.* 23, 213–226.
- Moawad, M.M., 2002. Complexation and Thermal Studies of Uric Acid with Some Divalent and Trivalent Metal Ions of Biological Interest in the Solid State. *J. Coord. Chem.* 55, 61–78.
- Mohapatra, B.R., Dinardo, O., Gould, W.D., Koren, D.W., 2010. Biochemical and genomic facets on the dissimilatory reduction of radionuclides by microorganisms - A review. *Miner. Eng.*
- Moon, H.S., Komlos, J., Jaffé, P.R., 2009. Biogenic U(IV) oxidation by dissolved oxygen and nitrate in sediment after prolonged U(VI)/Fe(III)/ SO_4^{2-} reduction. *J. Contam. Hydrol.* 105, 18–27.
- Moon, S.H., Komlos, J., Jaffé, P.R., 2007. Uranium reoxidation in previously bioreduced sediment by dissolved oxygen and nitrate. *Environ. Sci. Technol.* 41, 4587–4592.
- Moore, R.C., Sanchez, C., Holt, K., Zhang, P., Xu, H., Choppin, G.R., 2004. Formation of hydroxyapatite in soils using calcium citrate and sodium phosphate for control of strontium migration. In: *Radiochimica Acta*. pp. 719–723.
- Morin, G., Mangeret, A., Othmane, G., Stetten, L., Seder-Colomina, M., Brest, J., Ona-Nguema, G., Bassot, S., Courbet, C., Guillevic, J., Thouvenot, A., Mathon, O., Proux, O., Bargar, J.R., 2016. Mononuclear U(IV) complexes and ningyoite as major uranium species in lake sediments. *Lett. Geochemical Perspect. Lett. Geochem. Persp. Lett.* 2, 78–86.
- Morris, K., Law, G.T.W., Bryan, N.D., 2011. Geodisposal of Higher Activity Wastes. *Issues Environ. Sci. Technol.* 32, 129–151.
- Morrison, S.J., Metzler, D.R., Carpenter, C.E., 2001. Uranium precipitation in a permeable reactive barrier by progressive irreversible dissolution of zerovalent iron. *Environ. Sci. Technol.* 35, 385–390.
- Moyes, L.N., Parkman, R.H., Charnock, J.M., Vaughan, D.J., Livens, F.R., Hughes, C.R., Braithwaite, A., 2000. Uranium uptake from aqueous solution by interaction with goethite, lepidocrocite, muscovite, and Mackinawite: An x-ray absorption spectroscopy study. *Environ. Sci. Technol.* 34, 1062–1068.
- Mugwar, A.J., Harbottle, M.J., 2016. Toxicity effects on metal sequestration by microbially-induced carbonate precipitation. *J. Hazard. Mater.* 314, 237–248.

- Murakami, T., Ohnuki, T., Isobe, H., Sato, T., 1997. Mobility of uranium during weathering. *Am. Mineral.* 82, 888–899.
- Murray, A.E., Kenig, F., Fritsen, C.H., McKay, C.P., Cawley, K.M., Edwards, R., Kuhn, E., Mcknight, D.M., Ostrom, N.E., Peng, V., Ponce, A., Priscu, J.C., Samarkin, V., Townsend, A.T., Wagh, P., Young, S.A., Yung, P.T., Doran, P.T., Karl, D.M., 2012. Microbial life at $-13\text{ }^{\circ}\text{C}$ in the brine of an ice-sealed Antarctic lake. *PNAS* 109, 20626–20631.
- Muto, T., 1965. Thermochemical Stability of Ningyoite. *Mineral. J.* 4, 245–274.
- Muyzer, G., Stams, A.J.M., 2008. The ecology and biotechnology of sulphate-reducing bacteria. *Nat. Rev. Microbiol.* 6, 441–54.
- Myers, C.R., Carstens, B.P., Antholine, W.E., Myers, J.M., 2000. Chromium(VI) reductase activity is associated with the cytoplasmic membrane of anaerobically grown *Shewanella putrefaciens* MR-1. *J. Appl. Microbiol.* 88, 98–106.
- Myers, C.R., Myers, J.M., 1997. Cloning and sequence of *cymA*, a gene encoding a tetraheme cytochrome *c* required for reduction of iron(III), fumarate, and nitrate by *Shewanella putrefaciens* MR-1. *J. Bacteriol.* 179, 1143–52.
- Myers, C.R., Nealon, K.H., 1988. Bacterial manganese reduction and growth with manganese oxide as the sole electron acceptor. *Science* (80-). 240, 1319–1321.
- NAGRA, 2018. 2018 Annual Report.
- Nair, S., Karimzadeh, L., Merkel, B.J., 2014. Surface complexation modeling of Uranium(VI) sorption on quartz in the presence and absence of alkaline earth metals. *Environ. Earth Sci.* 71, 1737–1745.
- NANO FER 25S | NANOIRON [WWW Document], n.d. URL <http://nanoiron.cz/en/products/zero-valent-iron-nanoparticles/nanofer-25s> (accessed 5.9.19).
- NanoRem.eu, 2014. NanoRem - Injection of particles into a groundwater aquifer contaminated with chlorinated solvents - approach and first results from one pilot site Carbo-Iron NanoRem - Taking Nanotechnological Remediation Processes from Lab Scale to End User Applications.
- Nanoremediation Nanotechnology for Contaminated Land Remediation [WWW Document], n.d. URL <http://nanorem.eu/> (accessed 1.14.19).
- Natrajan, L., Burdet, F., Pécaut, J., Mazzanti, M., 2006. Synthesis and structure of a stable pentavalent-uranyl coordination polymer. *J. Am. Chem. Soc.* 128, 7152–7153.
- Natrajan, L.S., 2012. Developments in the photophysics and photochemistry of actinide ions and their coordination compounds. *Coord. Chem. Rev.* 256, 1583–1603.
- NDA, 2004. About us - Nuclear Decommissioning Authority - GOV.UK [WWW Document]. GOV.UK. URL <https://www.gov.uk/government/organisations/nuclear-decommissioning-authority/about> (accessed 8.30.19).
- NDA, 2013. Radioactive Wastes in the UK : A Summary of the 2013 Inventory, Department of Energy & Climate Change.
- NDA, 2016. Radioactive Wastes in the UK: A Summary of the 2016 Inventory 1–14.
- NDA, 2017. What are the main waste categories? - UK Radioactive Waste Inventory [WWW

- Document]. URL <http://ukinventory.nda.gov.uk/about-radioactive-waste/what-is-radioactivity/what-are-the-main-waste-categories/> (accessed 4.7.17).
- NDA, 2019a. Nuclear Provision: the cost of cleaning up Britain's historic nuclear sites - GOV.UK [WWW Document]. URL <https://www.gov.uk/government/publications/nuclear-provision-explaining-the-cost-of-cleaning-up-britains-nuclear-legacy/nuclear-provision-explaining-the-cost-of-cleaning-up-britains-nuclear-legacy> (accessed 4.7.17).
- NDA, 2019b. 2019 UK Radioactive Waste and Material Inventory.
- Nedwell, D.B., Banat, I.M., 1981. Hydrogen as an electron donor for sulfate-reducing bacteria in slurries of salt marsh sediment. *Microb. Ecol.* 7, 305–313.
- Neill, T.S., Morris, K., Pearce, C.I., Abrahamsen-Mills, L., Kovarik, L., Kellet, S., Rigby, B., Vitova, T., Schacherl, B., Shaw, S., 2019. Silicate stabilisation of colloidal UO₂ produced by uranium metal corrosion. *J. Nucl. Mater.* 526, 151751.
- Neill, T.S., Morris, K., Pearce, C.I., Sherriff, N.K., Burke, M.G., Chater, P.A., Janssen, A., Natrajan, L., Shaw, S., 2018. Stability, Composition, and Core-Shell Particle Structure of Uranium(IV)-Silicate Colloids. *Environ. Sci. Technol.* 52, 9118–9127.
- Neue Seite - Helmholtz-Centre for Environmental Research [WWW Document], n.d. URL <https://www.ufz.de/index.php?en=37425> (accessed 5.9.19).
- Nevin, K.P., Finneran, K.T., Lovley, D.R., 2003. Microorganisms associated with uranium bioremediation in a high-salinity subsurface sediment. *Appl. Environ. Microbiol.* 69, 3672–3675.
- Nevin, K.P., Lovley, D.R., 2000. Potential for nonenzymatic reduction of Fe(III) via electron shuttling in subsurface sediments. *Environ. Sci. Technol.* 34, 2472–2478.
- Nevin, K.P., Lovley, D.R., 2002. Mechanisms for Fe(III) Oxide Reduction in Sedimentary Environments. *Geomicrobiol. J.* 19, 141–159.
- Newsome, L., Cleary, A., Morris, K., Lloyd, J.R., 2017. Long-Term Immobilization of Technetium via Bioremediation with Slow-Release Substrates. *Environ. Sci. Technol.* 51, 1595–1604.
- Newsome, L., Masters-waage, N., Joshi, N., Nixon, S., Lloyd, J.R., 2016. Iron-based nanotechnology to remediate technetium- contaminated groundwater 1–19.
- Newsome, L., Morris, K., Cleary, A., Masters-Waage, N.K., Boothman, C., Joshi, N., Atherton, N., Lloyd, J.R., 2019. The impact of iron nanoparticles on technetium-contaminated groundwater and sediment microbial communities. *J. Hazard. Mater.* 364, 134–142.
- Newsome, L., Morris, K., Lloyd, J.R., 2014a. The biogeochemistry and bioremediation of uranium and other priority radionuclides. *Chem. Geol.* 363, 164–184.
- Newsome, L., Morris, K., Lloyd, J.R., 2015a. Uranium biominerals precipitated by an environmental isolate of *Serratia* under anaerobic conditions. *PLoS One* 10, 1–14.
- Newsome, L., Morris, K., Shaw, S., Trivedi, D., Lloyd, J.R., 2015b. The stability of microbially reduced U(IV); impact of residual electron donor and sediment ageing. *Chem. Geol.* 409, 125–135.
- Newsome, L., Morris, K., Trivedi, D., Atherton, N., Lloyd, J.R., 2014b. Microbial reduction of uranium(VI) in sediments of different lithologies collected from Sellafield. *Appl. Geochemistry* 51, 55–64.

- Newsome, L., Morris, K., Trivedi, D., Bewsher, A., Lloyd, J.R., 2015c. Biostimulation by Glycerol Phosphate to Precipitate Recalcitrant Uranium(IV) Phosphate. *Environ. Sci. Technol.* 49, 11070–11078.
- Newville, M., 2001. EXAFS analysis using FEFF and FEFFIT. *J. Synchrotron Radiat.* 8, 96–100.
- Novikov, A.P., Kalmykov, S.N., Utsunomiya, S., Ewing, R.C., Horreard, F., Merkulov, A., Clark, S.B., Tkachev, V. V., Myasoedov, B.F., 2006. Colloid transport of plutonium in the far-field of the Mayak Production Association, Russia. *Science* (80-). 314, 638–641.
- Nuclear Decommissioning Authority: NDA, NDA, 2019. 2019 UK Radioactive Waste and Material Inventory.
- Nurk, S., Bankevich, A., Antipov, D., Gurevich, A., Korobeynikov, A., Lapidus, A., Prjibelsky, A., Pyshkin, A., Sirotkin, A., Sirotkin, Y., Stepanauskas, R., McLean, J., Lasken, R., Clingenpeel, S.R., Woyke, T., Tesler, G., Alekseyev, M.A., Pevzner, P.A., 2013. Assembling genomes and mini-metagenomes from highly chimeric reads. In: *Lecture Notes in Computer Science (Including Subseries Lecture Notes in Artificial Intelligence and Lecture Notes in Bioinformatics)*. pp. 158–170.
- O’Loughlin, E.J., Kelly, S.D., Cook, R.E., Csencsits, R., Kemner, K.M., 2003. Reduction of uranium(VI) by mixed iron(II)/iron(III) hydroxide (green rust): Formation of UO₂ nanoparticles. *Environ. Sci. Technol.* 37, 721–727.
- O’day, P.A., Newville, M., Neuhoff, P.S., Sahai, N., Carroll, S.A., 2000. X-Ray Absorption Spectroscopy of Strontium(II) Coordination I. Static and Thermal Disorder in Crystalline, Hydrated, and Precipitated Solids and in Aqueous Solution. *J. Colloid Interface Sci.* 222, 184–197.
- Omoregie, E.O., Couture, R.M., Van Cappellen, P., Corkhill, C.L., Charnock, J.M., Polya, D.A., Vaughan, D., Vanbroekhoven, K., Lloyd, J.R., 2013. Arsenic bioremediation by biogenic iron oxides and sulfides. *Appl. Environ. Microbiol.* 79, 4325–4335.
- Openshaw, S., Carver, S., Fernie, J., 1989. Britain’s nuclear waste: siting and safety, Britain’s nuclear waste: siting and safety. Belhaven Press.
- Ortiz-Bernad, I., Anderson, R.T., Vrionis, H.A., Lovley, D.R., 2004. Vanadium respiration by *Geobacter metallireducens*: novel strategy for in situ removal of vanadium from groundwater. *Appl. Environ. Microbiol.* 70, 3091–5.
- Pan, Z., Giammar, D.E., Mehta, V., Troyer, L.D., Catalano, J.G., Wang, Z., 2016. Phosphate-induced immobilization of uranium in Hanford sediments. *Environ. Sci. Technol.* 50, 13486–13494.
- Paterson-Beedle, M., Readman, J.E., Hriljac, J.A., Macaskie, L.E., 2010. Biorecovery of uranium from aqueous solutions at the expense of phytic acid. *Hydrometallurgy* 104, 524–528.
- Patterson, R.J., Spoel, T., 1981. Laboratory measurements of the strontium distribution coefficient K_d Sr for Sediments From a Shallow Sand Aquifer. *Water Resour. Res.* 17, 513–520.
- Paulus, W.J., Komarneni, S., Roy, R., 1992. Bulk synthesis and selective exchange of strontium ions in Na₄Mg₆Al₄Si₄O₂₀F₄ mica. *Nature* 357, 571–573.
- Peruski, K.M., Maloubier, M., Kaplan, D.I., Almond, P.M., Powell, B.A., 2018. Mobility of Aqueous and Colloidal Neptunium Species in Field Lysimeter Experiments. *Environ. Sci. Technol.* 52, 1963–1970.
- Petrie, L., North, N.N., Dollhopf, S.L., Balkwill, D.L., Kostka, J.E., 2003a. Enumeration and

- Characterization of Iron(III)-Reducing Microbial Communities from Acidic Subsurface Sediments Contaminated with Uranium(VI). *Appl. Environ. Microbiol.* 69, 7467–7479.
- Petrie, L., North, N.N., Dollhopf, S.L., Balkwill, D.L., Kostka, J.E., 2003b. Enumeration and Characterization of Iron(III)-Reducing Microbial Communities from Acidic Subsurface Sediments Contaminated with Uranium(VI). *Appl. Environ. Microbiol.* 69, 7467–7479.
- Pidchenko, I., Kvashnina, K.O., Yokosawa, T., Finck, N., Bahl, S., Schild, D., Polly, R., Bohnert, E., Rossberg, A., Göttlicher, J., Dardenne, K., Rothe, J., Schäfer, T., Geckeis, H., Vitova, T., 2017. Uranium Redox Transformations after U(VI) Coprecipitation with Magnetite Nanoparticles. *Environ. Sci. Technol.* 51, 2217–2225.
- Pinto, A.J., Gonçalves, M.A., Prazeres, C., Astilleros, J.M., Batista, M.J., 2012. Mineral replacement reactions in naturally occurring hydrated uranyl phosphates from the Tarabau deposit: Examples in the Cu-Ba uranyl phosphate system. *Chem. Geol.* 312–313, 18–26.
- Pirbadian, S., Barchinger, S.E., Leung, K.M., Byun, H.S., Jangir, Y., Bouhenni, R.A., Reed, S.B., Romine, M.F., Saffarini, D.A., Shi, L., Gorby, Y.A., Golbeck, J.H., El-Naggar, M.Y., 2014. *Shewanella oneidensis* MR-1 nanowires are outer membrane and periplasmic extensions of the extracellular electron transport components. *Proc. Natl. Acad. Sci. U. S. A.* 111, 12883–12888.
- Ponder, S.M., Darab, J.G., Bucher, J., Caulder, D., Craig, I., Davis, L., Edelstein, N., Lukens, W., Nitsche, H., Rao, L., Shuh, D.K., Mallouk, T.E., 2001. Surface chemistry and electrochemistry of supported zerovalent iron nanoparticles in the remediation of aqueous metal contaminants. *Chem. Mater.* 13, 479–486.
- Pors Nielsen, S., 2004. The biological role of strontium. *Bone* 35, 583–588.
- Qadeer, R., Hanif, J., 1994. Kinetics of Uranium (VI) Ions Adsorption on Activated Charcoal from Aqueous Solutions, *Radiochimica Acta*.
- Qadeer, R., Hanif, J., Saleem, M., Afzal, M., 1992. Effect of alkali metals, alkaline earth metals and lanthanides on the adsorption of uranium on activated charcoal from aqueous solutions. *J. Radioanal. Nucl. Chem. Lett.* 165, 243–253.
- Ravel, B., Newville, M., 2005. ATHENA, ARTEMIS, HEPHAESTUS: Data analysis for X-ray absorption spectroscopy using IFEFFIT. In: *Journal of Synchrotron Radiation*. pp. 537–541.
- Regenesis, 2015. Metals Remediation Compound (MRC®) [WWW Document]. URL <https://regenesisc.com/eur/remediation-products/metals-remediation-compound-mrc/> (accessed 5.9.19).
- Regenesis, 2016a. In Situ Treatment of Chrome(VI) Plume in Fast Flowing Aquifer, NW Italy [WWW Document]. URL <https://regenesisc.com/eur/project/in-situ-treatment-of-chromevi-plume-in-fast-flowing-aquifer-nw-italy/> (accessed 5.9.19).
- Regenesis, 2016b. In Situ Hexavalent Chromium Remediation, Northern Italy [WWW Document]. URL <https://regenesisc.com/eur/project/in-situ-hexavalent-chromium-remediation-northern-italy/> (accessed 5.9.19).
- Reguera, G., 2012. Electron transfer at the cell–uranium interface in *Geobacter* spp. *Biochem. Soc. Trans.* 40.
- Reguera, G., McCarthy, K.D., Mehta, T., Nicoll, J.S., Tuominen, M.T., Lovley, D.R., 2005. Extracellular electron transfer via microbial nanowires. *Nature* 435, 1098–1101.

- Renshaw, J.C., Butchins, L.J.C., Livens, F.R., May, I., Charnock, J.M., Lloyd, J.R., 2005. Bioreduction of uranium: Environmental implications of a pentavalent intermediate. *Environ. Sci. Technol.* 39, 5657–5660.
- Roberts, H.E., Morris, K., Law, G.T.W., Mosselmans, J.F.W., Bots, P., Kvashnina, K., Shaw, S., 2017. Uranium(V) Incorporation Mechanisms and Stability in Fe(II)/Fe(III) (oxyhydr)Oxides. *Environ. Sci. Technol. Lett.* 4, 421–426.
- Röling, W.F.M., 2014. The Family Geobacteraceae. In: *The Prokaryotes*. Springer Berlin Heidelberg, Berlin, Heidelberg, pp. 157–172.
- RSC, 2018. Strontium [WWW Document]. URL <http://www.rsc.org/periodic-table/element/38/strontium> (accessed 9.6.18).
- Rui, X., Kwon, M.J., O’Loughlin, E.J., Dunham-Cheatham, S., Fein, J.B., Bunker, B., Kemner, K.M., Boyanov, M.I., 2013. Bioreduction of hydrogen uranyl phosphate: Mechanisms and U(IV) products. *Environ. Sci. Technol.* 47, 5668–5678.
- Runde, W., 2000. The Chemical Interactions of Actinides in the Environment. *Los Alamos Sci.* 26, 392–411.
- Sahai, N., Carroll, S.A., Roberts, S., O’day, P.A., O’day, P.A., 2000. X-Ray Absorption Spectroscopy of Strontium(II) Coordination II. Sorption and Precipitation at Kaolinite, Amorphous Silica, and Goethite Surfaces. *J. Colloid Interface Sci.* 222, 198–212.
- Saleem, M., Afzal, M., Qadeer, R., Hanif, J., 1992. Selective Adsorption of Uranium on Activated Charcoal from Electrolytic Aqueous Solutions. *Sep. Sci. Technol.* 27, 239–253.
- Sani, R.K., Peyton, B.M., Amonette, J.E., Geesey, G.G., 2004. Reduction of uranium(VI) under sulfate-reducing conditions in the presence of Fe(III)-(hydr)oxides. *Geochim. Cosmochim. Acta* 68, 2639–2648.
- Sani, R.K., Peyton, B.M., Dohnalkova, A., Amonette, J.E., 2005. Reoxidation of reduced uranium with iron(III) (Hydr)oxides under sulfate-reducing conditions. *Environ. Sci. Technol.* 39, 2059–2066.
- Satomi, M., 2014. The Family Shewanellaceae. In: *The Prokaryotes*. Springer Berlin Heidelberg, Berlin, Heidelberg, pp. 597–625.
- Saunders, J.A., Toran, L.E., 1995. Modeling of radionuclide and heavy metal sorption around low-and high- pH waste disposal sites at Oak Ridge, Tennessee. *Appl. Geochemistry* 10, 673–684.
- Schwalb, C., Chapman, S.K., Reid, G.A., 2003. The Tetraheme Cytochrome CymA Is Required for Anaerobic Respiration with Dimethyl Sulfoxide and Nitrite in *Shewanella oneidensis* †. *Biochemistry* 42, 9491–9497.
- Schwyn, B., Wersin, P., Rüedi, J., Schneider, J., Altmann, S., Missana, T., Noseck, U., 2012. FUNMIG Integrated Project results and conclusions from a safety case perspective. *Appl. Geochemistry* 27, 501–515.
- Scottish Environment Protection Agency, 2016. Guidance on Requirements for Release of Nuclear Sites from Radioactive Substances Regulation [WWW Document]. URL https://consultation.sepa.org.uk/operations-portfolio/grr/user_uploads/2016_02_01-grr-published-consultation-document.pdf (accessed 4.7.17).
- Sellafield Integrated Waste Strategy, 2009.

- Sellafield Ltd., 2015. Groundwater Monitoring at Sellafield: Annual Data Review 2015.
- Sellafield Ltd., 2017. Monitoring our environment: Discharges and Environmental Monitoring. Annual Report 2017, Military Engineer.
- Sellafield Ltd, 2018. Sellafield Ltd - GOV.UK [WWW Document]. Sellaf. Ltd Off. website. URL <https://www.gov.uk/government/organisations/sellafield-ltd> (accessed 8.30.19).
- Senko, J.M., Istok, J.D., Suflita, J.M., Krumholz, L.R., 2002. In-situ evidence for uranium immobilization and remobilization. *Environ. Sci. Technol.* 36, 1491–1496.
- Sharp, J.O., Lezama-Pacheco, J.S., Schofield, E.J., Junier, P., Ulrich, K.U., Chinni, S., Veeramani, H., Margot-Roquier, C., Webb, S.M., Tebo, B.M., Giammar, D.E., Bargar, J.R., Bernier-Latmani, R., 2011. Uranium speciation and stability after reductive immobilization in aquifer sediments. *Geochim. Cosmochim. Acta* 75, 6497–6510.
- Shelobolina, E.S., Coppi, M. V, Korenevsky, A.A., DiDonato, L.N., Sullivan, S.A., Konishi, H., Xu, H., Leang, C., Butler, J.E., Kim, B.C., Lovley, D.R., 2007. Importance of c-type cytochromes for U(VI) reduction by *Geobacter sulfurreducens*. *BMC Microbiol.* 7, 16.
- Shelobolina, E.S., Konishi, H., Xu, H., Roden, E.E., 2009. U(VI) sequestration in hydroxyapatite produced by microbial glycerol 3-phosphate metabolism. *Appl. Environ. Microbiol.* 75, 5773–5778.
- Shi, L., Richardson, D.J., Wang, Z., Kerisit, S.N., Rosso, K.M., Zachara, J.M., Fredrickson, J.K., 2009. The roles of outer membrane cytochromes of *Shewanella* and *Geobacter* in extracellular electron transfer. *Environ. Microbiol. Rep.*
- Shi, L., Rosso, K.M., Zachara, J.M., Fredrickson, J.K., 2012. Mtr extracellular electron-transfer pathways in Fe(III)-reducing or Fe(II)-oxidizing bacteria: A genomic perspective. In: *Biochemical Society Transactions*. pp. 1261–1267.
- Shi, L., Squier, T.C., Zachara, J.M., Fredrickson, J.K., 2007. Respiration of metal (hydr)oxides by *Shewanella* and *Geobacter*: A key role for multiheme c-type cytochromes. *Mol. Microbiol.* 65, 12–20.
- Shi, Z., Liu, C., Zachara, J.M., Wang, Z., Deng, B., 2009. Inhibition effect of secondary phosphate mineral precipitation on uranium release from contaminated sediments. *Environ. Sci. Technol.* 43, 8344–8349.
- Silberberg, M., 2014. *Chemistry: The Molecular Nature of Matter and Change*, 5th ed. McGraw-Hill Higher Education, New York.
- Simon, F.G., Segebade, C., Hedrich, M., 2003. Behaviour of uranium in iron-bearing permeable reactive barriers: Investigation with ²³⁷U as a radioindicator. *Sci. Total Environ.* 307, 231–238.
- Singer, D.M., Zachara, J.M., Brown, G.E., 2009. Uranium speciation as a function of depth in contaminated Hanford sediments - A micro-XRF, micro-XRD, and micro- and bulk-XAFS study. *Environ. Sci. Technol.* 43, 630–636.
- Smeaton, C.M., Weisener, C.G., Burns, P.C., Fryer, B.J., Fowle, D.A., 2008. Bacterially enhanced dissolution of meta-autunite. *Am. Mineral.* 93, 1858–1864.
- Smith, K.F., Bryan, N.D., Law, G.T.W., Hibberd, R., Shaw, S., Livens, F.R., Parry, S.A., Mosselmans, J.F.W., Morris, K., 2018. Np(V) sorption and solubility in high pH calcite systems. *Chem. Geol.* 493, 396–404.

- Smith, K.F., Bryan, N.D., Swinburne, A.N., Bots, P., Shaw, S., Natrajan, L.S., Mosselmans, J.F.W., Livens, F.R., Morris, K., 2015. U(VI) behaviour in hyperalkaline calcite systems. *Geochim. Cosmochim. Acta* 148, 343–359.
- Soldatov, A. V., Lamoen, D., Konstantinović, M.J., Van den Berghe, S., Scheinost, A.C., Verwerft, M., 2007. Local structure and oxidation state of uranium in some ternary oxides: X-ray absorption analysis. *J. Solid State Chem.* 180, 54–61.
- Spear, J.R., Figueroa, L.A., Honeyman, B.D., 2000. Modeling reduction of uranium U(VI) under variable sulfate concentrations by sulfate-reducing bacteria. *Appl. Environ. Microbiol.* 66, 3711–3721.
- Spycher, N.F., Issarangkun, M., Stewart, B.D., Sevinç Şengör, S., Belding, E., Ginn, T.R., Peyton, B.M., Sani, R.K., 2011. Biogenic uraninite precipitation and its reoxidation by iron(III) (hydr)oxides: A reaction modeling approach. *Geochim. Cosmochim. Acta* 75, 4426–4440.
- Stacey, W.M., 2007. *Nuclear Reactor Physics, Second Edi.* ed. Wiley-Interscience, New York.
- Stamper, A., Coughlin, D., Bowes, B., Ruddick, P., Laws, F., 2014. Groundwater monitoring at Sellafield, annual data review 2013 128 pp.
- Standing, W.J.F., Oughton, D.H., Salbu, B., 2002. Potential remobilization of ¹³⁷Cs, ⁶⁰Co, ⁹⁹Tc, and ⁹⁰Sr from contaminated Mayak sediments in river and estuary environments. *Environ. Sci. Technol.* 36, 2330–2337.
- Stocks-Fischer, S., Galinat, J.K., Bang, S.S., 1999. Microbiological precipitation of CaCO₃. *Soil Biol. Biochem.* 31, 1563–1571.
- Stolworthy, M., n.d. Live monitoring of the UK electricity National Grid [WWW Document]. URL <http://gridwatch.co.uk/> (accessed 2.7.19).
- Stookey, L.L., 1970. Ferrozine-A New Spectrophotometric Reagent for Iron. *Anal. Chem.* 42, 779–781.
- Stubbs, J.E., Veblen, L.A., Elbert, D.C., Zachara, J.M., Davis, J.A., Veblen, D.R., 2009. Newly recognized hosts for uranium in the Hanford Site vadose zone. *Geochim. Cosmochim. Acta* 73, 1563–1576.
- Stumm, W., Morgan, J.J., 1996. *Aquatic Chemistry: Chemical Equilibria and Rates in Natural Waters.* Wiley Interscience.
- Sudarsanan, K., Young, R.A., 1972. Structure of strontium hydroxide phosphate, Sr₅(PO₄)₃OH. *Acta Crystallogr. Sect. B Struct. Crystallogr. Cryst. Chem.* 28, 3668–3670.
- Sun, Y., Lan, J., Li, M., Hu, W., Liu, H., Song, G., Chen, D., Shi, W., Wang, X., 2018. Influence of aqueous sulfide on speciation of U(vi) adsorbed to nanomagnetite. *Environ. Sci. Nano* 5, 1981–1989.
- Sun, Y., Yang, S., Chen, Y., Ding, C., Cheng, W., Wang, X., 2015. Adsorption and desorption of U(VI) on functionalized graphene oxides: A combined experimental and theoretical study. *Environ. Sci. Technol.* 49, 4255–4262.
- Sundararajan, M., Campbell, A.J., Hillier, I.H., 2008. Catalytic cycles for the reduction of [UO₂]²⁺ by cytochrome c7 proteins proposed from DFT calculations. *J. Phys. Chem. A* 112, 4451–4457.
- Surovchak, S., 2017. Five Year Review Report for Rocky Flats Site, Jefferson County, Colorado.
- Suzuki, Y., Kelly, S.D., Kemner, K.M., Banfield, J.F., 2002. Radionuclide contamination: Nanometre-size products of uranium bioreduction. *Nature* 419, 134–134.

- Suzuki, Y., Kitatsuji, Y., Ohnuki, T., Tsujimura, S., 2010. Flavin mononucleotide mediated electron pathway for microbial U(vi) reduction. *Phys. Chem. Chem. Phys.* 12, 10081–10087.
- Szecsody, J.E., Fruchter, J.S., Rockhold, M.L., Mckinley, J.P., Oostrom, M., Vermeul, V.R., Moore, R.C., Covert, M.T., Burns, C., Wietsma, T.W., Williams, M.D., Breshears, A.T., Zhong, L., Garcia, B.J., 2009. Sequestration of Sr-90 Subsurface Contamination in the Hanford 100-N Area by Surface Infiltration of a Ca-Citrate-Phosphate Solution.
- Tang, G., Wu, W.M., Watson, D.B., Parker, J.C., Schadt, C.W., Shi, X., Brooks, S.C., 2013. U(VI) bioreduction with emulsified vegetable oil as the electron donor -microcosm tests and model development. *Environ. Sci. Technol.* 47, 3209–3217.
- Tang, J., Köhler, S.J., Dietzel, M., 2008. Sr²⁺/Ca²⁺ and ⁴⁴Ca/⁴⁰Ca fractionation during inorganic calcite formation: I. Sr incorporation. *Geochim. Cosmochim. Acta* 72, 3718–3732.
- Tebo, B.M., Obratsova, A.Y., 1998. Sulfate-reducing bacterium grows with Cr(VI), U(VI), Mn(IV), and Fe(III) as electron acceptors. *FEMS Microbiol. Lett.* 162, 193–198.
- Teo, B.K., 1986. EXAFS: basic principles and data analysis. New York.
- Tesoriero, A.J., Pankow, J.F., 1996. Solid solution partitioning of Sr²⁺, Ba²⁺, and Cd²⁺ to calcite. *Geochim. Cosmochim. Acta* 60, 1053–1063.
- The Department of Energy and Climate Change, 2014. Implementing Geological Disposal A Framework for the long-term management of higher activity radioactive waste.
- The Department of Energy and Climate Change, 2016. Nuclear power in the UK.
- Thomas, R.A.P., Macaskie, L.E., 1996. Biodegradation of tributyl phosphate by naturally occurring microbial isolates and coupling to the removal of uranium from aqueous solution. *Environ. Sci. Technol.* 30, 2371–2375.
- Thorpe, Boothman, C., Lloyd, J.R., Law, G.T.W., Bryan, N.D., Atherton, N., Livens, F.R., Morris, K., 2014. The interactions of strontium and technetium with Fe(II) bearing biominerals: Implications for bioremediation of radioactively contaminated land. *Appl. Geochemistry* 40, 135–143.
- Thorpe, C.L., Law, G.T.W., Lloyd, J.R., Williams, H.A., Atherton, N., Morris, K., 2017. Quantifying Technetium and Strontium Bioremediation Potential in Flowing Sediment Columns. *Environ. Sci. Technol.* 51, 12104–12113.
- Thorpe, C.L., Lloyd, J.R., Law, G.T.W., Williams, H.A., Atherton, N., Cruickshank, J.H., Morris, K., 2016. Retention of ^{99m}Tc at ultra-trace levels in flowing column experiments – insights into bioreduction and biomineralization for remediation at nuclear facilities. *Geomicrobiol. J.* 33, 199–205.
- Thorpe, Law, G.T.W., Boothman, C., Lloyd, J.R., Burke, I.T., Morris, K., 2012a. The Synergistic Effects of High Nitrate Concentrations on Sediment Bioreduction. *Geomicrobiol. J.* 29, 484–493.
- Thorpe, Lloyd, J.R., Law, G.T.W., Burke, I.T., Shaw, S., Bryan, N.D., Morris, K., 2012b. Strontium sorption and precipitation behaviour during bioreduction in nitrate impacted sediments. *Chem. Geol.* 306–307, 114–122.
- Tirafferri, A., Saldarriaga Hernandez, L.A., Bianco, C., Tosco, T., Sethi, R., 2017. Colloidal behavior of goethite nanoparticles modified with humic acid and implications for aquifer reclamation. *J. Nanoparticle Res.* 19.
- Tiwari, D.P., Singh, D.K., Saksena, D.N., 1995. Hg(II) adsorption from aqueous solutions using rice-husk

- ash. *J. Environ. Eng. (United States)* 121, 479–481.
- Todd, a. C., Yuan, M.D., 1992. Barium and Strontium Sulfate Solid-Solution Scale Formation at Elevated Temperatures. *SPE Prod. Eng.* 7, 85–92.
- Torrey, J.D., Killgore, J.P., Bedford, N.M., Greenlee, L.F., 2015. Oxidation behavior of zero-valent iron nanoparticles in mixed matrix water purification membranes. *Environ. Sci. Water Res. Technol.* 1, 146–152.
- Torstenfelt, B., Andersson, K., Allard, B., 1982. Sorption of strontium and cesium on rocks and minerals. *Chem. Geol.* 36, 123–137.
- Tsarev, S., Collins, R.N., Fahy, A., Waite, T.D., 2016a. Reduced Uranium Phases Produced from Anaerobic Reaction with Nanoscale Zerovalent Iron. *Environ. Sci. Technol.* 50, 2595–2601.
- Tsarev, S., Collins, R.N., Ilton, E.S., Fahy, A., Waite, T.D., 2017. The short-term reduction of uranium by nanoscale zero-valent iron (nZVI): Role of oxide shell, reduction mechanism and the formation of U(v)-carbonate phases. *Environ. Sci. Nano* 4, 1304–1313.
- Tsarev, S., Waite, T.D., Collins, R.N., 2016b. Uranium Reduction by Fe(II) in the Presence of Montmorillonite and Nontronite. *Environ. Sci. Technol.* 50, 8223–8230.
- U.S. Department of Energy, 2019. DOE - Office of Legacy Management -- Rocky Flats Site, Colorado [WWW Document]. URL https://www.lm.doe.gov/Rocky_Flats/Sites.aspx (accessed 11.28.19).
- UK Energy Statistics, Q1 2018 Trends in the use of renewable energy, 2018.
- UK Government, 2019. UK becomes first major economy to pass net zero emissions law [WWW Document]. URL <https://www.gov.uk/government/news/uk-becomes-first-major-economy-to-pass-net-zero-emissions-law>
- Ulrich, K.-U., Veeramani, H., Bernier-Latmani, R., Giammar, D.E., 2011. Speciation-Dependent Kinetics of Uranium(VI) Bioreduction. *Geomicrobiol. J.* 28, 396–409.
- United States Nuclear Regulatory Commission, 2017. NRC: The Student Corner: What Is Nuclear Energy? Landing Page [WWW Document]. URL <https://www.nrc.gov/reading-rm/basic-ref/students/what-is-nuclear-energy.html> (accessed 2.7.19).
- V. VenkataRamana, V. J. Thyagaraju, K.S., 1992. Chromium complexes of uric acid—synthesis, structure, and properties. *J. Inorg. Biochem.* 48, 85–93.
- Valentin, J. (Jack), 2007. The 2007 Recommendations of the International Commission on Radiological Protection. ICRP publication 103. *Ann. ICRP* 37, 1–332.
- Van Veelen, A., Preedy, O., Qi, J., Law, G.T.W., Morris, K., Mosselmans, J.F.W., Ryan, M.P., Evans, N.D.M., Wogelius, R.A., 2014. Uranium and technetium interactions with wüstite [Fe 1–x O] and portlandite [Ca(OH) 2] surfaces under geological disposal facility conditions. *Mineral. Mag.* 78, 1097–1113.
- Velimirovic, M., Schmid, D., Wagner, S., Micić, V., von der Kammer, F., Hofmann, T., 2016. Agar agar-stabilized milled zerovalent iron particles for in situ groundwater remediation. *Sci. Total Environ.* 563–564, 713–723.
- Verbeeck, R.M.H., Haiben, M., Thin, H.P., Verbeeck, F., 1977. Solubility and Solution Behaviour of Strontiumhydroxyapatite. *Zeitschrift fur Phys. Chemie* 108, 203–215.

- Vermeul, V.R., Szecsody, J.E., Fritz, B.G., Williams, M.D., Moore, R.C., Fruchter, J.S., 2014. An Injectable Apatite Permeable Reactive Barrier for In Situ ⁹⁰Sr Immobilization. *Groundw. Monit. Remediat.* 34, 28–41.
- Vettese, G.F., Morris, K., Natrajan, L.S., Shaw, S., Vitova, T., Galanzew, J., Jones, D.L., Lloyd, J.R., 2020. Multiple Lines of Evidence Identify U(V) as a Key Intermediate during U(VI) Reduction by *Shewanella oneidensis* MR1. *Environ. Sci. Technol.*
- Viollier, E., Inglett, P., Hunter, K., Roychoudhury, A., Van Cappellen, P., 2000. The ferrozine method revisited: Fe(II)/Fe(III) determination in natural waters. *Appl. Geochemistry* 15, 785–790.
- Vitova, T., Denecke, M.A., Göttlicher, J., Jorissen, K., Kas, J.J., Kvashnina, K., Prüßmann, T., Rehr, J.J., Rothe, J., 2013. Actinide and lanthanide speciation with high-energy resolution X-ray techniques. In: *Journal of Physics: Conference Series*. IOP Publishing, p. 012117.
- Von Canstein, H., Ogawa, J., Shimizu, S., Lloyd, J.R., 2008. Secretion of flavins by *Shewanella* species and their role in extracellular electron transfer. *Appl. Environ. Microbiol.* 74, 615–623.
- Vrionis, H.A., Anderson, R.T., Ortiz-Bernad, I., O'Neill, K.R., Resch, C.T., Peacock, A.D., Dayvault, R., White, D.C., Long, P.E., Lovley, D.R., 2005. Microbiological and geochemical heterogeneity in an in situ uranium bioremediation field site. *Appl. Environ. Microbiol.* 71, 6308–6318.
- Waite, T.D., Davis, J.A., Payne, T.E., Waychunas, G.A., Xu, N., 1994. Uranium(VI) adsorption to ferrihydrite: Application of a surface complexation model. *Geochim. Cosmochim. Acta* 58, 5465–5478.
- Wallace, S.H., Shaw, S., Morris, K., Small, J.S., Burke, I.T., 2013. Alteration of sediments by hyperalkaline k-rich cement leachate: Implications for strontium adsorption and incorporation. *Environ. Sci. Technol.* 47, 3694–3700.
- Wallace, S.H., Shaw, S., Morris, K., Small, J.S., Fuller, A.J., Burke, I.T., 2012. Effect of groundwater pH and ionic strength on strontium sorption in aquifer sediments: Implications for ⁹⁰Sr mobility at contaminated nuclear sites. *Appl. Geochemistry* 27, 1482–1491.
- Walter, M., Arnold, T., Reich, T., Bernhard, G., 2003. Sorption of uranium(VI) onto ferric oxides in sulfate-rich acid waters. *Environ. Sci. Technol.* 37, 2898–2904.
- Wang, C., Li, Y., Liu, Z., Wang, P., 2009. Bioremediation of nitrobenzene-polluted sediments by *Pseudomonas putida*. *Bull. Environ. Contam. Toxicol.* 83, 865–868.
- Wang, G., Um, W., Wang, Z., Reinoso-Maset, E., Washton, N.M., Mueller, K.T., Perdrial, N., O'Day, P.A., Chorover, J., 2017. Uranium Release from Acidic Weathered Hanford Sediments: Single-Pass Flow-Through and Column Experiments. *Environ. Sci. Technol.* 51, 11011–11019.
- Wang, Q., Garrity, G.M., Tiedje, J.M., Cole, J.R., 2007. Naïve Bayesian classifier for rapid assignment of rRNA sequences into the new bacterial taxonomy. *Appl. Environ. Microbiol.* 73, 5261–5267.
- Wang, Y., Salvage, K., 2005. Immobilization of uranium in the presence of FeO(s): Model development and simulation of contrasting experimental conditions. *Appl. Geochemistry* 20, 1268–1283.
- Wang, Z., Lee, S.W., Kapoor, P., Tebo, B.M., Giammar, D.E., 2013. Uraninite oxidation and dissolution induced by manganese oxide: A redox reaction between two insoluble minerals. *Geochim. Cosmochim. Acta* 100, 24–40.
- Wang, Z., Xiong, W., Tebo, B.M., Giammar, D.E., 2014. Oxidative UO₂ dissolution induced by soluble

- Mn(III). *Environ. Sci. Technol.* 48, 289–298.
- Wasserman, R.H., 1998. Strontium as a tracer for calcium in biological and clinical research. *Clin. Chem.*
- Watson, D.B., Kostka, J.E., Fields, M.W., Jardine, P.M., 2004. The Oak Ridge Field Research Center Conceptual Model.
- Watson, D.B., Wu, W.M., Mehlhorn, T., Tang, G., Earles, J., Lowe, K., Gihring, T.M., Zhang, G., Phillips, J., Boyanov, M.I., Spalding, B.P., Schadt, C., Kemner, K.M., Criddle, C.S., Jardine, P.M., Brooks, S.C., 2013. In situ bioremediation of uranium with emulsified vegetable oil as the electron donor. *Environ. Sci. Technol.* 47, 6440–6448.
- Wazne, M., Korfiatis, G.P., Meng, X., 2003. Carbonate effects on hexavalent uranium adsorption by iron oxyhydroxide. *Environ. Sci. Technol.* 37, 3619–3624.
- Wechsler, B.A., Lindsley, D.H., Prewitt, C.T., 1984. Crystal structure and cation distribution in titanomanganites ($\text{Fe}_3\text{-xTi}_x\text{O}_4$). *Am. Mineral.* 69, 754.
- Wellman, D., Pierce, E., Bovaird, C., Griswold, K.M., Gunderson, K., Webb, S., Bargar, J.R., 2009. Laboratory development of polyphosphate remediation technology for in situ treatment of uranium contamination in the vadose zone and capillary fringe, *Uranium: Compounds, Isotopes and Applications*.
- Wellman, D.M., Icenhower, J.P., Owen, A.T., 2006. Comparative analysis of soluble phosphate amendments for the remediation of heavy metal contaminants: Effect on sediment hydraulic conductivity. *Environ. Chem.* 3, 219–224.
- Wen, H., Pan, Z., Giammar, D., Li, L., 2018. Enhanced Uranium Immobilization by Phosphate Amendment under Variable Geochemical and Flow Conditions: Insights from Reactive Transport Modeling. *Environ. Sci. Technol.* 52, 5841–5850.
- Wester, D.W., Sullivan, J.C., 1980. Electrochemical and Spectroscopic Studies of Uranium(IV), -(V), and -(VI) in Carbonate-Bicarbonate Buffers. *Inorg. Chem.* 19, 2838–2840.
- Wickham, H., Hester, J., Chang, W., 2020. devtools: Tools to Make Developing R Packages Easier [WWW Document]. URL <https://cran.r-project.org/web/packages/devtools/index.html> (accessed 4.27.20).
- Wildung, R.E., Gorby, Y.A., Krupka, K.M., Hess, N.J., Li, S.W., Plymale, A.E., McKinley, J.P., Fredrickson, J.K., 2000. Effect of electron donor and solution chemistry on products of dissimilatory reduction of technetium by *Shewanella putrefaciens*. *Appl. Environ. Microbiol.* 66, 2451–60.
- Wilkins, M.J., Livens, F.R., Vaughan, D.J., Beadle, I., Lloyd, J.R., 2007. The influence of microbial redox cycling on radionuclide mobility in the subsurface at a low-level radioactive waste storage site. *Geobiology* 5, 293–301.
- Williams, K.H., Bargar, J.R., Lloyd, J.R., Lovley, D.R., 2013. Bioremediation of uranium-contaminated groundwater: A systems approach to subsurface biogeochemistry. *Curr. Opin. Biotechnol.* 24, 489–497.
- Williams, K.H., Long, P.E., Davis, J. a., Wilkins, M.J., N’Guessan, a. L., Steefel, C.I., Yang, L., Newcomer, D., Spane, F. a., Kerkhof, L.J., McGuinness, L., Dayvault, R., Lovley, D.R., 2011. Acetate Availability and its Influence on Sustainable Bioremediation of Uranium-Contaminated Groundwater. *Geomicrobiol. J.* 28, 519–539.

- Wilson, P.D., 1996. *The Nuclear Fuel Cycle: from Ore to Waste*. Oxford University Press, Oxford.
- Winstanley, E.H., Morris, K., Abrahamsen-Mills, L.G., Blackham, R., Shaw, S., 2019. U(VI) sorption during ferrihydrite formation: Underpinning radioactive effluent treatment. *J. Hazard. Mater.* 366, 98–104.
- Witmer, M., 2014. *Examination of Radionuclide Transport in the Vadose Zone Using Field Lysimeters*, Thesis.
- WNA -World Nuclear Association, 2019. *Nuclear Power Today | Nuclear Energy - World Nuclear Association*.
- World Health Organisation, 2006. *Guidelines for Drinking-water Quality [WWW Document]*.
- Wu, S., Fang, G., Wang, Y., Zheng, Y., Wang, C., Zhao, F., Jaisi, D.P., Zhou, D., 2017. Redox-Active Oxygen-Containing Functional Groups in Activated Carbon Facilitate Microbial Reduction of Ferrihydrite. *Environ. Sci. Technol.* 51, 9709–9717.
- Wu, W.M., Carley, J., Gentry, T., Ginder-Vogel, M.A., Fienen, M., Mehlhorn, T., Yan, H., Carroll, S., Pace, M.N., Nyman, J., Luo, J., Gentile, M.E., Fields, M.W., Hickey, R.F., Gu, B., Watson, D., Cirpka, O.A., Zhou, J., Fendorf, S., Kitanidis, P.K., Jardine, P.M., Criddle, C.S., 2006. Pilot-scale in situ bioremediation of uranium in a highly contaminated aquifer. 2. Reduction of U(VI) and geochemical control of U(VI) bioavailability. *Environ. Sci. Technol.* 40, 3986–3995.
- Wu, Y., Ajo-Franklin, J.B., Spycher, N., Hubbard, S.S., Zhang, G., Williams, K.H., Taylor, J., Fujita, Y., Smith, R., 2011. Geophysical monitoring and reactive transport modeling of ureolytically-driven calcium carbonate precipitation. *Geochem. Trans.* 12, 7.
- Wyckoff, R.W.G., 1963. *Crystal Structures 1*. *Cryst. Struct.* 1, 239–444.
- Xiao, J., Chen, Y., Zhao, W., Xu, J., 2013. Sorption behavior of U(VI) onto Chinese bentonite: Effect of pH, ionic strength, temperature and humic acid. *J. Mol. Liq.* 188, 178–185.
- Yabusaki, S.B., Fang, Y., Long, P.E., Resch, C.T., Peacock, A.D., Komlos, J., Jaffe, P.R., Morrison, S.J., Dayvault, R.D., White, D.C., Anderson, R.T., 2007. Uranium removal from groundwater via in situ biostimulation: Field-scale modeling of transport and biological processes. *J. Contam. Hydrol.* 93, 216–235.
- Yang, W.H., Weber, K.A., Silver, W.L., 2012. Nitrogen loss from soil through anaerobic ammonium oxidation coupled to iron reduction. *Nat. Geosci.*
- Yong, P., Macaskie, L.E., 1995. Enhancement of uranium bioaccumulation by a *Citrobacter* sp. via enzymically-mediated growth of polycrystalline $\text{NH}_4\text{UO}_2\text{PO}_4$. *J. Chem. Technol. Biotechnol.* 63, 101–108.
- Yung, M.C., Jiao, Y., 2014. Biomineralization of uranium by PhoY phosphatase activity aids cell survival in *Caulobacter crescentus*. *Appl. Environ. Microbiol.* 80, 4795–4804.
- Zachara, J.M., Cowan, C.E., Resch, C.T., 1991. Sorption of divalent metals on calcite. *Geochim. Cosmochim. Acta* 55, 1549–1562.
- Zachara, J.M., Liu, C., Dohnalkova, A., Fredrickson, J.K., Kennedy, D.W., Duff, M.C., Hunter, D.B., 2002. Influence of Mn oxides on the reduction of uranium(VI) by the metal-reducing bacterium *Shewanella putrefaciens*. *Geochim. Cosmochim. Acta* 66, 3247–3262.
- Zachara, J.M., Serne, J., Freshley, M., Mann, F., Anderson, F., Wood, M., Jones, T., Myers, D., 2007.

Geochemical Processes Controlling Migration of Tank Wastes in Hanford's Vadose Zone. *Vadose Zo. J.* 6, 985.

Zang, Y., Genta-Jouve, G., Sun, T.A., Li, X., Didier, B., Mann, S., Mouray, E., Larsen, A.K., Escargueil, A.E., Nay, B., Prado, S., 2015. Unexpected talaroenamine derivatives and an undescribed polyester from the fungus *Talaromyces stipitatus* ATCC10500. *Phytochemistry* 119, 70–75.

Zavarzina, D.G., Sokolova, T.G., Tourova, T.P., Chernyh, N.A., Kostrikina, N.A., Bonch-Osmolovskaya, E.A., 2007. *Thermincola ferriacetica* sp. nov., a new anaerobic, thermophilic, facultatively chemolithoautotrophic bacterium capable of dissimilatory Fe(III) reduction. *Extremophiles*.

Zhang, P., Van Nostrand, J.D., He, Z., Chakraborty, R., Deng, Y., Curtis, D., Fields, M.W., Hazen, T.C., Arkin, A.P., Zhou, J., 2015. A Slow-Release Substrate Stimulates Groundwater Microbial Communities for Long-Term in Situ Cr(VI) Reduction. *Environ. Sci. Technol.* 49, 12922–12931.

Zhang, W., Elliott, D.W., 2006. Applications of iron nanoparticles for groundwater remediation. *Remediat. J.* 16, 7–21.

Zhong, L., Liu, C., Zachara, J.M., Kennedy, D.W., Szecsody, J.E., Wood, B., 2005. Oxidative Remobilization of Biogenic Uranium(IV) Precipitates. *J. Environ. Qual.* 34, 1763.

Zhu, X.Y., Lubeck, J., Kilbane, J.J., II, 2003. Characterization of microbial communities in gas industry pipelines. *Appl. Environ. Microbiol.* 69, 5354–63.

Zimina, A., Dardenne, K., Denecke, M.A., Grunwaldt, J.D., Huttel, E., Lichtenberg, H., Mangold, S., Pruessmann, T., Rothe, J., Steininger, R., Vitova, T., 2016. The CAT-ACT Beamline at ANKA: A new high energy X-ray spectroscopy facility for CATalysis and ACTinide research. In: *Journal of Physics: Conference Series*. IOP Publishing, p. 012019.

Chapter 9: (Appendix 1) Travel Bursaries, Awards and Conference Presentations

9.1 Travel Bursaries

None were awarded.

9.2 Awards

None were awarded.

9.3 Conference Presentations

9.31 Oral Presentations

- Multiple lines of evidence identify U(V) as a key and persistent intermediate during U(VI) reduction by *Shewanella oneidensis*. G.F. Vettese, K. Morris, L. Natrajan, S. Shaw, T. Vitova, J. Galanzew, J. R. Lloyd. Royal Society of Chemistry Young Researchers Meeting. October 2019. London, UK.
- Multiple lines of evidence identify U(V) as a key and persistent intermediate during U(VI) reduction by *Shewanella oneidensis*. G.F. Vettese, K. Morris, L. Natrajan, S. Shaw, T. Vitova, J. Galanzew, J. R. Lloyd. Geomicrobiology Research in Progress. June 2019. Manchester, UK.
- Microbial reduction of U(VI) by *Shewanella oneidensis* MR1. G.F. Vettese, K. Morris, L. Natrajan, S. Shaw, J. R. Lloyd. 7th NDA Seminar. January 2019. Manchester, UK.
- Investigating the role of uranium(V) during microbially mediated reduction of uranium(VI). G. F. Vettese, K. Morris, L. Natrajan, S. Shaw, T. Vitova, J. Rothe, J. R. Lloyd. SEES PGRC. November 2018. Manchester, UK.
- Microbial reduction of U(VI) by *Shewanella oneidensis* MR1. G.F. Vettese, K. Morris, L. Natrajan, S. Shaw, J. R. Lloyd. 6th NDA Seminar. January 2018. Manchester, UK.

9.32 Poster Presentations

- Multiple lines of evidence identify U(V) as a key and persistent intermediate during U(VI) reduction by *Shewanella oneidensis* MR1. G.F. Vettese, K. Morris, L. Natrajan, S. Shaw, T. Vitova, J. Galanzew, J. R. Lloyd. Actinide Migration. September 2019. Kyoto, Japan.
- Multiple lines of evidence identify U(V) as a key and persistent intermediate during U(VI) reduction by *Shewanella oneidensis* MR1. G.F. Vettese, K. Morris, L. Natrajan, S. Shaw, T. Vitova, J. Galanzew, J. R. Lloyd. Dalton Community Event. November 2018. Manchester, UK.
- Multiple lines of evidence identify U(V) as a key and persistent intermediate during U(VI) reduction by *Shewanella oneidensis* MR1. U Biogeochemistry. October 2018. G.F. Vettese, K. Morris, L. Natrajan, S. Shaw, T. Vitova, J. Galanzew, J. R. Lloyd. Ascona, Switzerland.
- Microbial reduction of U(VI) by *Shewanella oneidensis* MR1. G.F. Vettese, K. Morris, L. Natrajan, S. Shaw, J. R. Lloyd. The geochemistry and mineralogy of contaminated environments (RSC). June 2018.
- Microbial reduction of U(VI) by *Shewanella oneidensis* MR1. G.F. Vettese, K. Morris, L. Natrajan, S. Shaw, J. R. Lloyd. Microbiology Society Annual Conference. March 2017. Edinburgh, UK.
- Microbial reduction of U(VI) by *Shewanella oneidensis* MR1. G.F. Vettese, K. Morris, L. Natrajan, S. Shaw, J. R. Lloyd. 5th NDA Seminar January 2017. Manchester, UK.

- Microbial reduction of U(VI) by *Shewanella oneidensis* MR1. G.F. Vettese, K. Morris, L. Natrajan, S. Shaw, J. R. Lloyd. Royal Society of Chemistry Young Researchers Meeting. October 2017. Leeds, UK.

Chapter 10: (Appendix 2) Using Urea as an Electron Donor/ pH Conditioner for Sr Contaminated Lands

Where deemed necessary by the author; a purpose, hypothesis, significance, an experimental and a conclusion have been given for each piece of work. Most of the work was carried out by the author; when necessary any other people's work is referred to. All chemicals used were analytical grade and solutions were made using deionised water (18 MΩ).

Abstract

Batch microcosm experiments assessed the viability of urea injections to Sr contaminated subsurfaces as a bioremediation technique, using non-radioactive Sr as a surrogate to ^{90}Sr . This work assesses the capability of bacteria native to Cumbrian sediments, in samples taken upstream from the Sellafield site, to hydrolyse added urea with the aim to drive calcite precipitation and Sr co-precipitation as a cheap and environmentally friendly bioremediation treatment. Sr transport in contaminated ground waters is primarily controlled by sorption with aquifer sediments. This process is, however, reversible and treatments can be further enhanced by the co-precipitation of Sr-carbonates to calcite-like phases. Urea addition to batch microcosms stimulated urease activity producing carbonate and ammonium as breakdown products ultimately resulting in elevated the pH (9.2) and the precipitation of CaCO_3 -like minerals. Monitoring other key geochemical indicators suggested that NH_4^+ can act as an electron donor under such circumstances although further investigation is required.

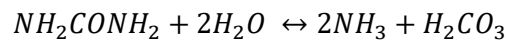
Introduction

Anthropogenic industrial activities have increased the amount of bioavailable toxic metals in the ecosphere; which, at elevated concentrations can be detrimental to all manner of life. One such pollutant is ^{90}Sr , a high yielding fission product that decays ($t_{1/2}$ 28.8 y) by beta emission to ^{90}Y ($t_{1/2}$ 64.2 h) ("Sellafield Integrated Waste Strategy," 2009). In the body Sr accumulates in areas with high Ca concentrations, such as the bones and teeth; ingestion leads to cancers of the bone, blood and skin (Huh et al., 1991; Pors Nielsen, 2004). It is therefore necessary to design a cost effective and economical method to remediate Sr contaminated lands.

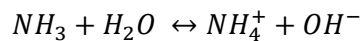
As the Sr^{2+} cation is not redox sensitive, its mobility is mostly governed by sorption. Due to their permanent structural charge and relatively low point of zero charge (PZC), Sr sorption to clays is important across a range of pH (Dyer et al., 2000; Hussain et al., 1996). At circumneutral pH and low ionic strengths ($< 10 \text{ mmolL}^{-1}$), ^{90}Sr sorbs rapidly by outer-sphere complexation to clay and mica structures; fortunately these conditions are typical of the Sellafield site ground-waters and aquifers (Paulus et al., 1992; Wallace et al., 2012). It also readily sorbs to aluminosilicates, Fe-oxides, clays and other minerals (Chorover et al., 2008; Higgo, 1987; O 'day et al., 2000; Patterson and Spoel, 1981; Saunders and Toran, 1995; Torstenfelt et al., 1982). Below pH 4, sorption to clays is limited due to occupation of the negatively charged sites within the structure resulting in repulsion of the Sr^{2+} cation

and its hydrated sphere; similarly, higher ionic strength reduces Sr sorption due to cation competition (Wallace et al., 2012). At high pH's, carbonate and strontium concentrations, Sr^{2+} may precipitate as strontianite ($SrCO_3$); or with lower Sr^{2+} concentration it may become incorporated into other carbonate or phosphate phases such as calcite or aragonite in natural and anthropogenic environments (Elderfield, 1996; Handley-Sidhu et al., 2011; Tesoriero and Pankow, 1996; Thorpe et al., 2012b; Zachara et al., 1991).

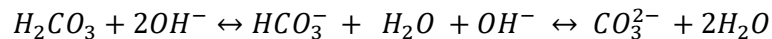
Despite not being redox sensitive, microbial metabolisms can still play an important role in the remediation of Sr contaminated lands, through either bio-sorption or changing the chemistry of the local environment (Anderson and Appanna, 1994; Ferris et al., 1995; Krejci et al., 2011). Sr can incorporate into microbially precipitated calcite. Urease producing microorganisms can hydrolyse urea to produce ammonia and carbonate, this increases pH and promotes the precipitation of carbonates and heavy metals (Burbank et al., 2012). Equations 17-20 describe the $CaCO_3$ precipitation by bacterial ureolysis in the presence of aqueous Ca^{2+} , equations 21 and 22 describe Sr incorporation/substitution into Calcite structure (Connolly et al., 2013; Stocks-Fischer et al., 1999).



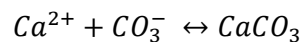
Equation 17: urea hydrolysis



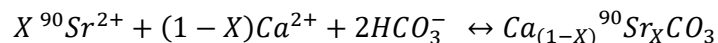
Equation 18: Protonation of ammonia causes an increase in pH



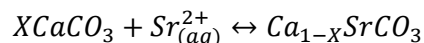
Equation 19: Deprotonation of carbonate equilibrium to try to lower pH



Equation 20: Carbonate ions precipitate calcium carbonate in the presence of calcium



Equation 21: Sr incorporation into the Ca sites within calcite structure



Equation 22: Sr Substitution into the Ca sites within calcite structure

Sr entrapment into forming calcite is highly dependent on: i) the precipitation rate of the calcite (Fujita et al., 2004; Gabitov and Watson, 2006; Lorens, 1981; Mitchell and Ferris, 2005); ii) the nature of the forming calcite, biotic calcite has a significantly higher Sr^{2+} concentrations than abiotic ($\Delta = 1250$ ppm) (Carpenter and Lohmann, 1992); iii) the temperature (Mitchell and Ferris, 2005) and iv) pH, where higher pH's also yield higher miscibility limits for $SrCO_{3(x)}$ in $CaCO_{3(s)}$ (Achal and Pan, 2011; Lorens, 1981; Tang et al., 2008; Tesoriero and Pankow, 1996). In pure culture work using *Bacillus pasteurii* and *Halomonas sp.* the rate of calcite precipitation is directly proportional to the rate of ureolysis, in accordance with (Achal et al., 2012; Fujita et al., 2000; Wu et al., 2011). Calcite precipitation can be induced on the cell surface and extracellularly. Specifically, *B. pasteurii* increased the size and size variance of crystals, and led to a greater crystal growth rate throughout the experiments, relative to bacteria-free samples (Mitchell and Grant Ferris, 2006). These precipitation mechanisms for heavy,

divalent metals has even been suggested as a protection mechanism after samples of *Sporocina pasteurii* could tolerate higher metal concentrations with added urea than without (Mugwar and Harbottle, 2016).

Urea is present in large quantities in the environment; it is present as a breakdown product in urine and is commonly used as an anthropogenic agricultural fertilizer. Ureolytic activity was demonstrated to be wide spread in Hanford sediments and geochemical modelling demonstrated consumption of urea to predict Sr removal from groundwater (Fujita et al., 2010). This work suggested not only that the degree of which Sr incorporates into calcite is proportional to the rate of calcite precipitation but also that Sr partitioning into Calcite structure would increase with time. Despite this experimental work has never been carried out to fully investigate the remediative capabilities of urea in contact with native microbial communities.

Moreover, as a major metabolite in biological anthropogenic systems; urea is the main waste product of the metabolisms of nitrogenous compounds in animals (proteins and amino acids). Uric acid is also produced, from the breakdown of nucleotides adenosine and guanosine; it may behave as a bio-ligand, interacting with metal ions (Mg, Ca, Fe, Co, Cu, Cr, Zn and UO_2); similarly it can form salts with metal ions (Davies et al., 1986; El-Megharbel et al., 2015; Moawad, 2002; V. VenkataRamana, V. J. Thyagaraju, 1992).

Methods

Sediment characterisation

Sample sediments representative of the UK Sellafield reprocessing site were collected from the Calder Valley, Cumbria, December 2017, as previously done (Law et al., 2010a). Here we believe to have similar bio-geochemical conditions to the actual site. Samples were transferred directly to Manchester in sealed sterile containers and stored at 7 °C prior to use.

Microcosm experimental

100 mL of modified artificial groundwater (Wilkins et al., 2007) (pH 7) was added to 10 g of Cumbrian sediment in 100 mL glass serum bottles. Filter sterilised urea was added by syringe and needle using aseptic technique to achieve a final concentration of 25 mM (experiments A-E); control systems contained 100 mL modified AGW and 25 mM urea (experiment S) or 100 mL of modified AGW and 10 g of Cumbrian sediment (experiments F and G). The microcosms were sampled anaerobically via syringe and needle using aseptic technique over a 95 day period, Eh, pH were measured using a calibrated electrode. $[\text{NH}_4]^+$ and $[\text{CO}_3^{2+}]$ concentrations measured by IC; Ca^{2+} and Sr^{2+} concentrations to be determined by ICPMS, urea concentration was determined spectrophotometrically (Knorst et al., 1997). 1 mL of slurry was reserved for 16S rRNA gene analysis.

Geochemical analyses

Sediment slurry was extracted from the microcosms under an Ar atmosphere using aseptic technique and centrifuged (14200 rpm, 5 min) to provide wet sediment pellets and supernatant water samples for analysis. Total aqueous Sr, Fe and Ca concentrations were measured by ICP-AES. Aqueous NH_4^+ was monitored by IC. Total bio-available Fe and bio-available Fe(II) concentrations were estimated spectrophotometrically by digestion in HCl (0.5 mL, 0.5 M, 1 hr) followed by the Ferrozine assay (Lovley and Phillips, 1987; Stookey, 1970). Urea concentrations were determined spectrophotometrically using an adapted version of the spectrophotometric assay by Knorst et al.

(Knorst et al., 1997). All standards used photometrically were calibrated daily and calibration regressions typically had $R^2 \geq 0.99$. The pH and Eh were measured with a pH/Eh meter, calibrated daily to pH 4, 7 and 10 and Eh +220 mV. The elemental composition and bulk mineralogy of the sediment were characterised by X-ray Fluorescence and X-ray Diffraction.

Results and discussion

Change in pH and consumption of urea

Microcosms spiked with urea (blue line) were able to consume 26 mM within 60 days of injection, after which they could reduce a further 50 mM of urea and a much faster rate. They also showed a steady increase in pH, up to 9.3. This correlates with urea consumption, consistent with PHREEQC modelling, the pKa of NH_4^+ (Silberberg, 2014; Stumm and Morgan, 1996) and similar work using pure cultures of *Bacillus pasteurii* (Fujita et al., 2004; Mitchell and Ferris, 2005). The slow incline towards pH 9.3 can be attributed to the buffering capacity of the sediments; this is consistent with pure culture experiments which can see major pH changes within an hour (Fujita et al., 2004; Mitchell and Ferris, 2005). In the absence of sediments, and thus a microbiological community, urea concentrations in solution control (orange line) showed negligible variation. Ammonium production was produced concomitant with urea degradation supporting ureolysis (data not included).

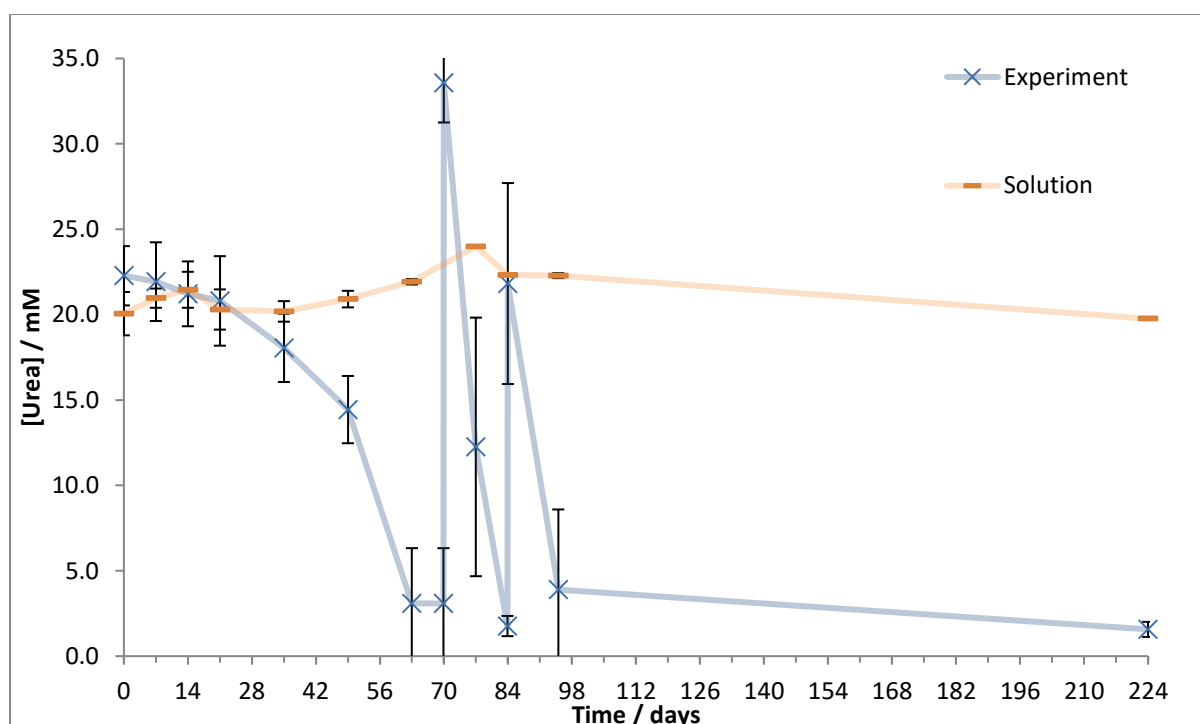


Figure 112: Urea consumption over 224 days. With the experiment in blue, and a no sediment, solution only control in orange. Error bars represent 1 standard deviation over triplicate measurements.

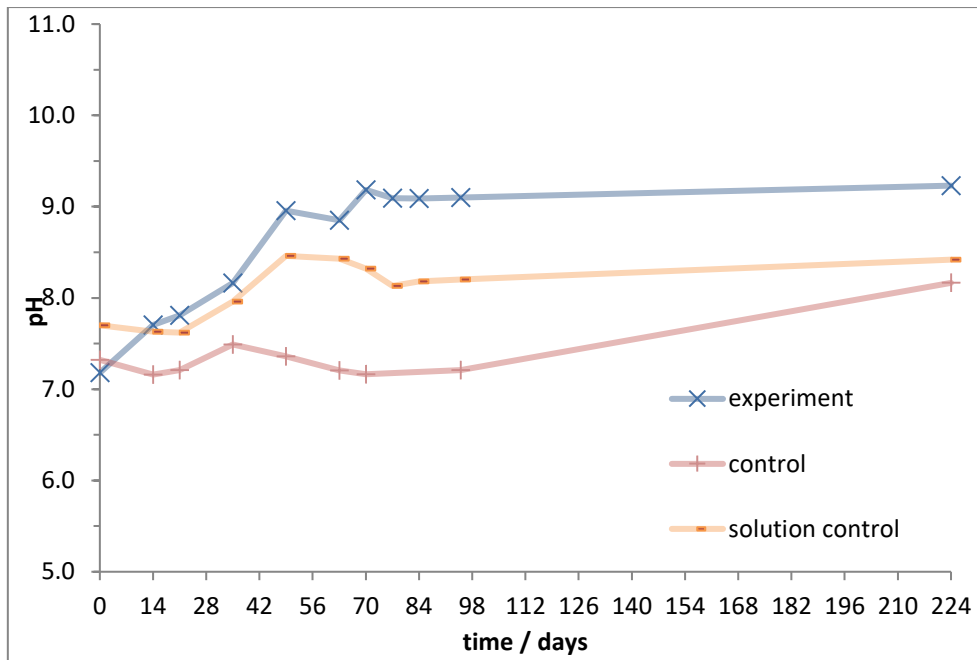


Figure 113: pH changes over 224 days. With the experiment in blue, a no urea added control in red and a no sediment, solution only (including urea) control in orange.

Sr Solution Chemistry

Initial Sr concentrations dropped due to sorption to sediments: -75 % in the experiment and -72 % in sediment control; these data are consistent with relevant literature (Wallace et al., 2012). After 225 days filtered experiments using saturated CaCO_3 solutions showed no enhanced Sr removal compared to sorption control experiments. This experiment was repeated three times and could not achieve enhanced Sr removal in urea treated microcosms.

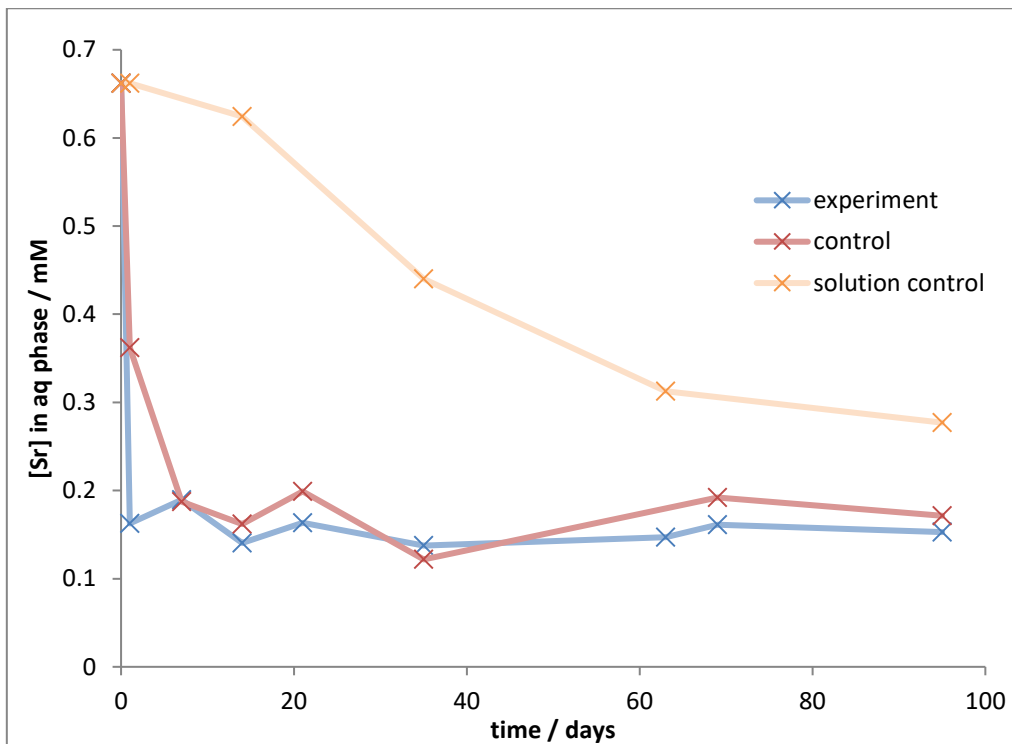


Figure 114: Sr removal in filtered experiments.

Saturation Index (PHREEQC)						
Initial Sr ²⁺ _(aq) / mM	pH	Siderite	Calcite (CaCO ₃)	Aragonite (CaCO ₃)	Strontianite (SrCO ₃)	Celestite (SrSO ₄)
1	2	-999.999	-12.1604	-12.3299	-10.5303	-0.4871
1	4	-999.999	-8.0928	-8.2623	-6.4564	-0.1758
1	6	-999.999	-4.2572	-4.4267	-2.6208	-0.1717
1	8	-999.999	-1.7755	-1.945	-0.1388	-0.172
1	9	-999.999	-0.8048	-0.9744	0.8333	-0.1725
1	10	-999.999	-0.0645	-0.2341	1.5808	-0.1746

Table 15: Saturation index for key carbonate minerals in the experimental set up as pH changes modelled using PHREEQC (ANDRA SIT database). Demonstrating strontianite precipitation between pH 8-9.

Reducing capabilities: Fe and Eh

In control sediment experiments which did not have added urea there was no change in bioavailable Fe(II) concentrations. In the experiments containing sediment and urea a significant increase in bioavailable Fe(II) concentrations was observed suggesting that the urea, or its breakdown products, may also act as a source of electrons in the presence of potential electron acceptors. Reactions involving Fe(III) reduction coupled to anaerobic ammonium oxidations producing N₂ and NO_x⁻ in sediments, coined *Femmox* reactions, have been reported but only scarcely (Yang et al., 2012). This work requires further investigation.

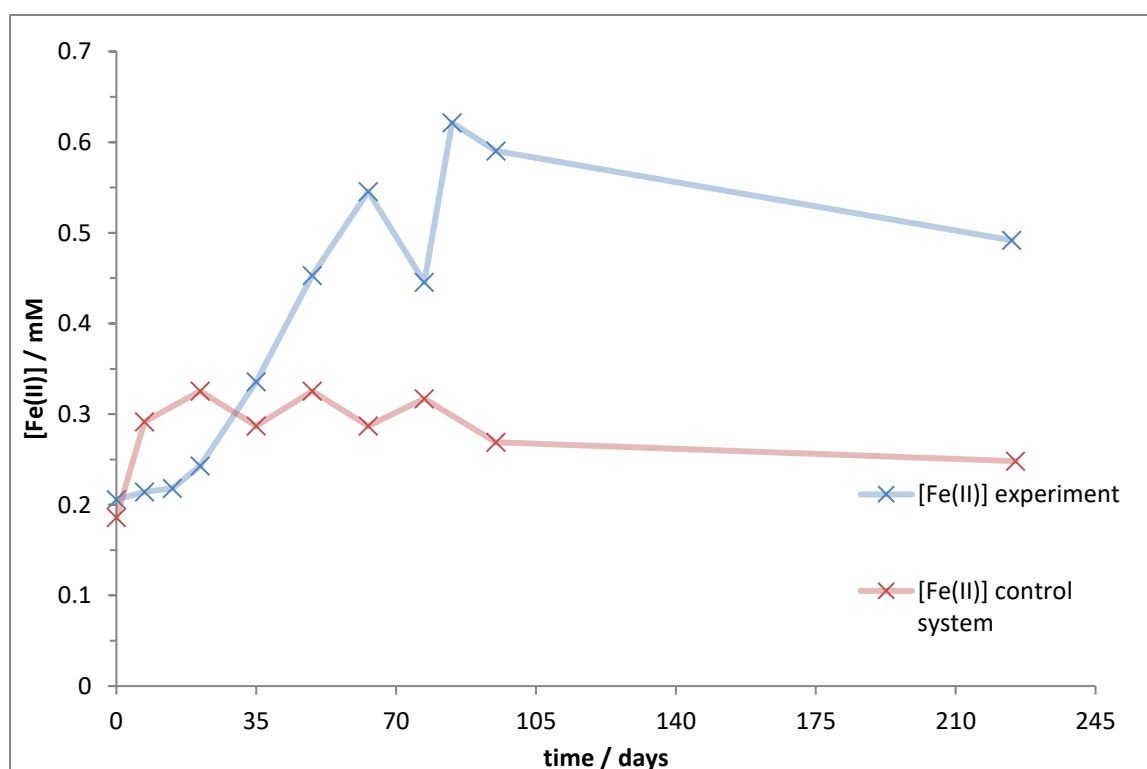


Figure 115: Changes in bio-available Fe(II) as determined *via* the Ferrozine assay.

Conclusions and Further work:

This work confirms that the indigenous bacteria present in Cumbrian soils can degrade urea, likely *via* microbial ureolysis. Unfortunately, the results did not find enhanced Sr removal after addition of urea compared to control experiments. Further work should attempt this experiment using a sediment of

a different lithology. Furthermore, the potential discovery of Fe(III) reduction connected to microbial ureolysis may provide a suitable candidate for the remediation of U or Tc contaminated sediments.

Chapter 11: (Appendix 3) Preparation of Uranyl dichloride Stock Solutions

UO_3 (1.369 g, mass U 1.139, 4.79 mmol) was dissolved in warm HCl (1 M, 10 mL) with a watch glass on top to minimize evaporation. The volume was reduced until the solution was on the point of recrystallization, over which time the colour changed from deep orange to bright yellow to a fluorescent green. The solution was dissolved in 10 mL DI water and allowed to cool. The cool solution was filtered through a 0.22 μm filter into a 25 mL volumetric flask which was then made up to 25 mL with DI water. Yield 1.016 g U_{nat} (89 %, 40660 ppm [determined by ICP-MS]), corresponding to 1.456 g UO_2Cl_2 pH 2.18 (**Error! Reference source not found.**). BromoPADAP assay yielded fast concentration measurements of 40838 ppm.

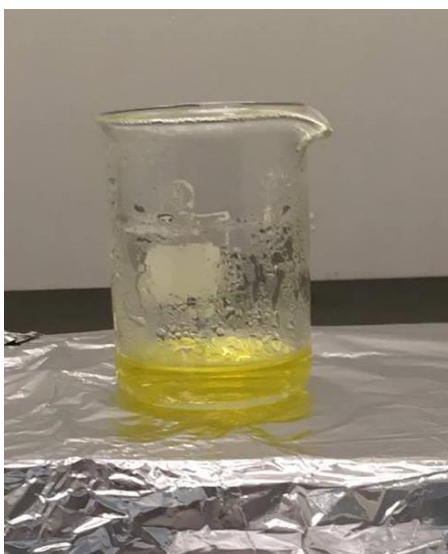


Figure 116: the bright yellow UO_2Cl_2 , HCl solution in the preparation of UO_2Cl_2 stock.

- End -